The Solar Origins and Earth Impacts of Space Weather

A dissertation submitted to the University of Dublin
for the degree of Doctor of Philosophy

Tadhg Garton
Trinity College Dublin, July 2020

School of Physics
University of Dublin
Trinity College

Declaration

I declare that this thesis has not been submitted as an exercise for a degree at this or any other university and it is entirely my own work.

I agree to deposit this thesis in the University's open access institutional repository or allow the library to do so on my behalf, subject to Irish Copyright Legislation and Trinity College Library conditions of use and acknowledgement.

Name: Tadhg Garton

Signature: .... **Date:** ....

For those who have loved and believed in me.
Without your support I would be nowhere.

Glossary

ACE	Advanced Composition Explorer
AIA	Atmospheric Imaging Assembly
ANNs	Artificial Neural Networks
ARs	Active Regions
ASSA	Automatic Solar Synoptic Analyzer
CCD	Charged-Couple Device
CDF	Cumulative Distribution Function
CH	Coronal Hole
CHARM	Coronal Hole Automated Recognition and Monitoring
CHIMERA	Coronal Hole Identification via Multi-thermal Emission Recognition Algorithm
CHs	Coronal Holes
CME	Coronal Mass Ejection
CMEs	Coronal Mass Ejections
CNNs	Convolutional Neural Networks
CNO	Carbon-Nitrogen-Oxygen
CRIS	Cosmic Ray Isotope Spectrometer
DCHB	Distance from Coronal Hole Boundary
DNs	Data Numbers
EIT	Extreme-Ultraviolet Imaging Telescope
EPAM	Electron, Proton, and Alpha-particle Monitor
ESA	European Space Agency
EUV	Extreme Ultraviolet
EVE	Extreme Ultraviolet Variability Experiment

GICs	Geo-Magnetically Induced Currents
GNSS	Global Navigation Satellite Systems
GOES	Geostationary Operational Environmental Satellite
HELIO	Heliophysics Integrated Observatory
HMI	Helioseismic and Magnetic Imager
HSI	Hue-Saturation-Intensity
HSSW	High Speed Solar Wind
L1	First Lagrangian Point
LASCO	Large Angle and Spectrometric Coronagraph
LASP	Laboratory for Atmospheric and Space Physics
LMSAL	Large Angle and Spectrometric Coronagraph
LOS	Line-Of-Sight
LWS	Living With a Star
MDI	Magnetic Doppler Imager
ML	Machine Learning
MOSWOC	Met Office Space Weather Operations Center
NASA	National Aeronautics and Space Administration
NNs	Neural Networks
NOAA	National Oceanic and Atmospheric Administration
PDF	Probability Distribution Function
PE	Prediction Efficiency
PFSS	Potential Field Source Surface
PIL	Polarity Inversion Line
QS	Quiet Sun

RGB	Red-Green-Blue
RMS	Root Mean Squared
SDO	Solar Dynamics Observatory
SEPICA	Solar Energetic Particle Ionic Charge Analyzer
SIS	Solar Isotope Spectrometer
SMART	SolarMonitor Active Region Tracker
SOHO	Solar and Heliospheric Observatory
SPoCA	Spatial Possibilistic Clustering Algorithm
STEREO	Solar Terrestrial Relations Observatory
SUVI	Solar Ultraviolet Imager
SWEPAM	Solar Wind Electron, Proton and Alpha Monitor
SWICS	Solar Wind Ion Composition Spectrometer
SWIMS	Solar Wind Ions Mass Spectrometer
SWPC	Space Weather Prediction Center
ULEIS	Ultra Low Energy Isotope Spectrometer
WDCG	World Data Centre for Geomagnetism
WS	Wang-Sheeley
WSA	Wang-Sheeley-Arge

Abstract

Coronal Holes (CHs) are expansive, low density, open magnetic field regions which appear dark in extreme-ultraviolet (EUV) images of the solar corona. CHs are associated with the acceleration of the high speed solar wind (HSSW), which in turn impacts the geomagnetic field of Earth, causing geomagnetic storms. To date, sufficient automated monitoring of CHs has not been performed, and CH properties have not been fully correlated with the properties of HSSW streams.

In order to accurately observe and monitor CHs, a new method of multi-thermal segmentation was created to rapidly, consistently, and effectively identify CHs in the solar atmosphere. This algorithm, named the Coronal Hole Identification via Multi-thermal Emission Recognition Algorithm (CHIMERA), is the first of its kind and has been used to segment CHs from spacecraft data over two solar cycles. CHIMERA continuously runs live at *SolarMonitor.org*, outputting segmented images and properties every hour.

A detailed investigation into the connections between CHs and their corresponding HSSW streams was undertaken using CHIMERA detections and L1 spacecraft measurements from 2016-2017. This comparison focused on the CH width properties of CHs and the duration and velocity properties of the corresponding HSSW streams. A strong correlation was found between CH widths and the aforementioned properties, and from this multiple new equations were derived from empirical measurements of the solar wind. These equations model the longitudinal expansion of both the solar wind and the expansion of the solar wind flux tube, accounting for a differential velocity of projection of plasma between the leading and trailing edge of HSSW streams. Most

notably a derivation was obtained for a simple prediction of solar wind duration, of the form $\Delta t_{SW} \approx 0.09\Delta\theta_{CH}$.

A long term investigation into the distribution of CH properties was performed for a 22-year time period from 1998 - 2019. This investigation rendered a probabilistic distribution of CH properties, such as area, flux, and magnetic polarity characteristics. These probabilistic distributions can be used to estimate the occurrences of CHs within a solar cycle, and furthermore as a predictor for more extreme CH events. These distributions combined with already established correlations between CHs and the HSSW renders the probabilistic distribution of corresponding HSSW streams, and hence, estimates the average number of geo-effective storms in an 11-year period.

Finally, the extensive CHIMERA catalogue of CH segmentations and properties was used to create a more accurate model for solar wind property predictions using machine learning techniques. A collection of machine learning methods applied to CHIMERA detection from 2010 - 2017 found an improvement of solar wind velocity predictions upon the current operational benchmark, a 27-day persistence model. These improvements were quantified through a number of fitting measurements, with persistence modelling having a coherence = 0.52, root mean squared = 93.7 km s^{-1}, and a running artificial neural network model with a coherence = 0.59, root mean squared = 77.4 km s^{-1}.

This thesis has culminated in a significant improvement in the identification of CHs and the predictability of their associated HSSW streams. Future work will expand upon these results through the application of more sophisticated machine learning methods on the entire CHIMERA property database, as well as further investigation into to the correlation of CH and HSSW stream properties to better predict the occurrence of geomagnetic activity. Furthermore, investigations into the correlations between CH magnetic polarities and spherical harmonics observed in helioseismology may assist in unveiling the mysteries of the internal structure of the Sun.

Acknowledgements

Foremost, I wish to acknowledge and thank my supervisors, Prof. Peter Gallagher and Dr. Sophie Murray, for their enthusiasm, guidance, knowledge, and patience they readily supplied to me during my research. Without them, this research would not be possible

I thank the members of the Astrophysical Research Group in both Trinity College and the Dublin Institute of Advanced Studies for their assistance, positivity and camaraderie during my studies.

Dr. Sean Blake and Dr. Joan Campanya in particular deserve my gratitude for their tolerance of a stressed out work mate as well as the inspiration and determination they have nurtured in me.

I would like to thank the Irish Research Council for funding my research and the subsequent stress it has caused. I hope my work stands testament to what is possible with a small amount of funding.

To my brothers and sisters (Cormac, Alana, Katie and Molly) I thank for providing a nurturing and intellectually stimulating environment for me to grow up in. People say you can't pick your family, but if I could I would still choose you all every time.

I wish to thank my parents (Aisling and Mark) for providing for me, for believing in me, for pushing me to do my best, and most importantly for relentlessly fighting to give me the best life you can.

Finally, I would like to thank Shauna for the laughter and love. I may work on the Sun, but you are still the brightest thing in my Universe.

List of Publications

1. **Garton, T.M.**, Gallagher, P.T., & Murray, S.A.
   "Automated Coronal Hole Identification via Multi-Thermal Intensity Segmentation"
   Journal of Space Weather and Space Climate, 2017
2. **Garton, T.M.**, Murray, S.A., & Gallagher, P.T.
   "Expansion of High Speed Solar Wind Streams from Coronal Holes through the Inner Heliosphere"
   Astrophysical Journal Letters, 2018
3. **Garton, T.M.**, McIntyre, O., Murray, S.A., & Gallagher, P.T.
   "Long Term Coronal Hole Statistics Across Two Solar Cycles"
   in preparation, 2019
4. **Garton, T.M.**, Maloney, S., Campanya, J., Murray, S.A., & Gallagher, P.T.
   "Improvements to Solar Wind Prediction using Machine Learning Methods"
   in preparation, 2020

Contents

List of Figures

List of Tables

1

Introduction

With the ever-increasing reliance on digital and electric technologies in the last two centuries, society has become exposed to an array of potentially damaging space weather effects. “Space weather” is an all encompassing descriptor of the conditions of Earth and near interplanetary space influenced by the dynamics of the Sun. The hazards these conditions can create include disruption to radio and GPS communications, damage to satellites, and increased radiation risk to polar flights. Arguably, the most reliable and regularly impactful cause of everyday space weather events at Earth (and the primary focus of this thesis) are Coronal Holes (CHs). In this chapter, the generation of solar phenomena and their outward transportation are discussed. Following this, the features of the Sun that produce space weather effects are described, and the impacts these features have on interplanetary space and on Earth are outlined, along with a summary of the other chapters in this thesis.

1.1 Solar Structure

Our lives revolve around the presence of a G2 type star located at the center of our solar system, the Sun. Being the closest star to Earth, it has the largest impact on our lives through radiative and magnetic processes. Throughout human history the importance of the Sun has been emphasized through religious figures, spiritual association or even scientific understanding. The early civilizations of Ireland recognized the importance of the Sun, and grew to understand its motion to a high enough degree to construct Newgrange, a neolithic passage tomb, built in ~3200 BC. The chambers of Newgrange become illuminated by the Sun only on the winter solstice, signifying the peak of winter and the gradual return of warmer seasons and associated plant blooming. Similar admiration was shown by early man for the aurora, the earliest dated record of which comes from an ancient Babylonian clay tablet. The tablet records the night of March 12/13th, 567BC, when an unusual "red glow" was observed in the sky (Stephenson *et al.*, 2004). Linking the presence of the aurora to the Sun was not proposed until the mid-19th century by Sabine (1852) who observed a correlation between geomagnetic disturbances and the appearance of aurora with times of high sunspot numbers on the solar surface. In 1859, a more accurate recognition was made of the properties of solar features by Carrington (1859) when a solar flare event was observed. Several hours later, a severe geomagnetic storm was recorded by magnetometers around the world (Tsurutani *et al.*, 2003). The aurora became brilliantly vibrant and currents generated in telegraph systems resulted in wide scale failure and fires in a telegraph office. These fires were caused by a power overload from currents induced into the telegraph wires, which ignited paper within the office. This event was considered as one of the largest historical geomagnetic storms and has subsequently been named the *Carrington event*. Since this first widely discussed event, many more observations of lesser flares and other geo-effective solar phenomena have occupied the attention of the field of space weather science. The study of the solar structure and causes of geo-magnetic activity have continued for the last 160 years.

The solar structure is categorized into the solar interior and exterior, the sub categories and features within are labeled in Figure 1.1.

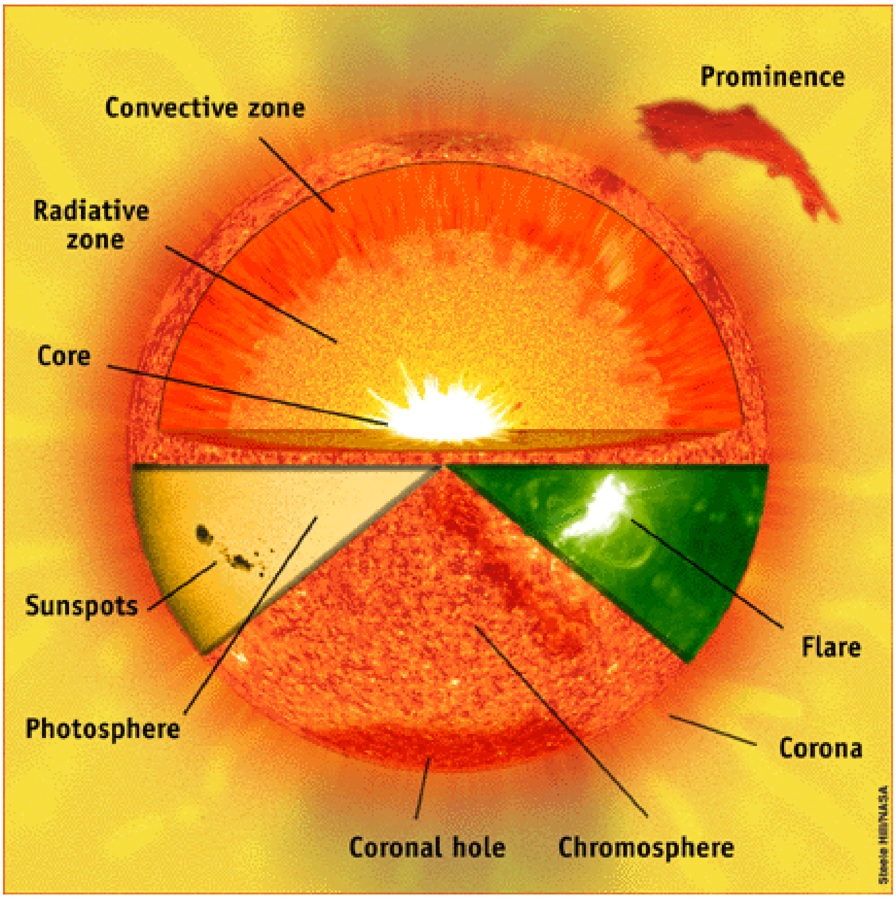

Figure 1.1: Layers and features of the solar interior and atmosphere. Image courtesy of Steele Hill/ NASA.

1.1.1 Solar Interior

The solar interior is segmented into three main zones, the core, radiative zone and convective zone, by the governing processes of energy transfer outwards from the solar center (Phillips, 1995).

The *core* is the hottest, 15 MK, and densest, $1.5 \times 10^5 kg/m^3$, part of the Sun, at an estimated pressure of 26.5 PPa at its center (Basu *et al.*, 2009; Grolier, 1998). Within the core, the bulk of energy comes from hydrogen nuclei, the most abundant primordial element (Molaro, 2008). These nuclei fuse together under intense gravitational pressure to produce helium nuclei, in an exothermic process, see Equations 1.1-1.3 (Adelberger *et al.*, 2011; Salpeter, 1952).

$$^{1}H +^{1} H \rightarrow^{2} D + e^{+} + \nu_{e} \tag{1.1}$$

$$^{2}D +^{1} H \rightarrow^{3} He + \gamma \tag{1.2}$$

$$^{3}He +^{3} He \rightarrow^{4} He +^{1} H +^{1} H \tag{1.3}$$

The remaining energy source originates from the Carbon-Nitrogen-Oxygen (CNO) cycle, however, due to its relatively low contribution to the global energy production within the core, it will not be discussed here.

The process of energy generation through fusion occurs within the core from 0 - 0.25 $R_{\odot}$ (García *et al.*, 2007) which undergoes rapid rotation at a rate four times higher than the outer radiative envelope of the Sun (Fossat *et al.*, 2017). Beyond the boundaries of the core the gravitational pressure becomes lessened to an extent that radiative pressure governs, and energy created by the core undergoes gradual transport outwards from the Sun's center through electromagnetic radiation (Ryan & Norton, 2010). This layer is known as the *radiative zone.* In this zone, plasma is hot, ∼2 - 7 MK, and density varies largely with radius, ranging from $2 \times 10^{4} kg/m^{3}$ at 0.25 $R_{\odot}$ to 200 kg/m^{3} at 0.75 $R_{\odot}$. Within this layer photons bounce from particle to particle becoming partially trapped in the radiative zone, where it takes ∼171,000 years to travel from 0.25 - 0.75 $R_{\odot}$ where upon it enters the *convective zone* (Christensen-Dalsgaard *et al.*, 1991; Spruit, 1974). The convective and radiative zones are separated by their underlying processes of energy transfer, with an interface layer, known as the tachocline, separating the two (Spiegel & Zahn, 1992). The convective zone has a temperature of 2MK at its deepest. At and below this temperature heavier ions are able to retain some of their electrons, which significantly increases the opacity of the convective zone. Energy supplied by the radiative zone is absorbed by particles in the convective zone, which further propagates upwards through convection columns to the solar atmosphere. Volumes of plasma traveling upward in this zone rapidly cool and expand, reaching ∼1 $R_{\odot}$ at a temperature of 5,800K and density of $2 \times 10^{-4} kg/m^{3}$, where their convective motions are visible as granules or supergranules (Stein & Nordlund, 1989).

1.1.2 Solar Atmosphere

The solar atmosphere exists above the convective zone and can be subdivided into the photosphere, chromosphere, transition region and the corona.

The photosphere is commonly known as the solar surface due to being the first observed section of the solar atmosphere. With an average temperature of ~5800K, the photosphere emits as a blackbody with a peak intensity at 500nm, appearing green within the visible spectrum. Hence, this layer is the easiest layer of the solar atmosphere to observe. The photosphere lacks large scale structure and generally appears to be a rather homogeneous mass, however it is possible to observe granulation caused by convection cells from the convective zone and small, dark regions known as sunspots on smaller scales. Cellular flow of these granules is indicative of a larger network flow of plasma known as supergranulation, which plays a role in the transport of magnetic flux around the photosphere via the large-scale motion of charged ions. The aforementioned sunspots are relatively cool compared to the surrounding photosphere with an average temperature of ~4500K and are known to be zones of high magnetic activity with an average magnetic field of ±1kG, compared to the ±10G of the surrounding quiet photosphere (Avrett, 1990; de Jager, 1965; Mackay & Yeates, 2012; McIntosh, 1990). When observing this layer of the solar atmosphere, regions near the solar limb typically appear darker. This effect is due the spherical geometry of the Sun and the optical depth of the photosphere. Photons originating with a perpendicular velocity to the solar surface will be able to escape from the solar interior from a further depth than a photon traveling with a slant to the solar surface. Photons escaping from deeper regions originate from a hotter and hence brighter region as described by the Stephan-Boltzmann Law

$$L = \sigma T^4 \tag{1.4}$$

where L describes the local luminosity, T is the local temperature, and σ is the Stephan-Boltzmann constant. Photons from near the solar limb travel perpendicular to the radial direction and hence travel through thick plasma for relatively longer. Thus, for a photon to escape the corona from the solar limb and be visible to an observer, it must originate from the upper, cooler, dimmer regions of the photosphere. The Solar rotation is not constrained to rigid body rotation. Typically differential rotation is observed in the photosphere with a rotational period of ~24 days at the equator and ~30 days at the poles (Schou *et al.*, 1998). This differential rotation is responsible for the shearing of sunspot regions and the general morphing of the solar magnetosphere (Babcock, 1961; Schou *et al.*, 1998). For operational purposes, these varying rotational periods are averaged to a value of ~27 days, known as a Carrington rotation.

Due to these varying rotational periods, as well as the orbiting of the Earth around the Sun, a variety of coordinate systems have been created to describe the location of solar features both on the Sun and relative to an Earth-based observer. Coordinate systems are separated into Helioprojective, Heliocentric, and Heliographic, all of which are described in great detail by Thompson (2006). Helioprojective coordinate systems describes locations on the Sun as if the Sun is a two-dimensional image in the sky. X and Y coordinates are described in arcsecond and arcminute angles relative to an observer at Earth, and are typically centered on the Sunward Sun-Earth line. Heliocentric coordinate systems describe locations on the Sun similarly to helioprojective coordinate systems, however locations are described in physical units, typically megameters (Mm). Heliographical coordinate systems describe locations on the Sun as locations on the surface of a sphere, hence use axes of latitude and longitude, typically in units of degrees. This coordinate system has two main variants, namely Stoneyhurst and Carrington heliographic coordinates. The Stonyhurst heliographic coordinate system is differentiated by its origin existing at the intersection of the solar equator and the central meridian as seen from Earth. Thus, the coordinate system remains fixed with respect to Earth, while the Sun rotates. The Carrington heliographic coordinate system is differentiated by its relative rotation with the Sun. This coordinate system can be further separated into a rotation rate following the sidereel rotation of the Sun, at ≈25 days, or at a synodic rotation with respect to the Earth's movement, at the aforementioned ≈27 day average.

The chromosphere ranges from ~0.1 - 1.5 Mm above the solar surface, across which the local temperature varies from ~6000 to 20000 K. The chromosphere is named for the red-pink colour exhibited due to the high abundance of Hα emission at a wavelength of 6563Å (Vernazza *et al.*, 1981). This atmospheric layer was only visible during eclipses due to the relatively low intensity in the visible spectrum compared to the photosphere, however, it can now be easily observed though telescopes using Hα filters. Observations of the chromosphere show large jets of material erupting from the surface in large explosive events known as solar flares, caused by a warping and resettling of the local magnetic fields. These flares can throw plasma up to ∼7Mm before cooling, condensing, and falling back under gravitational pull in the form of "coronal rain" (Antolin *et al.*, 2012). Filaments are another distinctly visible feature on the chromosphere, where a large amount of material becomes trapped, usually along the *polarity inversion* points in magnetic field lines. These polarity inversion points mark the spatial location separating a magnetic field structure based on its opposing polarities. These points form a continuous structure, known as a polarity inversion line (PIL) which separates two expansive regions of opposing magnetic polarity. The trapped filament material becomes dense and cool, allowing it to absorb light from the underlying solar atmosphere, causing the appearance of dark, thin, cloud like structures in Hα images.

The transition region separates the chromosphere from the hot corona. While an extremely thin layer (∼200 km), it is recognizable for the high temperature gradient ranging from 20000K to ∼1MK across it (Mariska, 1992; Phillips, 1995). This large temperature increase with height is visible in Fig. 1.2 and, to date, the cause of this phenomenon is not understood, however multiple theories have been proposed, ranging from small scale magnetic reconnection events occurring continually in the corona generating a large amount of energy (Parker, 1972), to a wave propagation carrying energy from the solar interior to the corona (Schatzman, 1949). Within this region magnetic forces become dominant and particle motion becomes governed by magnetic pressure instead of gravity or gas pressure.

The corona is an aura of plasma that surrounds the Sun and extends millions of kilometers into space (Aschwanden, 2005). This region can be seen with the naked eye during a total solar eclipse. The quiet corona has a mean electron density of $\sim 1.6 \times 10^9$ cm^{-3} and temperature of ∼1 MK (Allen *et al.*, 2000; Feldman *et al.*, 1978; Warren & Brooks, 2009), which allows the ionization of hydrogen into loose protons and electrons. The low ratio of plasma pressure to magnetic pressure concludes particle motion in the corona is governed by magnetic forces. This ratio

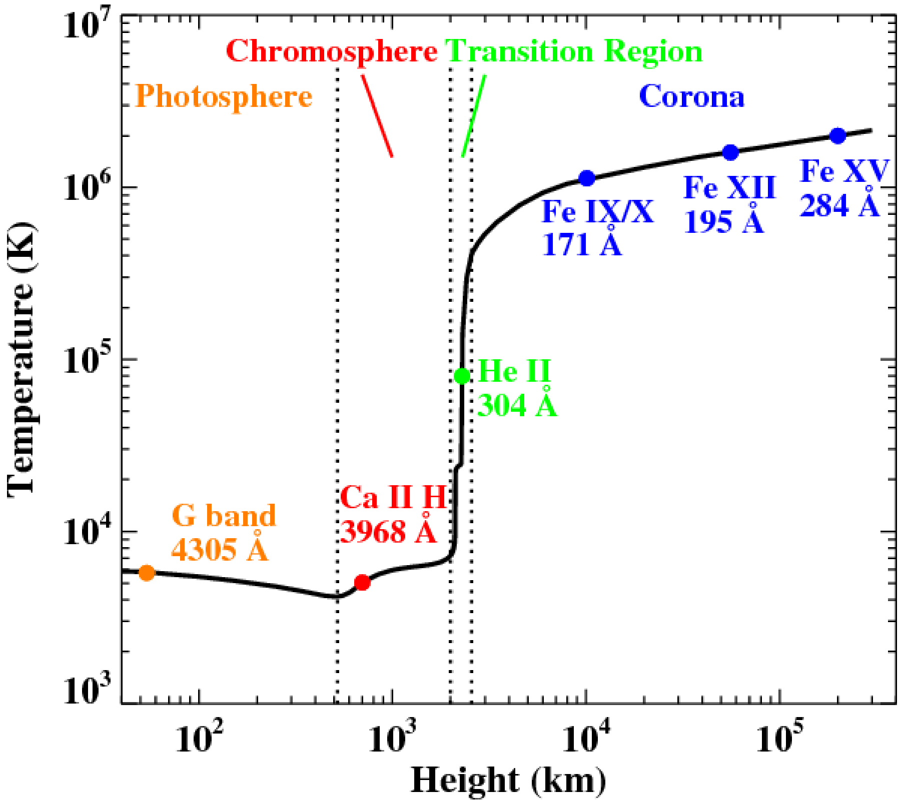

Figure 1.2: The model temperature profile of the solar atmosphere with height. Notable emission lines are marked within each atmospheric layer (Yang *et al.*, 2009).

is quantified by a measurement known as the plasma beta (β), and is calculated as:

$$\beta = \frac{8\pi n k_b T}{B^2} \tag{1.5}$$

where T is the plasma temperature, B is the magnetic field strength permeating through the plasma, n is the number density of the plasma, and k_b is the Boltzmann constant.

The plasma β is significantly in favour of magnetic motion due to the low relative atomic density of the high solar atmosphere and the relative strength of the underlying solar magnetic field. The solar magnetic field is generated by a dynamo at the tachocline. In its simplest form, the solar magnetic field takes a dipole-like shape, however due to the interchange between toroidal and poloidal magnetic field components in the dynamo, the magnetic field evolves to become progressively more complex (Babcock, 1961). The mechanism that produced the solar dynamo is an area still under research (Charbonneau, 2010). The complexity of the solar magnetic field reaches a peak at solar maximum before the magnetic poles are reversed and the field gradually returns to a solar minimum dipolar field. This process repeats on an $\sim$11 year cycle, typically referred to as the solar cycle or sunspot cycle. This cycle has been observed through evolutions in the emergence of ARs and CHs, and the overarching magnetic complexity observed in butterfly diagrams of magnetic features of the corona. After two solar cycles, $\sim$ 22 years (the Hale cycle), the magnetic field is restored to its initial state. The relative complexity of the magnetic field governs the shape of the corona plasma, and furthermore governs the predominance of typical features observed in the coronal plasma.

1.2 Coronal Features

Features of the corona plasma are differentiated by their relative temperature and density properties. The features are mostly magnetically dominated and hence their appearance is largely governed by the period of the solar cycle. These features are broadly categorized into quiet Sun (QS), active regions (ARs), flares, filaments, and CHs. A collection of these features are identified in a 193 Å image of the Sun taken by the Atmospheric Imaging Assembly (AIA; Lemen *et al.*, 2012) Instrument on-board the Solar Dynamics Observatory (SDO; Pesnell *et al.*, 2012) in Figure 1.3.

1.2.1 Quiet Sun

The QS is a relative term for the ambient corona remaining outside of other identified features of ARs, CHs, and filaments (Aschwanden, 2019). The QS is a dynamic system of energy and plasma transfer, ranging from small scales such as nanoflares, network heating, and bright points, to large scale structure such as transequatorial loops and coronal arches (Aschwanden, 2005). The differentiation between QS and ARs is made difficult due to the most large scale features of the QS being rooted in ARs. A simplistic definition of QS regions are all areas of closed magnetic field

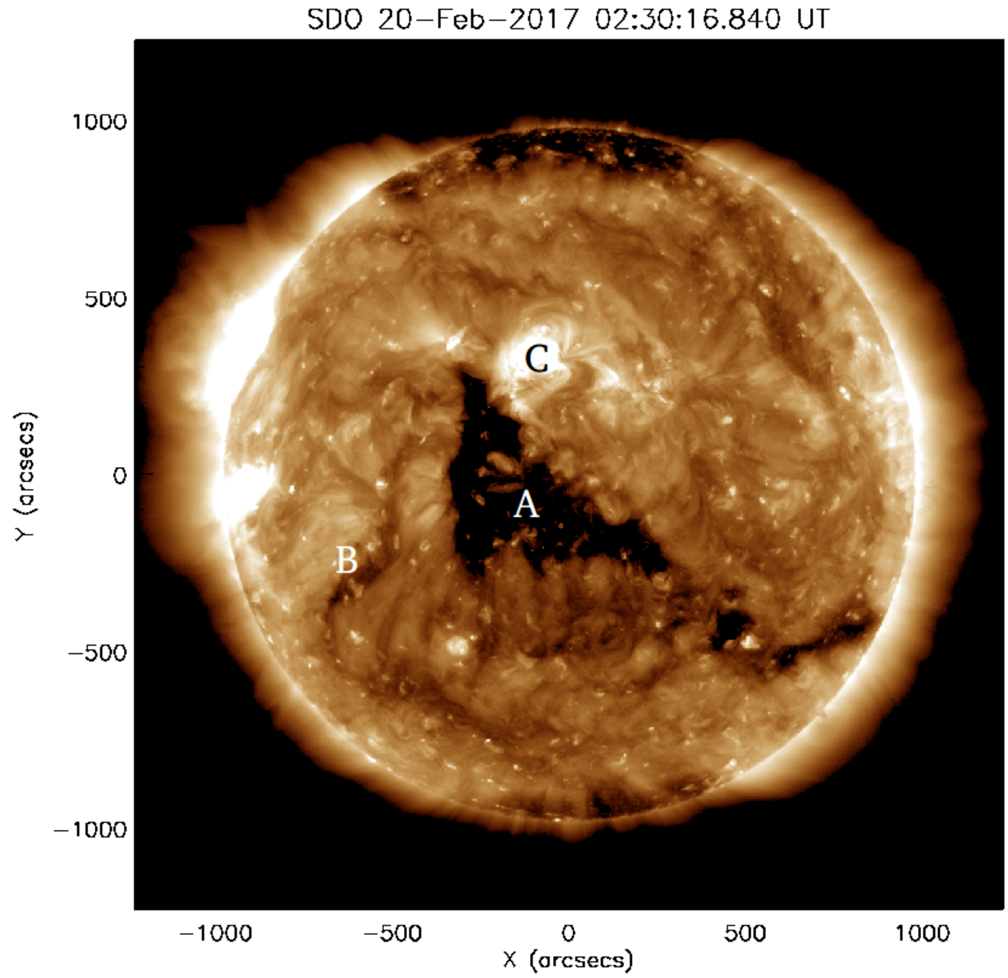

Figure 1.3: A 193 Å image observed by the Atmospheric Imaging Assembly onboard the Solar Dynamics Observatory for February 20th, 2017, with a coronal hole, filament, and an active region labeled A, B, and C respectively.

in the solar corona, not associated with ARs. QS can be further characterised by its relatively low, or lacking, plasma radial flow speeds. Within the quiet corona, plasma flow speeds range from 0-5.5 km s^{-1} (Brekke *et al.*, 1997a; Hassler *et al.*, 1991), which pales in comparison to the rapid flows of CHs, $\sim$10 km s^{-1} (Cushman & Rense, 1976; Orrall *et al.*, 1983), and AR loops, $\sim$25 km s^{-1} (Brekke *et al.*, 1997b).

1.2.2 Active Regions

ARs are a collection of local, strongly polarized magnetic loops which are connected to sunspot groups in the solar photosphere. These magnetic loops typically have a field strength of $\sim \pm 100$G and are observed in Extreme Ultra-Violet (EUV) images of the corona by the emitting plasmas of the corona trapped in their magnetic field (Phillips, 1995). Due to the intense magnetic structure of ARs, they exhibit a higher average temperature than the surrounding QS plasma of 3.2 MK (Landi & Feldman, 2008). AR formation typically is correlated with the presence of sunspots, which suggests they are more numerous during the solar maximum period of the solar cycle when sunspots are more common. AR footpoints are bound to these sunspot footpoints, however the sunspots are immersed in the convective currents of the solar convective zone. This effect combined with the differential rotation of the solar surface, known as the $\alpha - \omega$ effect, causes a drift of these sunspots relative to one another. This $\alpha - \omega$ effect is a combination of the ω effect, whereby magnetic fields are stretched and wound about the Sun in the latitudinal direction due to differential rotation, and the α effect, whereby magnetic fields are twisted due to the effect of the Sun's rotation on the rising tubes of magnetic field from deep within the Sun (Cameron *et al.*, 2017). This drifting causes distortions and twisting of the overlying magnetic loops, creating an ever-more complex magnetic region until a magnetic reconnection or flaring event occurs.

1.2.3 Flares

Flares are the release of radiation across the entire electromagnetic spectrum known to be associated with sudden reconnection of magnetic field lines in the solar corona to a less complex field state (Fletcher *et al.*, 2011). This reconnection is only possible when opposite polarity field lines come together in proximity and an inflow of plasma occurs perpendicular to the magnetic field lines and an outflow occurs parallel to field lines. This results in a pinching of the magnetic field until the field reaches an X-shaped point, snaps and is rearranged to a more simplistic loop structure, as observed in Figure 1.4 (Gold & Hoyle, 1960). This rearrangement releases a significant amount of energy such as high energy X-ray electromagnetic photons, low energy radio emissions, a Sun-ward projection of electrons within the

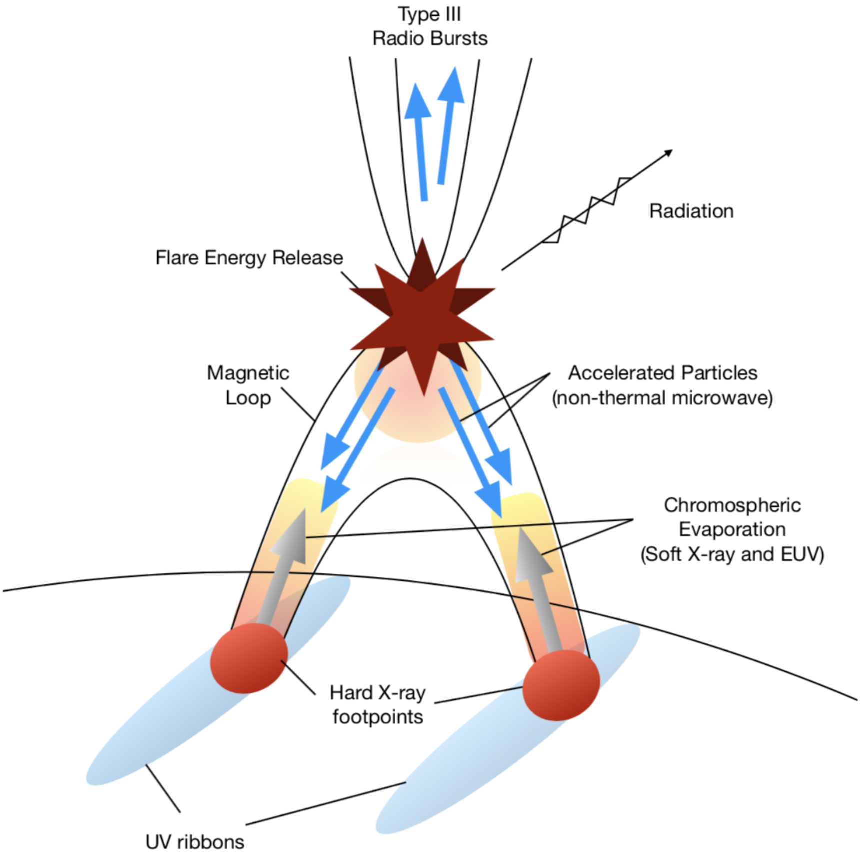

Figure 1.4: Model of magnetic reconnection in an active region causing a solar flare (Hayes, 2019). Magnetic fields reconnect at the red star releasing energy in the form of radiation and kinetic energy in electrons. The energetic electrons travel along the magnetic field lines through the low density corona until they are incident on the dense photosphere where electron scattering and hard X-ray emission occurs. The upper magnetic fields that undergo reconnection typically are projected outwards from the Sun and can produce a coronal mass ejection.

new magnetic loop structure, and sometimes an ejection of plasma outward from the Sun into interplanetary space referred to as a coronal mass ejection (CME; see Section 1.3.4). During this energy release, the average temperature in the flaring loop rapidly rises above typical AR temperatures to $\sim$ 10 MK (Ryan *et al.*, 2012). Flare occurrence rates are difficult to predict and can vary from $<$ 1 per month to multiple flares occurring within hours from a single AR. These flares are classified by the peak flux of X-ray photons observed at Earth by the Geostationary Operational Environmental Satellite (GOES; Menzel & Purdom, 1994.) into A, B, C, M, and X class flares, ranging logarithmically from A class, $<10^{-7}\ Wm^{-2}$, to X class, $>10^{4}\ Wm^{-2}$. Often magnitudes are associated to further differentiate flare energy within classes, e.g. M8.1 class flare is more energetic than an M1.0 flare. The severity of flaring events is inversely proportional to their frequency. Small scale flares (A, B, C) occur often while significant flares (M, X) occur rarely. The largest flare in recorded history during the Carrington event was estimated to emit enough energy to be classified as a X45 flare (Cliver, Edward W. & Dietrich, William F., 2013). This event was energetic enough to be visible to the human eye and had a significant impact on Earth, being powerful enough to indirectly cause disruption in telegraph offices.

1.2.4 Filaments

Filaments, known as prominences when observed off the solar limb against the dark background of space, are one of the most common features found in the solar corona. Filaments appear on-disk as elongated dark lines or curves against background optical or EUV images. However, off-limb these features appear relatively bright, as observed in Figure 1.5, and are known as prominences. Observations of filaments show rapid evolution and a fine dark structure composed of long thin magnetic loops, appearing like threads, aligned at $\sim 30^{\circ}$ to the prominence spine. Plasma within a filament is typically one hundred times cooler and denser than the surrounding coronal material, which causes the feature to be optically thick in EUV wavelengths (Parenti, 2014). To remain at such low relative temperatures and high relative densities, filaments must be thermally insulated and its plasma bound from convective or conductive dissipation of heat. Multiple models have been constructed to identify the formation of this insulated system from a simple collection of coronal loops along a magnetic PIL (Antiochos *et al.*, 1994; van Ballegooijen & Martens, 1989). The prevailing theory suggesting shearing motion between magnetic footpoints encourages reconnection and the creation of a trapped, elongated set of magnetic field lines where plasma becomes insulated

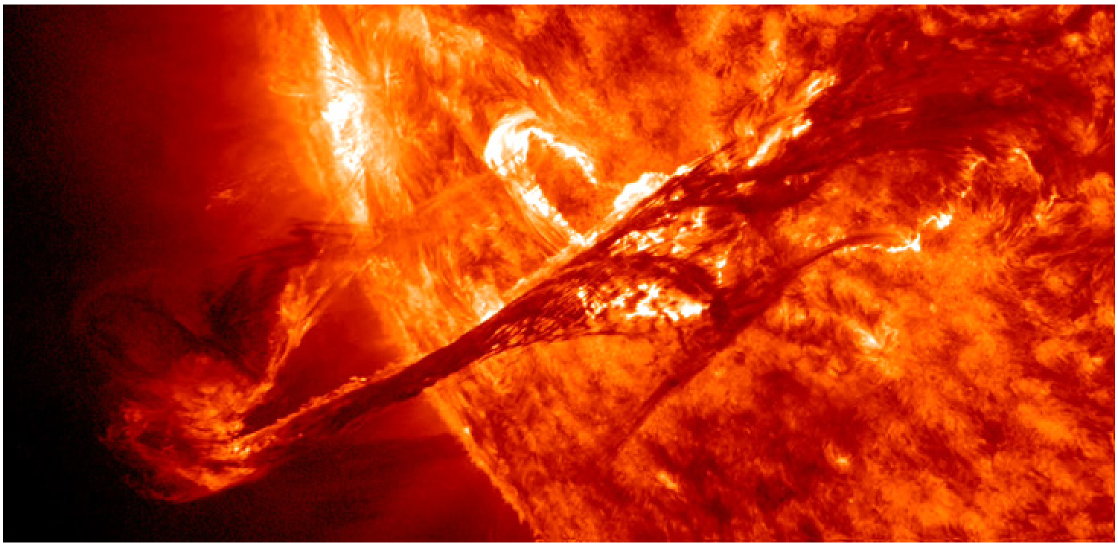

Figure 1.5: Filament near the solar limb on August 31st, 2012, from a combination of 171 Å and 304 Å AIA/SDO images courtesy of NASA.

and cools (Klimchuk & Sturrock, 1992). This suggests filaments form along the PIL which explains their irregular elongated shapes and their association with ARs. The association of these features to ARs are of particular interest to space weather forecasting due to the likelihood of flaring occurring. Magnetic reconnection and the associated energy release of a flaring event is enough to launch prominences outward from the Sun into interplanetary space where it can travel as a CME, see Section 1.3.4.

1.2.5 Coronal Holes

CHs are expansive dark regions of the solar corona which can be observed on-disk in EUV wavelengths or their high altitude components can be observed by eye off the solar disk during a solar eclipses (Cranmer, 2009). Their visibility by eye makes it likely CHs were one of the first coronal features to be observed alongside coronal streamers. The first quantitative observations of CHs were taken by Waldmeier (1956) where they were described as long-lived regions of negligible intensity in coronagraphic images. Figure 1.6 compares an early illustration of

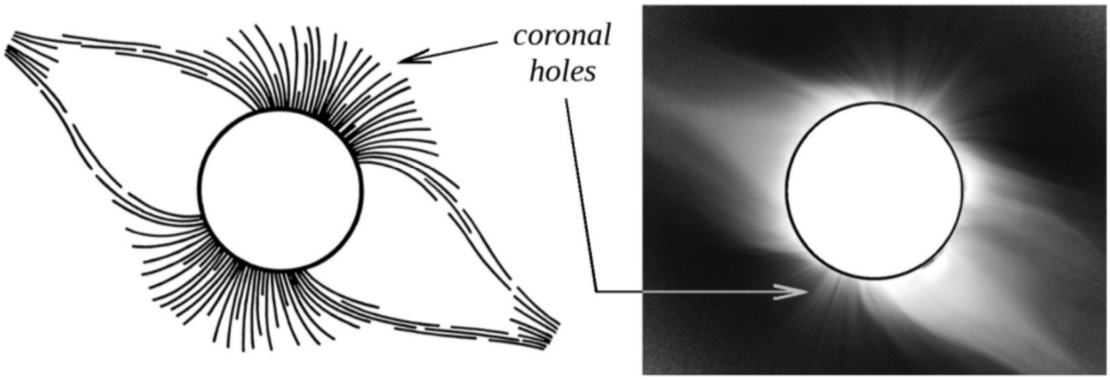

Figure 1.6: Left: Sketch of the quiet solar corona made by Piddington (1972), illustrating plasma trapped in the open polar coronal hole magnetic field lines. Right: Contrast adjusted eclipse image observed by the POISE instrument for February 26th, 1998, in Westpunt Curaçao demonstrating the presence of off-limb coronal holes (Cranmer, 2009).

the corona during an eclipse, illustrated by Piddington (1972), to an image of the corona from the POISE instrument during the February 26th, 1998 eclipse. The Piddington illustration shows two CHs existing at the solar magnetic poles and two equatorial streamers which appear to converge towards the equator. Plasma in this sketch is represented by a collection of lines, the structure of which reveals the underlying magnetic topology as described by Serviss (1909):

"The sheaves of light emanating from the poles look precisely like the lines of force surrounding the poles of a magnet. It will be noticed in this photograph that the corona appears to consist of two portions: one comprising the polar rays just spoken of, and the other consisting of the broader, longer, and less-defined masses of light extending out from the equatorial and middle-latitude zones. Yet even in this more diffuse part of the phenomenon one can detect the presence of submerged curves bearing more or less resemblance to those about the poles. Just what part electricity or electro-magnetism plays in the mechanism of solar radiation it is impossible to say, but on the assumption that it is a very important part is based the hypothesis that there exists a direct solar influence not only upon the magnetism, but upon the weather of the earth."

CHs have been established to be linked with the presence of open magnetic field lines through correlations between EUV images and magnetograms. An example of this link can be seen in Figure 1.6, where the structure of the CH regions match that of plasma trapped within vast open magnetic fields. These open magnetic fields are defined as magnetic lines that do not reconnect to the Sun within 2.5 $R^{\odot}$. The magnetic field of the surrounding streamers in Figure 1.6 are shown to reconnect within this boundary where they form a current sheet which extends out into interplanetary space (Schwartz *et al.*, 1985). These streamers are defined as bright loop-like structures which glow brightly due to the presence of energetic electrons trapped in their closed field loops. These closed loops are elongated by the solar wind into pointed tips. The structure of the magnetic field in the images in Figure 1.6 are dipolar in nature, suggesting a propensity for the presence of polar CHs during a solar minimum.

CHs are now recognized and differentiated from other coronal features based on their physical properties. Their dark appearance was found to be due to their lower relative density and temperatures compared to surrounding coronal features. CHs have an average temperature of ∼0.7-0.8 MK (David *et al.*, 1998) and average electron density of $\sim 10^7$ cm^{-3} (Doschek *et al.*, 1997), a significant difference from the brighter ARs and ambient QS, which accounts for a difference in intensity in high temperature passband observations. However, this significant variation is limited to the high altitude corona. Within the photosphere and chromosphere, CHs are more or less indistinguishable from the surrounding plasma. The cause of these properties is theorised to be related to the underlying magnetic structure of CHs and their significant deviation from other typical features, namely their unipolar nature. Figure 1.7 presents the structure of the magnetic field within a CH boundary on a variety of spatial scales (Cranmer & van Ballegooijen, 2005). This figure illustrates the variation of CH boundaries with height above the photosphere. This variation causes CHs boundaries to be difficult to accurately identify. On a large scale, $\sim$7R$_{\odot}$ as seen in Figure 1.7, the magnetic field appears purely open, only representing the global magnetic field structure of the Sun. The collection of magnetic field lines, known as a flux tube, can be seen to expand on a finer scale, 0.04R$_{\odot}$ (∼30 Mm). On this scale potential kinks and perturbations manifest from small scale magnetic reconnection or magnetic pressure, which rapidly travel outward from the Sun. On the supergranule scale, 0.002R$_{\odot}$ (∼1 Mm), the open

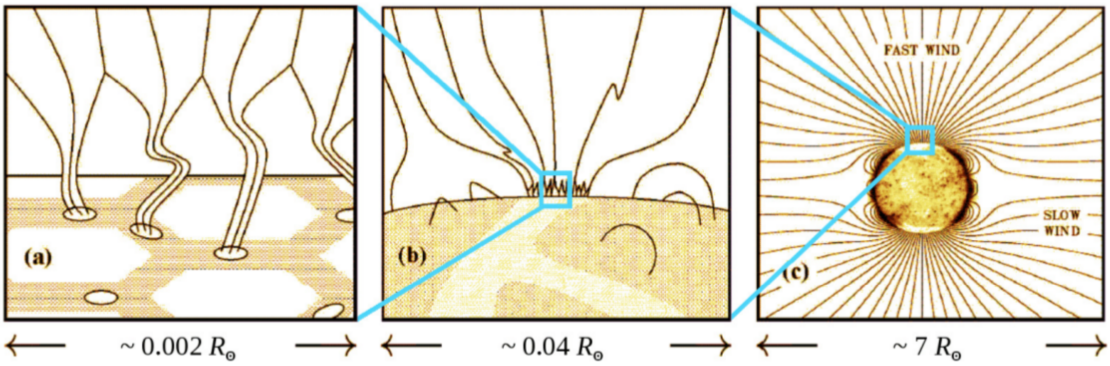

Figure 1.7: Illustration of the unipolar magnetic field structure of a polar coronal hole from the micro to macro scale (Cranmer & van Ballegooijen, 2005). (a) Intergranule footpoints of the open magnetic field which merge together to form a larger flux-tube superstructure. Kink-mode waves are illustrated which can be caused by the motion of the supergranule network of the solar photosphere. (b) Large scale magnetic funnel created from the merging of open fields from the collective footpoints within the coronal hole. (c) Magnetic field of the extended corona.

magnetic fields are traced to intergranule footpoints in the photosphere which rapidly expand due to a lack of magnetic pressure, and merge together to form the singular flux tube characteristic of CHs. The overall magnetic field strength of a given CH is relatively low compared to ARs, being of the order of $\sim 10^0$G, however, the consistent expansion of their magnetic flux tubes creates an outward force on charged particles within their boundaries (Wang & Sheeley, 1990). This force rapidly removes electrons and ions, creating and maintaining the relative deficit of density that characterises CHs. This low density plasma enables an almost collisionless environment, enabling the escape of higher energy ions, allowing for a relative temperature sink compared to surrounding regions. This association ensures the presence of CHs at the solar magnetic poles during solar minimum and potential equatorial CHs appearing dependant on the structure of the solar magnetic field during the solar cycle.

CHs are further individuated from other solar features by their relatively longer lifetimes, and the variance an individual CH can have from this average lifetime which is dependant on their location on the solar disk. CHs can last from a few days to a few solar rotations at the equator, however their lifetime at the magnetic poles can last up to 7 years (Bohlin, 1977; Cranmer, 2009; Timothy *et al.*, 1975). This variation in the CH lifespan is due to the potential evolution of the coronal magnetic field. In contrast to the differential rotation of the surrounding corona, CHs exhibit a rigid body rotation about the Sun. This discrepancy is conducive to reconnection and encourages a general shearing of CHs. Furthermore, at low-latitudes CHs tend to be located near ARs, with the possibility of ARs emerging within a CH boundary (Asai *et al.*, 2008; Shibata *et al.*, 1994). The evolving magnetic interactions between CHs and both the QS and nearby ARs, combined with the general differential motion of the surrounding corona, act to change the structure of CHs. This can lead to their disappearance, appearance, fracturing, and merging on the solar disk (Krista *et al.*, 2011; Nolte *et al.*, 1978). At the poles, these effects are less prevalent and hence impactful, which lends to the longer lifespan of polar CHs. The predominant destroyer of polar CHs is the changing solar dynamo, which governs the magnetic topology of the Sun. This shifting magnetic topology weakens and gradually destroys the polar magnetic field strength required to maintain the relative absence of coronal ions (Leighton, 1964, 1969; Webb *et al.*, 2018).

1.3 Interplanetary Space Weather

The lifetime of these coronal features, their evolution, and their physical properties are of particular interest to space weather forecasting due to the significant effect these features have on the plasma of interplanetary space. In this section, the mechanisms of transport from the solar surface outward into interplanetary space and eventually the edge of the heliosphere will be discussed, as well as the perturbing effects the features of the solar corona can have on this flow of plasma.

1.3.1 Solar Wind

The solar wind is a name given to the wind-like flow of plasma released from the solar corona that travels through interplanetary space out to the edge of the heliosphere. Originally, it was believed that the corona was in a state of hydrostatic equilibrium (Chapman & Zirin, 1957):

$$\frac{dP}{dr} = -\rho g \tag{1.6}$$

where P describes the local pressure of the corona plasma, r describes the radial distance from the solar center, ρ describes the local plasma density and g is the acceleration due to gravity.

The solar wind is a dynamic system of plasma flow dependant on some conditions of the Sun and interplanetary space. The term was originated by Eugene Parker in the late 1950s (N. Obridko & Vaisberg, 2017). Parker discussed the extension of the corona and its particles in both Parker (1958) and Parker (1959), among others, but it was not until Parker (1965) that a full model for the acceleration and velocities of the solar wind with distance were derived. For this Parker solar wind model, outflows are assumed to be radial and steadily expanding, giving:

$$\frac{dP}{dr} + \frac{GM_{\odot}\rho}{r^2} + \rho\frac{dv}{dt} = 0 \tag{1.7}$$

Where v is the radial wind velocity, r is the radial distance from Sun center, P is the pressure of the interplanetary plasma, ρ is the momentum of the outflowing plasma, and all other values have their typical meanings. This equation is simplified using Equation 1.8 to form the momentum equation, Equation 1.9.

$$\frac{dv}{dt} = \frac{dv}{dr}\frac{dr}{dt} = v\frac{dv}{dr} \tag{1.8}$$

$$v\frac{dv}{dr} + \frac{1}{\rho}\frac{dP}{dr} + \frac{GM_{\odot}}{r^2} = 0 \tag{1.9}$$

Assuming the wind is an ideal gas, $P = R\rho T/\mu$ (R is a gas constant and μ is the mean atomic weight), and perfectly isothermal, the second term of the momentum equation simplifies to:

$$\frac{dP}{dr} = \cancelto{0}{\frac{R\rho}{\mu}\frac{dT}{dr}} + \frac{RT}{\mu}\frac{d\rho}{dr} = \frac{RT}{\mu}\frac{d\rho}{dr} \tag{1.10}$$

From a radial differentiation of the conservation of mass equation, shown in Equation 1.11, a substitution equation is obtained, Equation 1.12.

$$\frac{dM}{dt} = 4\pi r^2 \rho v = const \Rightarrow r^2 \rho v = const \tag{1.11}$$

$$\frac{1}{\rho}\frac{d\rho}{dr} = -\frac{1}{v}\frac{dv}{dr} - \frac{2}{r} \tag{1.12}$$

Substituting Equations 1.10 and 1.12 into the momentum equation and setting the constants $c_s = \sqrt{RT/\mu}$ and $r_c = GM_\odot/2c_s^2$, the momentum equation is obtained in terms of flow velocity:

$$\left(v^2 - c_s^2\right)\frac{1}{v}\frac{dv}{dr} = 2\frac{c_s^2}{r^2}\left(r - r_c\right) \tag{1.13}$$

An acceptable solution to this flow velocity equation is when $r = r_c$ and $v = c_s$, known as the critical point. Direct integration of this equation renders Equation 1.14, known as Parker's "Solar Wind Solutions". These solutions are illustrated in Fig. 1.8 from Parker (1965).

$$\left(\frac{v}{c_s}\right)^2 - ln\left(\frac{v}{c_s}\right)^2 = 4ln\left(\frac{r}{r_c}\right) + 4\frac{r_c}{r} + C \tag{1.14}$$

An infinite number of solutions exist for this equation, however they can be categorised into six types illustrated in Figure 1.8, namely (1) A→C, (2) D→B, (3) C→B, (4) A→D, (5) C→D, and (6) A→B. While these solutions exist mathematically, physically only one solution replicates the observable velocity properties of the solar wind. Solutions (1) and (2) cannot exist due to both having two velocities at the same radial distance, and neither connects the solar corona to the heliosphere. Solutions (3) and (5) exhibit excessively large velocities that have not been observed, being supersonic at the coronal height. Solution (4) is commonly termed the solar breeze having relatively low velocities regardless of radial distance, however the velocity of the wind approaches zero at high distances, essentially creating an extremely dense and pressurized plasma at the heliosphere, which is observably not the case. Solution (6) is the last possible solution and is found to be mathematically and physically possible. It starts slow at the corona, is rapidly accelerated through the critical point and reaches a near constant velocity at some relatively large height. Furthermore, this solution predicts a density and

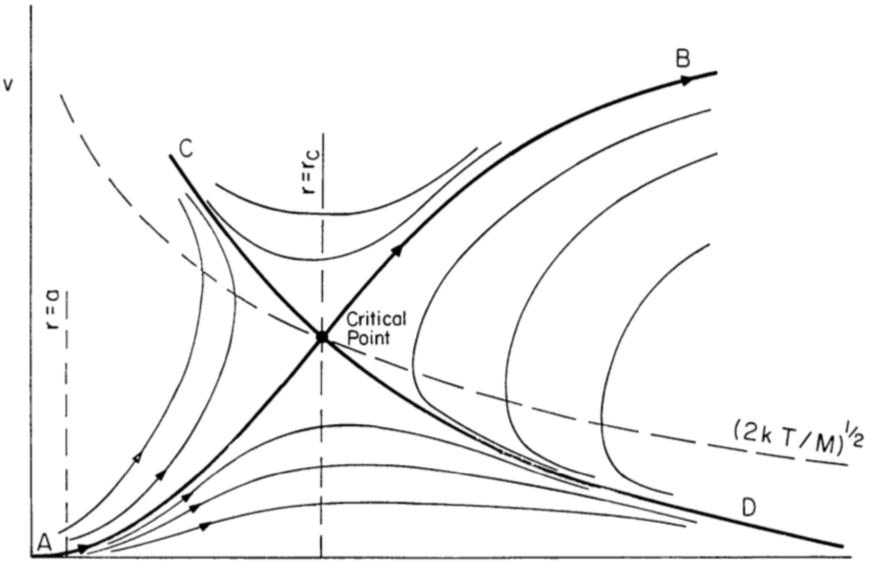

Figure 1.8: Solutions of the Parker solar wind model from Equation 1.14 (Parker, 1965). Six mathematical solutions exist to the Parker model equation which connect: (1) A→C, (2) D→B, (3) C→B, (4) A→D, (5) C→D, and (6) A→B.

pressure of zero at large distances, which was confirmed by the Mariner 2 space probe in 1962 (Coleman, 1968; Neugebauer & Snyder, 1966).

The solar wind can be separated into two categories; the slow solar wind and the high speed solar wind (HSSW), which differ in velocities, temperatures, densities, and chemical compositions. The presence of these solar wind types is found to be dependant on the on-disk coronal features on the Sun.

The slow solar wind consists mainly of corona-like plasma at a temperature of $\sim 1.5 \times 10^6$ K travelling radially from the corona at a velocity of $\sim$ 400 km s^{-1} (Neugebauer, 1976). Typical number densities of the solar wind are found to range with radial distance from the solar surface, being $\sim 10^8$ cm^{-3} at the corona base, to $\sim$ 10 cm^{-3} at Earth. The acceleration processes of this type of solar wind is still debated (Antiochos *et al.*, 2011; Fisk, 2003) due to composition of this wind type implying a continuous magnetic reconnection between open and closed magnetic fields, however, the extreme angular width of projection implies the sources extend far from open-closed magnetic boundaries. The generally accepted theory is that slow solar wind likely originates in reconnection between the QS and

CH boundaries where reconnection continuously occurs, this wind then rapidly expands under a magnetic pressure gradient to occupy a large angular width, forming coronal streamers (Antiochos *et al.*, 2011; Brooks *et al.*, 2015).

The HSSW consists almost exclusively of photospheric plasma at a temperature of $\sim 8 \times 10^5$ K, which can travel at a range of velocities $\sim 500 - 800$ km s^{-1}. This type of space weather causes the majority of regular, periodic interruptions to the slow ambient solar wind during the solar minimum. Observations of the presence of HSSW at Earth have long been correlated with the presence of on-disk CHs (Cranmer, 2002a,b). The HSSW is known to be accelerated from photospheric heights of CH magnetic fields (Hassler *et al.*, 1999; McComas *et al.*, 2007; Tu *et al.*, 2005). Charged ions become trapped within the magnetic field and travel outwards from the Sun along open magnetic field lines, being accelerated in the process. As the magnetic field strength decreases the particles reach a velocity and height sufficient to escape the gravitational potential of the Sun. These streams of plasma then travel out radially from the Sun through interplanetary space.

1.3.2 Parker Spiral

As highlighted in Section 1.3.1, both types of solar wind are projected radially from the Sun with no angular component. For a star with no rotational momentum, the radial coronal expansion would produce radial magnetic field lines. However, due to the rotation of the Sun, $\Omega = 2.7\times10^{-6}$ rad sec^{-1}, the interplanetary magnetic field is dragged into an Archimedian spiral, known as a Parker spiral (Smith, 2001; Zirin, 1998). From spherical polar coordinates centered and rotating with the Sun the velocity of the solar wind can be written as $v_r = v$,$v_\theta = 0$, and $v_\phi = -\Omega r \mathrm{Sin}\theta$. Thus, the solar wind stream lines can be described as:

$$\frac{1}{rSin\theta}\frac{dr}{d\phi} \simeq \frac{v_r}{v_\phi} \simeq -\frac{v}{\Omega rSin\theta} \tag{1.15}$$

The angular dependence, or Parker spiral (Equation 1.16), is thus found through the integration of Equation 1.15. An artistic representation of the spiraling solar wind streams is illustrated in Figure. 1.9.

$$r - r_0 = -\frac{v}{\Omega}(\phi - \phi_0) \tag{1.16}$$

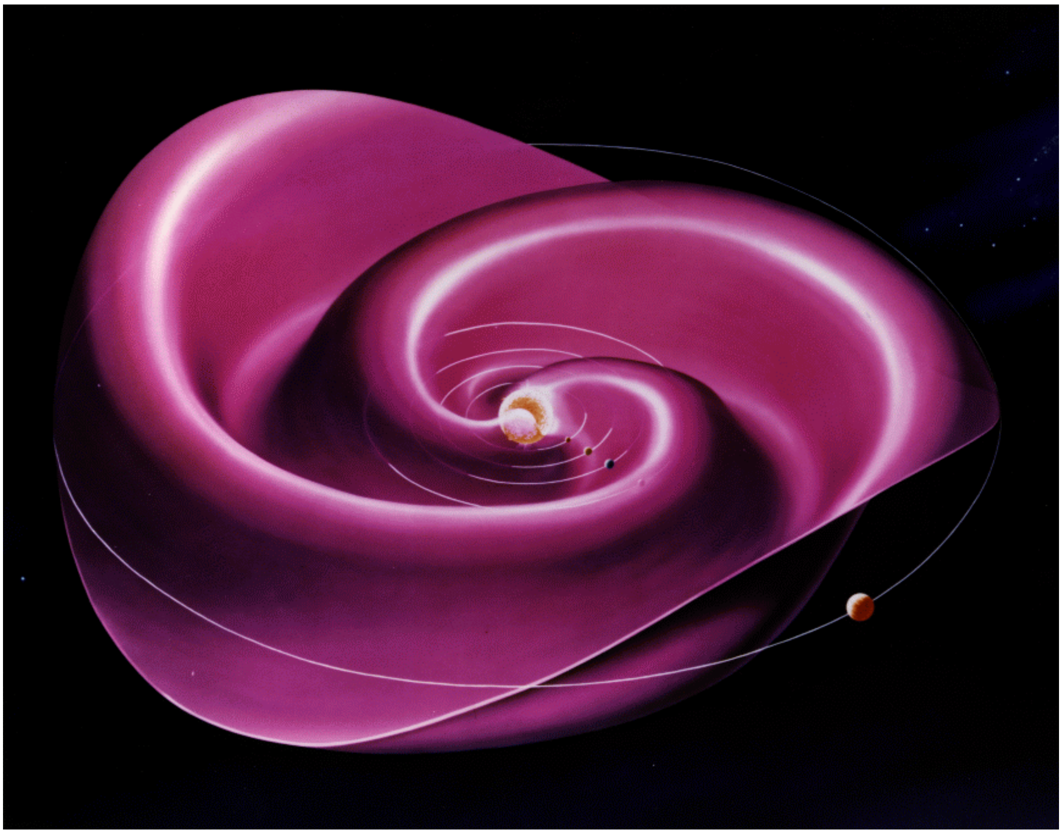

Figure 1.9: Artistic representation of solar wind streams within interplanetary space demonstrating the Parker spiral. Courtesy of Wilcox Solar Observatory, Stanford University.

1.3.3 Co-rotating Interactive Regions

Co-rotating interactive regions are a feature of the solar wind brought about by the interaction of a fast solar wind stream catching up to and influencing a slow solar wind stream in front of it (Heber *et al.*, 1999). As previously mentioned slow solar wind streams are denser than the faster variant, however the streams are magnetically bound, causing both streams to exert a force upon one another at their boundaries, creating a compression region. The compression regions are seen as more significant events, as they contain a denser assortment of charged ions than the slow variant of the solar wind, and travel at speeds comparable to the high speed solar wind variant outward from the Sun in a Parker spiral fashion.

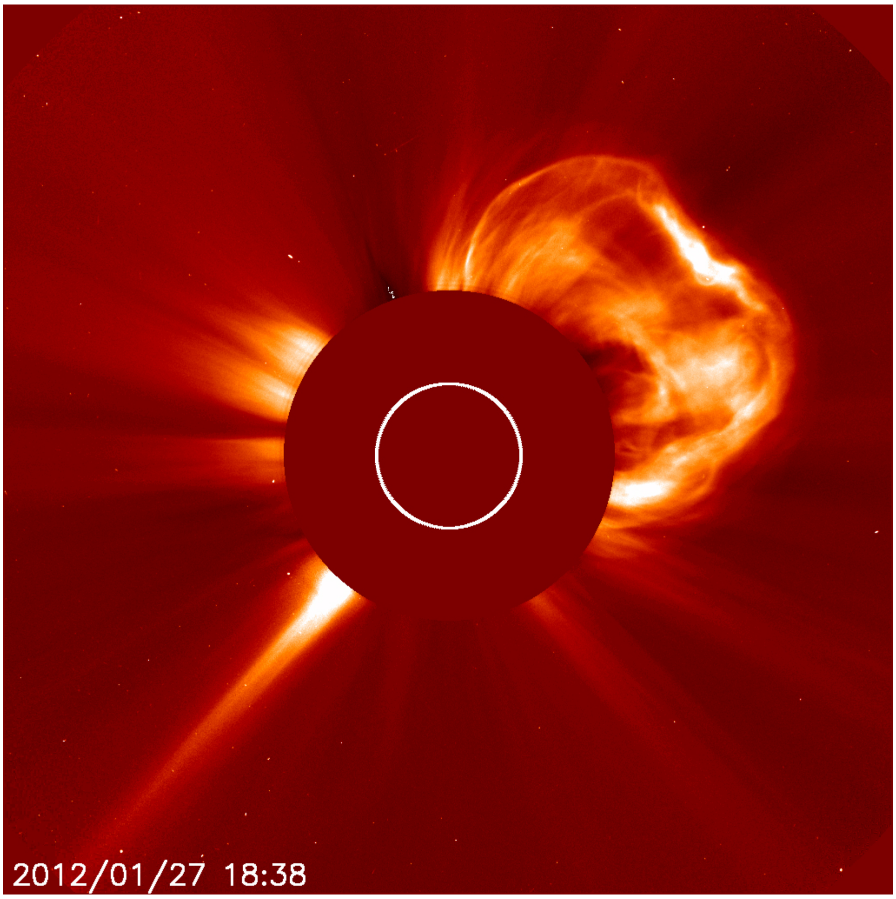

Figure 1.10: LASCO/SOHO C2 white light coronograph capturing the emission of a CME from the solar corona for January 27th, 2012.

1.3.4 Coronal Mass Ejections

Coronal Mass Ejections (CMEs) are large emissions of plasma bounded by a magnetic field, often associated with the occurrence of a flare (Kahler, 1992). An example of this eruptive event is displayed in Figure 1.10, a coronagraph observation from the Large Angle and Spectrometric Coronagraph (LASCO; Brueckner *et al.*, 1995) instrument taken on January 27th, 2012. Typical CMEs are composed of three elements: a low electron density cavity, a dense core, and a bright leading edge. CMEs are generally created through the trapping of plasma within a magnetic field, such as prominences in the corona, followed by a large eruptive magnetic reconnection event, such as associated with a solar flare. This eruption launches the prominence, still bounded within a magnetic field outward into interplanetary space. The energy release in this event is dependant on the strength of the flaring region, and with the high variation of both flare eruptive energy, and prominence mass, leads to a significant variation in the kinetic energy imparted on the CME. Due to this effect, speeds have been observed at low solar wind speeds, ~ 200 km s^{-1}, to more than double the highest speeds achieved by the HSSW, ~ 2000 km s^{-1}, and higher (Sheeley *et al.*, 1985). These solar features are made more interesting by their magnetic bounding. An observer traveling directly through a CME will experience a sudden intense magnetic field which gradually decreases as they approach the dense core of the CME. Continuing out of the core, the observer will experience an increase in magnetic field of opposing polarity which will reach some peak strength before sharply returning to background levels. The high potential mass, kinetic energy, magnetic variability, and unpredictability of CMEs make them one of the most hazardous types of extreme space weather events. CMEs have been associated with some of the most intense space weather damage at Earth, including the Carrington event.

1.4 Space Weather Interactions with Earth

Space weather is of interest not just to the scientific community but also to industry, government, and the general public due to the potential effects it can have on our daily lives. When a gust of solar wind or a CME strikes a planet with an atmosphere it has two primary effects. In Earth's case, a third effect exists on technological systems. Figure 1.11 illustrates a range of effects that space weather can have on the technological systems both on Earth's surface, and in planetary orbit. These effects are caused by solar wind and eruptive events' interactions with both the magnetosphere and ionosphere of the planet.

1.4.1 Magnetosphere

Similar to the Sun, Earth is covered by a large magnetic envelope named the *magnetosphere* that extends out to ~ 65000 km. Similar to the Sun at solar minimum, the Earth's magnetic field is dipolar and is powered by a dynamo deep within the

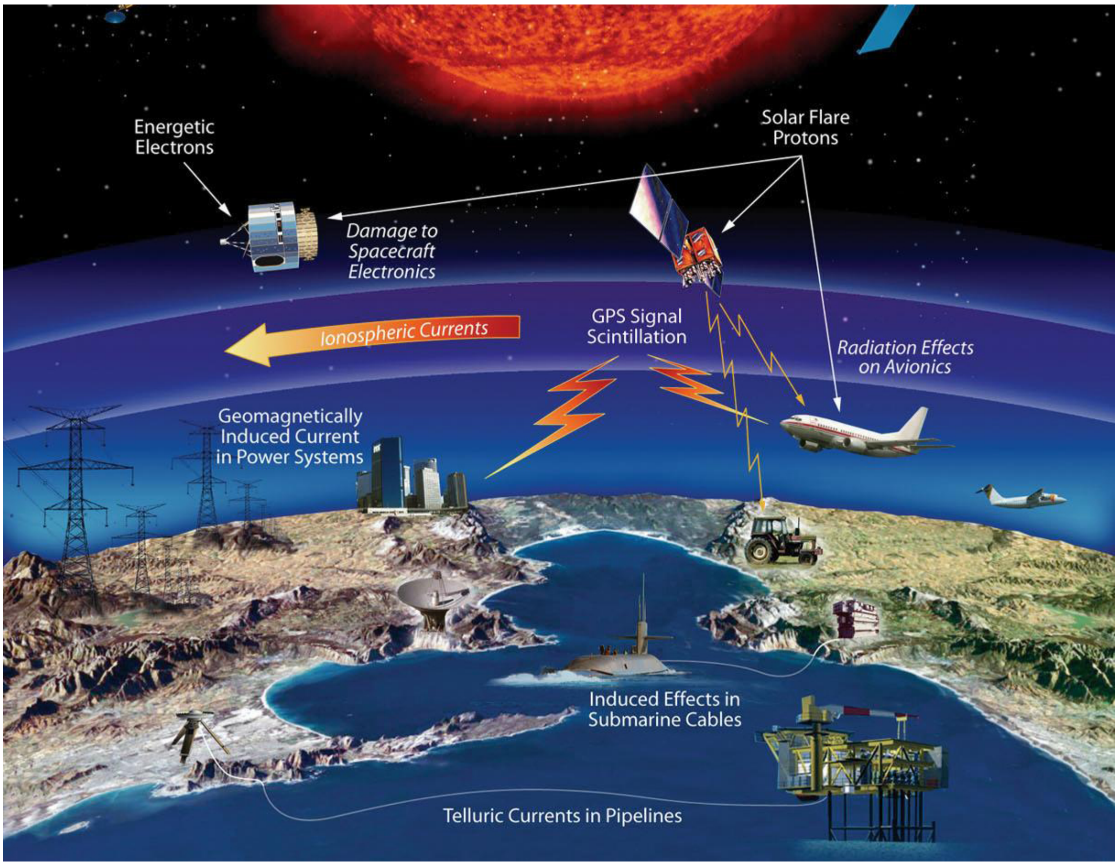

Figure 1.11: Space weather effects on the local environment of Earth, courtesy of NASA. Most notably are the high impact space weather has on technology, which humans have grown an ever larger dependence on. Particularly bad space weather storms are known to cause severe damage to satellites and induce currents in power networks strong enough to destroy electrical transformers.

mantle of Earth. The magnetic field has also been observed to reverse at regular intervals similar to the Sun, although with a much longer period than the Sun, $\sim$6000 years (Cox, 1973). Currently the magnetosphere exhibits a varying field strength with height, being $\sim 25\ G$ at the outer core, and $\sim 0.4\ G$ at the surface (Finlay *et al.*, 2010). While the exact creation of this dynamo and induction of our magnetic field is still a debated topic (Dormy, 2006), its presence is of interest to space weather forecasting due to the interaction between Earth's magnetosphere, and the relatively rapidly varying interplanetary magnetic field. The structure

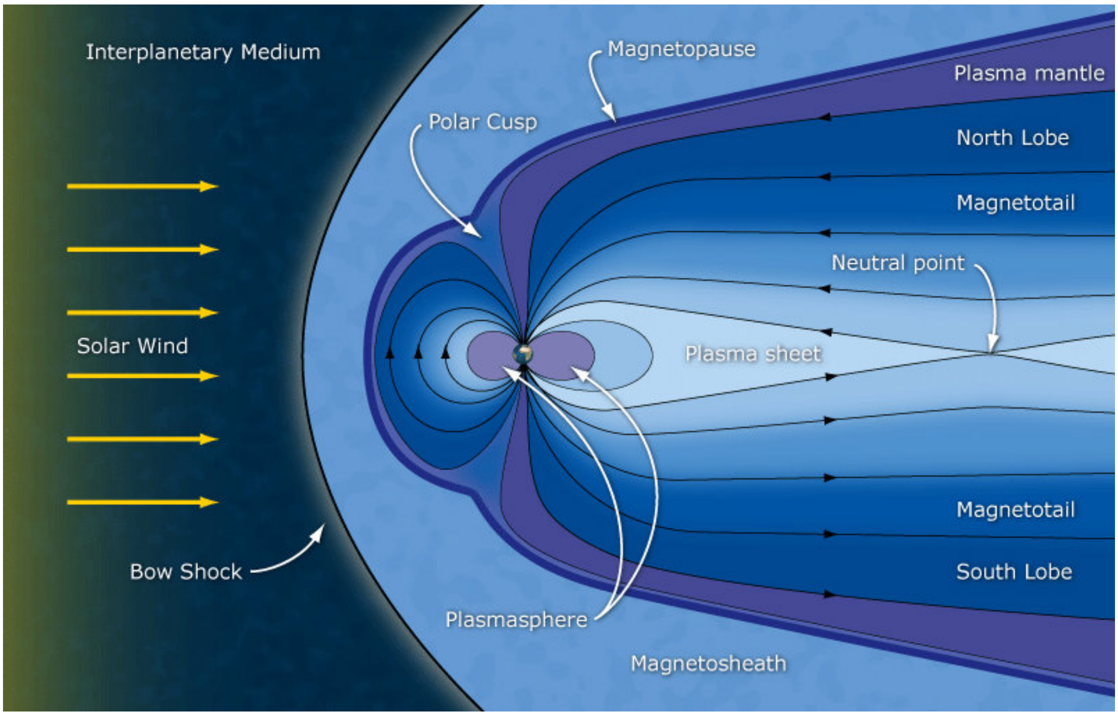

Figure 1.12: Model of Earth's asymmetric magnetic field due to pressure from solar wind streams (Case, 2014). This magnetic pressure creates a number of features in Earth's magnetic field that would otherwise not be present in a basic dipole magnetic field. Most notably is the presence of a bow shock forming due to the relative motion between the Earth's magnetopshere and the solar wind, and the presence of a long magnetotail created by a magnetic pressure gradient. Within the magnetotail exists a current sheet undergoing regular reconnection, located at the neutral point.

of the magnetosphere can be broken down to its key components. Figure 1.12 encapsulates the structure of the magnetosphere and highlights notable features within. In a neutral environment the Earth is expected to demonstrate a simple dipolar magnetic field that roughly aligns with Earth's rotational poles with polar cusps above each magnetic pole. However due to the presence of the solar wind and the ambient magnetic pressure associated with it, the Earth's magnetic field is distended in the direction of the Sun-Earth line. Also created by this interaction is a magnetopause, the edge of the magnetosphere where the ram pressure of the shocked solar wind balances the magnetic pressure of the confined magnetic dipole (Eastwood *et al.*, 2015). Above this magnetopause is a magnetosheath, a collection of solar wind plasma in a high particle energy flux, with a turbulent magnetic field. This layer acts as a cushion to the magnetosphere, transferring pressure from the solar wind to the magnetopause. Above the magnetosheath is the bow shock of Earth's magnetosphere. The bow shock is the edge of the magnetosphere's influence, below it is where the interactions between solar wind and magnetosphere occurs, above it the solar wind travels unimpeded. A magnetotail occurs on the night-side of Earth's magnetosphere, a feature created by a lack of magnetic pressure on the anti-sunward side of a planetary magnetic field, the field extends out much further from the source. This extension essentially creates a current sheet on Earth's night-side that undergoes continuous reconnection under the turbulent pressure of the solar wind, identified as a neutral point in Figure 1.12.

The turbulent flow of the solar wind combined with the relative constant strength of the magnetosphere causes a significant variation of the magnetopause and the structure of the magnetosphere as a whole (Kavanagh & Denton, 2007; Shue *et al.*, 1998). This variation of magnetic field induces a current in the upper atmosphere, from Faraday's Law (Faraday, 1832; Maxwell, 1865):

$$\int_{loop} \mathbf{E}.ds = -\frac{d}{dt}\int_{S} \mathbf{B}.d\mathbf{a} \tag{1.17}$$

where the atmosphere around Earth acts as a conductive loop. In this equation, an electric field, $\mathbf{E}$, is generated about a loop seperated into infinitesimal lengths, ds, due to a time variant magnetic field, $\mathbf{B}$, through a surface bounded by the loop, S, seperated into infinitesimal vector elements, $d\mathbf{a}$. This induced current, combined with the already varying magnetic field allows for more charged ions in the upper atmosphere. These charged ions combined with the impact of incident charged particles within the solar wind can cause damage to spacecraft in orbit. Damage to satellites can range from bulk charging to satellite drag which can negatively effect the lifetime of most satellites. The more severe a space weather event, the more potential it has to cause damage to the established, space-based systems. Considering the high cost of components and cost of getting a satellite into orbit, ∼€100 million, it is beneficial to be able to predict these space weather events and mitigate their negative impact. The effect these space weather storms can have are significant enough that they are now included in national risk assessments of some countries[1].

1.4.2 Ionosphere

The ionosphere is an ionized layer of plasma within the Earth's atmosphere. The ionization of this layer is maintained by photoionization of the neutral atmosphere by solar radiation and high energy particles that penetrate the upper atmosphere. This reliance on photoionization causes the ionosphere to vary with solar radiance, being observed to light up during solar events (Hayes *et al.*, 2017; Mitra, 1974). Due to the population of charged ions and electrons, this layer acts as a conductor. It is within this ionized layer that an evolving magnetic field, caused by the buffeting of the solar wind, can further energize the ions within to create an atmospheric anomaly. The aurora, often nick-named the northern or southern "lights", is an observed colourful wispy feature that appears in the sky at high latitudes of Earth (Chamberlain, 1961). This feature is associated with solar wind and geomagnetic storms, and its location can vary depending on the strength of space weather storms, appearing lower in latitude with storm strength (Hayakawa *et al.*, 2018). Furthermore, this layer of the atmosphere has the ability to reflect radio waves directed into the sky, and can refract high frequency radio waves. The dependence of radio waves on this atmospheric layer means that radio waves are likely to be disrupted and scintillated, a process of rapid variation in electromagnetic wave amplitude, with significant variation of the ionosphere. Particularly severe conditions can even prevent Global Navigation Satellite Systems (GNSS) receivers from locking onto a signal. With the ever growing dependence on communications and the creation of self-driving automobiles, the disruption of these communications are costly on both a national and individual scale (Eastwood *et al.*, 2017).

1.4.3 Geo-Magnetically Induced Currents

Coinciding with the geomagnetic field, a geo-electric field exists which permeates both Earth's atmosphere and its surface. Similarly like the Earth's magnetic field, this electric field is variable with the near Earth space environment, or more simply,

---

[1] https://researchbriefings.files.parliament.uk/documents/POST-PB-0031/POST-PB-0031.pdf

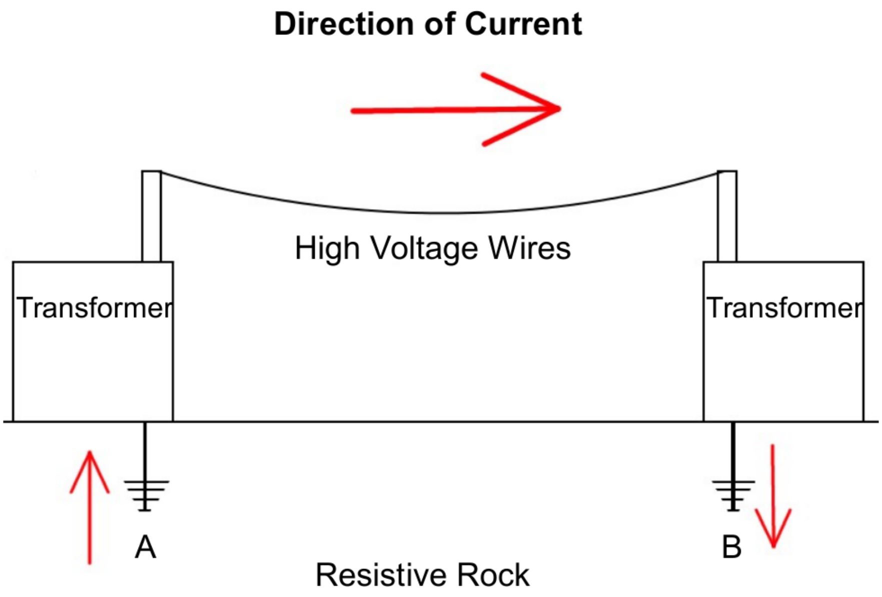

Figure 1.13: Conditions under which a geo-magnetically induced current is likely to be caused by a space weather storm (Blake, 2018). A potential difference is induced by space weather effects between location A and B. Due to current taking the path of least resistance, it is more viable for electrons to travel through the established power network via the grounding connection from A to B, than to travel through the resistive rock.

the geo-electric field is influenced and induced by the geomagnetic field. Significant variations of this electric field, such as during a space weather storm, often create a potential difference across land masses (Pirjola, 2000). This induced potential difference can be hazardous to Earth technologies which utilize grounded conductors (such as power networks, pipelines, and railway systems). As a potential is induced between two surface locations on the Earth, geo-magnetically induced currents (GICs) naturally arise. These currents will flow through man-made conductors such as power lines, which are by design more conductive than the surrounding ground rock. The introduction of these quasi-DC currents to a power network occurs via the grounding elements of transformers as illustrated in Figure 1.13. As GICs are slowly varying (relative to the operational frequency of the transformers), these can saturate transformers, leading to spot-heating, harmonics generation and power losses.

During particularly strong space weather storms power networks have been observed to fail, causing mass blackouts and in extreme circumstances destruction of components within the power network. One instance in 1989, known as the Quebec event, saw a surge in load on the Quebec, Canada power network causing a nine-hour power outage and irreparable damage to some ground based transformers, costing the country millions in replacements and leaving certain areas without power for up to two weeks (Cid, C. *et al.*, 2014). This particular event is one of many extreme space weather events that caused significant damage and black outs. Small scale storms, while not immediately destructive on the power network, do increase the base load on the system. Most power systems are designed with specific expected loads to take. A small increase on the current traveling through it can accelerate the rate of degradation of the system. Essentially shortening the lifespan of components within the network.

For these reasons, it is essential to improve our understanding of the connections between the Sun and Earth, covered by the term space weather. As humanity increases its dependence on technology, it has become more susceptible to space weather storms (Eastwood *et al.*, 2017; Oughton *et al.*, 2018). In order to prevent the potential future damage, and to save nations and individuals from a significant cost, it is crucial to be able to model and predict all space weather events, and to prevent the damage they can cause.

1.5 Aims of this Work

To date, the understanding of space weather causes and related effects is in its infancy. To predict and prepare for the most severe of space weather events, it is essential to identify and catalogue the creators of these events and their properties. The research presented in this thesis attempts to further the understanding of space weather specifically caused by CHs, and their associated high speed solar wind streams. The current start-of-the-art for CH analysis and correlation are heavily focused on single wavelength observations (Delouille *et al.*, 2012; Krista & Gallagher, 2009) with CH area being the predominant property analyzed as an indicative driver of space weather events (Nolte *et al.*, 1976). This aim of improving upon these methods will be achieved by the following chapters in this thesis, outlined below:

- Chapter 2, Instrumentation and Analytical Techniques: Describes the relevant instrumentation used in this research to attain our science goals, as well as describing previous methods of CH segmentation used to identify CHs and their properties.

- Chapter 3, Theory: Outlines previous theory on solar wind predictive models from CH regions and discusses the background theory of machine learning methods.

- Chapter 4, Multi-Thermal Coronal Hole Identification: Chronicles the construction of a three-EUV multi-thermal CH segmentation algorithm named the Coronal Hole Identification via Multi-thermal Emission Recognition Algorithm (CHIMERA). This algorithm is then compared to competing methods of segmentation and the properties it extracts are defined. This chapter is focused on the work published in Garton *et al.* (2018a).

- Chapter 5, The Expansion of High Speed Solar Wind Streams: Details a discovery in the correlation of CH width as extracted by CHIMERA with solar wind duration and peak velocities as identified by the Advanced Composition Explorer satellite. Furthermore, this chapter describes a derivation of the high speed solar wind longitudinal expansion through interplanetary space via geometric methods and in-situ observations. This chapter is focused on the work published in Garton *et al.* (2018b).

- Chapter 6: Long-term Coronal Hole Statistics and Machine Learning Models of Solar Wind: Describes the long-term variations of CH geometric and magnetic properties across two solar cycles, and new insights into the long term structure of CH regions within this same time-span. Furthermore, this chapter details the use of machine learning on CHIMERA segmentations to build more accurate CH segmentation algorithms, as well as more robust solar wind predictive models than humans are capable of creating. This chapter is focused on the work which is yet to be published.

- Chapter 7, Conclusions and Future Work: Summarizes and concludes the research of this thesis, as well as outlines future potential works to continue improving the state of space weather forecasting.

2

Instrumentation and Analytical Techniques

As our understanding of the Sun and its effect on the Earth has evolved, so too has our technological capabilities. Observations of the origins and impacts of space weather require the use of various instruments, both space and ground-based, as well as a number of analytical techniques. Space weather observations are divided into three categories: the origin in the solar atmosphere, the transition through the heliosphere, and the arrival and impacts of space weather phenomena. In this chapter, the instruments that monitor space weather effects that will be used in the work of this dissertation will be discussed, as well as some analytical techniques for predicting high speed solar wind streams which are aimed to be improved upon.

2.1 Solar Dynamics Observatory (SDO)

The Solar Dynamics Observatory (SDO; Pesnell *et al.* 2012) was designed as the first space weather mission of the National Aeronautics and Space Administration's (NASA) Living With a Star (LWS) program. The aim of the LWS program is to develop the understanding of the connections between the Earth and our nearest star, the Sun, and the effects these connections have on both life and technological systems, ultimately advancing our predictive capabilities of potentially hazardous events. SDO was launched in early 2010 from Kennedy Space Center aboard an Atlas V 401 rocket and was designed to study the solar atmosphere with multiple temperature passbands in high temporal and spatial resolution. Initially orbiting Earth in a geosynchronous transfer orbit it was gradually relocated to a circular geosynchronous orbit with a 28° inclination through a series of apogee-motor firings. SDO is composed of a spacecraft bus with three unique observing instruments: the Extreme Ultraviolet Variability Experiment (EVE; Woods *et al.* 2012), AIA, and the Helioseismic and Magnetic Imager (HMI; Scherrer *et al.* 2012).

Figure 2.1 shows a scaled image of the SDO spacecraft with observing instruments and the on-board solar panels highlighted. SDO was constructed by a team composed of a number of scientific research institutes and bodies, namely the Goddard Space Flight Center, Stanford University in Palo Alto, California, the Lockheed Martin Solar Astrophysics Laboratory (LMSAL) in Palo Alto, California, and the Laboratory for Atmospheric and Space Physics (LASP), University of Colorado in Boulder, Colorado. Goddard is the lead designer and builder of the spacecraft and many of its components, while the other institutes were responsible for construction of individual instruments, and their running after launch.

SDO is designed to provide data and scientific understanding essential to predicting solar activity, from predicting the occurrence of flares and CMEs on a daily basis to predicting the level of solar activity in upcoming solar cycles. The specific aims of the SDO mission is to monitor magnetic field topology and evolution to discover the magnetic structure required to allow reconnection events. This monitoring gives insight into the creation and propagation of flare and CME events. On a longer time scale, SDO aims to monitor how the magnetic field is transported, amplified and destroyed in the Sun, which will improve predictions of when and

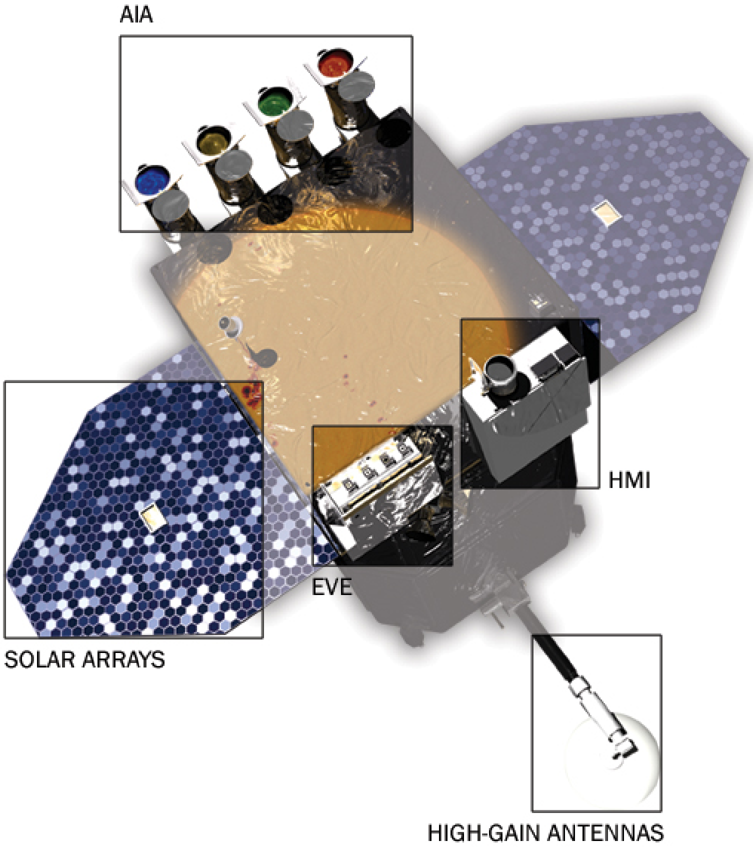

Figure 2.1: The SDO spacecraft with boxes highlighting individual instruments, power sources and ground communications. The Atmospheric Imaging Assembly (AIA) is composed of four individual telescopes used to take full disk EUV observations of the solar atmosphere. The Helioseismic and Magnetic Imager (HMI) is the instrument responsible for taking dopplergrams, continuum filtergrams, and both line-of-sight (LOS), and vector magnetograms of the solar disk. The Extreme Ultraviolet Variability Experiment (EVE) is the instrument that measures the EUV spectral irradiance. Solar Arrays are the power source of the spacecraft, solar panels which absorb solar radiation emitted from the Sun. High-Gain Antennas highlights the communication section of the spacecraft, where data gained from the three observing instruments are transport to ground teams for dissemination.

where magnetically complex ARs will emerge, as well as how these magnetic fields will erupt and decay.

SDO observes and transports 150000 high resolution full-Sun images and 9000

EUV spectra daily, amounting to a data transfer of 1.5TB of scientific data, which are converted to images, dopplergrams, magnetograms and spectra. Across SDO's planned five years of operation, this amounts to a transfer of 3-4 petabytes of raw data. However, the SDO spacecraft has long outlived its mission lifespan and is still operational today, approximately nine years since its launch.

While three observing instruments are available, this work only makes use of the AIA and HMI instruments, hence they will be described in further detail below.

2.1.1 Atmospheric Imaging Assembly (AIA)

AIA takes multiple high resolution, full-disk measurements of UV and EUV emission from both the solar corona and the transition region. These full-disk measurements cover 1.5 $R_\odot$ from Sun centre, have a high spatial resolution of 1.5 arcsecs and are taken in each temperature passband at a 12-second temporal resolution. High cadence and resolution images of the solar corona are desirable due to previous images of the corona from earlier missions, such as Yohkoh, which found that the evolution of density, temperature and position of all coronal features occurs on timescales of the order of seconds.

Figure 2.2 shows a schematic of the AIA device which is mounted onto the SDO spacecraft bus. The AIA instrument consists of 4 unique telescopes that employ normal-incidence, multilayer-coated optics to capture narrow-band images of seven EUV and one UV spectral emission line: Fe XVIII (94 Å, 6.3 MK), Fe VIII (131 Å, 0.4 MK), Fe IX (171 Å, 0.7 MK), Fe XII (193 Å, 1.6 MK), Fe XIV (211 Å, 2 MK), He II (304 Å, 50000 K), Fe XVI (335 Å, 2.5 MK), and C IV (1600 Å, 0.1 MK). These filters are split into pairs, with each pair sharing a telescope, charged-couple device (CCD), and observing time. Labeled 1-4 in Figure 2.2 are the guiding telescopes, one of which is mounted onto each AIA main observing telescope. These guiding telescopes provide signals for an active secondary mirror within the main telescope to stabilize the solar images on the CCD. Each of the main AIA telescopes are Cassegrain telescopes, meaning the telescope is a combination of a primary concave mirror and a secondary convex mirror. The optical path of incident light is folded back on itself and this design has the advantage of creating a much longer relative focal length for the telescope in a physically shorter system, and hence is less

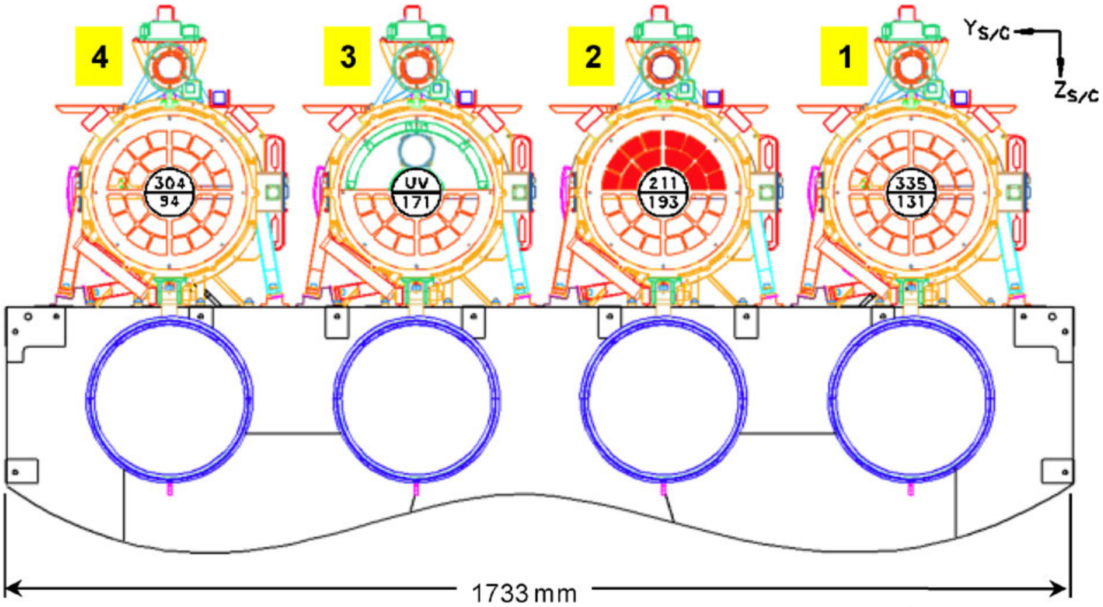

Figure 2.2: Schematics of the 4 telescopes of the AIA instrument (Lemen *et al.*, 2012). Labels 1-4 highlight the guiding telescopes which provides a signal for an active secondary mirror to stabilize the solar image on a CCD. Filters cover the main telescopes labeled with the appropriate wavelengths, namely, 94 Å, 131 Å, 171 Å, 193 Å, 211 Å, 304 Å, 335 Å, and a UV filter peaking at 1600 Å. Each of these telescopes are mounted onto the main SDO spacecraft bus, with aperture doors attached to each telescope shown in blue.

expensive to get into orbit. Highlighted in dark blue in Figure 2.2 are the aperture doors for each telescope which were closed over to protect the filter during launch and were opened to allow viewing once SDO reached a stable orbit.

The AIA telescopes uses a CCD style photon detector to obtain images. Photons that enter the telescope aperture are incident on a metal-oxide-semiconductor capacitor which releases a loose electron. When observations are finished the CCD passes all the electrons released into their corresponding capacitive bin in a conveyor belt style fashion to a charge amplifier which converts the electron charge into a voltage which can be read out by the instrument. This reading occurs one at a time which gives corresponding data numbers (DNs) for each pixel in the image. This one dimensional vector can then be converted digitally into a 2D image array of these DNs.

Figure 2.3 shows 228×216 arcsecs images of an AR on February 15th, 2011, observed in the eight passbands on-board AIA compared to a single LOS magnetogram observed by the HMI instrument. Due to its high resolution, AIA is capable showing the detailed structure of an AR and its magnetic loops due to the various instruments temperature response functions. 171 Å has a temperature-response peak at 0.63 MK which makes it optimal for observing coronal holes, the quiet corona and the upper transition region. 193 Å's peak response at 1.6/20 MK corresponds to corona and hot flare plasma. 211 Å peaks at 2 MK and corresponds to AR plasma. Similarly, 335 Å observes higher temperature AR plasma at 2.5 MK. 94 Å monitors the high temperature flaring regions at 6.3 MK. Lastly, 131 Å has a noticeable double peak at 0.4 and 10 MK which corresponds to transition region and the flaring corona, however, this passband is often saturated during flaring and is difficult to use for reliable observations of the transition region.

Figure 2.4 shows the various temperature response functions for the filter passbands. Most notably are the 171 Å, 193 Å, and 211 Å filters which demonstrate the highest peak responses and have peaks in the typical QS temperatures 0.7 MK - 2 MK. Figure 2.4 demonstrates the key differences in temperature response that are responsible for the unique insights into the corona seen in Figure 2.3. These differences enable feature segmentation methods that are typically used in space weather forecasting. These methods of segmentation will be discussed further in Section 2.4.

This research within this thesis is heavily focused on rapid and real-time identification of features within the solar corona, hence much of this work relies on the level 1 data products from the AIA instrument. The data product level of an observation describes the post-processing and calibrations undergone to produce a cleaned observation. The initial calibration of the AIA instrument is discussed in detail in Boerner *et al.* (2012), where the photometric calibrations and instrument characterization is outlined. Due to the difficulty in obtaining a well-calibrated, narrowband, collimated EUV source, end-to-end EUV calibration measurement of the AIA response function was not feasible. Hence, photometric calibrations were made through component-level measurements of all the optical elements in the AIA telescopes which were combined analytically to produce a model of the system performance. This model accommodates for the relative transmission within the each EUV filters, the reflective performance of mirrors within the telescope and the quantum efficiency within the CCD detectors, all of which was performed

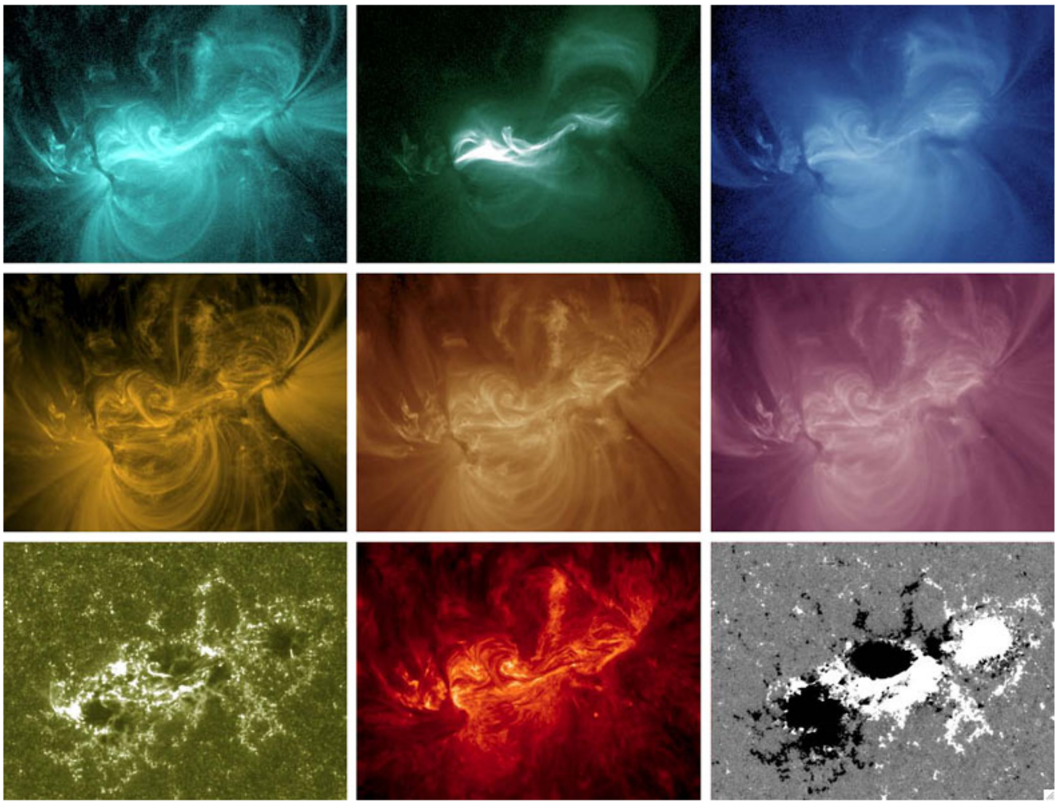

Figure 2.3: 288×216 arcsecs image of an AR observed on February 15th, 2011, across multiple AIA passbands and a HMI magnetogram (Lemen *et al.*, 2012). Top panels show observations from 131 Å, 94 Å, and 335 Å (left to right). Middle panels show observations from 171 Å, 193 Å, and 211 Å (left to right). Bottom panels show observations from 1600 Å, 304 Å, and a HMI LOS magnetogram (left to right). Across these passbands, the full range of features of the AR are observed, from the footpoints in the upper photosphere to the magnetic loop tops in the high corona.

within a clean environment to prevent contamination which may lead to more rapid deterioration of the instrument components. Through the instrument characterization, the flat field, filter mesh diffraction pattern and stray light can be modeled and removed from observations, after which the observations are co-aligned. These calibrations data undergoes continual update via a time dependant algorithm that accommodates for the camera gain, effective area, pointing information, bad-pixel list, flat field, and average band pass effective area. As newer calibration data becomes available, level 1 data can be reprocessed using the most recent calibration

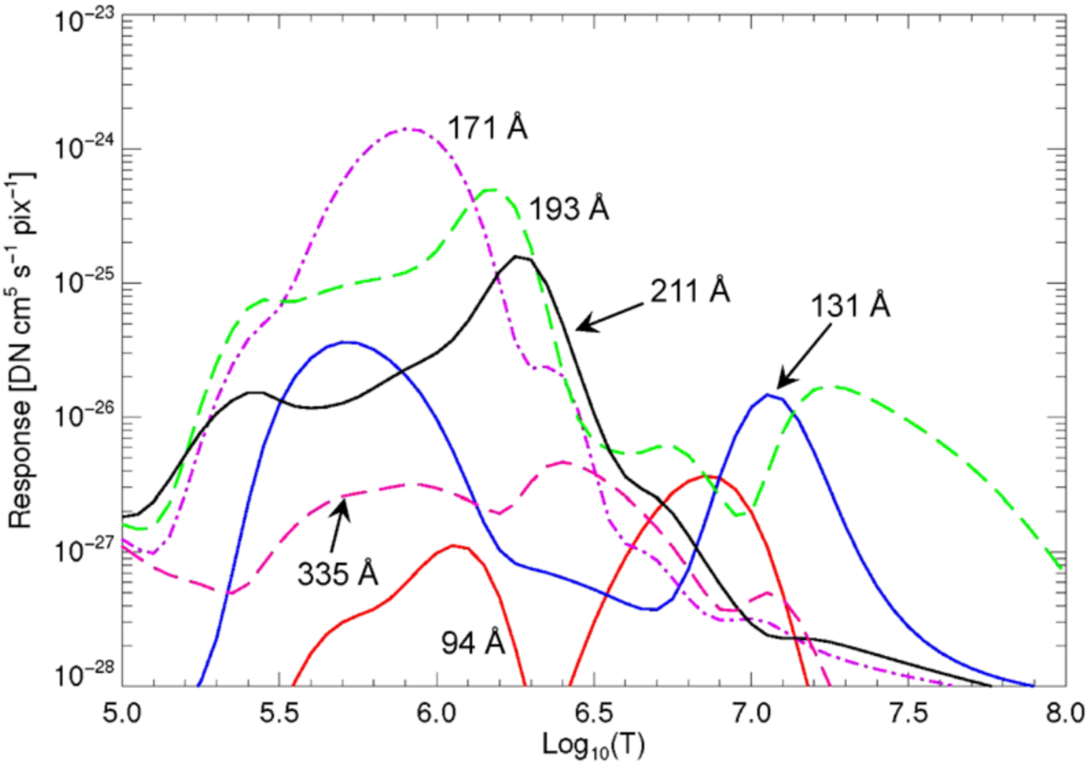

Figure 2.4: Temperature response function of the six iron emission dominated EUV AIA passbands (Lemen *et al.*, 2012). Notably, 171 Å, 193 Å, and 211 Å passbands have the highest peak responses, and all passbands have peaks within corona temperatures (0.4-7MK).

data.

2.1.2 Helioseismic and Magnetic Imager (HMI)

The HMI instrument is designed to produce measurements in the form of filtergrams in a set of polarizations and spectral-line positions and is the successor to the Michelson doppler imager, which will be discussed in Section 2.2.2 (Scherrer *et al.*, 2012). HMI makes measurements of the motion of the solar photosphere to study solar oscillations and makes measurements of the polarization in a spectral line to study the properties of the photospheric magnetic fields. Similar to the AIA instrument on-board SDO, HMI is capable of taking high resolution images at a relatively high cadence. HMI takes 4096×4096 full disk observations of Doppler velocity, LOS magnetic flux, and continuum with a spatial resolution of 0.5 arcsecond per pixel and a cadence of 45 seconds. HMI also observes vector magnetic field maps every 90-135 seconds depending on the image frame sequence selected. These vector magnetograms are then typically averaged into a 12 minute product for increased accuracy.

Magnetograms supplied by HMI are essential in this work for differentiating magnetic polarity regions to calculate severity of space weather events. An example magnetogram is shown in Figure 2.3, where white regions represent positive polarities and black regions represent negative polarity regions. Magnetograms of the Sun are measured indirectly via splitting in spectral emission lines due to a process known as "the Zeeman effect". The Zeeman effect occurs when an electron's energy levels within an atom are changed due to the presence of a magnetic field. If the atom is positively aligned in the direction of the magnetic field the electron energy is slightly increased, which causes the spectral emission line associated with the atom to be slightly skewed to shorter wavelengths, with a similar effect for atoms negatively aligned with the magnetic fields having less electron energy and subsequently longer wavelengths. Hence, placing a collection of energized atoms with no preferred orientation in a magnetic field will produce spectra with 3 similar lines. The photons emitted in these divided wavelengths have preferred polarizations that will depend on the direction of the magnetic field. Through the observation of Zeeman splitting and the polarization of incident light it is possible to calculate the properties of the magnetic field that the incident photons originated from.

2.2 Solar and Heliospheric Observatory (SOHO)

The Solar and Heliospheric Observatory (SOHO; Domingo *et al.*. 1995) mission was designed as a collaborative project between the European Space Agency (ESA) and NASA to study the Sun from the internal core to the outer corona and solar wind. The observatory was planned with three scientific objectives: to study the solar interior using helioseismology methods, to study coronal heating and the mechanisms responsible, and to study the acceleration of solar wind and their originating regions. SOHO launched in 1995 observes at the first Lagrangian point (L1) between Earth and the Sun, a point in space relative to the Earth's orbit

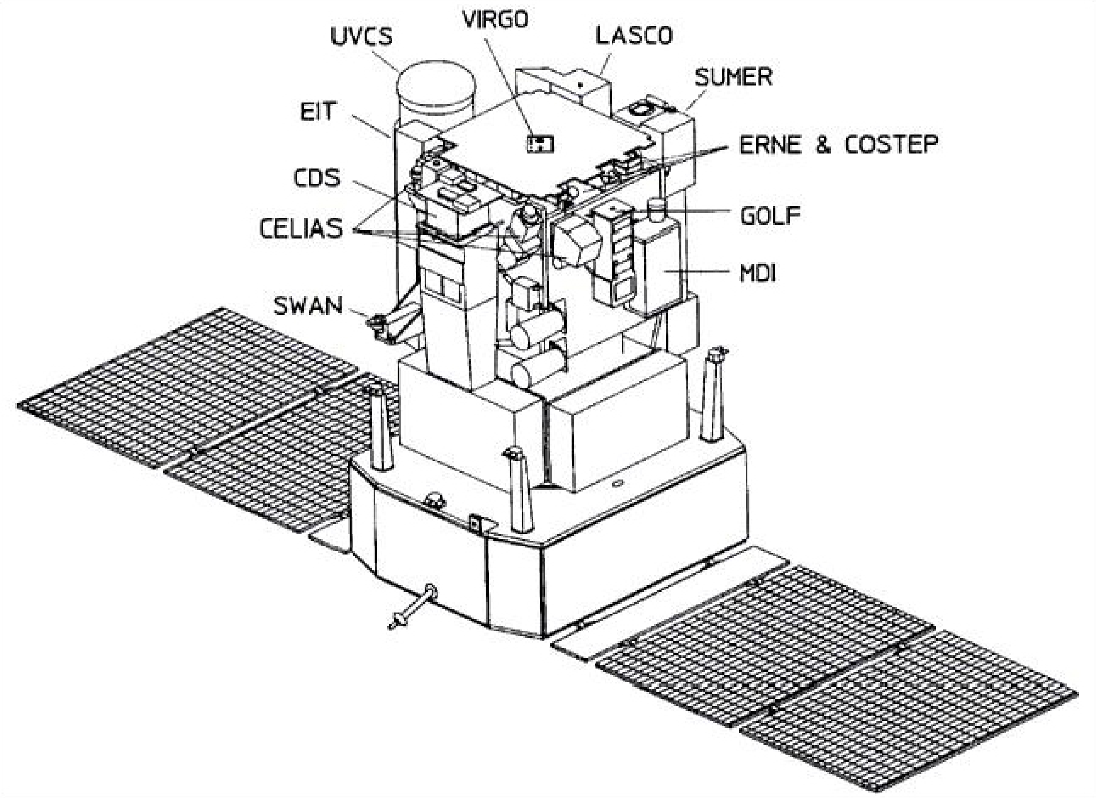

Figure 2.5: Schematics of the SOHO spacecraft and the numerous observing instruments on-board (Domingo *et al.*, 1995).

around the Sun that has an equal gravitational pull between the two massive objects. Similar to the SDO spacecraft, SOHO has long outlived its 2 year planned mission lifetime to ≈23 years. Figure 2.5 shows a schematic for the SOHO spacecraft bus with 12 attached instruments labeled. This schematic illustrates a wide variety of instruments responsible for studying the Sun and its effects at a variety of solar radii. Each instrument, similar to the SDO mission, was constructed by a unique team. The research presented later in this dissertation makes use of only two of these instruments and hence discussion will focus only the operations of these two instruments: the Extreme-Ultraviolet Imaging Telescope (EIT; Delaboudinière *et al.*. 1995) constructed under Institut d'Astrophysique Spatiale, France, and the Magnetic Doppler Imager (MDI; Scherrer *et al.*. 1995) constructed under Stanford University, United States of America.

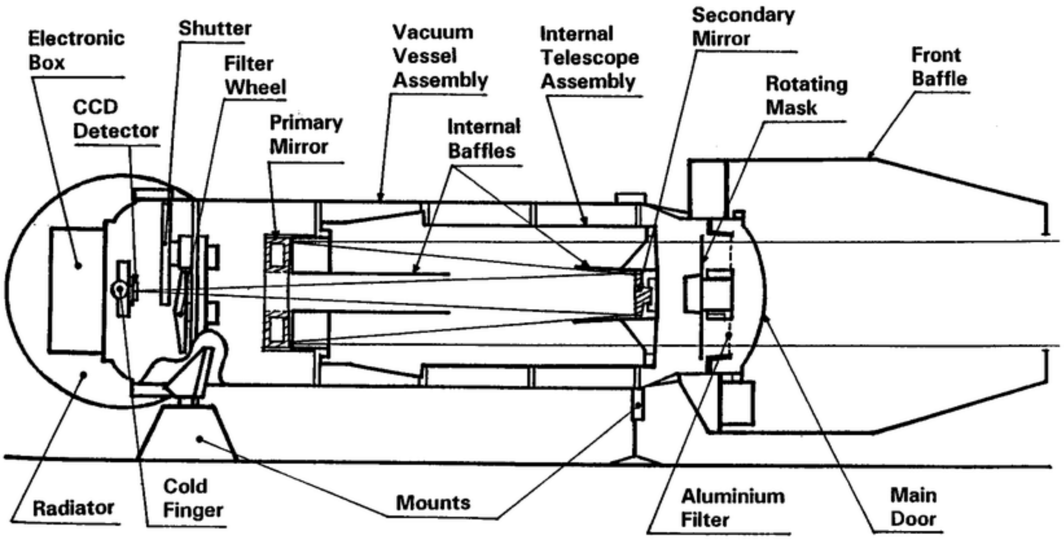

Figure 2.6: Schematics of the EIT telescope indicating major subsystems (Delaboudinière *et al.*, 1995). EIT is a Ritchey-Chretien telescope, meaning it has a hyperbolic primary mirror and a hyperbolic secondary mirror designed to eliminate off-axis optical errors

2.2.1 Extreme-Ultraviolet Imaging Telescope (EIT)

Similar to AIA, EIT observes the full solar disk of the transition region and solar corona to $1.5R_{\odot}$ at a variety of EUV wavelengths. These 1024×1024 full disk images have a spatial resolution of 2.6 arcsec per pixel with a temporal cadence ranging from seconds to several minutes, making the instrument less equipped for short term evolution of the corona than SDO's AIA.

Figure 2.6 shows the schematic for the EIT instrument with the path of two light rays traced within the instrument (Delaboudinière *et al.*, 1995). EIT is a Ritchey-Chretien telescope, which is a special variant of the Cassegrain telescope, with the most notable difference being a hyperbolic primary and secondary mirror, designed to remove off-axis optical errors. As can be seen in the instrument schematic, light enters the aperture of the telescope passing through an aluminium filter. The light is then reflected off the hyperbolic primary and secondary mirror, passing through a filter wheel onto a CCD detector. EIT uses a method known as multilayer normal incidence extreme-ultraviolet optics, whereby the telescope mirrors are coated to isolate certain wavelengths of emission. The mirrors onboard

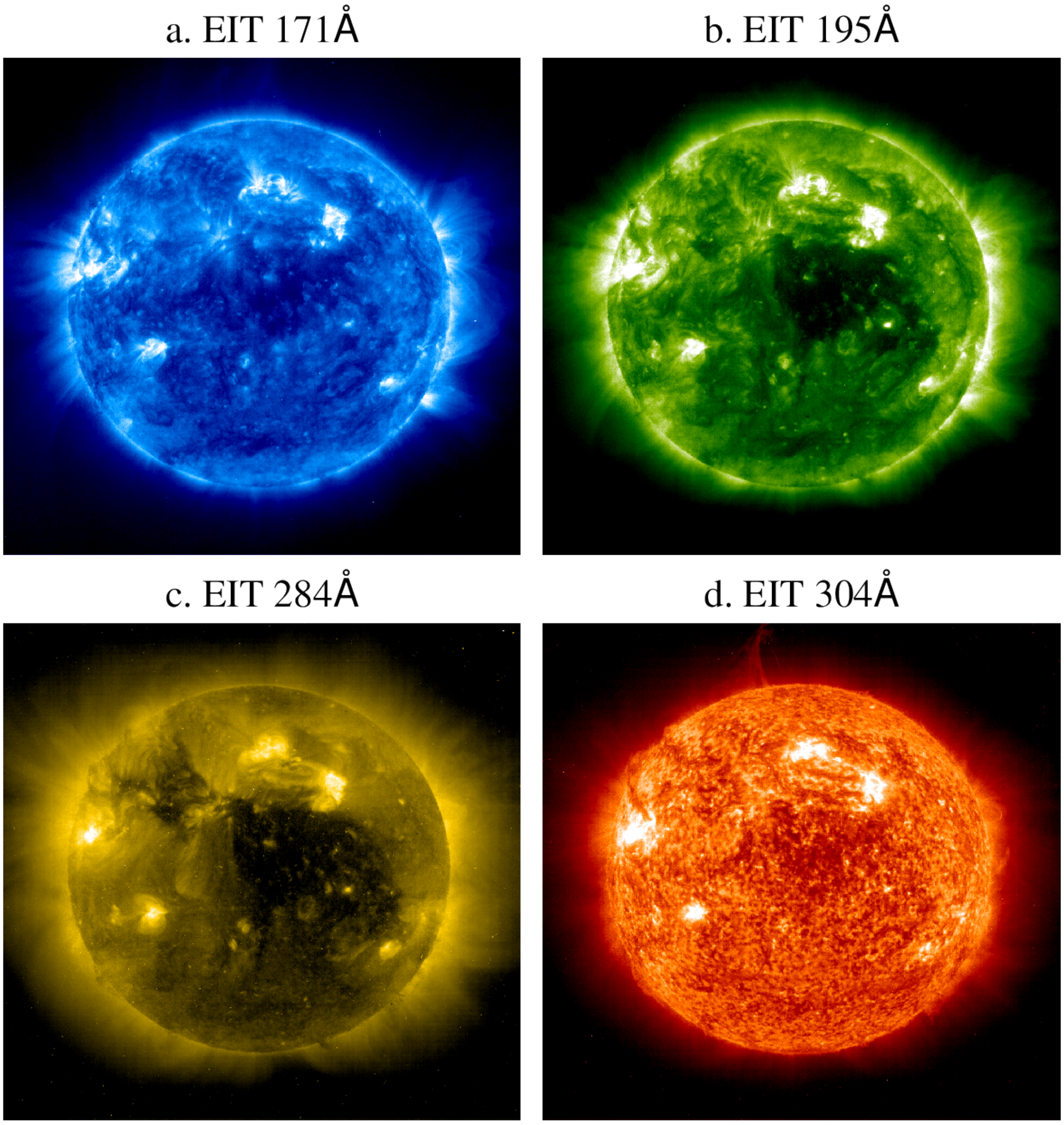

Figure 2.7: Full disk images of the Sun in the four EIT passbands, (a) 171 Å, (b) 195 Å, (c) 284 Å, and (d) 304 Å, for January 1st, 2000.

EIT are split into quadrants, the isolated emissions of which are He II (304 Å, 80000 K), Fe IX,X (171 Å, 1.3 MK), Fe XII(195 Å, 1.6 MK), and Fe XV (284 Å, 2.0 MK).

Figure 2.7 shows an example of four full disk images of the Sun from the four EIT passbands on January 1st, 2000. These images have a 1024×1024 pixel resolution covering ∼2600×2600 arcsec field of view. Similar to the AIA instrument,

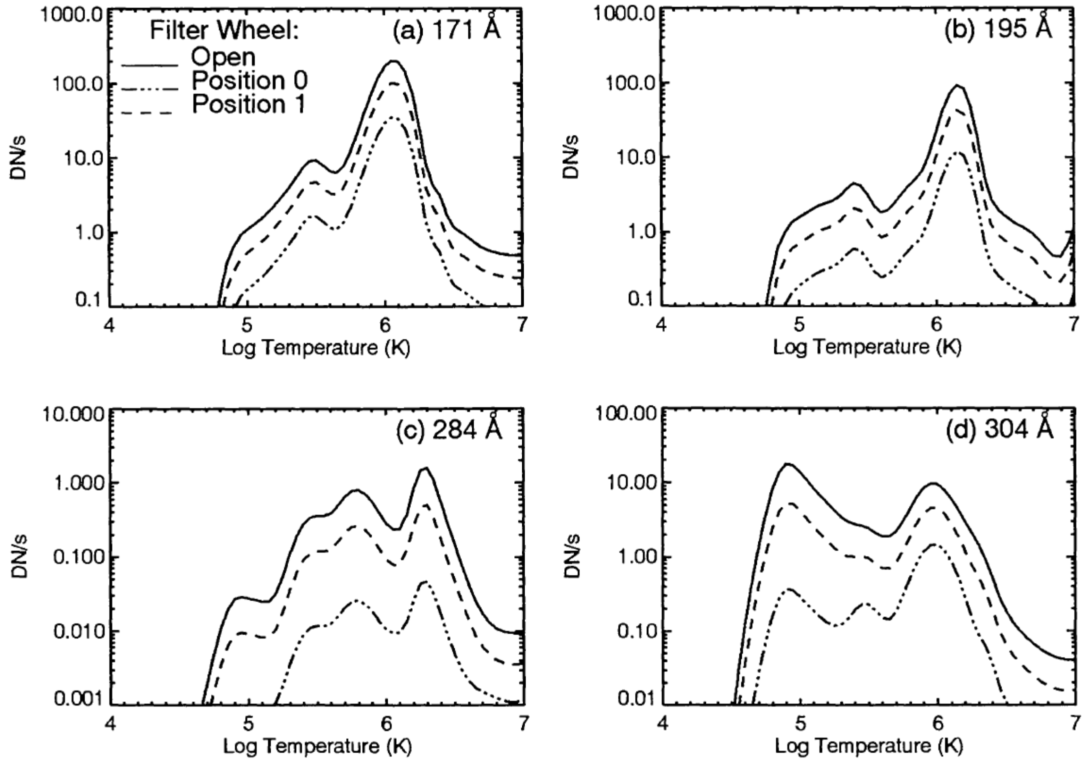

Figure 2.8: Temperature response function of the four EIT passbands (Delaboudinière *et al.*, 1995). Notably, the 284 Å passband receives significantly less counts incident photons than the 171 Å, and 195 Å passbands.

these images show the fine detailed structure of the solar atmosphere and the features within. ARs are noticeable at various points on the disk across the four passbands and a large central CH is noticeable in the higher temperature, 195 Å and 284 Å, passbands. Compared to the more modern AIA instrument, EIT is lacking in spatial and temporal resolution, and number of spectral passbands. The 171 Å and 304 Å passbands are common between the two instruments, however each instrument recommends a unique colour table when displaying observations from this wavelengths due to subtle differences in the filter wheels and mirrors to single out these wavelengths. The 193 Å passband from AIA and 195 Å passband from EIT are very similar and used for similar purposes in the scientific community due to their observation of similar temperature plasmas composed of the same iron ions. The EIT 284 Å has the least direct comparison between telescopes but is most similar to the 211 Å passband due to a similar peak observing temperature.

Figure 2.8 shows the temperature response of the four EIT passbands. As mentioned above, the EIT and AIA passbands have similar peak temperature responses which is demonstrated in this figure, as well as the similar shapes of the temperature response functions. 195 Å and 284 Å passbands both have significant peaks in the QS an AR temperatures, however, 284 has a significant wing to its distribution for colder temperature plasma. The 211 Å passband has a similar wing in its distribution however at a significantly lower ratio to the peak response, 10:1, than the 284 Å passband, 2:1. Furthermore, the difference in response between 284 Å and the other EIT coronal temperature passbands, two orders of magnitude, is significantly greater than 211 Å passband's difference to the other AIA coronal temperature passbands. The 171 Å passband for EIT has a higher peak temperature response than that of AIA, peaking at QS temperatures. This EIT passband however has a relatively wider base to the peak which extends to CH temperature plasmas.

2.2.2 Michelson Doppler Imager (MDI)

The MDI instrument takes observations using two tunable Michelson interferometers which define a 94 mÅ bandpass that tunes across the Ni i, 6768 Å, solar absorption line (Scherrer *et al.*, 1995). MDI takes similar observations to the HMI instrument on board SDO. HMI, in fact, is considered the successor to MDI, with improvements allowing high resolution observations of AR magnetic fields. MDI computes the Doppler velocity, continuum intensity and magnetic field in 1024×1024 full disk images on-board, which are then transmitted to ground teams. The full field of view of the instrument covers 34×34 arcmin^2 with a three second exposure. A number of these exposures are combined into a single observation occuring with a cadence of one minute. The internal elements of MDI are illustrated in Figure 2.9 with a light path through the instrument components, most notably the two Michelson Interferometers, before being detected by the CCD array. Colour in this image separates the instrument components into the telescope section (green), the interferometry section (blue), and the beam splitting and detector section (red). Magnetograms from MDI are created using a combination of Zeeman splitting and polarization of incident light, similar to that of HMI.

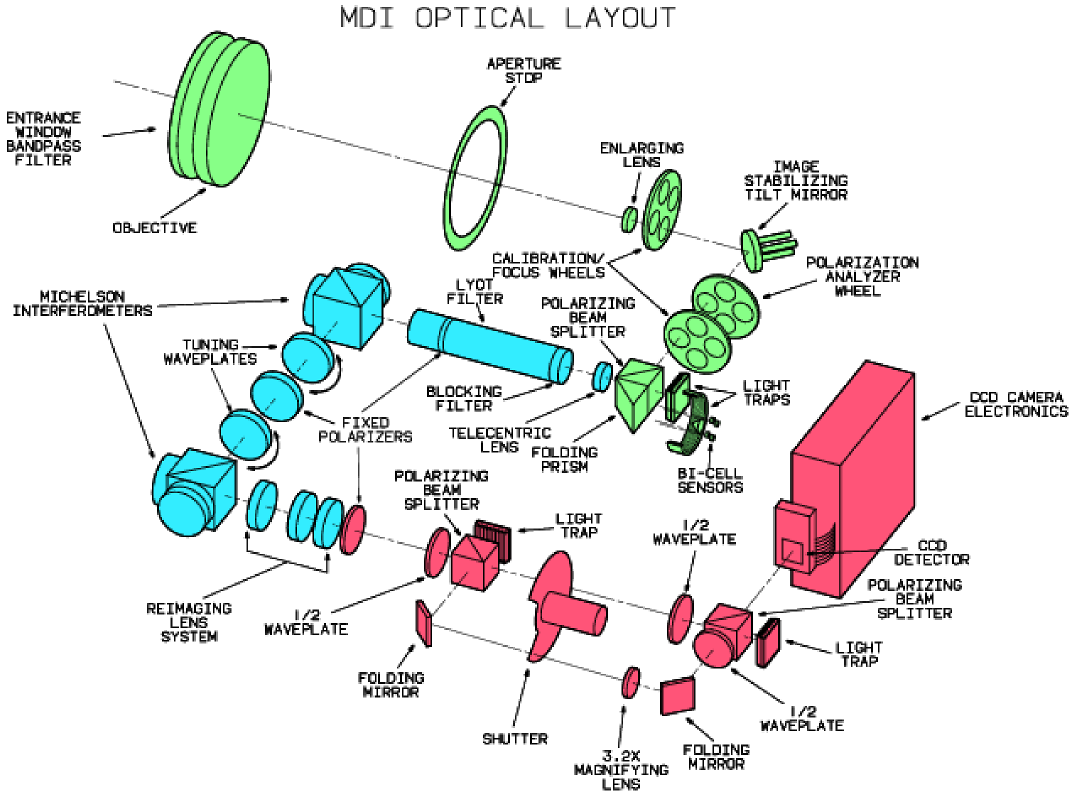

Figure 2.9: Schematic of the internal components of the MDI telescope with a light path showing the processes incoming light undergoes before being incident on the CCD detector (Scherrer *et al.*, 1995).

However, MDI only creates LOS magnetograms compared to the LOS and vector magnetograms created by HMI.

2.3 Advanced Composition Explorer (ACE)

The ACE instrument was launched in 1997 carrying six high resolution spectrometers, and three instruments that measure the properties of the interplanetary medium (Stone *et al.*, 1998). The instruments on-board ACE are shown in Figure 2.10 and are labeled as: Cosmic Ray Isotope Spectrometer (CRIS), Solar Isotope Spectrometer (SIS), Ultra Low Energy Isotope Spectrometer (ULEIS), Solar Energetic Particle Ionic Charge Analyzer (SEPICA), Solar Wind Ions Mass Spectrometer (SWIMS), Solar Wind Ion Composition Spectrometer (SWICS), Elec-

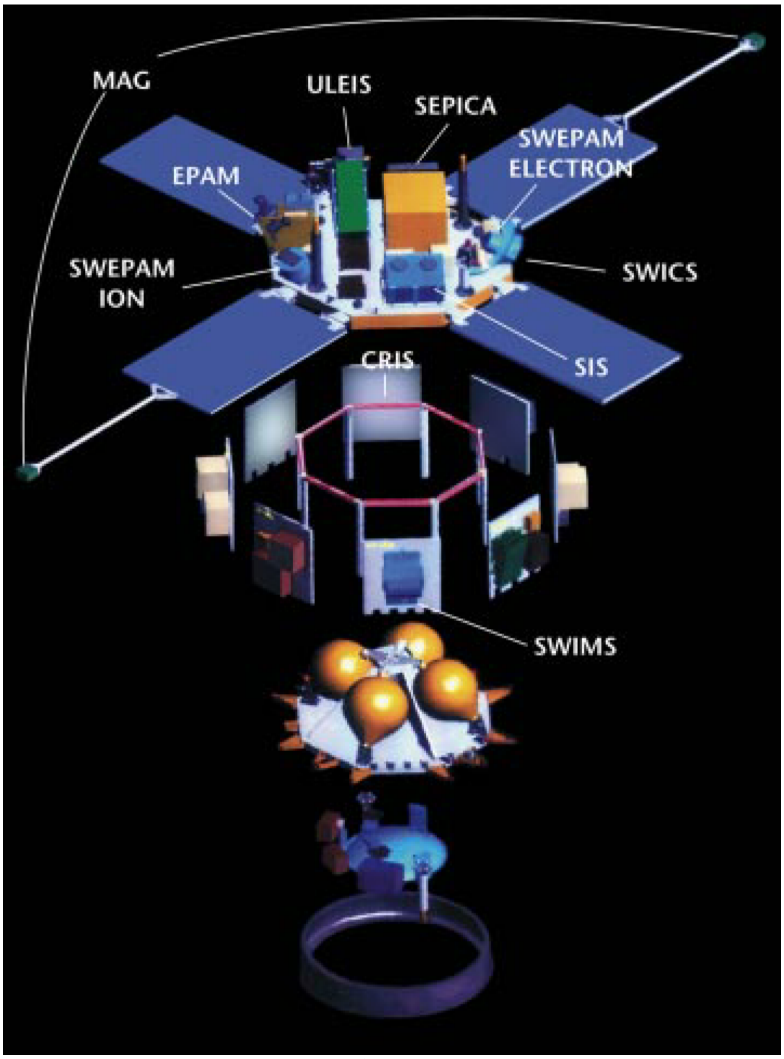

Figure 2.10: Exploded view of the ACE spacecraft, with observing instruments labeled (Stone *et al.*, 1998).

tron, Proton, and Alpha-particle Monitor (EPAM), and Solar Wind Electron, Proton and Alpha Monitor (SWEPAM). The objective of the ACE mission is to measure and observe elements in interplanetary space to gain a better understanding of the elemental and isotopic composition of the solar wind, and their sources, to understand the formation of the solar corona and to understand the processes that accelerate the solar wind.

SWEPAM is the primary observing instrument for solar wind observations, which identifies the proton densities, temperatures, speeds, relative abundances of

He to H^+, and velocities of solar wind ions in three spatial dimensions. Similar to the SOHO instrument, ACE is currently located at the L1 point and has enough fuel to maintain its location until 2024. The location of ACE at the Earth's L1 point is very interesting for space weather forecasting as it gives a measurement of the solar wind which is heading directly toward Earth. A space weather observatory at this location can act as an early warning system if other space weather prediction methods break down or make inaccurate predictions. ACE also carries on-board a magnetometer, MAG, to provide measurements of the local magnetic field of the interplanetary medium. Due to the orientation of the Earth's magnetic field, the non-ecliptic orientation of the solar wind's magnetic field can have a range of effects on Earth. Typically, a solar wind magnetic field with an opposing orientation to Earth's magnetic field will have an associated higher risk to humans and technology, due to the magnetic reconnection that occurs between the magnetic fields which allows the solar wind to penetrate more into the Earth's atmosphere. The MAG instrument is constructed as two, boom-mounted, triaxial flux gate sensors, kept far from the main spacecraft bus to avoid saturation of measurements from magnetic fields created by the instruments electronics.

2.4 Coronal Hole Identification methods

The research presented in this dissertation aims to improve the understanding of space weather effects and their origins in solar CHs. To understand the underlying processes that govern space weather effect from CHs, it is essential to identify and segment CH regions from the surrounding QS plasma and ARs. While CHs have long been observed off the solar limb (Serviss, 1909) on-disk segmentation had not been performed until the late 20th century when electron density measurements and X-ray images of the solar corona of significant quality became available, see Altschuler *et al.* (1972); Munro & Withbroe (1972). Since these initial segmentations, numerous methods have been created to segment CHs, both manually and automatically.

2.4.1 Human Segmentations

Human segmentation of CHs was the initial, easiest, and most rapid form of CH segmentation. Human segmentation was often performed in the high temperature passbands, such as the 193 Å passband observed by AIA, which demonstrated the greatest contrast between CHs and surrounding QS plasma. Humans are particularly good at identifying and categorizing features based not only on their contrast to surrounding features, but have evolved to subconsciously identify and differentiate features based on properties not recognized by the active consciousness (Barra *et al.*, 2008). A common example of this subconscious recognition is a feeling of being watched, which is often due to some object in their vicinity that resembles a face or pair of eyes, a phenomenon known as pareidolia. In the area of solar corona feature segmentation, this ability is invaluable and allows humans to differentiate CHs from surrounding plasma, as well as discern CHs from other dark coronal features such as filaments. In the event of filaments humans can differentiate CHs based on the size, shape, texture, and previous knowledge of filament locations and properties. This differentiation can occur in a fraction of second allowing a human to fully segment a CH from an image of the solar corona.

Human segmentations of coronal features have the advantage of being relatively accurate with a minimum time requirement while creating a segmentation that is typically well agreed upon. However, compared to automated methods, these segmentations are slow, do not create fully accurate boundaries and are inefficient for creating large scale databases of segmentations. Due to its relative simplicity and relative accuracy, manual human segmentations are still used by the leading space weather forecasters at both the National Oceanic and Atmospheric Administration (NOAA) Space Weather Prediction Center (SWPC), and the United Kingdom's Met Office Space Weather Operations Center (MOSWOC). An example of a MOSWOC hand segmentation map is shown in Figure 2.11.

While these human segmentation methods make reasonable estimates of CH boundaries, it is not possible to create a regular rapid, continuous segmentations. Furthermore, humans segmenting by eye/hand will have a tendency to differ in segmentations from person to person, with the same person even providing varying segmentations for the same observations. These problems can be solved with

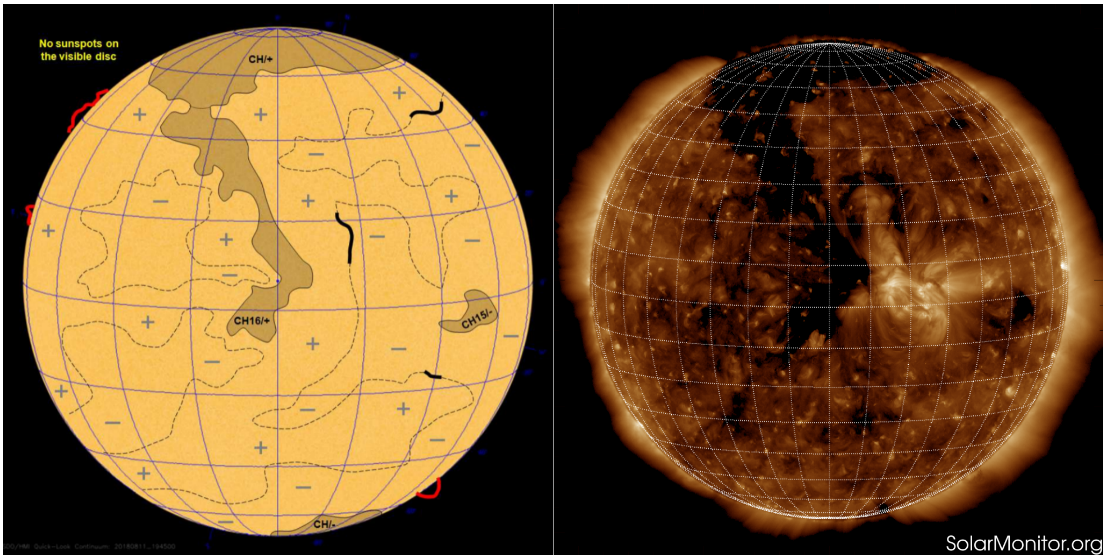

Figure 2.11: MOSWOC human segmentation of on disk CHs (left) compared to the 193 Å AIA observation for the same time sourced from *solarmonitor.org* for August 11th, 2018 (right). Other features are identified in the MOSWOC segmentation, such as filaments, prominences, and polarity inversion lines.

the use of an automated segmentation method which can rapidly segment many observations of the solar corona, as well as being consistent in segmentations based on specific rules programmed into the automated algorithms. Below, a number of automated segmentation algorithms commonly used in space weather predictions are discussed, and their methods for extracting CH boundaries from observations of the solar corona.

2.4.2 Coronal Hole Automated Recognition and Monitoring (CHARM)

The CHARM algorithm, developed by Krista & Gallagher (2009), makes use of the contrast existing between the intensity of CH regions and all other regions of the solar corona. The algorithm was designed to use a local intensity thresholding technique on 193 Å images from AIA and 195 Å images from SOHO. Intensity thresholding is performed by splitting pixels in an image into a binary segmentation based on the pixels intensity relative to some determined threshold value. For CHs, a pixel intensity below some threshold is typically considered to be a CH pixel, or binary 1, while pixels above this threshold are considered non CH pixels, or binary 0. Typically intensity thesholding techniques are performed on a global scale, where all pixels in an image are sorted into intensity histograms, where a peak of intensities would represent the existence of a particular feature. CHs, however, can have a significant range of areas, and can vary in number across the solar disk. This makes a global intensity segmentation technique less viable for automates CH segmentations as a computer will find it very difficult to automatically identify the peaks in intensity histograms if very few pixels are available to represent a feature. Krista & Gallagher were able to circumvent this issue by creating a local intensity thresholding method which divided a larger scale image of the solar corona into smaller sub-images, as displayed in Figure 2.12. This figure demonstrates multiple sub images of a 195Å image taken from SOHO focusing on a CH region, and the corresponding histograms of pixel intensity within each subimage. From these smaller sub images, features such as CHs can occupy a more significant portion of the histogram, and hence be easier for an automated segmentation method to identify an optimal threshold between the two intensity peaks. For the CHARM method of segmentation, the minimum value existing between a range of 30-70% of the QS peak values (red dashed lines) is selected as the optimal threshold (black solid/ green dashed line) and the sub image is segmented based on all pixels falling below this intensity threshold. These individual sub maps can then be combined together to create a single full-disk CH segmentation.

This method of segmentation, however, has its drawbacks. Using only a single wavelength for CH thresholding means the local intensity thresholding method cannot differentiate between CH regions and other regions of the solar corona that appear as dark in the 193 Å/195 Å passbands. Filaments for example are often confused for CHs in automated segmentation algorithms due to both features having a lower temperature than the ~1.3 MK passband used to identify them, with CH temperature ≈ 0.7 MK and filament temperature ≈ 0.4 MK. Krista & Gallagher used the known magnetic unipolarity of CHs to differentiate CH regions from spurious detections of filaments, or relatively cool QS regions. This unipolarity verifcation was initially performed using MDI magnetogram images, however the algorithm has now been expanded to also include HMI magnetograms where applicable. In essence, Krista & Gallagher used the known temperature

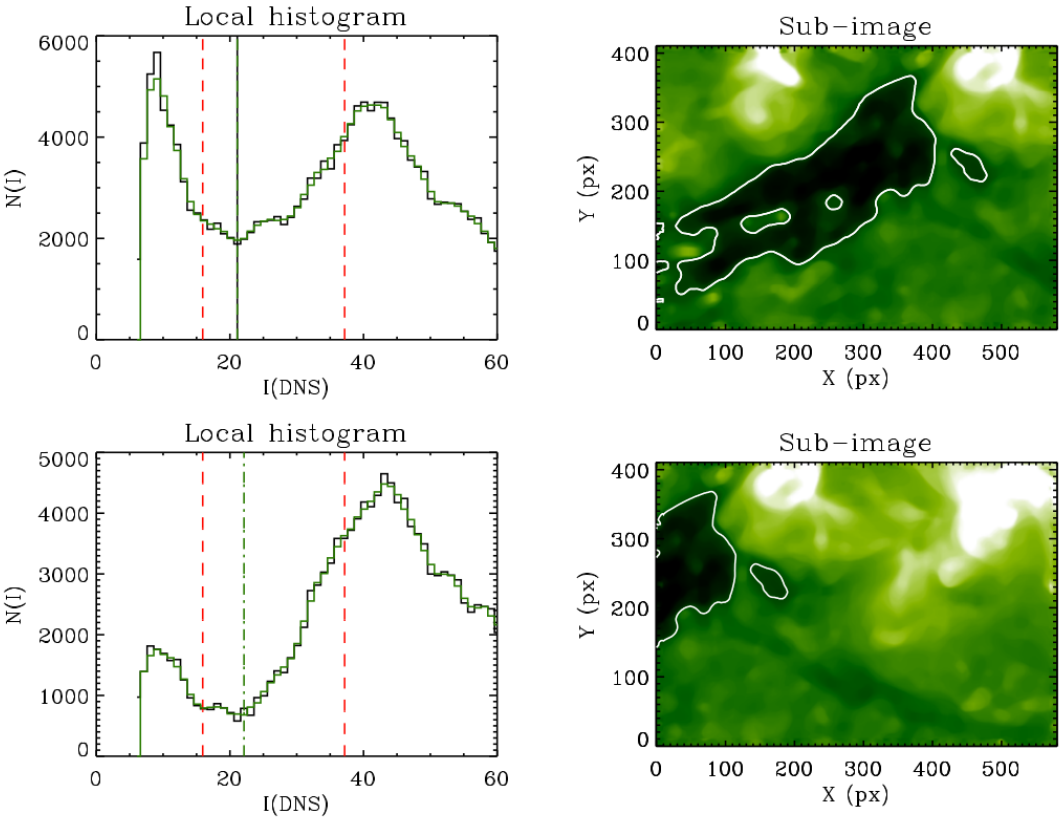

Figure 2.12: Demonstration of local intensity thresholding techniques used by Krista & Gallagher (2009) to identify CHs. Left plots show histograms of intensities in the corresponding sub-images on the right. Within the histograms, two significant peaks are apparent, a lower intensity peak associated with the presence of CH intensity pixels and a higher intensity peak associated with the QS pixels. By identifying the local minima (black solid/ green dashed lines) located between 30-70% of the peak of QS intensities (red dashed lines) as a threshold, lower intensity regions can be classified as CHs and segmented accordingly. This renders the segmentations available in the right panels where CHs are outlined with contours.

and magnetic properties of CHs to segment them from EUV images of the solar corona.

2.4.3 Spatial Possibilistic Clustering Algorithm (SPoCA)

The SPoCA algorithm estimates the non-normalized probability of pixels in each supplied passband to be classified into individual features (Barra *et al.*, 2008, 2009; Delouille *et al.*, 2012). These probabilities separate every on-disk pixel into cate-

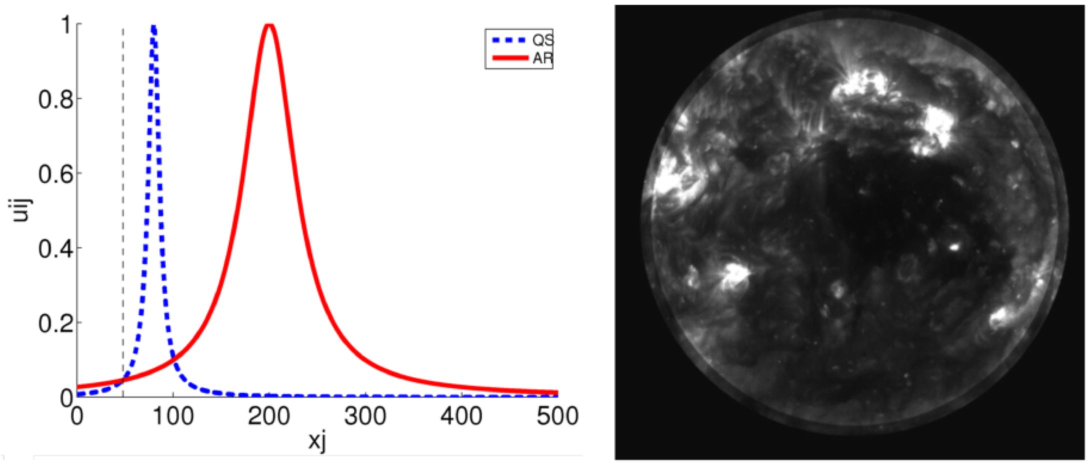

(a) membership function for AR and QS (b) EIT 195 Å image

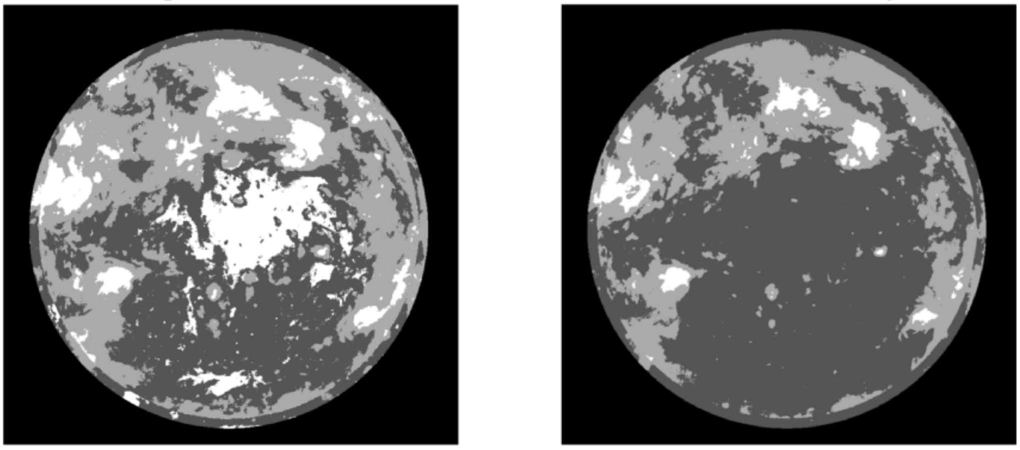

(c) Original segmented map (d) Segmented map with constraints

Figure 2.13: Example of the SPoCA classification method to segment ARs from surrounding QS (Delouille *et al.*, 2012). (a) The membership function used to classify AR pixels from the QS pixels using some descriptor, x_j. Here, the intensity of the EIT 195 Å image (b) is used as the descriptor for classification. (c) Segmented map classifying regions with a higher probability of being AR showed in white. (d) Segmented map classifying ARs similarly to (c) but with an intensity constraint to prevent misclassification due to the wider full width half maximum of the AR cluster, indicated by the grey dashed line in (a).

gories of CH, AR, or QS. Probabilities are calculated based on a pixels properties relative to some property descriptor of the desired feature. Figure 2.13(a) shows an example of probabilities for AR and QS relative to the intensity of pixels in a full disk EIT 195 Å image as seen in Figure 2.13(b). A pixel intensity in (a) indicates the probability that pixel belongs to a certain feature cluster and these features can then be segmented as seen in (c). In some instances, however, the spread of intensity of the feature cluster can cause a misclassification, as seen in the low intensity end of Figure 2.13(a). To combat this effect, constraints on the clusters are applied, here preventing pixels below some threshold being considered AR. Segmentation based on these combined methods produces a segmented map that excludes the cooler, dark regions (d). This probability method is used to segment CHs, ARs, and QS for input intensities, which can then be combined together to form a single multi-wavelength probability segmentation which is described for a combination of a 171 Å and 195 Å segmentation in Equation 2.1:

$$\pi_C(x) = max\left[\frac{min(\pi_C^{171}(x), \pi_C^{195}(x))}{h}, min(max(\pi_C^{171}(x), \pi_C^{195}(x)), 1-h)\right] \tag{2.1}$$

where π represents the probability value, C represents a feature label, e.g. CH, x is a given descriptor, h is a function of x such that $h(x) = \mid \pi_C^{171}(x) - \pi_C^{195}(x) \mid$, and the superscripts of 171 and 195 describe the wavelengths each probability value is sourced from. Alternatively, segmentations in each wavelength can be displayed separately to illustrate the variation of CH boundary with height. The SPoCA method was later improved upon by Reiss *et al.* (2015) through the use of machine learning methods to remove misidentifications between CHs and filaments.

Both the SPoCA and CHARM algorithms, as well as human segmentations, utilize measurements of intensity in EUV wavelengths as estimations of CH properties, such as temperature and density. However, both of these methods rely on single passband segmentations or a combination of segmentations from single passbands to segment images. These methods are unreliable for CH segmentation as they depend on a large contrast existing between the identifying feature and surrounding intensities which is not often the case for CHs, as will be demonstrated in Chapter 4. These methods however are often adequate for segmenting ARs from surrounding QS plasma due to the relatively higher contrast between the two. While other automated methods of feature segmentation do exist, such as active contours without edges (Boucheron *et al.*, 2016), and watershed approaches (Nieniewski, 2002), here CHARM and SPoCA are described in depth due to their prevalence in the forecasting community, and their use of physical or semi-physical properties of CHs to segment them from surrounding QS.

All of these aforementioned automated have different advantages and disadvantages. For the highlighted algorithms of CHARM and SPoCA, both are relatively quick, typically being used for real-time segmentations, and produce reasonable segmentations that can give a decent first estimate of coronal hole locations. However, almost all previous algorithms are disadvantaged through their use of monochromatic methods. Many coronal features are exhibit similar intensity signatures in single wavelengths, for example, CHs and filaments having similar intensity profiles. Furthermore, previous segmentation methods have focused on a computer science specific interpretation of their data for segmentation, however they are attempting to identify a feature which is better described via its physical characteristics. These are disadvantages of previous automated CH segmentation algorithms that will be addressed within this research.

3

Theory

In the field of space weather forecasting, theoretical modelling is essential to accurately predict space weather events. To date, numerous models have been created to predict properties of the solar wind from observable properties of the solar corona. In this chapter, the theory behind previous models used to forecast properties of the solar wind will be discussed, as well as methods to improve estimations of the local temperature and density for regions of the solar corona, and machine learning (ML) methods which can yield complex models that allow for more accurate space weather predictions than previous techniques.

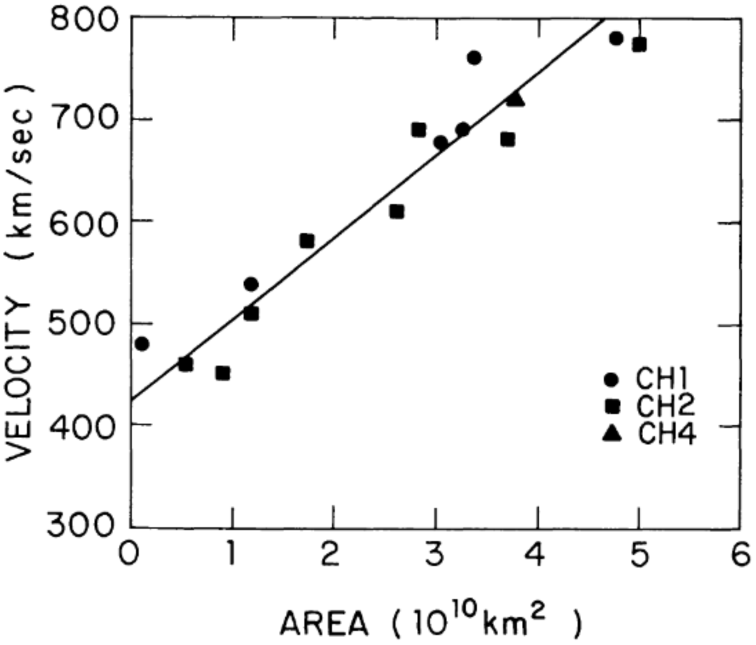

Figure 3.1: Empirical model for predicitng HSSW velocity from corresponding CH area found by Nolte *et al.* (1976).

3.1 Solar Wind Velocity Predictive Models

As mentioned in Chapter 1, CHs cause most of the regular interruptions to the slow ambient solar wind at Earth during the solar minimum. These interruptive streams of HSSW are known to be geo-effective and can cause space weather storms at Earth. The severity of these storms is entirely dependant on the properties of the HSSW stream, with stream velocity being a particularly influential factor. The properties of the HSSW streams are in turn dependant on the properties of their originating coronal hole regions (Arge & Pizzo, 2000; Rotter *et al.*, 2012; Vršnak *et al.*, 2007). Multiple models have been created to predict the speed of solar wind as it emanates out of the corona, and as it reaches Earth. Figure 3.1 illustrates a simple model for predicting the HSSW proposed by Nolte *et al.* (1976) from an empirical correlation of CH area found from Skylab observations and peak solar wind velocity from near Earth solar wind measurements performed by the Interplanetary Monitoring Platform (IMP)-8 instrument. This model predicts the peak solar wind speed from empirical measurements of both solar wind speeds and the areas occupied by their originating coronal holes. A correlation exists between these two properties and by measuring both and creating a least squared fit linear regression from the results, a new empirical model is created. The linear regression methodology will be described later in this chapter. Nolte *et al.* (1976) found from their measurements a relation of the form:

$$v_{SW} = (80 \pm 2)A_{CH} + 426 \pm 5 \tag{3.1}$$

where v_{SW} is the peak velocity of the HSSW stream in km s^{-1}, and A_{CH} is the CH area in units of 10^{10} km^2. Since this initial model was found, more sophisticated methods have been developed to predict properties of the solar wind from smaller scale magnetic and topological properties of CHs.

3.1.1 Wang-Sheely Model

The Wang-Sheeley (WS) model is an empirical model capable of predicting the solar wind speed and interplanetary magnetic field polarity (Wang & Sheeley, 1990; Wang & Sheeley, 1991; Wang & Sheeley, 1995). This model bases its predictions on the inverse relationship between the expansion of magnetic flux-tubes and the velocity of the emanating solar wind from coronal hole regions (Levine *et al.*, 1977). An example of magnetic flux-tube expansion is shown in Figure 3.2, where a tube of magnetic field lines increases in angular area, and hence decreases in magnetic field density, across a height of 20 Mm. However, in general the expansion of a magnetic flux tube can be measured across any heights. This flux-tube expansion is described by a two-dimensional unitless comparison of magnetic flux density between two surfaces (Wang *et al.*, 1997), as follows:

$$f(r) = \left(\frac{R_\odot}{r}\right)^2 \frac{B_r(R_\odot, \theta_\odot, \phi_\odot)}{B_r(r, \theta, \phi)} \tag{3.2}$$

In the Wang *et al.* (1997) case, the expansion factor, f, is described between the solar surface and the source surface at radial distance $r = 2.5\ R_\odot$, where B_r describes the magnetic field for a given surface, and θ and ϕ define latitude and longitude position information along the magnetic fields lines respectively. To accurately estimate the magnetic field at the source surface, they are extrapolated from the

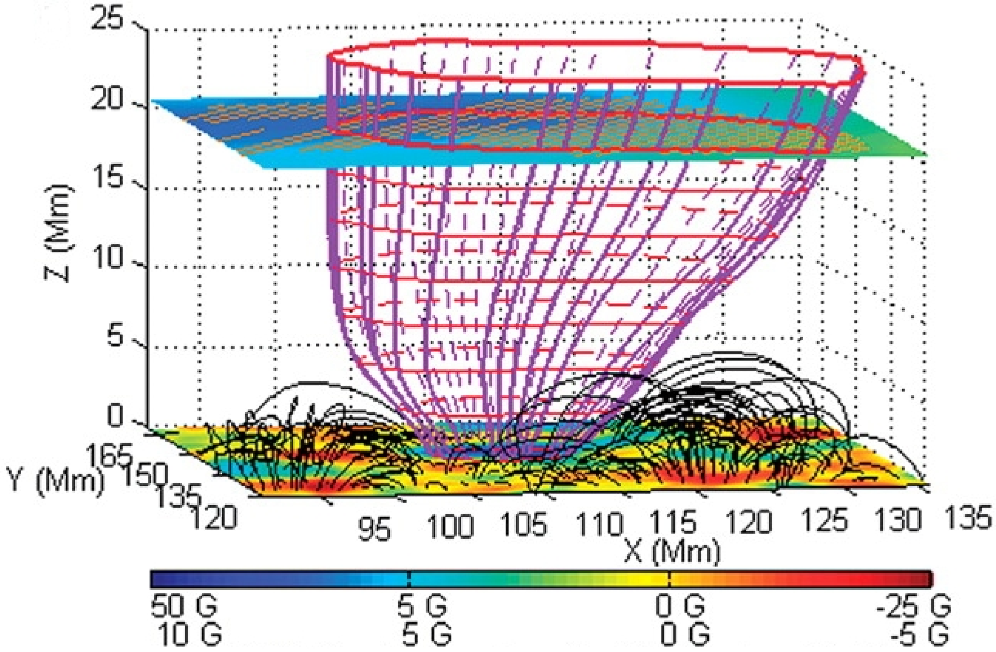

Figure 3.2: Model of a flux tube (purple lines) expanding from an open magnetic field region on the solar surface (Z = 0 Mm) to a source surface height (Z ≈ 20 Mm) while surrounded by closed magnetic loops (black lines) (Tu *et al.*, 2005).

solar surface through a potential field source surface (PFSS) model (Altschuler *et al.*, 1972; Wang & Sheeley, 1992). A PFSS model provides an approximation of the three dimensional structure of the solar magnetic field from extrapolations of surface measurements of magnetic field. Pinto & Rouillard (2017) simplified the flux-tube expansion factor to a dimensionless comparison of the area, A, occupied by a flux-tube at two surface heights, $r_\odot$ and r, as follows:

$$f = \frac{A_r}{A_\odot}\left(\frac{r_\odot}{r}\right)^2 \tag{3.3}$$

Equations 3.2 and 3.3 enabled Wang & Sheeley (1990) to empirically correlate and categorize solar wind speeds, and make a predictive model of wind speeds from coronal hole flux-tube expansion factors, as shown in Table 3.1.

3.1.2 Distance From Coronal Hole Boundary Model

Riley *et al.* (2001) developed an empirically-driven global MHD model of the solar

f	$v_{HSSW}(kms^{-1})$
<3.5	>650
3.5-9	650-550
9-18	550-450
>18	<450

Table 3.1: Correspondence between flux-tube expansion factors and daily wind speeds from Wang & Sheeley (1990). These expansions are calculated between the distance of the solar radius, 1 $R_\odot$, to the source surface height, 2.5 $R_\odot$.

corona and inner heliosphere which includes a method of HSSW velocity prediction of regions of CHs from their spatial distance from the nearest CH boundary. This model assumes that regions of the CH that are far from CH boundaries, i.e. regions of exclusively open magnetic flux, emit solar wind which travels at the fast wind speeds observed by Feldman *et al.* (1976). However, at the boundary of open and closed magnetic regions flow speed is slow. The change in flow speeds between these regions are considered to be continuous, and over a short distance the Riley *et al.* (2001) model raises the flow speed to match that of the fast flow speed as described by the Distance from Coronal Hole Boundary (DCHB) equation:

$$v_r(d) = v_{slow} + \frac{1}{2}(v_{fast} - v_{slow})\left[1 + tanh\left(\frac{d-\alpha}{w}\right)\right] \tag{3.4}$$

where d is the distance from the nearest CH boundary measured along the photosphere, α is the thickness of the slow flow band which is assumed to be ~6°/0.1 radians, and w is the width over which the flow speeds are raised to coronal hole values, which is assumed to be ~3°/0.05 radians. Figure 3.3 illustrates an example of (a) a segmentation of CH boundaries compared to (b) the radial solar wind speeds derived from Equation 3.4, both predicted at photospheric heights, which is then (c) projected out to 30 $R_\odot$ along magnetic field lines. This model has since been empirically validated by Riley *et al.* (2003) via Ulysses spacecraft (Bame *et al.*, 1992; Wenzel *et al.*, 1992) measurements of polar CHs across 12 Carrington rotations[1].

---

[1] An estimate of solar rotation period from measurements of sunspot rotation rates, ~27.2753 days

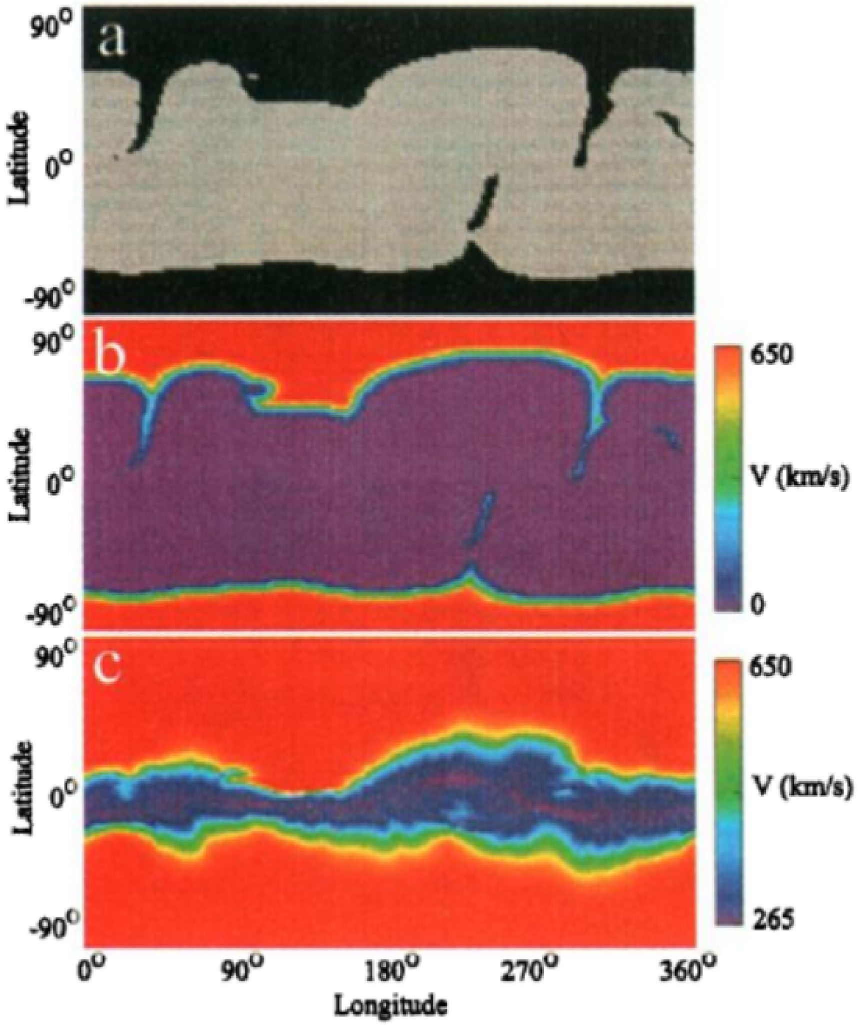

Figure 3.3: (a) CH segmented map of the Sun at a photospheric level. (b) Model of solar wind radial velocities emitted at the photospheric level using the DCHB model in Equation 3.4. (c) Radial wind velocities at a height of 30 $R_{\odot}$, which are found from projections along field lines from (b) (Riley *et al.*, 2001). These images are displayed in a Carrington heliographic coordinate system to best show the global structure of the solar magnetic fields.

3.1.3 Wang-Sheely-Arge Model

A number of significant improvements were made to the quality and time resolution of the WS model, see Arge & Pizzo (2000) and references therein. Most significantly, Arge & Pizzo modified the WS model by establishing a continuous empirical function that related the magnetic expansion factor to the velocity of corresponding solar wind streams at the source surface height, which is described by:

$$v(f_s) = 267.5 + \frac{410}{f_s^{2/5}} \tag{3.5}$$

where $v(f_s)$ is the velocity of the solar wind at the source surface and f_s is the flux tube expansion factor between the solar surface and the source surface, as described by Equation 3.2. The model was further changed to propagate the solar wind from the source surface to Earth using an assumption of radial solar wind streams with an allowance for simple stream interactions. The PFSS modelling remains unchanged, however, the model was updated to use daily magnetograms to construct synoptic maps, exclude problematic magnetograms, and to better account for projection effects of near limb magnetic fields. Due to these significant improvements, the updated model was renamed the Wang-Sheeley-Arge (WSA) model. This model is now used in space weather predictions to create 3D models of the ambient solar wind speeds and interplanetary magnetic fields within the local solar environment, $\leq$30 $R_\odot$ (Arge *et al.*, 2004; Riley *et al.*, 2015; Sheeley, 2017). This model is also used as a starting point for the WSA-Enlil solar wind prediction model (Odstrcil, 2003; Odstrčil & Pizzo, 1999a,b), which is regularly used by the UK Met Office, and NOAA SWPC. This method of modelling focuses primarily on the magnetic structure of the solar surface and its extrapolation. It does not take into account the features within the solar corona, which govern the majority of space weather phenomena. Features within the corona could automatically be identified and used to prune poor ensemble members within the WSA-Enlil model if the model is driven by an ensemble of input magnetograms e.g. those produced by the Air Force Data Assimilative Photospheric flux Transport (ADAPT; Hickmann *et al.* 2015) model. Such an approach is under consideration by SWPC and the UK Met Office.

3.2 Machine Learning Methods

Machine Learning (ML) is a relatively new approach to handling data, making classifications and predictions. Typically, ML models operate more efficiently and accurately than human built models (Cramer, 2002; Mitchell, 1997). ML models are underutilized in space weather forecasting, hence the construction of a new ML model for predicting solar wind properties may make a significant improvement to the accuracy of forecasting within the field. ML is often split into supervised and unsupervised methods. Supervised ML requires some amount of already known sets of data to train a model, whereby any new results can be inferred from the training set. Unsupervised learning is the method of classification or regression without any previously known training data. The model of an unsupervised system will create a classification or regression from unknown input data and classes are typically found through some clustering method. Supervised learning methods typically produce more accurate, robust models than unsupervised methods and are of more use to space weather predictions due to the existence of large catalogues of solar features and associated solar wind streams.

3.2.1 Linear Regression

Linear regression is a simple form of ML often used in science to build predictive models. Linear regression depends on a correlation existing between some number of properties, or more appropriately, it attempts to create a correlation between some number of properties (Zou *et al.*, 2003). A simple 2D example is illustrated in Figure 3.4, where a set of properties are observed for a number of features and are plotted against one another (Kassambara, 2018). Assuming that these points are correlated, a linear fit is applied through a least squared fit method (Bevington & Robinson, 2003; Press *et al.*, 2007). This least squared fit now acts as a linear regression model for future predictions of either property from a measurement of only one. This two dimensional example can be extrapolated to N dimensions, where N is the number of properties of each feature measured. The computational time of these ML methods are heavily correlated with the number of properties measured, i.e. $t_{regress} \propto \mathrm{N}^{\gamma}$, where γ is some positive power. Linear

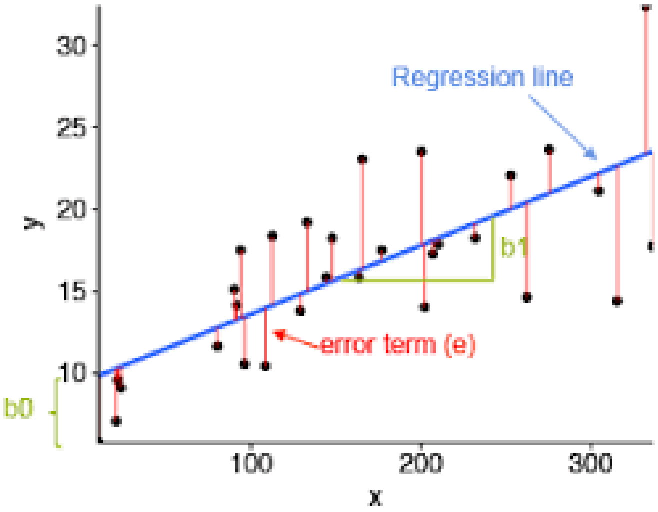

Figure 3.4: Example linear regression fit (blue) to individual measurements of two properties, x and y, represented by points (black) (Kassambara, 2018). The optimal linear fit is found by varying the parameters of the linear fit equation, b0 and b1, to produce a line with the least total of the absolute error terms, e. This linear fit can henceforth be used to make predictions of the y properties from measurements of the x properties, i.e. drawing a correlation between the two properties. This method can be applied in multiple dimensions, using a varying number of input (x-axis) properties to predict an output (y-axis) property.

regression models fail to accurately model non-linear relationships. Due to the relative unknown relationships between properties of solar features and associated solar wind, this failure to identify non-linearity makes these models less preferential than other ML methods.

3.2.2 Decision Tree Classification and Regression

Decision tree methods of ML allow for the modelling of more complicated relationships between measured properties (Quinlan, 1986). A decision tree is a supervised ML method which acts as a collection of “if” statements, typically Boolean, that categorize a data-set based on the properties of said data-set. Figure 3.5 illustrates an example of decision tree classification (Tan *et al.*, 2005). Data points are categorized as either circles or triangles based on their x and y properties. This ML method is built from the displayed training set in Figure 3.5 (left) as a two depth

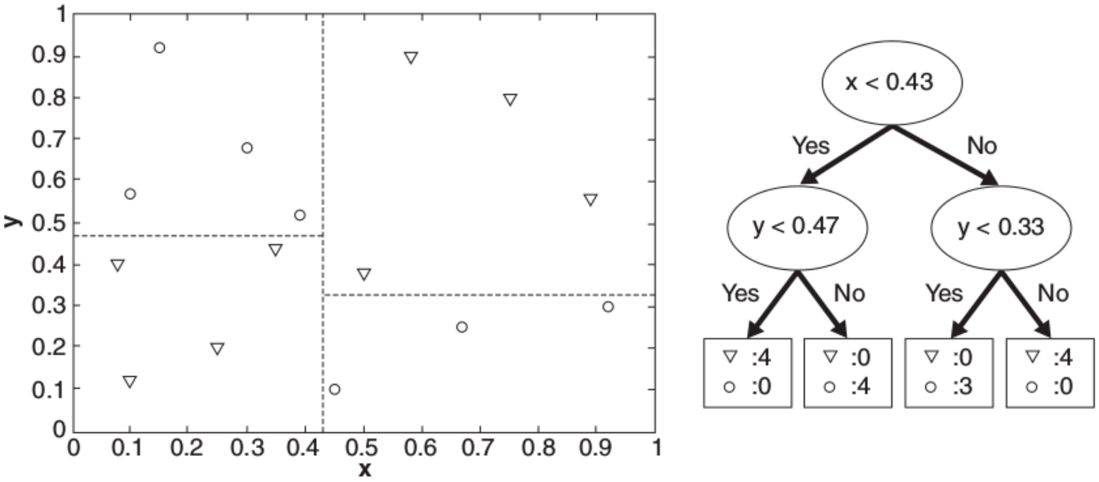

Figure 3.5: Supervised classification of an input data-set (left) through a two-depth Boolean decision tree (right) (Tan *et al.*, 2005). The constructed decision tree can be used to automatically classify new input data-sets based on their x-axis and y-axis properties.

decision tree which can now act as a predictive model for future classification.

This method of ML can be further applied to create regression models through a process of multiple local linear regressions fit to a data-set. However, as with most methods of ML, overfitting the training data-sets can create a model that attempts to align too well with outlying data points. Figure 3.6 shows an example of two decision tree regression models for a sinusoid with some outlying points, likely caused by measurement error. Neither of these models accurately represent the sinusoid due to the depth of their decision trees. The two depth decision tree model oversimplifies the data-set, however, the five depth decision tree model overfits the data-set, neither of which appear sinusoidal. To solve this issue, decision trees should be built with an appropriate depth. This issue of appropriate selection of decision tree depth is relevant for space weather forecasting as every property of a solar feature measured, e.g. CH area, has an associated error margin. Hence, training an inappropriately deep decision tree on space weather properties will likely cause a simplification or will overfitting of the model to erroneous property measurements.

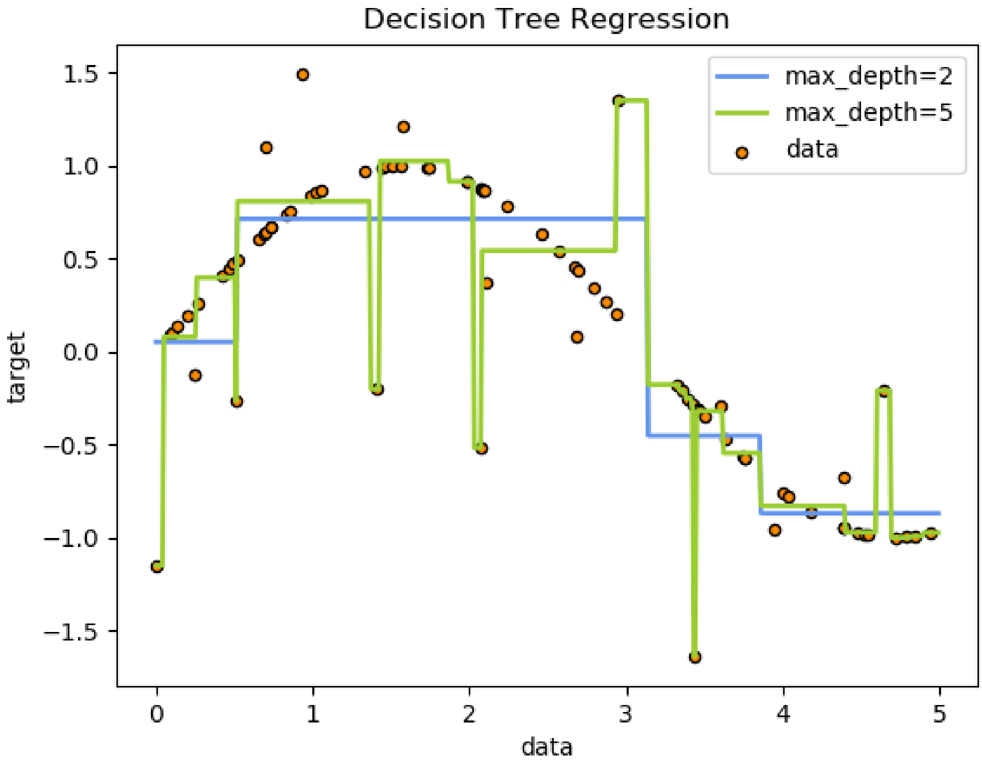

Figure 3.6: Example of decision tree regression attempting to approximate a sinusoidal signal with some outliers (Pedregosa *et al.*, 2011). The importance of not underestimating or overestimating the required depth of the decision tree depth is emphasized here, where a two depth decision tree oversimplifies the sinusoid and a five depth tree over fits the data and deviates from the sinusoidal relation to accommodate outlying data points.

3.2.3 Random Forest Classification and Regression

Random forest ML models involve the construction of a "forest" of multiple decision tree models built independently through some training set (Biau, 2012; Breiman, 2001). Each decision tree has a unique structure and can give differing results from identical inputs. Random forests will combine the results from each decision tree in some manner to produce a single result for the model output. Figure 3.7 shows an example of a random forest classification model composed of n decision trees. For a given input, or instance, each decision tree makes a clas-

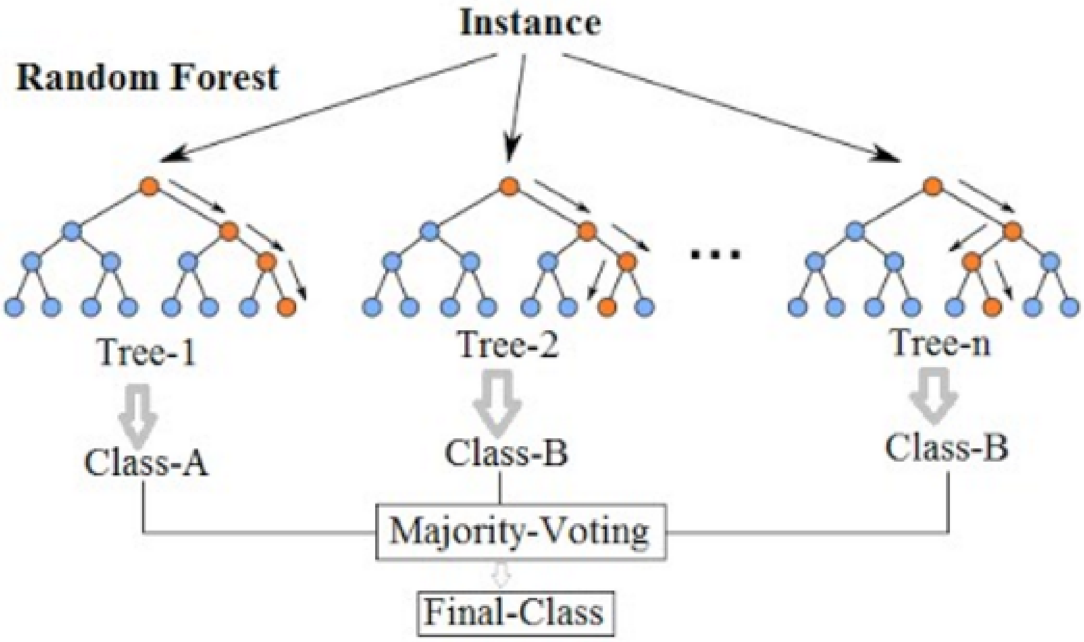

Figure 3.7: Method of combining independently built Decision Tree classifications together under a majority voting scheme to decide a final classification for a given set of input parameters (Koehrsen, 2017). The same method can be applied for regression techniques with all output property predictions being averaged to give a more statistically accurate estimation of output properties.

sification and a final classification is reached by majority voting from all decision trees. This method is similarly applied to regression where the resulting regression of each decision tree is averaged to give the output of the random forest regression model. This method of modeling further allows for decision trees of varying depths that can pick up smaller features in the data-set. Furthermore, this method is advantageous over single decision tree models as it averages out overfitting and simplification.

3.2.4 Neural Networks

Neural Networks (NNs) are among the more complicated methods of ML. NNs are built on the principle idea of how information travels through neurons in a human brain to make predictions. Many types of neural networks exist for classification and regression (Lecun *et al.*, 2015; Parisi *et al.*, 2019; Schmidhuber, 2015), but here the structure of feed forward (simply termed “artificial”) neural networks (ANNs), and convolutional neural networks (CNNs) will be focused on.

Artificial Neural Network

Figure 3.8 shows the structure for a simple ANN. This particular structure is formed from a collection of input bias nodes located on the left hand side which feeds into a second hidden layer of nodes, which then feed into the final node in the output layer (Aggarwal, 2018; Sazli, 2006). Each of the input nodes typically represent some property, x_n, for a given feature, X. These nodes then undergo some weighting, indicated by the connecting arrows, which feed into a second layer of nodes in the neural network. This second layer of nodes is referred to as a hidden layer due to their lack of a true representation of a property of the feature. These hidden layer nodes are then fed through a second round of weights into a single output node, $f(X)$. This describes a very simple example of an ANN, however, more complex structures can be created through the inclusion of more hidden layers, more nodes within each hidden layer, or the creation of a feed back loop within the system to account for more complex feature recognition. The weights and biases of an ANN typically start randomly aligned and through the use of a supervised training set, the weights and biases are modified to create a model that best fits the entirety of the training set. Similar to decision tree and random forest models, this method is susceptible to simplification and over fitting depending on the number of hidden layers and number of bias nodes therein.

Convolutional Neural Network

CNNs are deep learning algorithms that are typically used in image recognition and classification (Khan *et al.*, 2018; Krizhevsky *et al.*, 2012). CNNs operate similarly to ANNs with an additional stage of convolution before a secondary stage that acts as a simple ANN, see Figure 3.9. The convolutional stage is often referred to as the feature learning stage. Within this stage, the input image is convolved with a number of kernels designed to identify various aspects and objects of features therein, in efforts to differentiate them from eachother. These kernels range from edge detection, to spot detection and colour gradient scaling, all with the intent

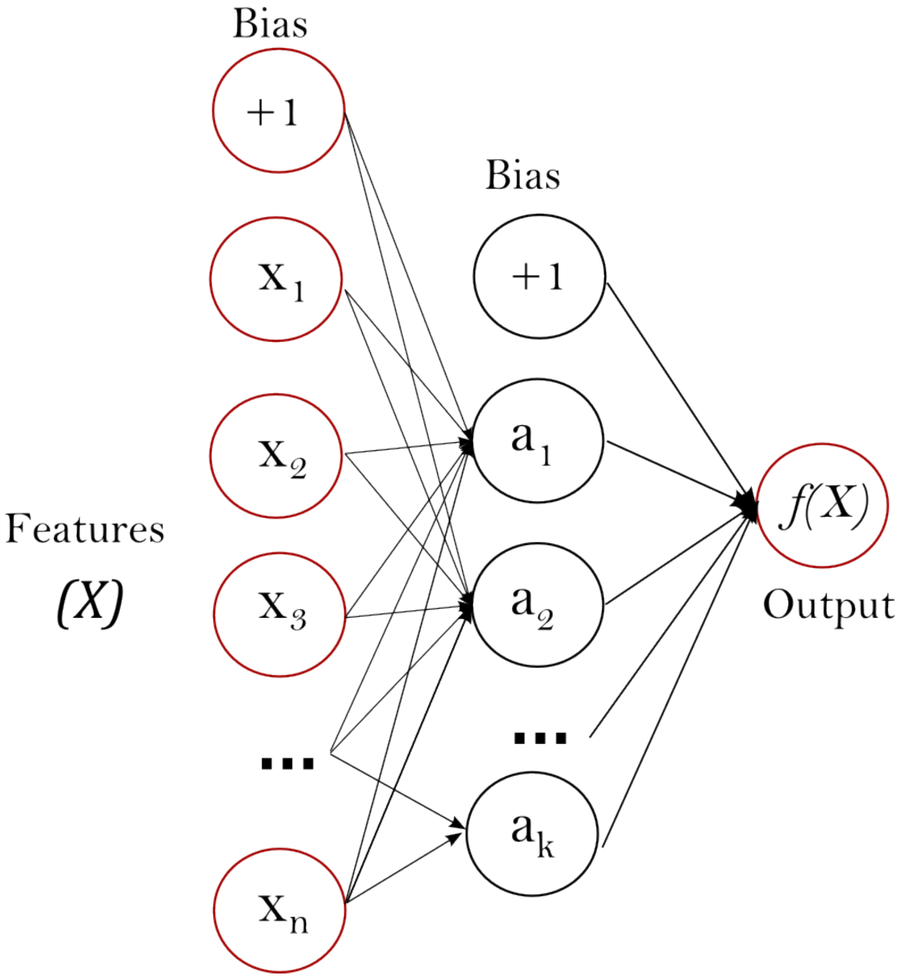

Figure 3.8: Example of a single hidden layer Artificial Neural Network (Pedregosa *et al.*, 2011). The Neural Network is constructed from a number of neurons (circular nodes), and weights and biases (arrows). The weights and biases are tuned through a training data-set with known input (x) and output (f(x)) parameters, with the goal to be to create a set of weights and biases that will most accurately predict all values of f(x) from the input x values. This artificial neural network has a single input layer, which corresponds to a collection of measured input parameters, a single output layer, which corresponds to the neural networks prediction of the output parameter, and a single hidden layer which does not correspond to an observable property of the input data-set, but allows the neural network to predict the output using more complex methods.

to identify unique patterns associated with specific features within an image. This method of learning was inspired by the visual cortex of the human brain where individual neurons are stimulated by a restricted region of the visual field known as

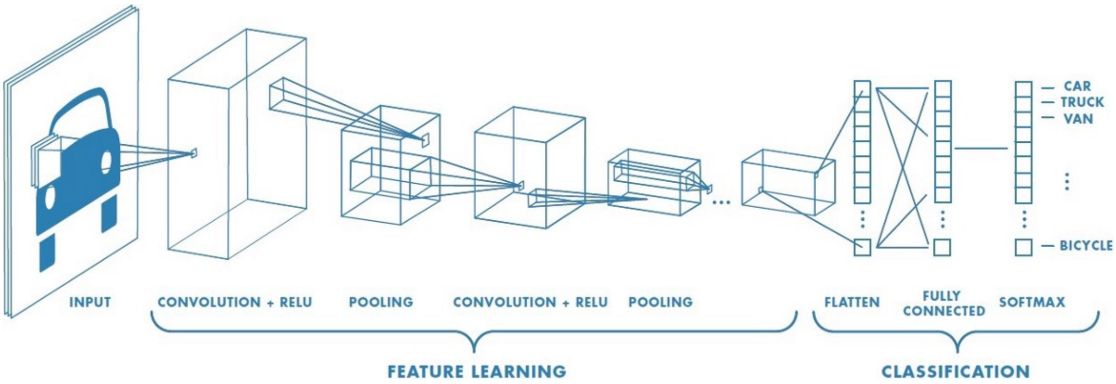

Figure 3.9: Example of a convolutional neural network structure trained to classify images of transportation vehicles (Saha, 2018). Images are convolved with a number of 2D kernels trained to find edges, texture, and other sub-structure features in an image to classify objects within, similar to methods of sub-conscious classification by humans discussed in Chapter 2. This feature recognizing stage is the first section of a Convolutional Neural Network and differentiates it from other simpler neural networks. Values found in this stage are then fed into a trained Artificial Neural Network which then classifies the image as described in the previous section.

the receptive field (Saha, 2018). After convolution, areas are typically reduced in size by pooling, with the aim of reducing the data load and hence the computation time. The pooling involves taking a local collection of convoluted pixels, say 3×3, and either averaging the pool or finding the maximum in the pool. After these layers in the first stage, the output two dimensional convolved layer is flattened into a one dimensional array of vectors which can then be processed as input properties into an ANN. Similarly to all aforementioned ML methods, CNNs are a form of supervised ML and typically require large training sets to become operationally useful. Figure 3.9 shows the full structure of an example CNN designed to identify transportation vehicles from an input image.

4

Multi-Thermal Coronal Hole Identification

Many CH detection and segmentation methods have been created, however, due to CHs irregular shapes and comparable intensities to nearby closed magnetic field regions, these methods are often inconsistent or do not accurately represent CHs and their known properties. In this chapter a new method of CH segmentation is described which focuses on extracting areas from the solar corona with magnetic structure, temperatures and densities that are typically expected of CHs as described by Antonucci *et al.* (2004); Cranmer (2002a, 2009); Doschek *et al.* (1997). This chapter is based on the work published by Garton *et al.* (2018a) which is published in the *Journal of Space Weather and Space Climate.*

4.1 Multi-Thermal Intensity Segmentation

Multiple images are regularly taken of the solar corona across the EUV and ultraviolet spectrum by SDO/AIA, SOHO/EIT and even far side images have been observed by spacecraft in the Solar Terrestrial Relations Observatory (STEREO) missions. Each individual passband is typically good at identifying certain coronal features, e.g. active regions being easily identified in 94 Å images. By looking at a specific coronal feature across multiple passbands it is possible to construct a pseudo-spectrum for that coronal feature. This is most notable in tri-colour images of the solar corona, see Figure 4.1, where individual features, such as CHs appearing dark blue, are easily identified by eye. In these tri-color images it is typically easier to identify coronal features due to features being separated in a three colour vector space instead of a singular intensity scaler to describe an image. Identifying and segmenting features based on this vector representation of data is known as colour segmentation and this method has not been used before in coronal feature segmentation.

4.1.1 Colour Segmentation

Colour segmentation comes in two main varieties. Hue-Saturation-Intensity (HSI) segmentation and Red-Green-Blue (RGB) vector space segmentation. HSI segmentation focuses on separating an image into its hue, saturation and intensity components, and then by applying a threshold to the image saturation a binary mask can be obtained. A product operation on this binary saturation mask with the image hue creates an image of coloured regions with high saturation. These images can then be thresholded to extract specific colours. This method of segmentation is typically used to extract vibrantly coloured regions from otherwise dull images. Tricolour images of the Sun however are already typically well saturated and vibrant throughout. Hence this method of segmentation is not used for this work.

As mentioned in Gonzalez & Woods (2006), "*working in HSI space is more intuitive, segmentation is one area in which better results are generally observed by using RGB color vectors*". When attempting to segment objects of a specified

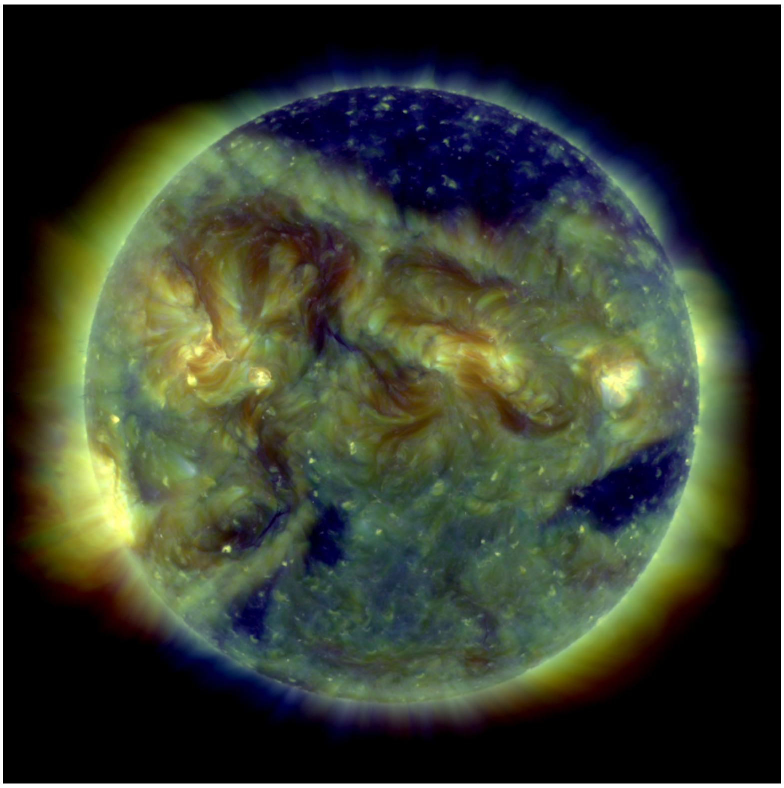

Figure 4.1: Tri-colour image of the 171 Å(blue), 193 Å(green), and 211 Å (red) wavelength observations for October 31st, 2016 taken by AIA on-board SDO.

colour range in a RGB image, a sample of colour points representative of the colours of interest can be obtained. An average of these representative points gives a model vector of a specified colour in RGB space, $\mathbf{a}$. The objective of RGB segmentation is to classify each pixel in an image being within a specified range to this vector $\mathbf{a}$. Euclidean distance is typically used as a measurement of similarity such that an arbitrary vector, $\mathbf{z}$, is at a distance, $D(\mathbf{z}, \mathbf{a})$, less than some specified threshold distance, D_0, such that:

$$D(\mathbf{z}, \mathbf{a}) = \|\mathbf{z} - \mathbf{a}\| \tag{4.1}$$

$$D(\mathbf{z}, \mathbf{a}) = \left[(\mathbf{z} - \mathbf{a})^T (\mathbf{z} - \mathbf{a})\right]^{\frac{1}{2}} \tag{4.2}$$

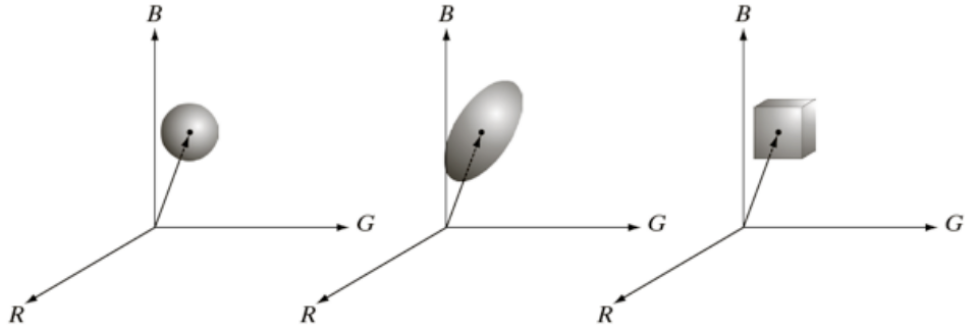

Figure 4.2: Three approaches for enclosing data regions for RGB vector segmentation. See Gonzalez & Woods (2006)

$$D(\mathbf{z},\mathbf{a}) = \left[(z_R - a_R)^2 + (z_G - a_G)^2 + (z_B - a_B)^2\right]^{\frac{1}{2}} \tag{4.3}$$

where the subscripts R,G, and B, denote the RGB components of vectors **a** and **z**. Identifying points such that $D(\mathbf{z},\mathbf{a}) \leq D_0$ creates a solid sphere of radius D_0 as illustrated in Figure 4.2(left). Equation 4.2 can be generalized for non spherical shapes as:

$$D(\mathbf{z},\mathbf{a}) = \left[(\mathbf{z} - \mathbf{a})^T \mathbf{C}^{-1} (\mathbf{z} - \mathbf{a})\right]^{\frac{1}{2}} \tag{4.4}$$

where **C** is the covariance matrix of the samples representative of the sought after colour. The points satisfying this $D(\mathbf{z},\mathbf{a}) \leq D_0$ describe an elliptical body as seen in Figure 4.2(middle). For images of practical size, both Equation 4.2 and 4.4 can be computationally intensive. The solution is often to use a simplified bounding box as illustrated in Figure 4.2(right).

This method of segmentation can perform very well for identifying regions within images based on colour. Figure 4.3 shows an example segmentation of an image using RGB vector space segmentation. A mass of reddish colour was enclosed by a rectangle for building a colour model. Thresholding was then performed using the rectangular box method as described for Figure 4.2(right) with thresholds selected at 1.25 times the standard deviation, σ, of the data along the corresponding axis, i.e. thresholds along the red dimension are $(a_R - 1.25\sigma_R)$ to $(a_R + 1.25\sigma_R)$.

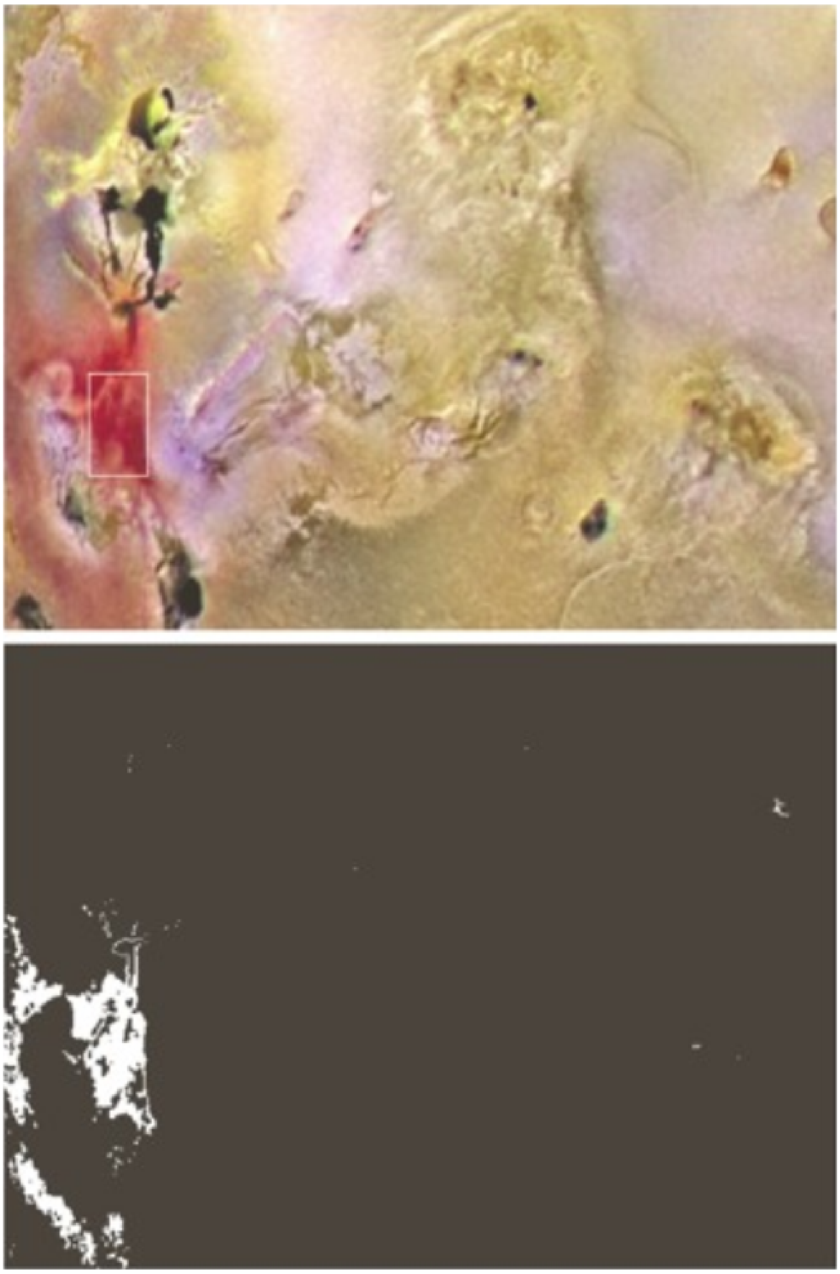

Figure 4.3: Segmentation of a coloured image using RGB vector space segmentation, see Gonzalez & Woods (2006). (Top) Original image with colours of interest shown enclosed by a rectangle. (Bottom) Result of segmentation in RGB vector space.

Images of the solar corona are typically high resolution, hence the spherical and elliptical body method of RGB vector segmentation can be computationally strenuous, and will take long times to segment individual images. However, due to the complex structure of solar corona images in RGB intensity space, it is difficult to use the rectangular box thresholding method while obtaining accurate segmentations of coronal features. Instead a non-linear adaptive hyper-plane threshold method for segmenting CHs from surrounding coronal features will be employed. This method is used in the published automated Coronal Hole Identification via Multi-thermal Emission Recognition Algorithm (CHIMERA) and is elaborated for the SDO instrument below (Garton *et al.*, 2018a)[1].

4.1.2 SDO Calibration

An overview of the CHIMERA method of segmentation for AIA observations is shown in Figure 4.4. The AIA instrument on board SDO takes observations of the solar corona every 12 seconds in six wavelengths. For use in RGB segmentation, these six wavelengths must be narrowed down to three which best illustrate the feature desired to be segmented from surrounding plasma. Figure 4.5 illustrates multiple observations of the solar corona from AIA in these six wavelengths on September 22nd, 2016. An intensity slice is shown across the CH located at central meridian, the profile of which is displayed in Figure 4.6. Notably, from these intensity cuts, the relatively comparable intensities of CHs to surrounding plasma as well as their ill defined boundaries are seen, regardless of wavelength. CHs show highest contrast to surrounding plasma in the 171 Å, 193 Å, and 211 Å passbands as shown by the contrast values calculated using the Michelson contrast equation (Equation 4.5; Michelson, 1927).

$$C = \frac{I_{max} - I_{min}}{I_{max} + I_{min}} \tag{4.5}$$

For this equation, I_{max} is the mean intensity of non-CH pixels near this CH, and I_{min} is the mean intensity of CH pixels within the CH center. Furthermore, these three wavelengths exhibit the highest signal to noise ratio for identifying CH

---

[1] github.com/GartontT/CHIMERA

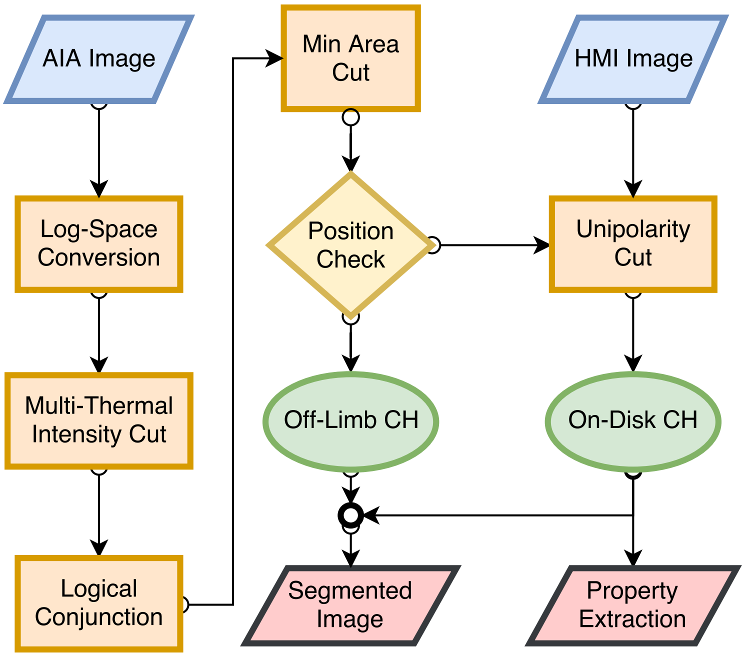

Figure 4.4: Operational flowchart of the methods CHIMERA uses to identify CH candidates and verify each candidate into a finished segmented image and array of CH properties.

regions.

Taking these three wavelengths as axes in a three EUV intensity vector space, corresponding to a RGB vector space, it is possible to illustrate all the pixels in the AIA image in three individual scatter plots which correspond to a projection of these points onto 2D planes, see Figure 4.7(a, c, e). Due to the large number of pixels in each AIA image, the lower intensity regions of each scatter plot are saturated with points. To see the finer structure in these low intensity sections, 2D histograms are created for all points that fall within the red rectangles and are illustrated in Figure 4.7(b, d, f). These histograms show a clear structure of points falling into one of two visible clusters. One cluster exhibits a larger spread, has more points and is centered higher in the hotter channels of 193 Å and 211 Å, while the other cluster has fewer points overall and is centered lower in hotter channels.

From the understanding of the AIA passbands it is known the 171 Å, 193 Å, and 211 Å wavelengths correspond to plasmas with peak emission at temperatures

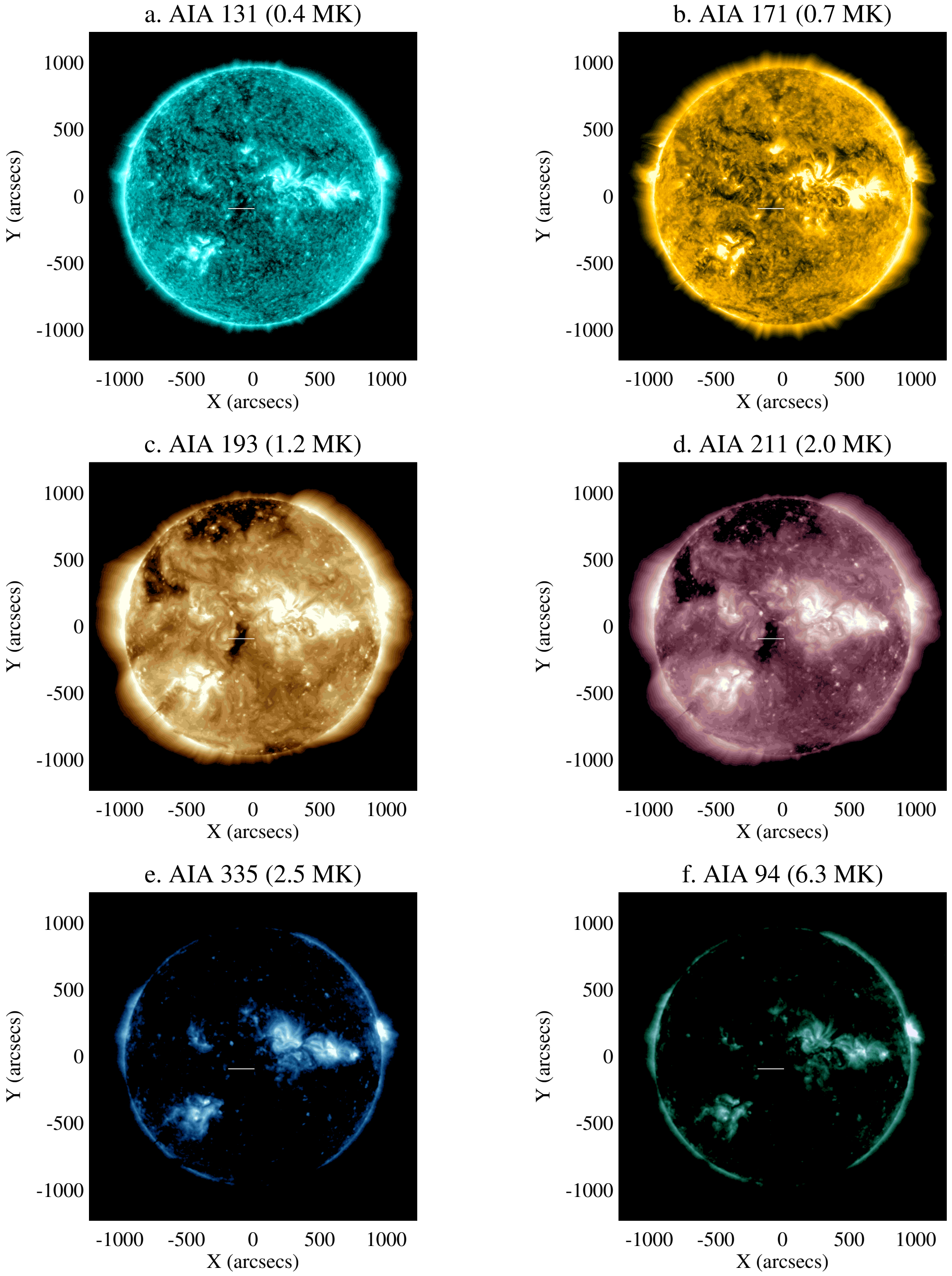

Figure 4.5: Comparison of AIA observations in the (a) 131 Å, (b) 171 Å, (c) 193 Å, (d) 211 Å, (e) 335 Å, and (f) 94 Å AIA passbands on September 22nd, 2016. An intensity cut is made across the small CH located at central meridian, highlighted by a white horizontal line.

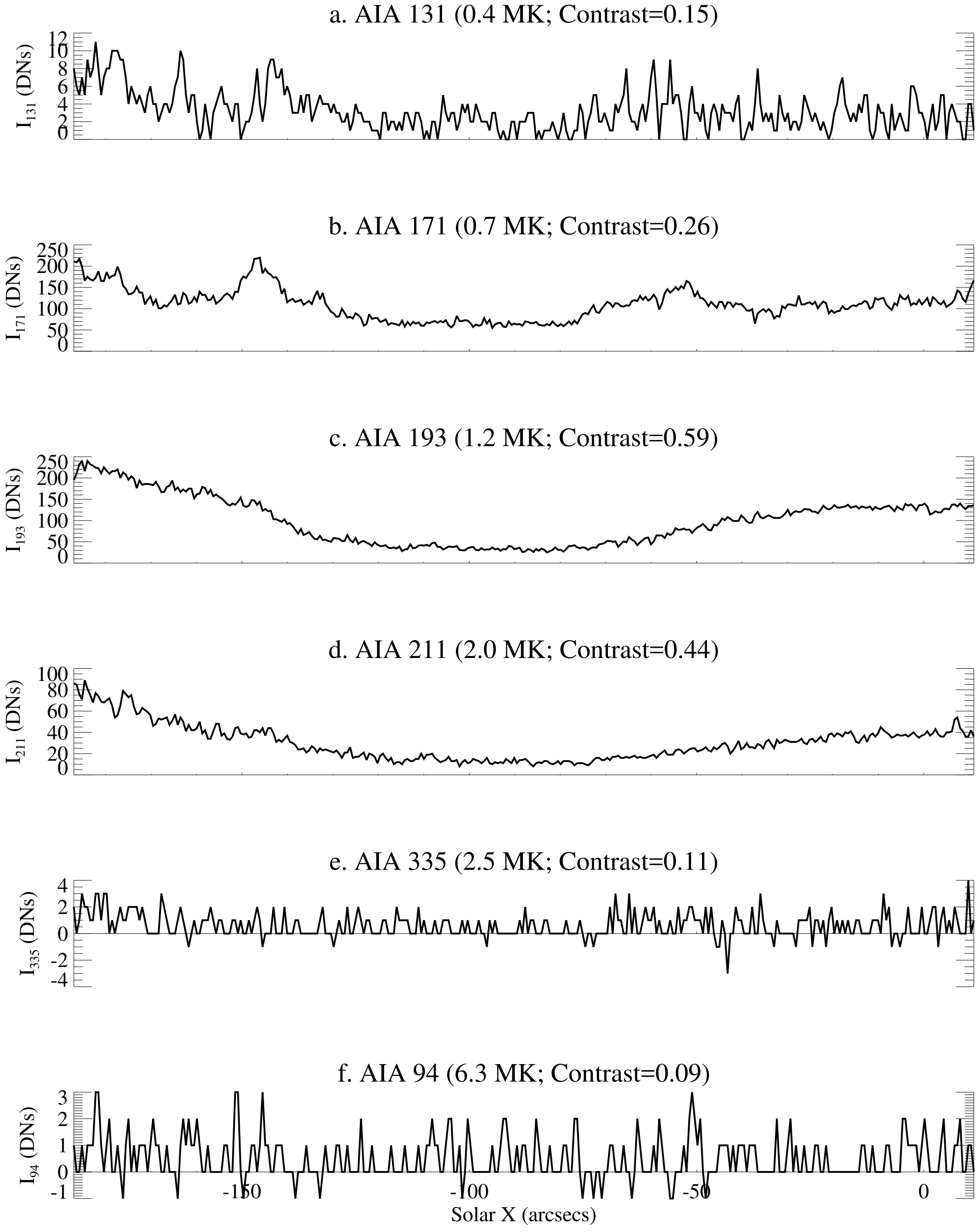
a. AIA 131 (0.4 MK; Contrast=0.15)

b. AIA 171 (0.7 MK; Contrast=0.26)

c. AIA 193 (1.2 MK; Contrast=0.59)

d. AIA 211 (2.0 MK; Contrast=0.44)

e. AIA 335 (2.5 MK; Contrast=0.11)

f. AIA 94 (6.3 MK; Contrast=0.09)

Figure 4.6: Comparison of an intensity slice across the CH at central meridian in Figure 4.5 in the (a) 131 Å, (b) 171 Å, (c) 193 Å, (d) 211 Å, (e) 335 Å, and (f) 94 Å AIA passbands on September 22nd, 2016.

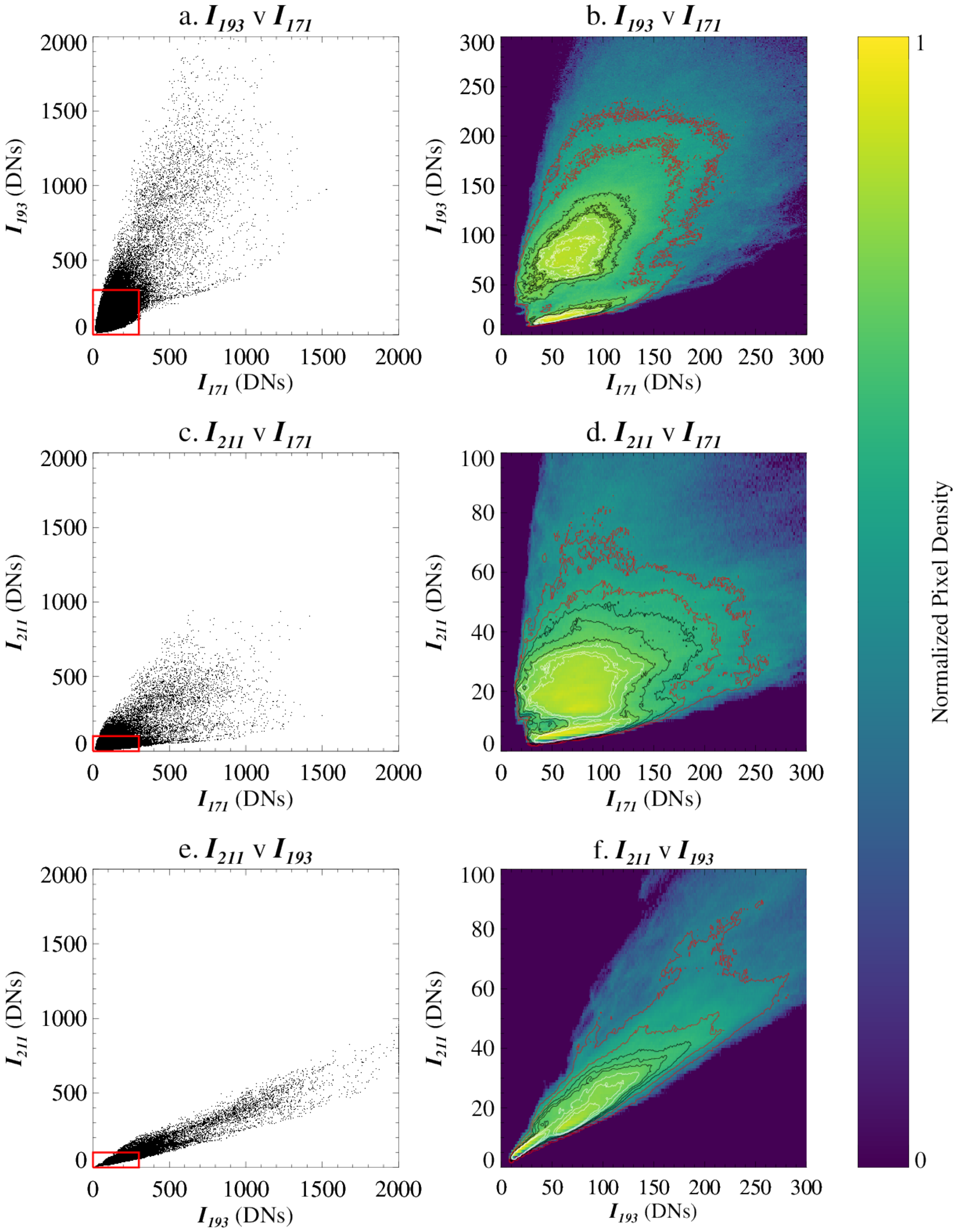

Figure 4.7: Projection of solar images in a three EUV intensity vector space onto the (a) 171/193 Å, (c) 171/211 Å, and (e) 193/211 Å planes for ease of visualization. Histograms (b), (d), and (f) show the structure of the high density points located within the red rectangles in (a), (c), and (e) respectively.

of ∼0.7, 1.2, and 2.0 MK respectively, see Figure 2.4. In these 2D histograms, pixels that exist closer to the 171 Å intensity axis represent plasma that is cooler than that of pixels existing closer to the higher temperature intensity axis. However, this idea is based on the assumption that the emission lines within the bandpass have relatively low temperature sensitivity outside their peak temperature range. Furthermore, pixels located closer to the origin of these histograms have a lower density of corresponding iron isotopes than other pixels of similar temperature. Therefore, these 2D intensity histograms can be interpreted as 2D histograms in a temperature and density coordinate system, shown in Figure 4.8, where increased radial distance from the origin describes plasma with higher densities, and an increased angle from the I_{cool} axis describes plasmas of higher temperatures. Notably, this method only describes physical properties of a region with respect to the other regions within the image. One regions can be assumed cooler than another based on its angle from the I_{cool} axis, however it is not yet possible to definitively declare a regions exact temperature and densities from these 2D histograms. As mentioned in Chapter 1, coronal holes are well documented to be lower temperature and density than surrounding plasmas, and therefore would have typical intensities in our chosen wavelengths that would place them in the previously mentioned cluster which has a lower average emission in hotter channels. It can be assumed that this lower cluster corresponds to the vast number of pixels from CH regions present in the image.

As highlighted above, images of the solar corona have too many pixels to be efficiently segmented by traditional RGB vector space segmentations. Instead a linear threshold can be found to best separate the the two clusters present in each of our three histograms. For this work a linear threshold is simply found by finding the minima points existing between the two large clusters of points and fitting a line to them. Converting these histograms to log space and finding an optimal threshold will allow for a non-linear threshold that can change in both location and shape to better separates CH pixels from other coronal features. Equation 4.6 and 4.7 describes the linear threshold in log-space and its subsequent non-linear threshold in a linear intensity space:

$$\log I_y = m \log I_x + \log c \tag{4.6}$$

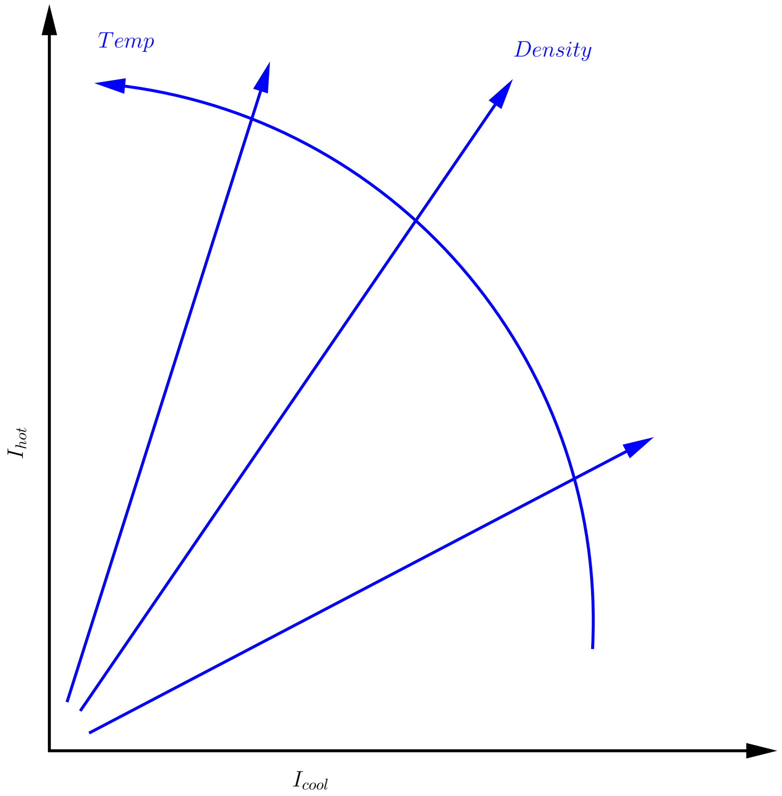

Figure 4.8: Conversion of Intensity units from the three EUV intensity vector space to physical units of temperature and density.

$$=> I_y = c\, I_x^m \tag{4.7}$$

where I_x and I_y describe the intensity vectors for two chosen variable intensity measurements from a solar image, $c = I_y(I_x = 0)$, and m describes the slope of a linear equation. An example of this non-linear threshold is shown in both log and linear intensity space in Figure 4.9. The separation of these two clusters is, however, not always easy to identify through automated methods. To accommodate for this issue, the non-linear segmentation shown in Figure 4.9 is stored within CHIMERA, and is adapted for each image individually, relative to the average intensity observed in each passband, i.e. the non-linear threshold for a given observation is multiplied along the I_y axis by $(< I_y >)/(< I_m >)$, where $< I_m >$ is the mean intensity of on-disk pixels in that wavelength for October 31st, 2016.

This method of non-linear adaptive thresholding accounts for observations with little to no CH pixels, and also accounts for instrument degradation.

Taking all pixels that fall within the threshold shown in Figure 4.9 as CH candidate pixels, three unique binary masks of CH candidates are obtained, shown in Figure 4.10. These CH candidates have been identified as having temperature and density properties similar to those expected of CH regions. This method evidently segments CH regions quite accurately when compared to the tri-coloured image present in Figure 4.10(a), however each segmentation includes additional features known to be non-CH regions, e.g. a CH candidate in Figure 4.10(b) located at coordinates (-250, 250) arcsecs which corresponds to a filament region in (a) located at the same coordinates. These additional incorrect CH candidates are not present in each of the three CH candidates segmentations obtained, while CH candidates that visibly correspond to CHs on the solar disk are omnipresent in each these segmentations. To remove incorrect CH candidates from our segmentations, each CH candidate must undergo some verification tests to confirm their properties are similar to that expected of CHs.

4.2 Verification

As mentioned in Chapter 1, CHs are typically large, cool, low density, and unipolar regions in the solar corona. These known properties can be used to further remove incorrect CH candidates from our segmentations. Above, it has been shown that the three binary masks of CH candidates have temperatures and densities that fall within our three thresholds from Figure 4.9, however, to be accurately classified as a CH, these identified features fall within the calculated thresholds in each of the three segmentations. Described physically, each CH candidate must exhibit thermal and density properties expected of a CH in each segmentation to be classified as a CH. Hence, a logical conjunction of our binary masks will remove a large number of incorrectly segmented pixels. The logical conjunction for these three binary masks is shown in Figure 4.11.

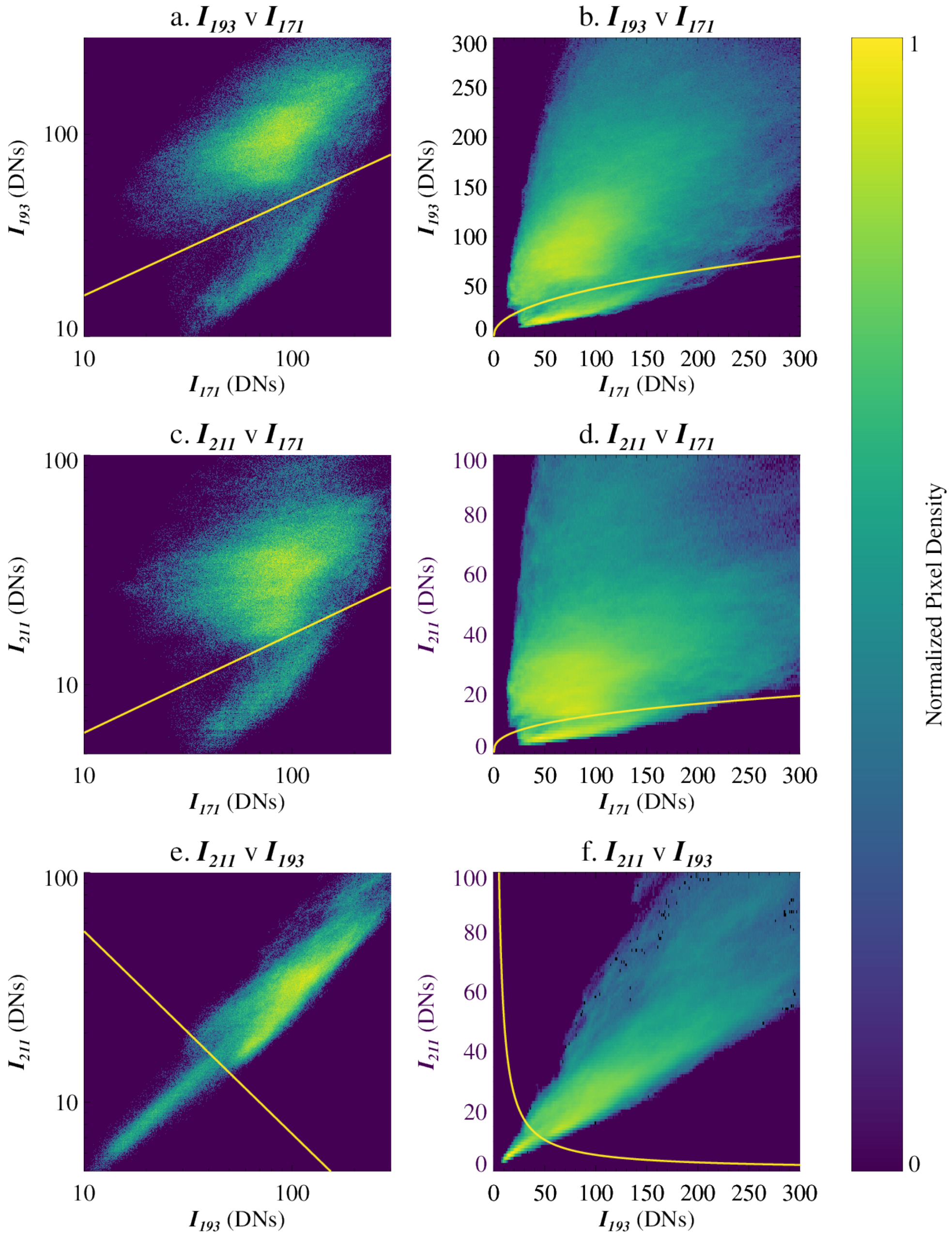

Figure 4.9: Histograms of the three EUV vector space planes converted into log space (a), (c), and (e). From these log space histograms, an optimal linear threshold is found for each plane to separate the cool, low density CHs from the surrounding plasma. This optimum threshold is also shown in the linear EUV vector space histograms (b), (d), (f).

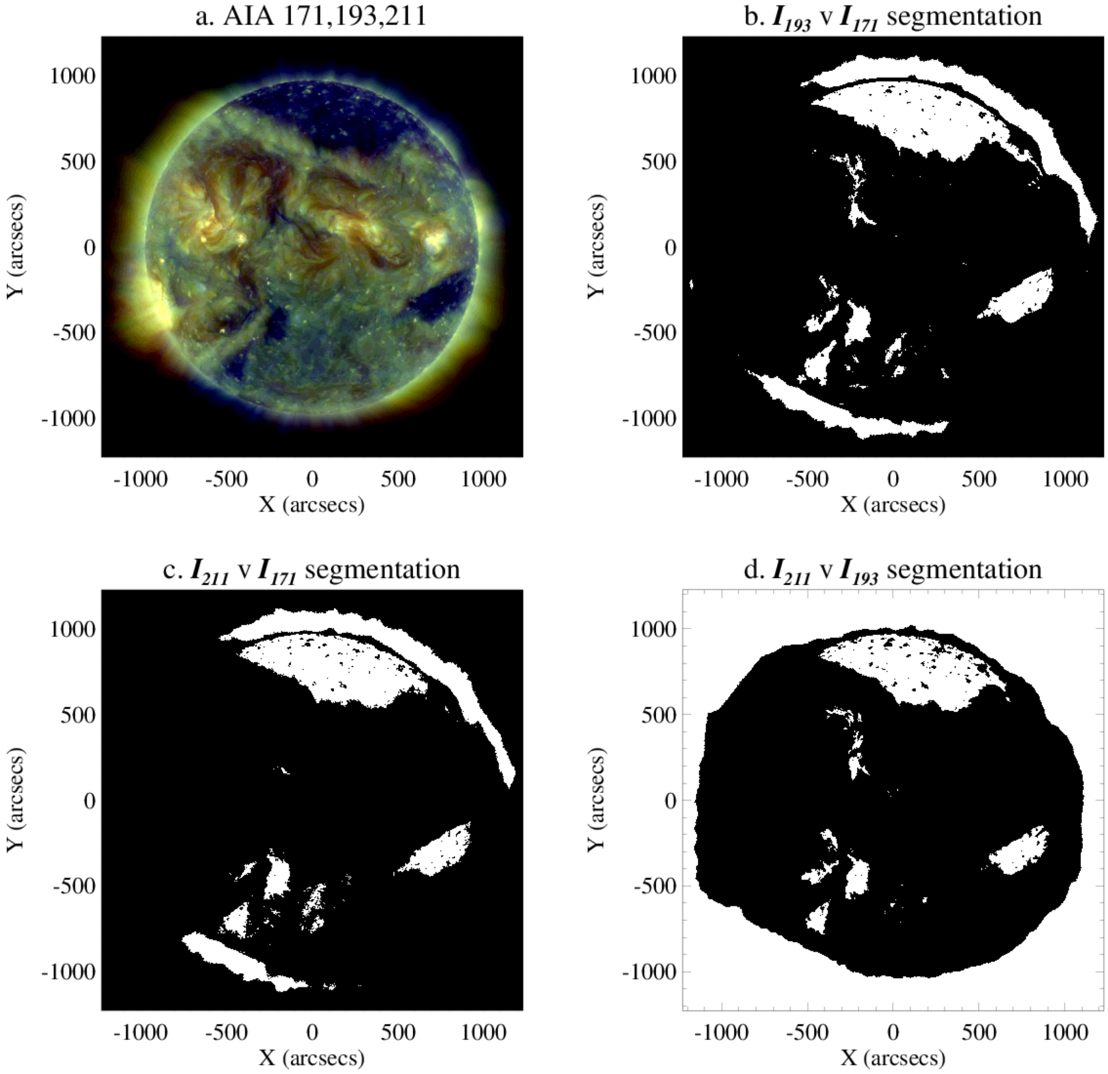

Figure 4.10: Comparisons between (a) the original tri-colour image obtained from AIA 171 Å, 193 Å, and 211 Å to the binary masks highlighting CH candidates obtained from the non-linear thresholds shown in Figure 4.9 for the (b) 171/193 Å, (c) 171/193 Å, and (d) 193/211 Å histograms.

4.2.1 Area and Location

From this newly constructed binary map potential erroneous detections are further removed through a minimum area threshold. CHs are known to be large in area, and their geo-effectiveness is often correlated with their area. Hence, smaller CH candidates can be removed from our segmentations as these candidates are most

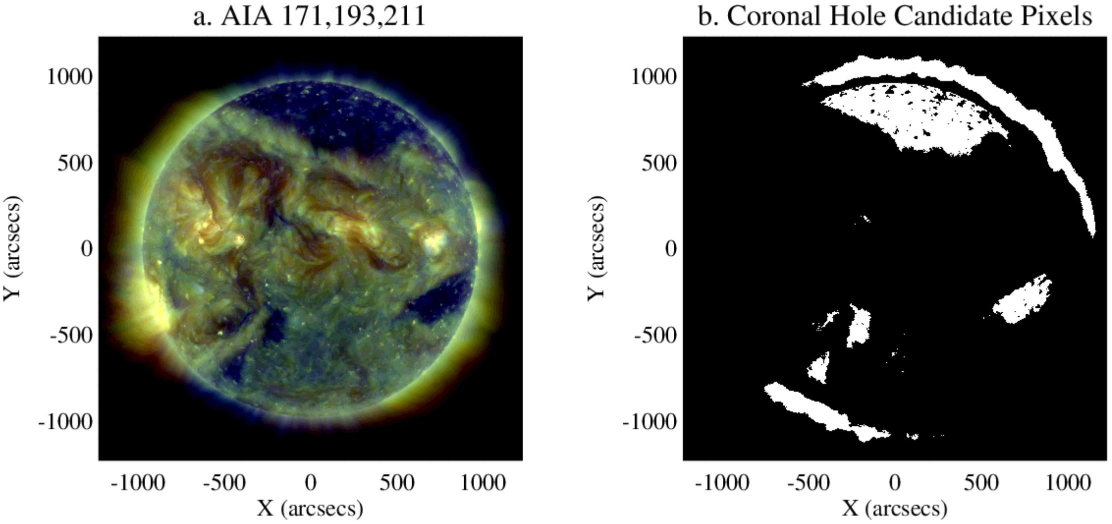

Figure 4.11: Comparison between (a) the original tri-colour image obtained from AIA 171 Å, 193 Å, and 211 Å to the logical conjunction of the CH candidates in the binary maps from Figure 4.10.

likely to be spurious detections, and in the event of removing a true CH from segmentation predictions of solar wind (SW) properties will not be significantly affected. A minimum area threshold of 1000 arcsec^2 (∼30”×30”) was found from empirical analysis of CHIMERA thresholded images. After this area thresholding, CH candidates are separated into two categories, on-disk and off-limb CH candidates, the latter of which is discussed later in this chapter.

4.2.2 Unipolarity

As previously mentioned, CHs are typically open magnetic field regions, i.e. they are unipolar. This unique property can be used as a final verification for our remaining CH candidates. To verify magnetic unipolarity images taken by the HMI instrument are used. The CH candidates are projected onto the HMI observations and the mean magnetic polarity within their boundaries is calculated. Non-CH regions are observed to have no strong magnetic polarity, i.e. $<B>_r \approx 0$ G. The CHIMERA threshold for this cut is calculated relative to the total area of the CH candidate, with the highest stringency being placed on smaller candidates. A small CH candidate is accepted if $<B>_r$ is greater than 1 G, and a large CH candidate with an area above 60000 arcsec^2 is accepted if $<B>_r$ is greater than 0.1 G. This varying stringency prevents large candidates being excluded due to a wider range of polarities being present within their boundaries. These thresholds were found from empirical measurements of magnetic properties of the CH candidates that were present after the previous conjunction and minimum area cut-off. Remaining CH candidates are considered to have passed verification and are assumed to be true CH regions. An example finished segmentation for October 31st, 2016 is shown in Figure 4.12. From these segmentations CHIMERA calculates and stores a number of properties for each CH region, shown in Table 4.1.

Each property extracted by CHIMERA gives some insight into the current and potential geo-effectivity of a CH. CH area gives possible estimation of the

Extracted Property	Explanation
N_t	Coronal hole identification number for time t. This ID number is assigned in descending order of size.
$X/Y cen_N$	Coronal hole centroid coordinates in arcseconds and Stonyhurst heliographic coordinates.
$X/Y extent_N$	Most Eastern-Western/Northern-Southern positions in arcseconds.
$\Delta\phi$	Longitudinal angular extent of the coronal hole in Stonyhurst heliographic coordinates and absolute degrees.
$A_{tot,N}$	True coronal hole area. $(\Sigma_{pix} A_{cos,N})$
$A_{\%,N}$	Percent coverage of the solar disk by the coronal hole area. $\left(\frac{1e(+6)\times A_N}{\pi R_{sun}^2}\right)$
$< B_{los} >_N$	Mean magnetic polarity along the line-of-sight. $\left(\frac{\Sigma_{pix} B_{los,N}}{\Sigma_{pix,N}}\right)$
$< B_{los}^{-/+} >_N$	Mean negative/positive magnetic polarity for a coronal hole along the line-of-sight. $\left(\frac{\Sigma_{pix} B_{los}^{-/+}}{\Sigma_{pix,N}^{-/+}}\right)$
$B_{los,N}^{min/max}$	Minimum/maximum magnetic polarity along the line-of-sight within coronal hole boundaries.
$B_{tot,N}^{-/+}$	Absolute total polarity for all negative/positive pixels within a coronal hole boundary. $(\Sigma_{pix} B_{los,N}^{-/+})$
$< \Phi >_N$	Mean magnetic flux through the surface bounded by the coronal hole boundaries. $(< B_{los} >_N A_{tot,N})$
$< \Phi^{-/+} >_N$	Mean negative/positive magnetic flux through the surface bounded by the coronal hole boundaries. $(< B_{los}^{-/+} >_N A_{tot,N})$

Table 4.1: CH properties extracted by CHIMERA.

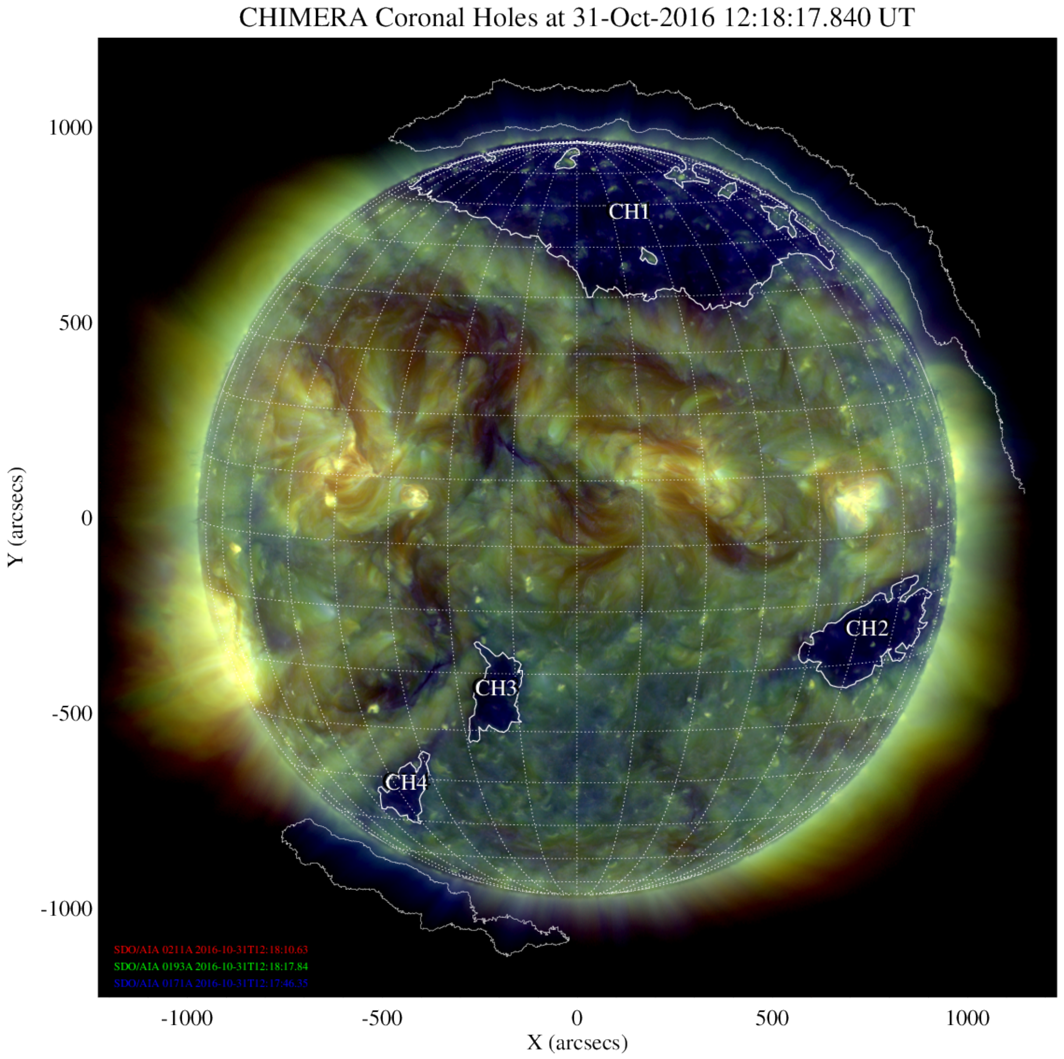

Figure 4.12: CHIMERA finished product of a CH identified and segmented image.

high speed SW duration (Krieger *et al.*, 1973; Krista & Gallagher, 2009) and velocity (Nolte *et al.*, 1976), CH extent and positioning can give further insight into duration, as well as arrival time of SW streams (Cranmer, 2002a), and magnetic polarity and flux are commonly associated with potential geo-effectivity of SW streams. Making these CH properties readily available outputs of CHIMERA allows a statistical analysis of the detected CHs and the SWs they create, an example of one such study is discussed in depth in Chapter 5.

4.2.3 Comparison and Stability

Unfortunately, there is currently no reliable system to validate a CH detection method or the accuracy of said method and techniques of validation from other space weather prediction models cannot apply to CH detections. For example, in flare forecasting methods of prediction are validated based on the occurrence of a flaring event. If a flare probability is predicted from an active region at a 40% chance of occurring, a statistical analysis can be taken on all active regions that have this same percentage of flaring and the number of times these regions have flared should be expected to match the flare probability, 40% in this case. In CH segmentation this solution is not available as the understanding of CHs and their links to SW events are not yet fully understood and in the current state of the art what defines a CH boundary is still in debate. Instead, the automated segmentations of CHIMERA can be compared to other automated CH segmentation algorithms and to manually segmented maps created by trained personnel in both the Met Office Space Weather Operations Center (MOSWOC) and the National Oceanic and Atmospheric Administration (NOAA) Space Weather Prediction Center (SWPC). Figure 4.13 shows one comparison of (a) SWPC, (b) MOSWOC, (c) Automatic Solar Synoptic Analyzer (ASSA), (d) Spatial Possibilistic Clustering Algorithm (SPoCA) segmentations, and (e) a Potential Field Source Surface (PFSS) compared to (f) the CHIMERA segmentation for the same time. As can be seen, the CHIMERA segmentation has a high similarity to the hand segmented maps (a) and (b) while also representing a similar magnetic structure to that estimated by the PFSS simulation (e). This similarity backs up CHIMERA's ability to segment images as it agrees with segmentations done by experts and is representative of the underlying physics in the corona. Furthermore, in this particular segmentation CHIMERA outperforms and more accurately segments boundaries than both the SPoCA (b) and ASSA (c) automated segmentation methods.

CHIMERA's segmentations method can be further validated based on the slow evolution of CHs. As previously mentioned CHs are slow evolving, long lived regions of the solar corona, therefore an accurate segmentation of their boundaries should show little to no overall evolution on a short timescale (daily) and evolution should be slow on long timescales (weekly). Figure 4.14(a-c) shows three

a. SWPC

b. MOSWOC

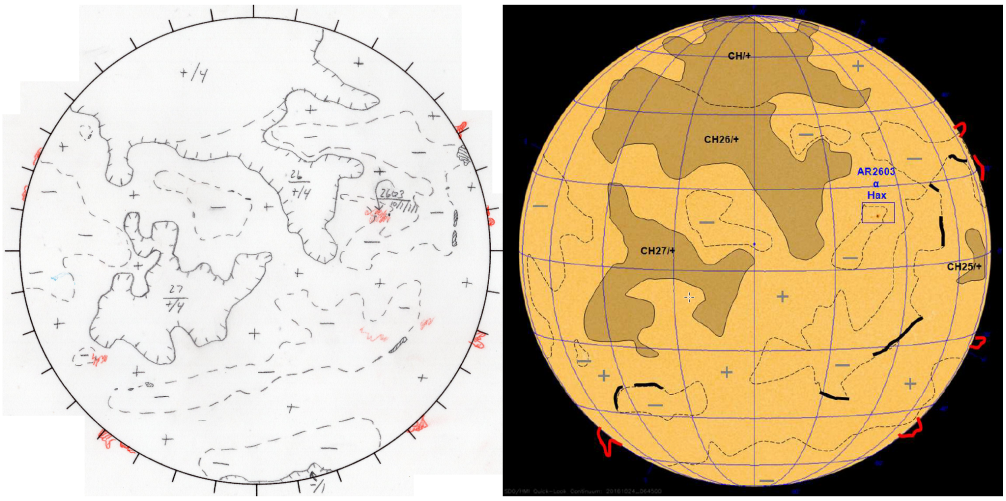

c. ASSA

d. SPoCA

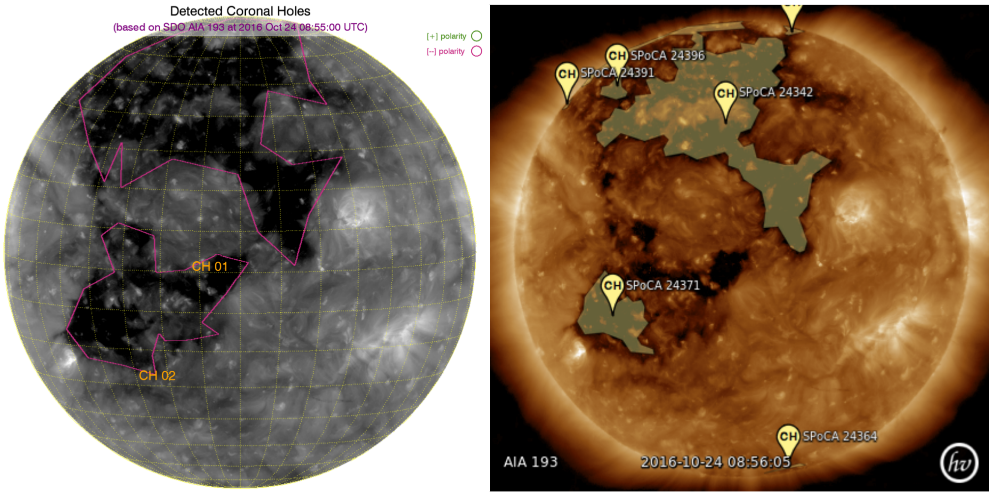

e. PFSS

f. CHIMERA

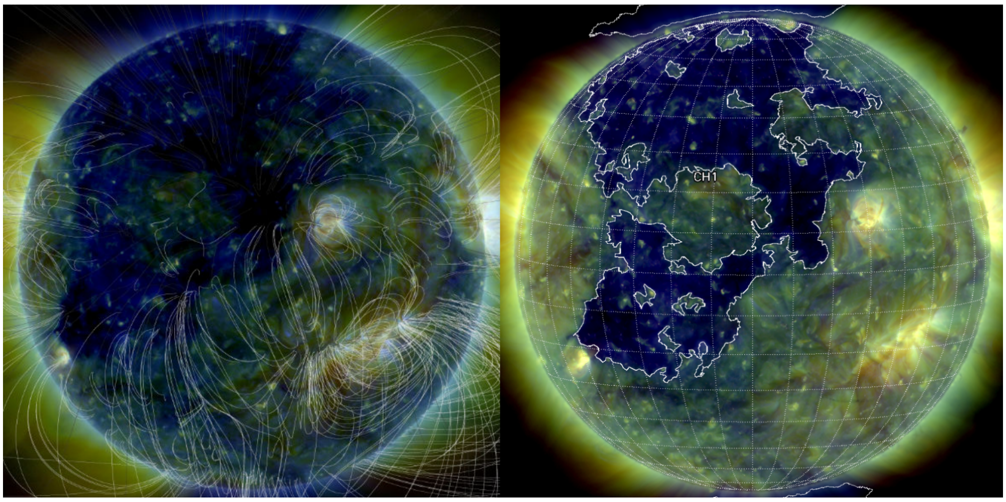

Figure 4.13: Comparison of (a) SWPC, (b) MOSWOC, (c) ASSA, (d) SPoCA, (e) PFSS, and (f) CHIMERA CH segmentations.

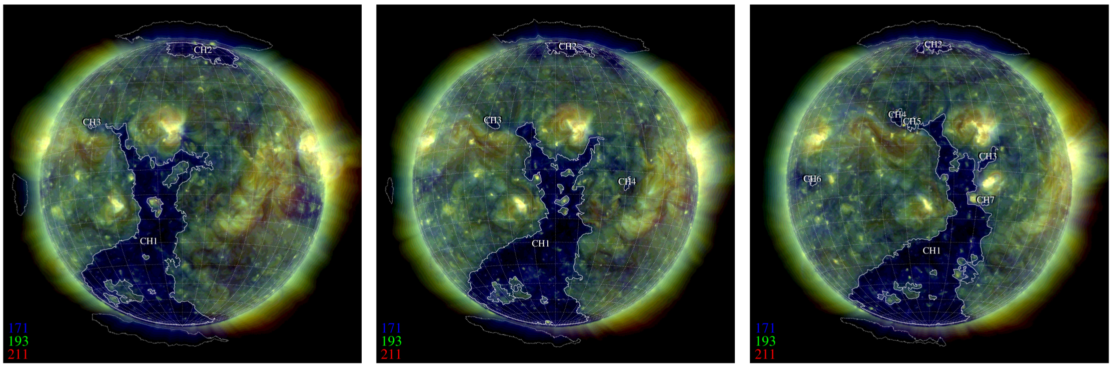

a. CHIMERA at 29-Jan-2017

b. CHIMERA at 30-Jan-2017

c. CHIMERA at 31-Jan-2017

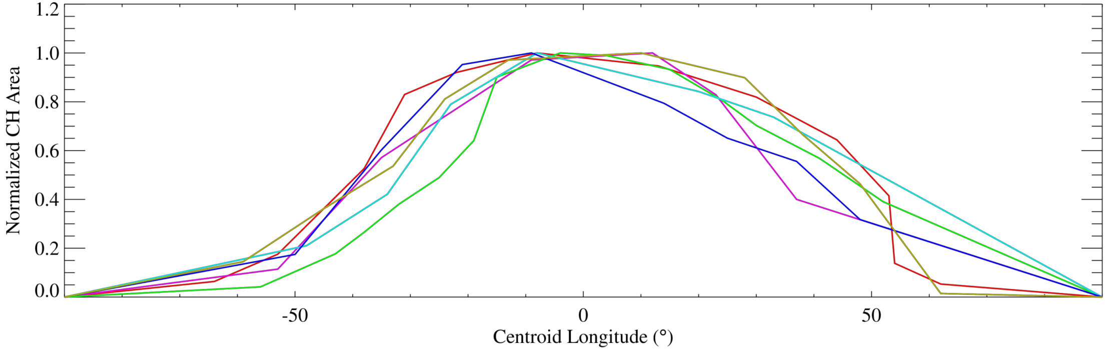

d. Coronal Hole Area v Longitude

Figure 4.14: Demonstration of the short-term (a-c) and long-term (d) stability of the CHIMERA segmentation algorithm.

CHIMERA segmentations taken at daily intervals on January 29th - 31st, 2017. These days were selected due to the large polar CH located at central meridian which corresponded to a minor geo-magnetic storm at Earth, registered as a Kp5o by the World Data Centre for Geomagnetism (WDCG), Kyoto. Minimal change is observed in CH area in (a-c) showing the algorithm is stable for CH segmentations on short timescales. Figure 4.14(d) shows the normalized projected area of six randomly selected CHs between January 2016 to July 2017 as they transition the solar disk. In this plot small scale variations are due to projection effects of the irregularly shaped CH regions. Excluding these small scale variations, rise and falls of CH area is similar to that expected of an area projection over time on a rotating sphere. Through all the aforementioned verification methods, the segmentations performed by CHIMERA have been verified to a high standard.

4.3 Tracking Solar Features

To understand CHs and their impacts on space weather, it is essential to observe their evolution in the solar corona. To automatically create a database for CHs, an automated tracking method is needed, many of which are currently available. However, a new method can be created specifically for solar features which predominantly accounts for features rotating on the solar disk at the Carrington mean synodic rotation rate of $\omega_{\odot} \approx 13.2° day^{-1}$.

4.3.1 On-Disk Tracking

On-disk features of the solar corona can be tracked by identifying the centroid of segmented features. This centroid can then be projected forward on the solar disk assuming a rotation at the Carrington mean synodic rotation rate. By recreating the segmentation around this newly projected centroid, a prediction of the features location is obtained. Overlap between this forward projection and newly segmented images are then used to track features, with the largest overlap of two feature being considered the tracked object. This method of tracking can be seen in Figure 4.15, where (a) is a CHIMERA CH segmentation for October 31st, 2016, (b) is a CHIMERA segmentation for November 1st, 2016, and (c) shows an overlap of (a) forward rotated and projected onto (b). Tracking features with this method focuses on the similarity in area between a feature at time t_0 and time t_n. This requires the time interval between tracking attempts, n, to be less than the evolution timescale of the tracked feature. For CHs, which evolve slowly, daily tracking is not an issue, however tracking of features which can evolve on shorter timescales, e.g. active regions, require shorter tracking intervals, sub-hour tracking. This method of tracking is available in the CHIMERA algorithm and is also used in the python updated version of the SolarMonitor Active Region Tracker (SMART; Higgins *et al.*. 2011[1]) algorithm.

Even when ensuring that tracking timescales are short, tracked features will naturally evolve, join together, separate and disappear. In the event of feature separation, the largest feature at t_n will be considered the tracked feature and

---

[1] github.com/TCDSolar/SMART

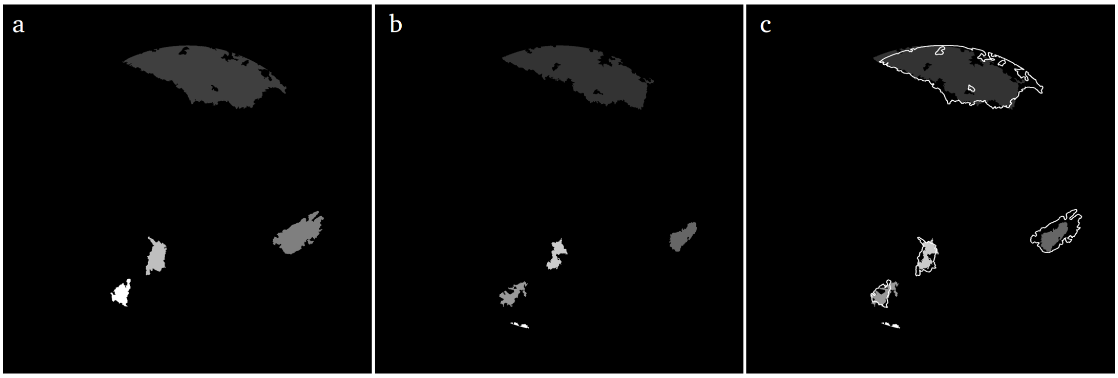

Figure 4.15: CH segmented masks for (a) October 31st and (b) November 1st, 2016. (c) shows an overlap of the forward projected mask from (a) onto the segmentation in (b).

other segments will be considered as the appearance of new features and tracked accordingly. In the event of multiple features joining together, the largest overlapping feature from t_0 projected onto t_n will be considered the tracked feature. All other previous features will be considered disappeared and their tracking will be decommissioned. Features that appear or disappear will be considered as the natural cycle of the features on the disk and will be tracked and decommissioned accordingly. Due to the long life of CHs, existing across multiple solar rotations, performing two separate attempts at tracking is ideal. One tracking attempt should be made for t_N at $t_{N-T_\odot}$, where $T_\odot$ is the rotational period of the sun, to maintain tracking of CHs that have been long lived in the solar corona, such as polar CHs. The second tracking attempt should be made at t_{N-i}, where i is a timescale less than the evolution timescale of the feature, n.

4.3.2 Off-Limb Detections

In CHIMERA's segmentation some detections exist off the solar limb, as seen in Figure 4.16. These detections are assumed to be higher altitude components of on disk CHs which are caused by the open magnetic fields that exist within CH boundaries extending far into the high corona. This high extension causes a similar low density and temperature region to that of on disk CHs. This assumption is made due to these features tracing out similar shapes to that of on disk CHs present close to the solar limb, commonly being seen above identified polar CHs,

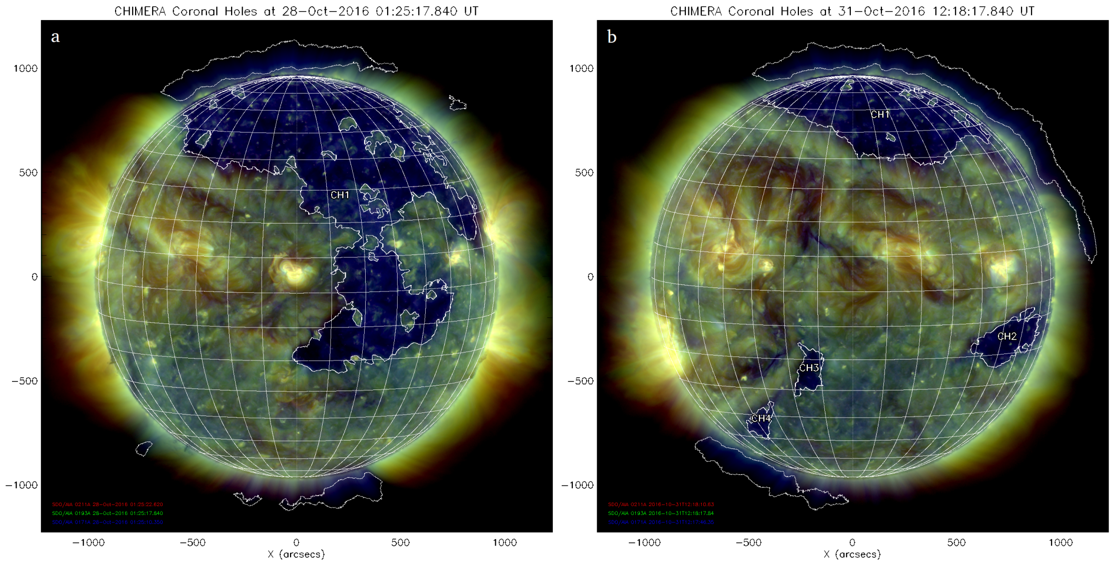

Figure 4.16: CH identifications for (a) October 28th, 2016, and (b) October 31st, 2016, showing the coincidence of a CH rotating off the western limb and a subsequent high altitude CH appearing off the western limb.

and these features having matching thermal properties to that of CHs, as per the CHIMERA segmentation method. Due to the CHIMERA method of segmentation focusing on identifying regions of similar thermal and density properties, it is capable of identifying these typically lower intensity off limb CH regions, which are typically not detected in other automated coronal feature segmentation techniques. These features are included in detection due to the assistance they can provide in predicting the structure of CHs that have rotated off the western limb, or that are about to rotate on the disk from the eastern limb. For example, the off-limb detection to the north-west of Figure 4.16(b) shows that CH1 extends further down towards CH2 on the opposite side of the Sun. These two features are, in fact, connected as a single feature which can be seen in (a).

4.4 Recalibration of CHIMERA

The CHIMERA method of feature identification applies for identifying multiple CH features as it acts as a simplified DEM of coronal images. For identification of active regions using the SDO/AIA instrument, a simple recalibration of the non-linear thresholds in EUV intensity space could be used to segment regions that exhibit the high temperature and density expected of active regions. Furthermore this method can be applied across multiple instruments through a simple recalibration to accommodate instrument sensitivities and differing available observing passbands.

4.4.1 SOHO Calibration

The SOHO observations share many similarities with the SDO observations, namely the capturing of 171 Å images of the solar corona and the similarities in the SDO 193 Å images and the SOHO 195 Å images. Furthermore SOHO had an earlier first light observation and has been running for a longer period of time. The key difference between observatories for this segmentation technique is the lack of a 211 Å filter on SOHO/EIT. However, this filter can be replaced for this work using the EIT 284 Å passband. A recalibration of CHIMERA to identify CHs in both SDO and SOHO images will enable a greater understanding of CHs and their evolution across multiple solar cycles. Figure 4.17 shows a comparison of the EUV vector space projections for a SDO/AIA image in the 171, 193 and 211 Å passbands observed on October 31st, 2016 (a, c, e), and for a SOHO/EIT image in 171, 195 and 284 Å passbands observed on April 24th, 1998 (b, d, f). Most notably the 284 Å passband has significantly lower average pixel counts than the 211 Å passband. However, relatively similar patterns of separation exist between two clusters of pixels in EUV vector space. Using similar methods as for the SDO/EIT calibration, a new optimal non-linear threshold can be found for SOHO/EIT images to identify CHs and other coronal features from surrounding plasma. Figure 4.18 shows the segmented SOHO/EIT calibration image observed on April 24th, 1998. Due to HMI being associated with the SDO instrument and not having observations for the entirety of the SOHO observations, the MDI instrument is instead used for the verification of CH regions.

4.4.2 Future Recalibration

This method of recalibration can apply to any instrument that observes the solar corona in 3 distinct wavelengths. To ensure best segmentations, it is recommended

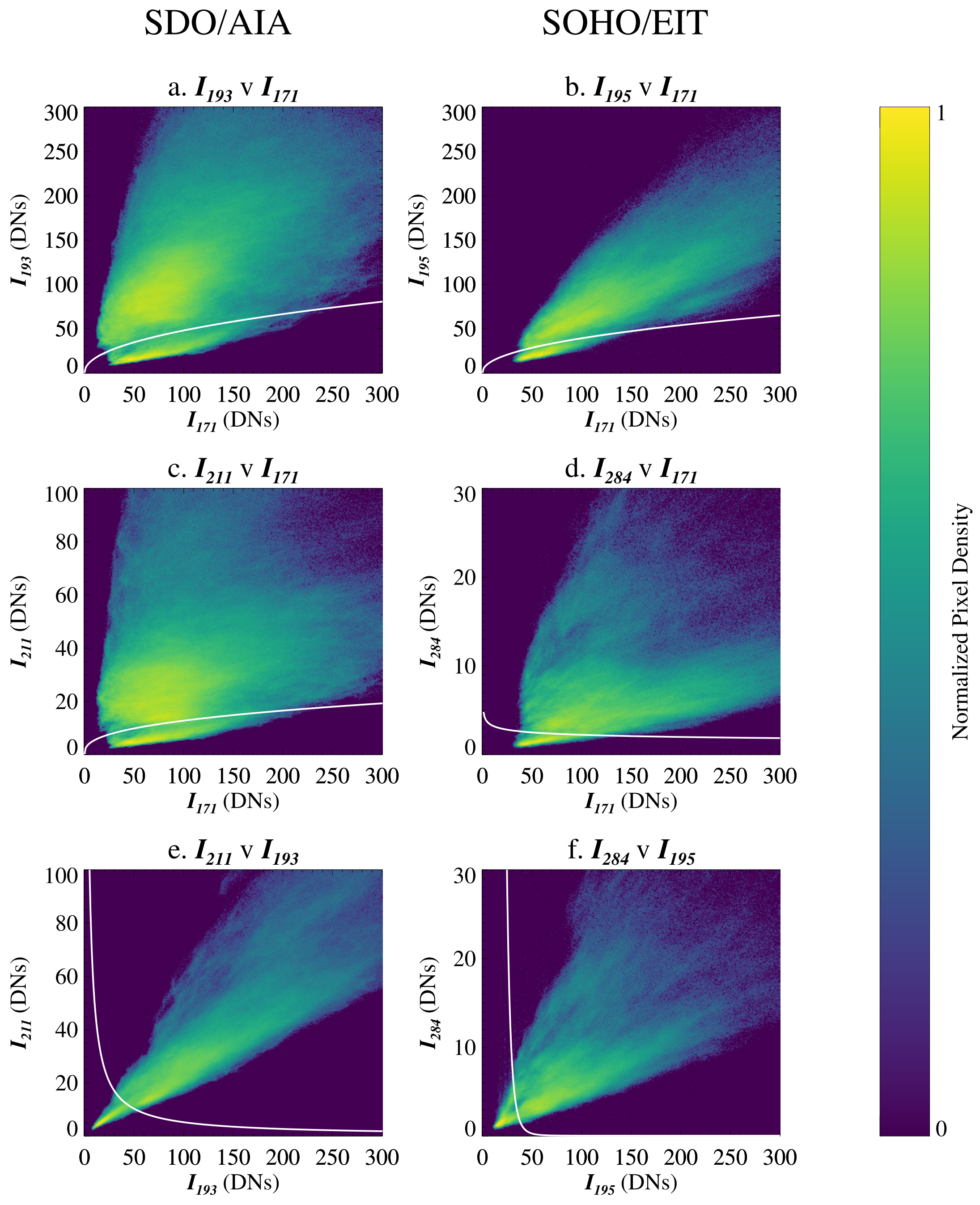

Figure 4.17: EUV vector space projections onto the Axis of the observing wavelengths for SDO/AIA observations on October 31st, 2016 (a, c, e) and identical projections for SOHO/EIT observations on April 24th, 1998 (b, d, f).

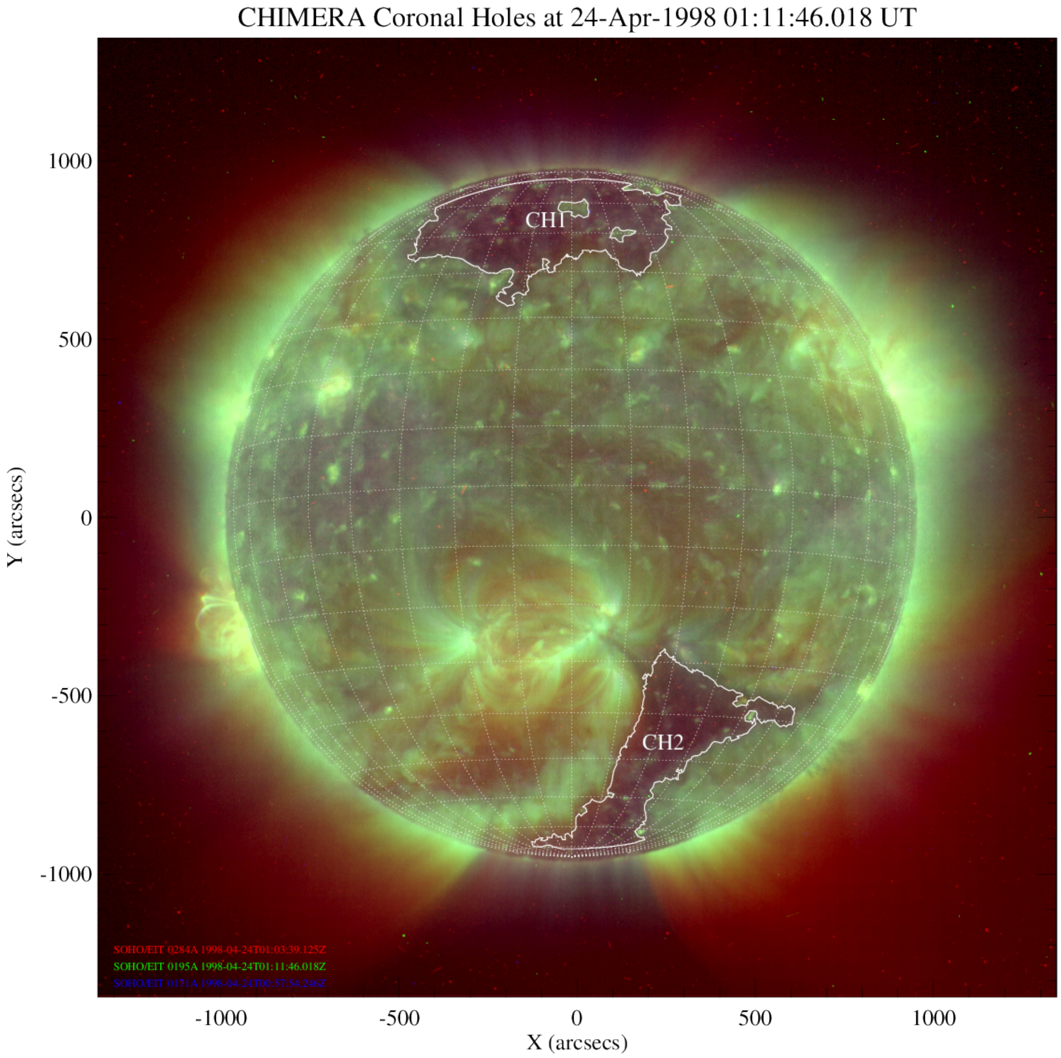

Figure 4.18: CHIMERA identification of CHs using the EIT instrument on board SOHO for April 24th, 1998.

that one of the observing passbands have its peak in the temperature range of the desired segmented feature, 171 Å for CHs, and for the remaining passbands to have a high intensity contrast between pixels of the desired feature and pixels of surrounding features. The ease of recalibration of the CHIMERA method, and its relation to the physical properties of observed features ensures it will be of use to any upcoming coronal observatory, such as GOES-SUVI, for the foreseeable future.

4.5 Real-Time Application of CHIMERA

CHIMERA is a fast ($\sim$30 second run-time per full disk segmentation) and robust feature identification, tracking and property extracting technique which has been run in real-time since the completion of its first version in early 2017 on *SolarMonitor.org/chimera*. Figure 4.19 shows an example of the real-time CH observations available from *SolarMonitor* with red boxes highlighting tools for easy scientific research and space weather forecasting. 1 highlights the search function for accessing a historical archive of CH data, 2 highlights the download feature for obtaining CH segmented images or image masks for overlaying onto other solar images, 3 highlights the central CH segmentation for a specified date, and 4 highlights some key properties of the observed CHs in 3. Furthermore, at the same site a large repository of segmentations has been created from SOHO observation in early 1998 to segmentations performed today. The algorithm classifies each pixel in an image individually by the exhibited thermal and density properties across 3 EUV passbands and for CHs makes use of magnetograms to verify CH candidates. The simplicity of the method of segmentation and its basis in real world observable physical properties for segmentation ensures it provides accurate and rapid segmentations of the solar corona. Furthermore, CHIMERA automatically extracts and stores properties of identified CHs. All of these features of CHIMERA make it an excellent resource for real time space weather forecasting. The images and properties extracted CHIMERA can be used with already well established relations between CHs and the HSSW on a rapid, regular and accurate basis. CHIMERA is already used by space weather forecasters in the UK Met Office Space Weather Prediction Center (MOSWOC) for comparison of CH segmentations and space weather predictions.

The primary limitation of the CHIMERA method is the classification of partially or fully occulted features. In the case of CHs, which are known to be low density, low temperature, open magnetic field regions of the corona, occultation can occur for near limb CHs by the high altitude components of other more dense and higher temperature solar features, such as filaments, active regions, and even the quiet Sun plasma. This effect can see identified features disappear artificially before they rotate around the solar limb. This effect can cause errors in boundary

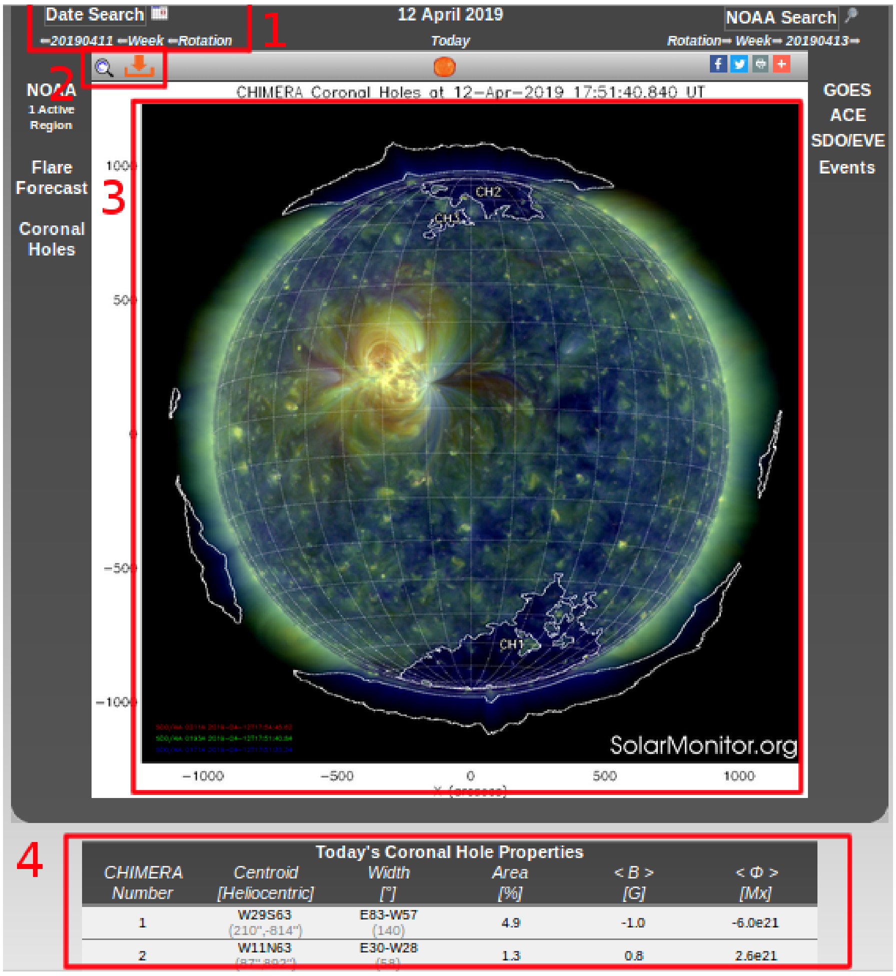

Today's Coronal Hole Properties

CHIMERA Number	Centroid [Heliocentric]	Width [°]	Area [%]	< B > [G]	< Φ > [Mx]
1	W29S63 (210",-814")	E83-W57 (140)	4.9	-1.0	-6.0e21
2	W11N63 (87",892")	E30-W28 (58)	1.3	0.8	2.6e21

Figure 4.19: View of the CHIMERA page on the SolarMonitor website (*SolarMonitor.org/chimera*) where real-time CH segmentations are permanently available to space weather forecasters. Red boxes highlight important features available to forecasters. 1 highlights the date search tool where forecasters can look through ~20 years of CH segmentations. 2 highlights a download dropbox where forecasters can obtain local versions of the CHIMERA segmented image, or a semi transparent mask to overlay on other solar images, e.g. to identify CH regions in solar continuum images. 3 highlights the the central CH segmentation for a specified date. 4 highlights some key properties of CHs observed in 3, taken from Table 4.1.

segmentation and area estimation of near-limb CHs, however, it is currently not possible to accommodate these effects without the use of multiple viewpoints, or possibly a swarm mission. This issue is also not unique to the CHIMERA method of segmentation. All methods of segmentation, both automated and manual, are susceptible to this issue of feature occultation.

Due to the current lack of a standard for verifying a CH segmentations accuracy, quantifying CHIMERA's level of accuracy is difficult. However, the CHIMERA method of segmentation is assumed to be accurate due it agreeing in segmentations to those done by eye from experts in the field. These accurate segmentations can now be compared and correlated with the *in-situ* observed properties of the HSSW streams produced by CHs at L1 in Chapter 5.

5

The Expansion of High Speed Solar Wind Streams

The appearance of on-disk CHs have long been connected to changes in the solar wind (Cranmer, 2002a, 2009; Krieger *et al.*, 1973; Tu *et al.*, 2005), however, the exact properties of CHs that govern these changes in the solar wind are as of yet unknown. Many correlations have been drawn between the two phenomena, such as the connection between CH area and HSSW stream velocity. In this chapter, improvements are made to space weather forecasting methods by (1) comparing and correlating CH identifications from CHIMERA to *in-situ* measurements of HSSW stream properties, (2) using these correlations to build a prediction model for HSSW stream properties, such as peak velocity and duration, and (3) deriving from these findings the longitudinal expansion of CH magnetic flux tubes from the corona to Earth's first Lagrangian point, located between the Earth and Sun. This Chapter is based on work published by Garton *et al.* (2018b) in the *Astrophysical Journal Letters.*

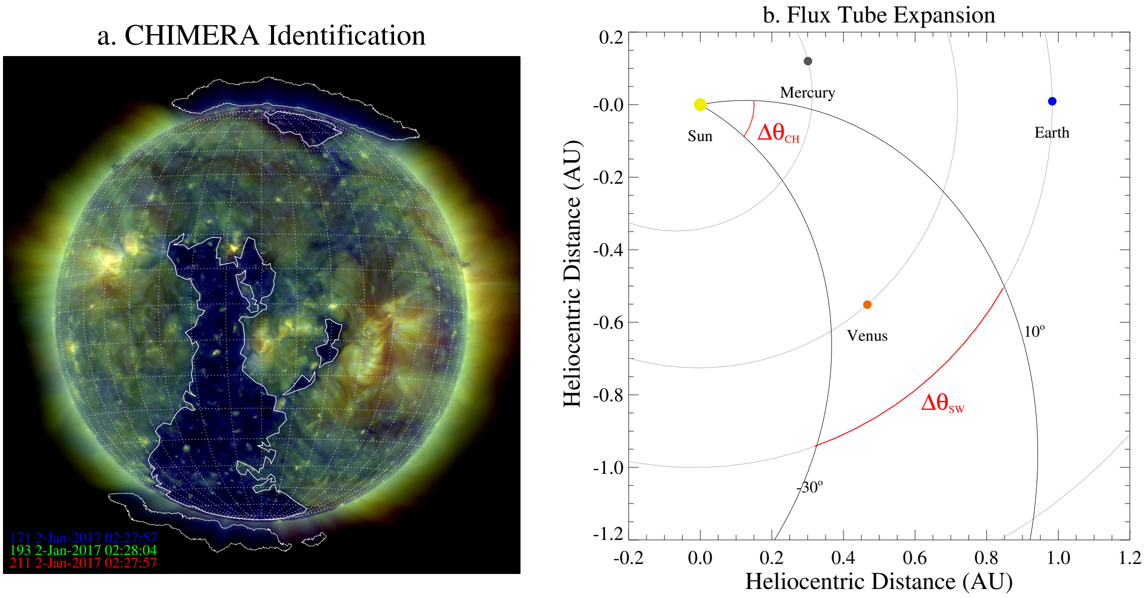

Figure 5.1: (a.) Five on-disk CH regions on 2017 January 2 segmented by the CHIMERA algorithm on a tri-colour image of AIA 171 Å, 193 Å, and 211 Å. The largest CH on disk is located near the central meridian. (b.) A simple ballistic propagation model for the HSSW stream emanating from the central on-disk CH obtained using HELIO. This model assumes the HSSW stream is emitted at ∼600 km s^{-1} from within the equatorial latitudes of the CH boundaries, ±60°, across the entire CH width, -30° to +10°. $\Delta\theta_{CH}$ and $\Delta\theta_{SW}$ denote the angular width of the CH on the solar disk and the HSSW stream at 1 AU respectively.

5.1 Coronal Holes and the Expansion of High Speed Solar Wind Streams

From CHIMERA segmented images it is possible to extract on-disk CH boundaries, and from them, their magnetic properties and physical geometry. These characteristics can be statistically compared and correlated with *in-situ* measurements of the solar wind to build a predictive model of the solar wind using only segmentations made by CHIMERA as an input.

Figure 5.1 (a) shows an on-disk CH located at central meridian segmented by the CHIMERA algorithm. The CH geometric properties of Eastern and Western boundaries are inserted into the HELiophysics Integrated Observatory (HELIO; Pérez-Suárez *et al.* 2012) ballistic propagation model in Figure 5.1 (b) which illustrates the boundaries, -30° to 10°, of the HSSW stream emanating from the on-disk CH at a velocity of $\sim$600 km s^{-1}. The HELIO model operates through the creation of solar wind streams emanating from the Sun at a given location, with a given velocity with no acceleration applied to the stream. The stream position is calculated spatially with respect to the rotation of the Sun, which creates a Parker spiral as described in Chapter 1. In this figure, the angular width of the on-disk CH is represented as $\Delta\theta_{CH}$ and the angular width of the corresponding HSSW stream when it reaches L1 is represented as $\Delta\theta_{SW}$. In the case where the leading and trailing boundaries of the HSSW stream are considered to be moving at the same radial speed, then $\Delta\theta_{SW}$ is equal to $\Delta\theta_{CH}$. For this model a longitudinal expansion of the HSSW stream can be derived from the Pinto & Rouillard variant of the flux tube expansion factor as described in Chapter 3, Equation 3.3:

$$f = \frac{A_r}{A_\odot}\left(\frac{r_\odot}{r}\right)^2 \tag{5.1}$$

Assuming that the flux tube does not change boundary shape, merely expands in area, Equation 5.1 can be factorized:

$$f = \frac{c l_r^{lat} l_r^{lon}}{c l_\odot^{lat} l_\odot^{lon}}\left(\frac{r_\odot}{r}\right)^2 \tag{5.2}$$

where c is a constant for area multiplication, l_r^{lat} and l_r^{lon} are the arclengths of the flux tube in the latitudinal and longitudinal directions at a radial distance r = L1, and similarly, $l_\odot^{lat}$ and $l_\odot^{lon}$ are the arclengths of the flux tube in the latitudinal and longitudinal directions at the coronal footpoint, $r_\odot$. From this latitudinal and longitudinal separation, the flux tube expansion factor, f, can be separated into two angular components, $f = f^{lat} f^{lon}$:

$$f^{lat} f^{lon} = \left(\frac{l_r^{lat}}{r}\right)\left(\frac{r_\odot}{l_\odot^{lat}}\right)\left(\frac{l_r^{lon}}{r}\right)\left(\frac{r_\odot}{l_\odot^{lon}}\right) \tag{5.3}$$

to analyze the solar wind expansions at L1, only the longitudinal vectors are considered, i.e. $f^{lon} = f_{SW}$. Furthermore, the ratio of arclengths to radius can be described in terms of angular widths for the flux tube at the coronal footpoint, $l_\odot^{lon}/r_\odot = \Delta\theta_{CH}$, and at the source surface height at L1, $l_r^{lon}/r = \Delta\theta_{SW}$. Hence,

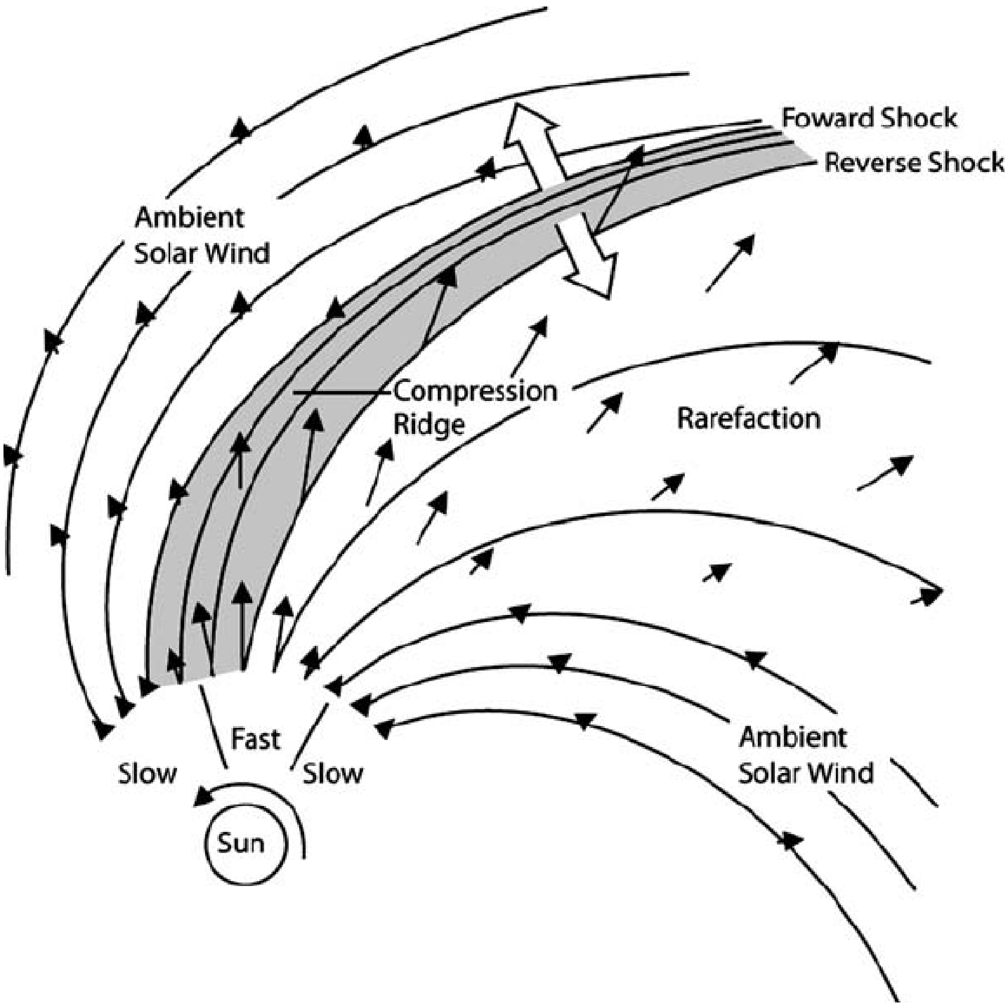

Figure 5.2: Model of the compression and rarefaction in HSSW streams interacting with the ambient slow solar wind (Pizzo, 1985).

the longitudinal component of solar wind expansion can be defined as:

$$f_{SW} = \frac{\Delta\theta_{SW}}{\Delta\theta_{CH}} \tag{5.4}$$

For the modeled case from Figure 5.1 a longitudinal solar wind expansion of $f_{SW} = 1$ is found. This is due to the simplicity of the model and the leading and trailing boundary of the HSSW stream having identical speeds. However, *in-situ* measurements of the solar wind indicate speeds emitted from CH regions vary across their area and is dependant on the distance from the nearest CH boundary.

This dependence finds areas near CH boundaries exhibiting lower speeds, and radial speed increasing as distance from the CH boundary increases Riley *et al.* (2001). Since radial solar wind speed from CHs is non-uniform, higher speed winds will catch up with slower winds and accelerate them through magnetic pressures. This causes a compression and rarefaction of the HSSW stream as seen in Figure 5.2. This compression and rarefaction is responsible for two prevailing features in *in-situ* observations of the solar wind. Firstly, HSSW streams that have a symmetry of radial speeds emitted from the coronal hole surface will become skewed towards the leading boundary of the HSSW stream, causing the inclining phase of the HSSW stream measured at L1 to be sharper in slope when compared to the declining phase of the same stream. This effect is demonstrated in Figure 5.3. Secondly, from this compression and rarefaction it is expected and will be shown that the HSSW stream will appear to expand in the longitudinal direction due to the excess time taken for the slower traveling trailing boundary to reach L1, i.e. $f_{SW} > 1$.

5.1.1 Widths and Durations of High Speed Streams

Figure 5.4 shows *in-situ* measurements of the solar wind, taken by ACE, for the month of January 2017. The HSSW is observed to range between $\sim$300 km s^{-1}, ambient slow solar wind, to $\sim$800 km s^{-1}, HSSW streams. As illustrated in the figure, all HSSW streams present in this figure are skewed such that the duration of their inclining phase is shorter than their declining phase, which implies the HSSW stream is undergoing the compression and rarefaction as previously discussed. An estimate for the expansion of the solar wind is more difficult to calculate as it is not currently possible to take measurements of the width of HSSW streams, $\Delta\theta_{SW}$. Instead, measurements of the duration of the HSSW stream at a point in space Δt_{SW}, stationary relative to the rotation of the Earth around the Sun can be used to approximate the angle of the solar wind as:

$$\Delta\theta_{SW} = \omega_{\odot}\Delta t_{SW} \tag{5.5}$$

where $\omega_{\odot}$ is the angular velocity of the solar wind, which is assumed to be identical to the mean Carrington synodic rotational angular velocity of the Sun,

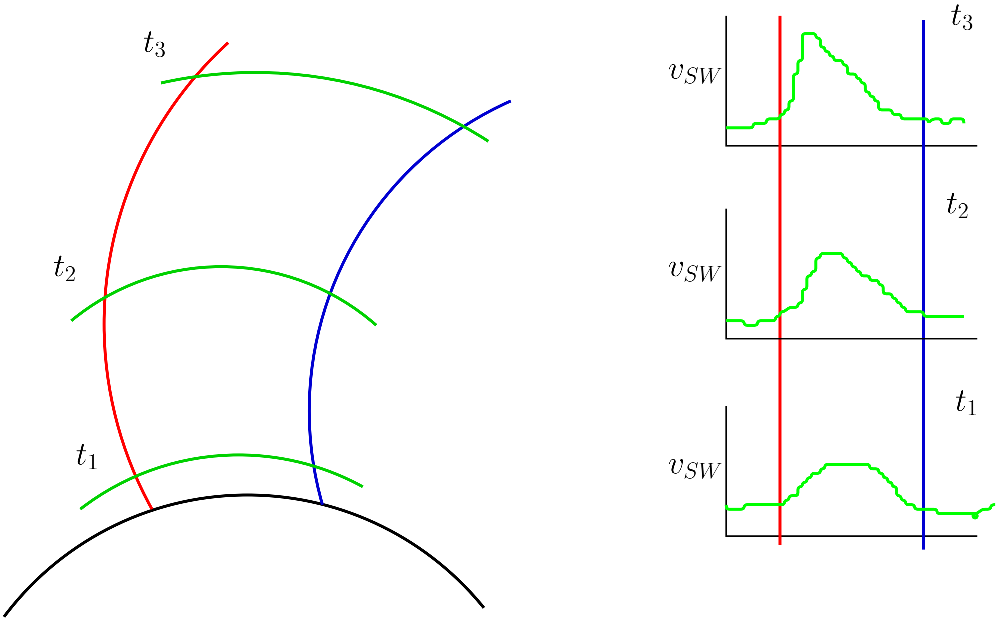

Figure 5.3: Illustration of increased skewness appearing in symmetrical solar wind streams as they travel radially from the Sun. Green slices across the leading (red) and trailing (blue) boundaries of the HSSW stream depict measurements of stream velocity for three different times, t_1, t_2, and t_3. Right plots illustrate the increased skewness of a HSSW stream with a starting symmetrical model of solar wind velocities.

$\sim 13.199°\text{day}^{-1}$. A comprehensive study by Oghrapishvili *et al.* (2018) of CHs finds a variation of rotational velocities with latitude, with a plateau existing between ±40°. Here, only CHs associated with a measurable HSSW stream at L1 are analysed, typically with some component of CH boundary existing within ±40°, hence this constant value of rotational velocity is assumed. Defining the duration of HSSW streams is difficult due to the inconsistencies of the ambient solar wind. The simplest definition of the start and end times of a HSSW stream is when the harsh change in slope to/from a HSSW stream begins and ends. However, this method cannot account for overlapping of unique HSSW streams originating from clustered on-disk CHs. Figure 5.5 shows an example where three on-disk CHs (CH1, CH3, CH4) spaced close together produce a triple peaked stream of HSSW with no return to background solar wind speeds between peaks, despite their originating CHs not being connected. This occurrence is likely due to the aforementioned expansion of these HSSW streams overlapping, the differences in

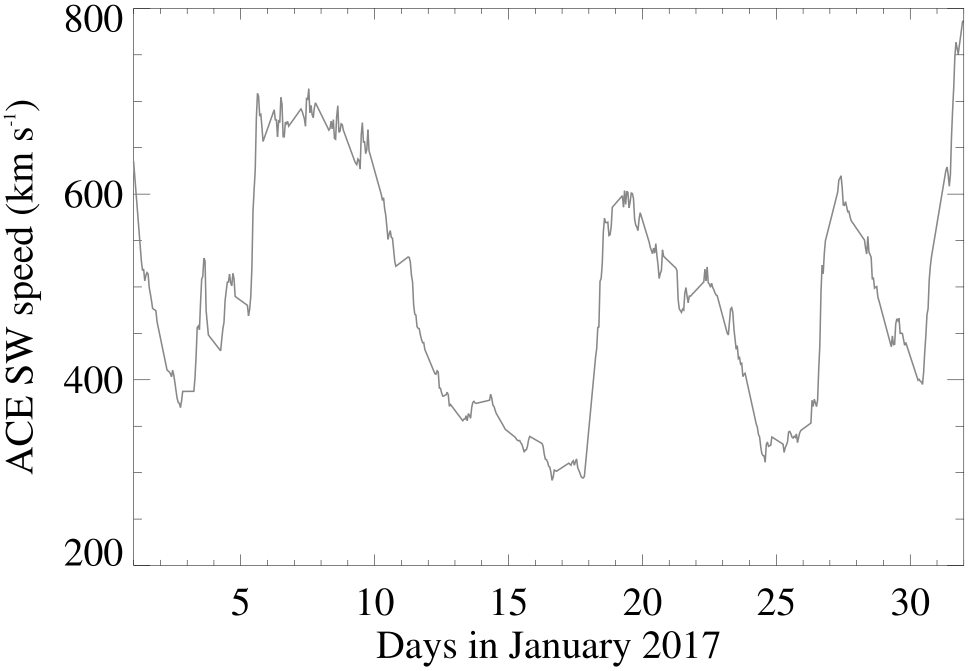

Figure 5.4: HSSW streams detected within the ambient solar wind by the ACE satellite for January 2017. HSSW streams are notable for their velocities ∼400-800 km s^{-1} (Cranmer, 2002a). Observably, all HSSW streams have a sharper inclining phase than declining phase.

peak velocities of each individual HSSW stream, as well as these CHs having a longitudinal overlap.

Here, an alternative method is used to classify the start and end times of the HSSW stream in hopes of preventing mis-classification due to HSSW stream overlap. The start and end times are classified as if the HSSW stream in question is the only one against the background of slow ambient solar wind. This is achieved by fitting a line to the inclining and declining phases of HSSW streams and finding the intersection of these lines with the mean monthly background solar wind. Figure 5.6 shows an example of the classification of the start and end times of the HSSW stream associated with CH1 from Figure 5.5. Dark blue lines show the linear fits to the inclining and declining phases of the HSSW stream and the mean monthly background solar wind is shown as a horizontal line calculated as 337.4 km s^{-1} for the month of January 2017. The intersection of these lines describe the start time, t_i, and the end time, t_f of the HSSW stream, which are associated

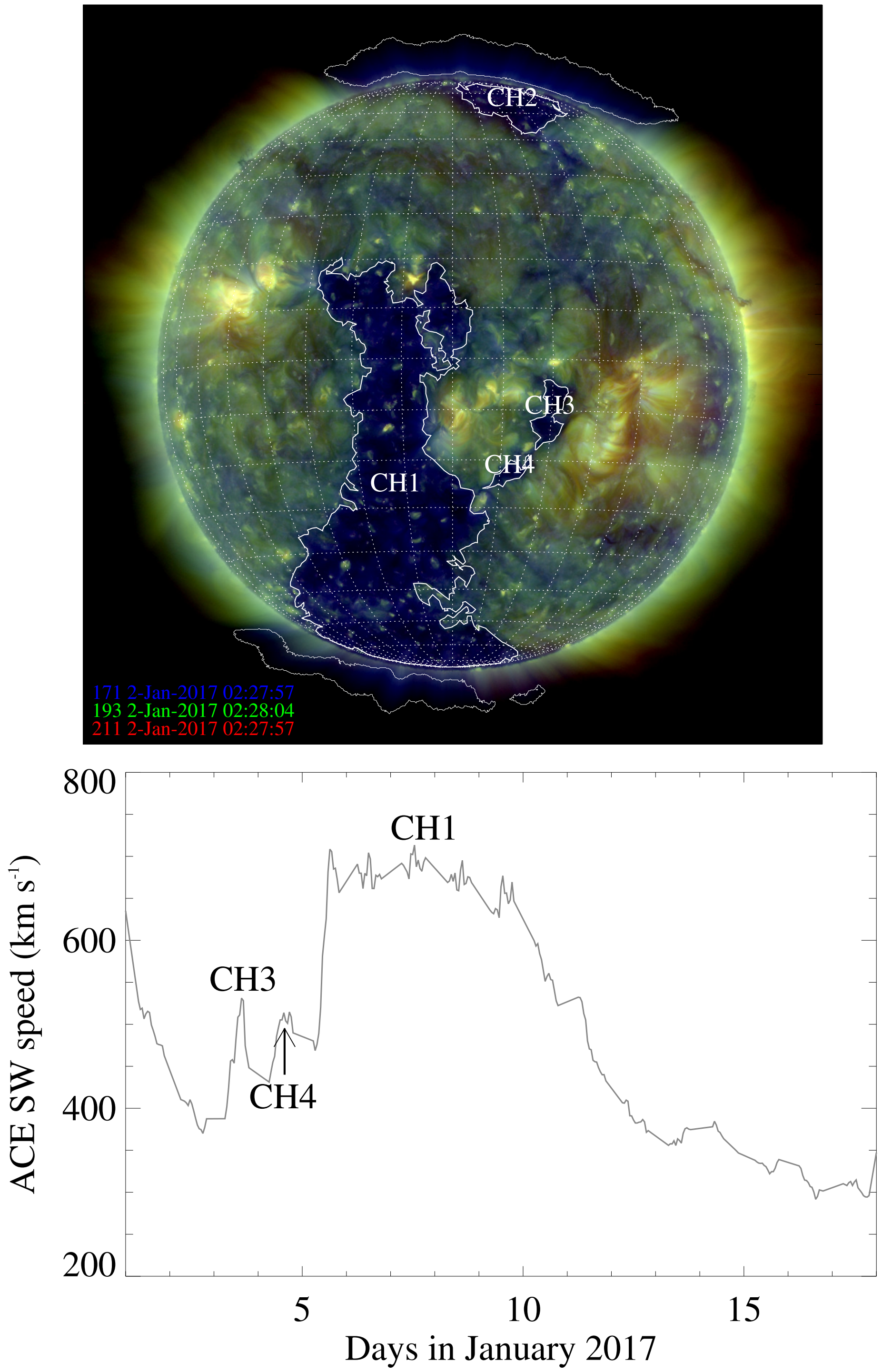

Figure 5.5: (Top) Demonstration of three on-disk CHs (CH1, CH3, CH4) detected and segmented by CHIMERA producing (Bottom) a HSSW stream that consists of the overlapping of each HSSW stream produced by these labeled CHs.

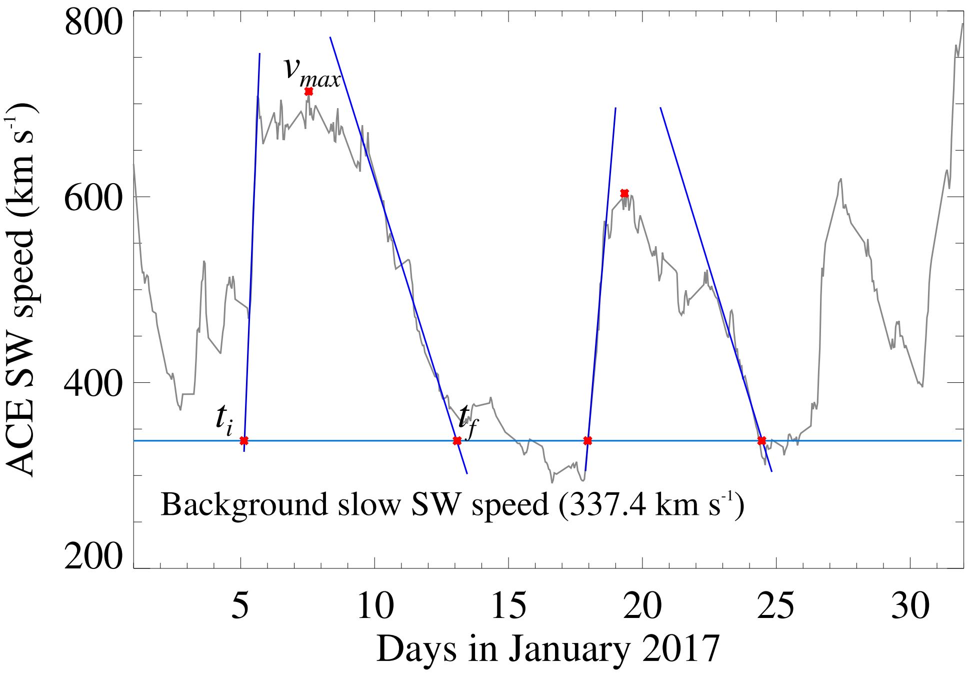

Figure 5.6: Example start (t_i) and end (t_f) times for high-speed solar wind streams from ACE measurements of the solar wind speed for January 2017. These times are calculated as the point of intersection between a line fit to the inclining and declining phase of the solar wind stream with the mean background slow SW speed for that month. Maximum velocities (v_{max}) between these two times is considered as the peak wind velocity for that particular HSSW stream.

with the leading and trailing boundaries of the HSSW stream respectively. From these boundary times the peak HSSW stream velocity, v_{max}, can be found and the duration of the HSSW stream is found as $\Delta t_{SW} = t_f - t_i$. From these measurements and Equations 5.4 and 5.5 the flux tube equation can be simplified to:

$$f_{SW} = \omega_{\odot} \frac{\Delta t_{SW}}{\Delta \theta_{CH}} \tag{5.6}$$

Equation 5.6 can be rearranged to form a relation between the measurable parameters Δt_{SW} and $\Delta \theta_{CH}$ as follows:

$$\Delta t_{SW} = \frac{f_{SW}}{\omega_{\odot}} \Delta \theta_{CH} \tag{5.7}$$

This relationship predicts the duration of upcoming HSSW streams from measurements of CH width at the central meridian, at $1R_\odot$.

5.2 Predictions of High Speed Solar Wind Stream Properties at L1 from Coronal Hole Properties

From these *in-situ* measurements of the solar wind, it is possible to build an empirical relationship between its properties and properties of their originating CHs extracted from CHIMERA as described in Chapter 4. Here, two main properties of CHs are compared with those of the solar wind, namely $\Delta\theta_{CH}$ is compared with both the Δt_{SW} and the v_{max} of the solar wind to estimate the f_{SW} for operational purposes, and A_{CH} is also compared to the same properties of the solar wind to find the more accurate predictors of HSSW properties.

5.2.1 Predicting High Speed Solar Wind Speed and Duration from Coronal Hole Width

Figure 5.7 shows two comparisons of 47 measurements of CH properties extracted by CHIMERA to in-situ measurements of their corresponding solar wind properties for June 2016 to June 2017. In these plots, square symbols refer to CHs that have some connection to the polar CHs caused by the solar dipole magnetic field, and diamond symbols refer to equatorial CHs with no visible connection to polar CHs.

Figure 5.7 (a) shows a comparison of the CHIMERA CH widths, here defined as $\Delta\theta_{CH}$, to v_{max}, with significant outliers highlighted in red which will be discussed later in this section. Previous studies have shown v_{max} is closely related to the area of the on-disk CHs, A_{CH}, i.e. $v_{max} \propto A_{CH}$ (Hofmeister *et al.*, 2018; Nakagawa *et al.*, 2019; Nolte *et al.*, 1976). Here, a similar positive correlation is observed until a cut-off value of $\Delta\theta_{CH} \approx 67^\circ$ where this positive correlation stops and values of v_{max} become a constant value, v_{max} ~710 km s^{-1} with a standard deviation of ~50 km s^{-1}, which is shown as a light blue horizontal line. For CHs with smaller

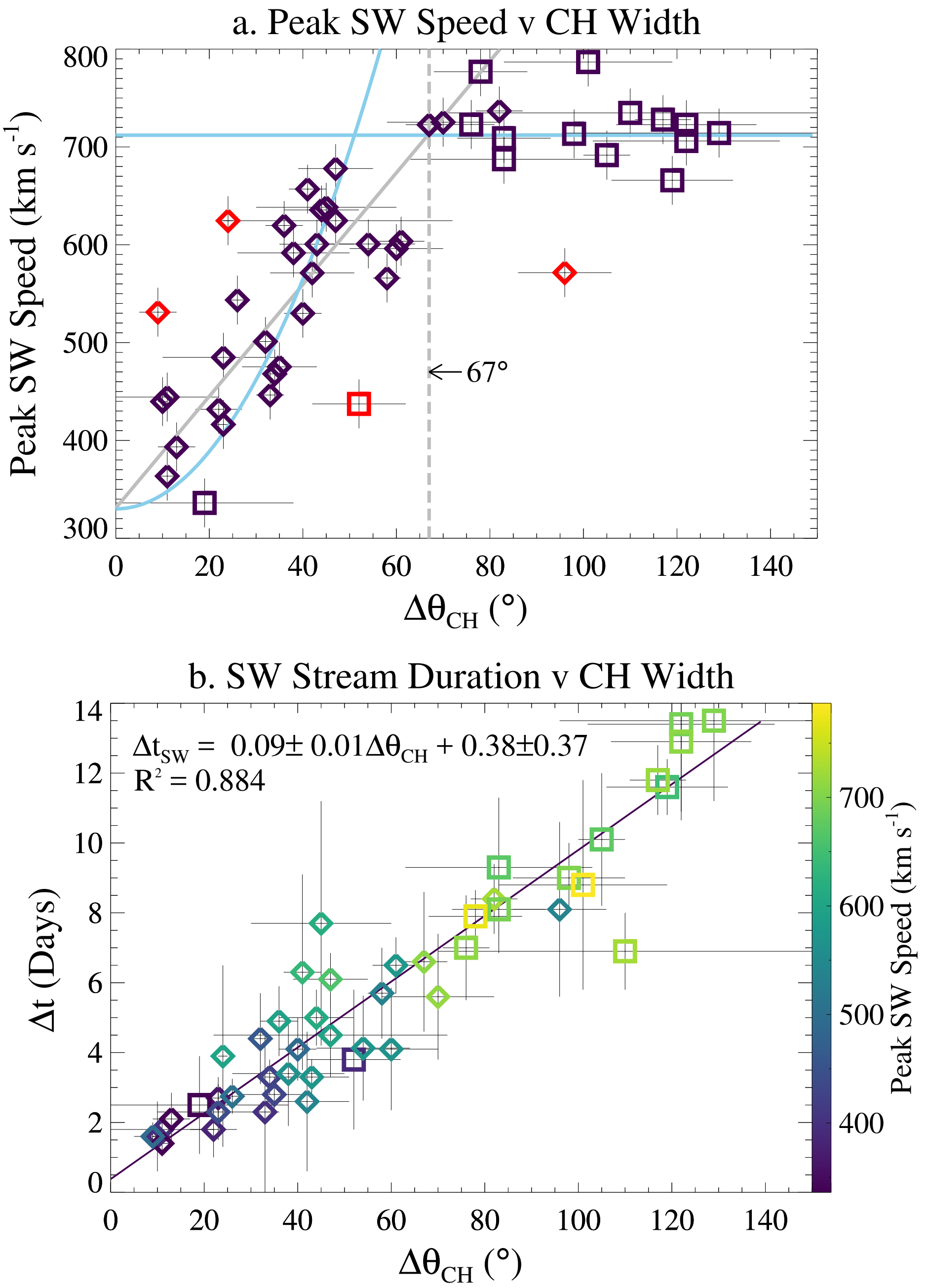

Figure 5.7: (a.) Peak solar wind speed versus longitudinal width of detected CHs. A linear fit for high width CHs is shown in blue, a linear fit to small width CHs is shown in grey, and a quadratic fit to small CHs is shown in blue ($v_{sw} \propto A_{CH}$). Significant outliers (red) are due to irregularly shaped CHs. (b.) Correlation between the duration of HSSW streams to CH width. Symbol colour represents peak SW speed observed and scales from purple, ∼400 km s^{-1}, to yellow, ∼700 km s^{-1}. Squares represent CHs connected to solar magnetic poles and diamonds represent CHs with no polar connection.

angular widths, $\Delta\theta_{CH} \leq 67°$, a linear relation, grey line, is found as:

$$v_{max} = 330.8(\pm 16.6) + 5.7(\pm 0.5)\Delta\theta_{CH} \tag{5.8}$$

where $\Delta\theta_{CH}$ is measured in degrees and v_{max} is found in km s^{-1} and this fit has a corresponding R squared (R^2) value of 0.34 and Chi squared (χ^2) value of 95.73. However, this relation assumes $v_{max} \propto \Delta\theta_{CH}$ which contradicts the correlation found by Nolte *et al.* (1976), $v_{max} \propto A_{CH}$. This discrepancy can be explained by the assumptions previously made in Equations 5.1 and 5.2:

$$A_{CH} = c l_{CH}^{lat} l_{CH}^{lon} \tag{5.9}$$

$$A_{CH} = c\Delta\phi_{CH}\Delta\theta_{CH} r^2 \tag{5.10}$$

where $\Delta\phi$ represents the angular height of the CH region. This correlation implies $v_{max} \propto A_{CH} \propto \Delta\theta_{CH}$. Hence, $\Delta\theta_{CH}$ can be used as a direct predictor to v_{max} but with a larger margin of error than using A_{CH}. However, CHs exhibit no directional preference in their shape and generally $\Delta\phi_{CH} \approx \Delta\theta_{CH}$. Hence, v_{max} can also be considered as proportional to ${\Delta\theta_{CH}}^2$. A quadratic fit using this relationship is illustrated in Figure 5.7(a) as a curved blue line and is described by:

$$v_{max} = 330.0(\pm 61.9) + 0.15(\pm 0.06)\Delta\theta_{CH}^2 \tag{5.11}$$

with a R^2 value of -0.79 and χ^2 value of -765.16. This negative value of R^2 implies this quadratic fit is a worse fit than a simple horizontal fit at the mean value of velocity. The scatter of points around both the linear and quadratic fit make both appear as equally good predictors but Equation 5.8 is quantifiably more accurate with a R^2 value being closer to 1. Furthermore, Equation 5.8 is recommended for operational space weather forecasts due to its simplicity and ease for predicting v_{max}.

As previously mentioned, four points in Figure 5.7 are highlighted in red as significant outliers to both the linear and quadratic fits. Upon investigation, CHs associated with these points were found to be significantly oblate, i.e. $\mid \Delta\phi_{CH} - \Delta\theta_{CH} \mid \gg 0$, an example of which is displayed in Figure 5.8. Hence,

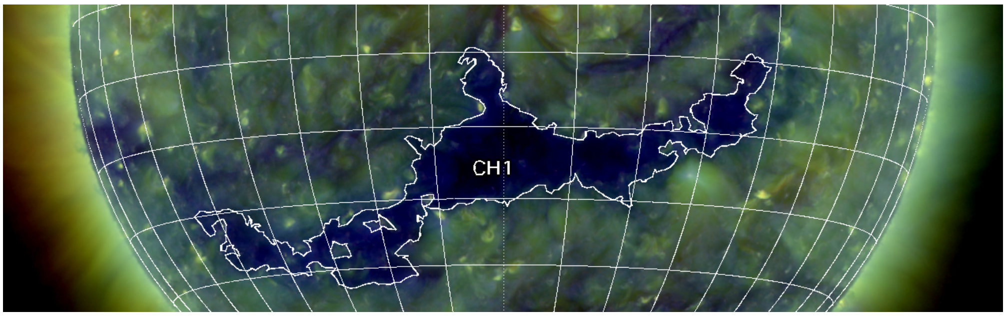

Figure 5.8: Example of a particularly oblong CH on the solar disk, responsible for a HSSW stream with properties that deviate significantly from the model found in Figure 5.7. This CH has a measured width of ~95°, produced a HSSW stream with a peak speed of ~570 km s^{-1} and was observed at disk center on February 15th, 2017..

Equations 5.8 and 5.11 fail to accurately predict v_{max} of CH regions which are particularly oblate but Equation 5.8 makes a reasonable estimate for regularly shaped CHs.

Figure 5.7(b) shows a comparison of CHIMERA CH widths, $\Delta\theta_{CH}$, to HSSW stream duration, Δt_{SW}, where points are coloured to represent their associated v_{max}, with slower peak speeds, ~400 km s^{-1}, coloured purple and faster peak speeds, ~700 km s^{-1}, coloured yellow. A strong correlation between this property of the CH and the associated HSSW stream is evident and is demonstrated by the best fit line:

$$\Delta t_{SW} = 0.09(\pm 0.01)\Delta\theta_{CH} + 0.38(\pm 0.37) \tag{5.12}$$

where $\Delta\theta_{CH}$ is measured in degrees and Δt_{SW} is predicted in days. This best fit line shows a high level of accuracy, $R^2 = 0.884$, which may be due to 2016 having a larger number of very extended CHs than is typical. This relation enables the prediction of the durations of HSSW streams at Earth. From the slope of this best fit linear relation and Equation 5.7 it is possible to estimate the average longitudinal solar wind expansion factor using:

$$\frac{f_{SW}}{\omega_{\odot}} = 0.09 \pm 0.01 \tag{5.13}$$

Assuming this angular velocity is equal to that of the synodic Carrington rotation, 13.199°day^{-1}, a general longitudinal expansion factor for HSSW streams of $f_{SW} = 1.2 \pm 0.1$ is obtained. This value implies HSSW streams will expand longitudinally while traveling through interplanetary space and is consistent with the aforementioned theoretical models by Wang & Sheeley.

5.2.2 Predicting HSSW Speed and Duration from CH Area

Figure 5.9 illustrates a similar comparison to Figure 5.7, however, here rather than comparing CH widths to HSSW properties the focus will be on the well established relationship between CH area and the properties of the solar wind. For these plots, A_{CH} is described as the percentage ratio of CH area in arcsecs^2 to the solar disk area, also in arcsecs^2. This classification of area as a projection onto a 2D disk instead of a 3D sphere is justified by all measurements of area being taken when CHs are at central meridian and projection effects are at their minimum.

Figure 5.9 (a) shows a comparison of the CHIMERA CH area, here defined as A_{CH}, to v_{max}, with the previous significant outliers from Figure 5.7(a) highlighted in red. These outliers are significantly closer to the linear optimal fit, indicating predictions of v_{max} of HSSW streams coming from CH areas are more accurate when considering both the latitude and longitude. Similar to $\Delta\theta_{CH}$ correlations, a positive correlation is observed until some cut-off value, $A_{CH} \approx 10\%$, where v_{max} become a constant value, v_{max} ~710 km s^{-1} with a standard deviation of ~50 km s^{-1}, which is shown as a light blue horizontal line. For small area CHs, $A_{CH} \leq 10\%$, a linear relation is found as:

$$v_{max} = 355.9(\pm 21.6) + 50.9(\pm 6.0) A_{CH} \tag{5.14}$$

where this fit has a corresponding R^2 value of 0.21 and χ^2 value of 50.33. Comparing these values to those found for $\Delta\theta_{CH}$ above, it is notable that the A_{CH} measurements appear to have a lower variance about the linear fit than $\Delta\theta_{CH}$, however, the $\Delta\theta_{CH}$ fit has smaller differences between the expected and observed values of v_{max} as shown by the relative R^2 values. This implies that $\Delta\theta_{CH}$ acts as a better predictor for v_{max}. Furthermore, the lower slope of the $\Delta\theta_{CH}$ fit means that a marginal error of measuring $\Delta\theta_{CH}$ will have a lesser impacts on predictions of HSSW peak speeds. This implies that area based predictions of HSSW peak

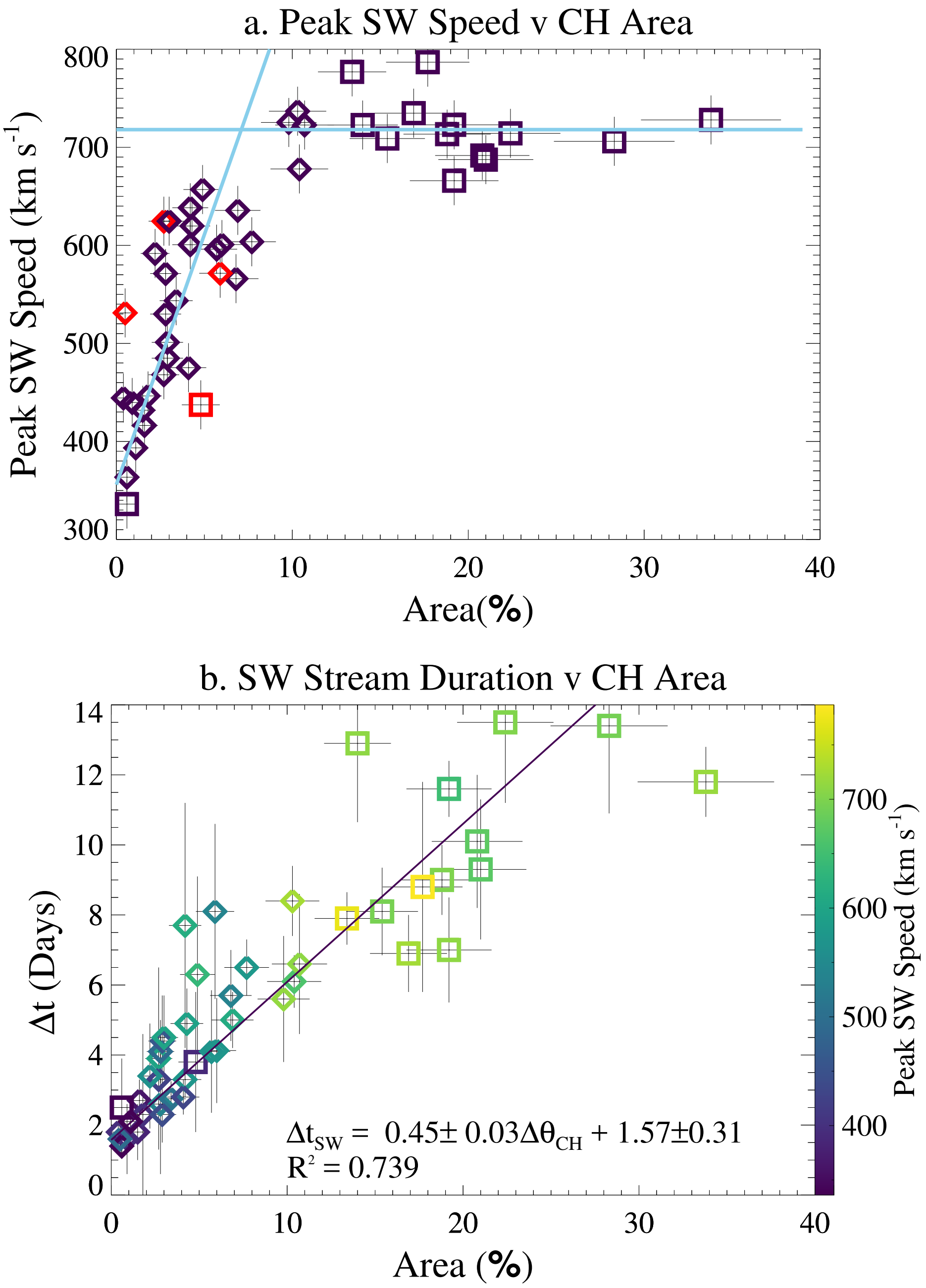

Figure 5.9: (a.) Peak solar wind speed versus area percentage of total solar disk for detected CHs. Two linear fits are shown, one fit shows a linear correlation between small area CHs ($A_{CH} \leq 10\%$) and peak SW speed which is described by Equation 5.14, and a second horizontal fit showing a plateau of peak SW speed for larger area CHs ($A_{CH} > 10\%$). Previous significant outliers from Figure 5.7(a) (red) are again highlighted to show the correction made to these points when both the longitudinal and latitudinal extent are observed. (b.) Correlation between the duration of HSSW streams to CH width. Symbol colour represents peak SW speed observed and scales from purple, ~400 km s^{-1}, to yellow, ~700 km s^{-1}.

v_{max} Prediction Fits	R^2	χ^2
Linear $\Delta\theta_{CH}$	0.34	95.73
Quadratic $\Delta\theta_{CH}$	-0.79	765.16
Linear A_{CH}	0.21	50.33

Table 5.1: Goodness of fit metrics for correlating $\Delta\theta_{CH}$ and A_{CH} to the v_{max} of the solar wind.

speeds are worse than CH width predictions for small CHs.

Figure 5.9(b) shows a comparison of CHIMERA CH areas, A_{CH}, to HSSW stream duration, Δt_{SW}, where points are coloured to represent their associated v_{max}, with slower peak speeds, ∼400 km s^{-1}, coloured purple and faster peak speeds, ∼700 km s^{-1}, coloured yellow. A correlation is observed between these properties and a linear fit is applied to the points described by:

$$\Delta t_{SW} = 0.45(\pm 0.03)A_{CH} + 1.57(\pm 0.31) \tag{5.15}$$

where A_{CH} is measured as a percentage of the total solar disk and Δt_{SW} is predicted in days. This best fit line demonstrates that $\Delta\theta_{CH}$ is a better predictor for HSSW stream duration as it shows a higher level of accuracy, $R^2 = 0.884$, compared to this area prediction, $R^2 = 0.739$. Notably, this A_{CH} fit has a significant constant, which implies a CH with an area of zero will create a HSSW stream lasting 1.57 days. This is obviously not possible and is not observed within *in-situ* observations of the solar wind. This discrepancy is likely due to very small CHs being difficult to detect, and CHIMERA having a minimum area cut-of, as discussed in Chapter 4, which may cause a statistical skew in the data set. The alternative being small area CHs have open magnetic fields which are expected to expand more than larger area CHs before a magnetic equilibrium is reached, causing these CHs to have HSSW streams which last longer at 1AU. When considering the width of CHs it is possible to estimate the longitudinal expansion factor, as described in the previous section, however it is not possible to estimate the area expansion of the magnetic flux tubes due to a lack of observatories able to detect the latitudinal extent of the flux tube at 1AU. Furthermore, the found values of f_{SW} are more useful for space weather operations than the area expansion. This expansion only considers the boundaries of the HSSW streams when they intersect with Earth. However, a true measurement of the magnetic flux tube longitudinal expansion must consider the different arrival times of both boundaries of the HSSW stream at 1AU due to both boundaries having differing radial speeds.

5.3 Flux Tube Expansion of Coronal Hole Magnetic Fields from Solar Surface through the Inner Heliosphere

Due to the varying velocity profile across a CH, the calculation of f_{SW} includes an additional component caused by the extra time for the relatively slower solar wind emitted from the eastern boundary of the CH to reach L1. This effect is clear in Figure 5.10 where the leading boundary of the HSSW, red line, reaches a distance of R_F, while in the same travel time the trailing boundary, blue line, only reaches a boundary of R_S such that:

$$R_S = R_F \left(\frac{v_S}{v_F} \right) \tag{5.16}$$

where v_F and v_S are the velocities of the solar wind at the leading and trailing boundaries respectively, and $v_F = v_{max}$. By correcting for this velocity variation across the HSSW stream, it is possible to estimate the longitudinal expansion of the CH flux-tube from the corona to L1 as follows:

$$f_{FT}^{long} = \frac{\Delta\theta_{FT}}{\Delta\theta_{CH}} = \frac{\Delta\theta_{SW} - \Delta\theta_{rot}}{\Delta\theta_{CH}} \tag{5.17}$$

where $\Delta\theta_{SW}$ can be expressed as $f_{SW}\Delta\theta_{CH}$ and $\Delta\theta_{rot}$ can be calculated from Figure 5.10 as the angle the Sun has rotated in the time taken for the slow boundary to reach a distance R_F traveling radially from R_S:

$$\Delta\theta_{rot} = \omega_{\odot} t = \omega_{\odot} \left(\frac{R_F - R_S}{v_S} \right) \tag{5.18}$$

substituting in Equation 5.16:

$$\Delta\theta_{rot} = \omega_{\odot} \left(\frac{R_F}{v_S} - \frac{R_F v_S}{v_S v_F} \right) = [(1/v_S) - (1/v_F)] \tag{5.19}$$

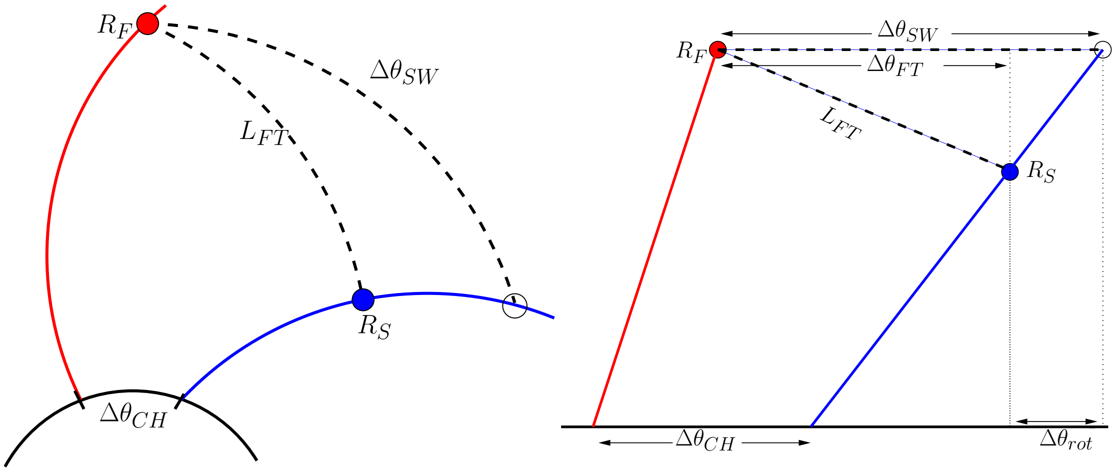

Figure 5.10: (a.) Projection of a HSSW stream with a leading boundary (red) originating from the western CH boundary and a trailing boundary (blue) originating from the eastern CH boundary. R_F and R_S show the distance traveled by plasma packets emitted at the same time but traveling at different velocities. $\Delta\theta_{SW}$ represent the path of Earth through the HSSW stream and L_{FT} approximates the continuous line of plasma packages, emitted from the Sun at the same time, when the leading boundary reaches some R_F (b.) An identical projection of the HSSW in polar space. $\Delta\theta_{rot}$ here represents the angular difference between the trailing boundary of the HSSW at R_F and R_S and $\Delta\theta_{FT}$ is the longitudinal angular width of the HSSW flux-tube projected out to R_F.

is obtained. Hence, f_{FT}^{long} can be written as:

$$f_{FT}^{long} = f_{SW} - \frac{\omega_{\odot} R_F}{\Delta\theta_{CH}} \left(\frac{1}{v_S} - \frac{1}{v_F} \right) \tag{5.20}$$

Furthermore, it is possible to estimate the width expansion of the overall open magnetic field of the coronal hole, which will henceforth be referred to as the coronal hole flux-tube expansion factor (f_{FT}):

$$f_{FT} = \frac{L_{FT}}{r} \left(\frac{r_{CH}}{l_{CH}} \right) = \frac{1}{\Delta\theta_{CH}} \int_0^{L_{FT}} \frac{dL_{FT}}{r} \tag{5.21}$$

where the length L_{FT} is approximated as a segment of the spiral shown in Figure 5.10. A shortened derivation for this equation will now be presented, however, the full derivation is described in Appendix 8.1. Using the calculation of the length of a spiral arm Equation 5.21 can be expressed as:

$$f_{FT} = \frac{1}{\Delta\theta_{CH}} \int_0^{\Delta\theta_{FT}} \frac{\sqrt{r^2 + (\partial r/\partial\theta)^2}}{r} d\theta \tag{5.22}$$

where ∂r and $\partial\theta$ represent infinitesimal segments of the spiral. The radius of a given spiral changes as a function of θ, in this case calculated from Figure 5.10 as:

$$r(\theta) = R_S + \frac{(R_F - R_S)}{\Delta\theta_{FT}}\theta \tag{5.23}$$

where $\Delta\theta_{FT}$ is the angular width of the flux-tube ($\Delta\theta_{FT} = \Delta\theta_{SW} - \Delta\theta_{rot}$). Substituting Equation 5.16 and 5.23 into Equation 5.22 simplified to:

$$f_{FT} = \frac{1}{\Delta\theta_{CH}} \int_0^{\Delta\theta_{FT}} \sqrt{1 + \left(\frac{\Delta v}{v_S\Delta\theta_{FT} + \theta\Delta v}\right)^2} d\theta \tag{5.24}$$

where Δv is the difference of velocities between the leading and trailing HSSW stream boundary, $(v_F - v_S)$. Integrating across the angle of the spiral renders the general equation for the CH flux-tube expansion factor as:

$$f_{FT} = \frac{\alpha - \beta}{\Delta v \Delta\theta_{CH}} + \frac{1}{2\Delta\theta_{CH}} ln\left(\frac{[\beta + \Delta v][\alpha - \Delta v]}{[\beta - \Delta v][\alpha + \Delta v]}\right) \tag{5.25}$$

where

$$\alpha = \sqrt{(v_F\Delta\theta_{FT})^2 + \Delta v^2} \tag{5.26}$$

$$\beta = \sqrt{(v_S\Delta\theta_{FT})^2 + \Delta v^2} \tag{5.27}$$

These derivations make it possible to estimate the range of possible expansion factors. Empirical measurements find that f_{SW} will remain averaged at ~1.2 regardless of CH width, but the variance of expansions is inversely correlated with CH width. Figure 5.11 shows the range of values of f_{FT}^{long} for varying values of $0° \leq \Delta\theta_{CH} \leq 180°$. The light blue line in this figure represents the relation between f_{FT}^{long} at 1AU if it is assumed that $v_{max} \propto {\Delta\theta_{CH}}^2$. f_{FT}^{long} will range from 1.2 for small CHs to ~ 0.5 for $\Delta\theta_{CH} \approx 60°$. Above $\Delta\theta_{CH} \approx 60°$, f_{FT}^{long} tends towards a constant value of 1. The grey line represents the same relation if it is assumed that $v_{max} \propto \Delta\theta_{CH}$. For this case, f_{FT}^{long} will range from 0 for small CHs to ~0.5 for $\Delta\theta_{CH} \approx 60°$. Above $\Delta\theta_{CH} \approx 60°$, f_{FT}^{long} tends towards a constant value of 1. Within both of these models a discontinuity exists, most noticeably in the model of $v_{max} \propto \Delta\theta_{CH}{}^2$ at $\sim 55°$. A similar discontinuity exists in the $v_{max} \propto \Delta\theta_{CH}$ model at 67°, and both of these discontinuities are due to the plateau like relationship between v_{max} and $\Delta\theta_{CH}$. Simply, a discontinuity exists because somewhere between 50 and 70° v_{max} no longer scales with CH width. From the comparison of calculated values of f_{FT}^{long} to both of these models, it is not possible to conclude which model is better as points have a large spread and large margin of error, particularly for small width CHs.

The f_{FT} model from Equation 5.25 becomes undefined as $\Delta v \to 0$, however due to the correlation between Δv and $\Delta\theta_{CH}$, $\Delta v = 0$ only when $\Delta\theta_{CH} = 0$, i.e. when no CH is present on the solar disk. Hence, Equations 5.25-5.27 only apply when both $\Delta v > 0$ and $\Delta\theta_{CH} > 0$, i.e. when a CH is present on the solar disk. Figure 5.12 shows multiple time slices of a full 180° comparison of the derived model of f_{FT} with $\Delta\theta_{CH}$ at 1AU to values calculated from the HELIO ballistic propagation model. Here, the blue line in Figure 5.12 (b, d, f) represents values of the f_{FT} model and grey points show values of f_{FT} found from the model at a one degree step size. These found values fit the model of f_{FT} with minor variations likely due to the simplicity of the HELIO ballistic model. The notable limits of f_{FT} are derived in Appendix 8.2, and it is found that f_{FT} approaches a value of 1.2 for very small CHs, $\lim_{\Delta\theta_{CH}\to 0} f_{FT}(\Delta\theta_{CH}) = 1.2$, and as $\Delta\theta_{CH}$ increases to a small width CH (~20°), f_{FT} approaches a value of ~0.8. Above this CH width, values of f_{FT} tend towards ~1.

5.4 Discussion and Conclusions

Here, the relationship between CH width and area, CH properties made available by the CHIMERA algorithm, and the properties of the associated solar wind measured at L1 by the ACE satellite has been investigated. The results show that a positive correlation exists between the peak SW speed of HSSW stream and the width of their originating CHs for widths $\lesssim$67° as well as the already established relationship of HSSW speed and CH area. Variations of $\Delta\theta_{CH}$ and v_{max}

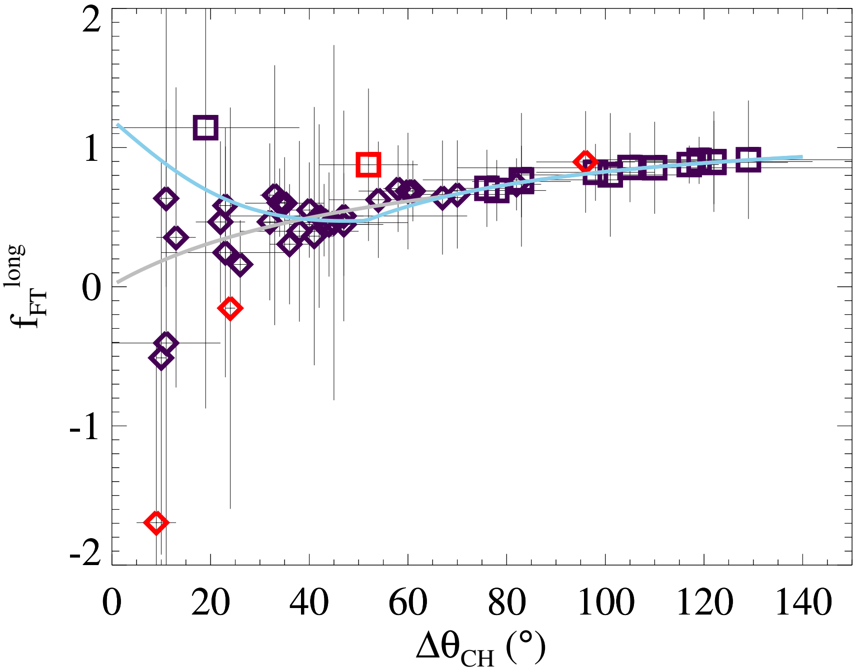

Figure 5.11: Comparison of the derived models of f_{FT}^{long} to calculated values from *in-situ* observations of HSSW properties. The light blue line shows a model for f_{FT}^{long} if it is assumed that $v_{max} \propto \Delta\theta_{CH}{}^2$ and the grey line shows a separate model if it is assumed that $v_{max} \propto \Delta\theta_{CH}$. Also plotted with these models are the real calculated values of f_{FT}^{long} for all CHs from Figure 5.7(a). Colour and shape of points identify the same properties as described in Figure 5.7. Some calculated values of f_{FT}^{long} exhibit negative values, implying the angular width of the HSSW streams projected at equal times become negative, or the boundaries flip sides relative to the Sun's reference frame. This is not likely as plasma packets are projected radially. These values only occur for small area CHs where relative error on observed properties are large.

from a direct correlation are due to the HSSW speed being related to the area of CH regions, which varies independently from longitudinal width, and possible near misses of HSSW streams. Furthermore, other CH properties likely have a further contribution to the solar wind speed. Above ∼ 67° width the peak SW velocity appears to become constant at ∼710 km s^{-1} regardless of CH width, with a standard deviation of ∼50 km s^{-1}. These speeds are consistent with the theory of HSSW streams emanating from CH regions by Cranmer (2009). Furthermore, this relation is similar to the relation between HSSW velocity and distance from a coronal boundary found by Riley *et al.* (2003). Most notably are the advantages of

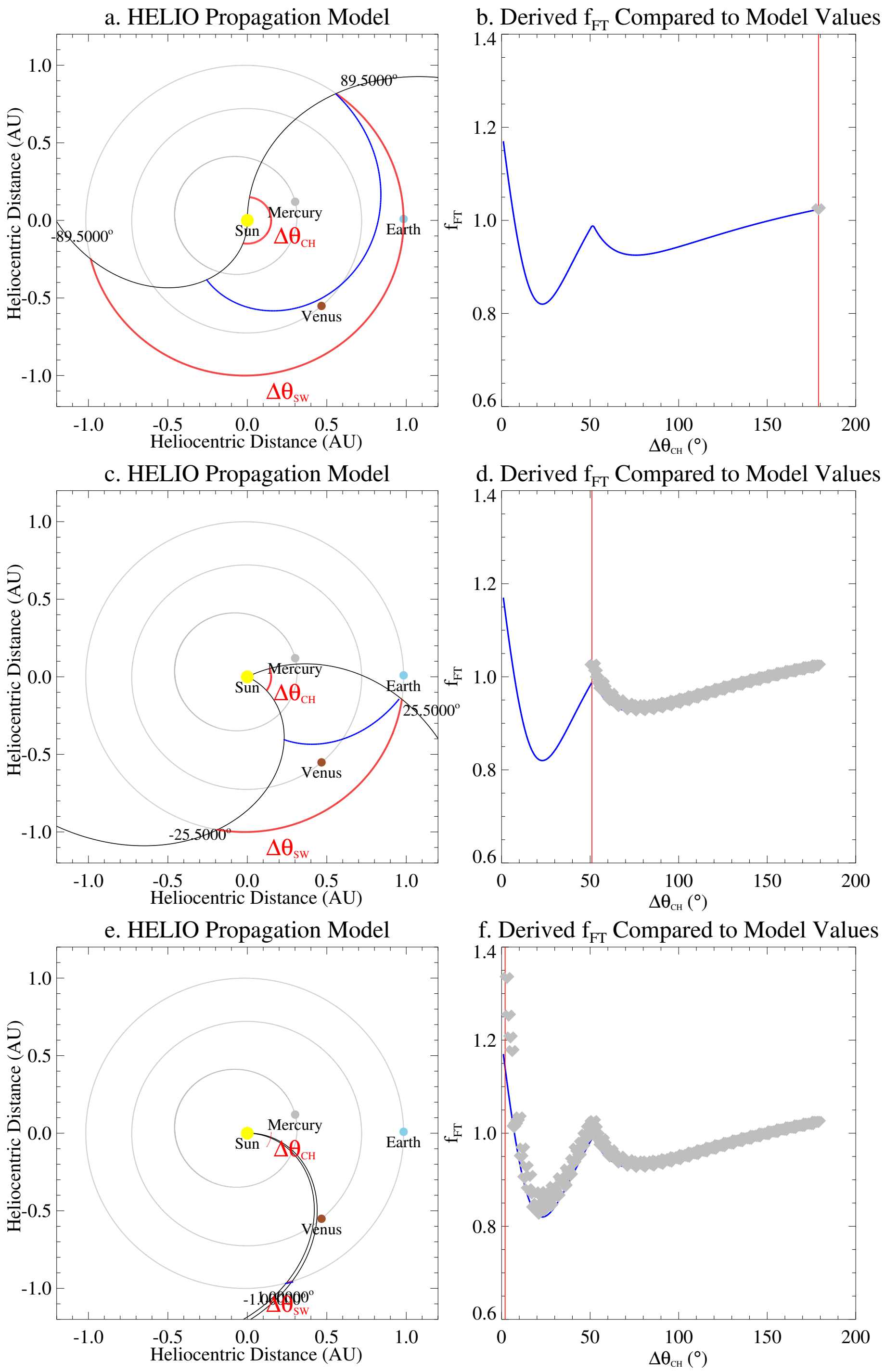

Figure 5.12: Comparison of the derived f_{FT} model to values calculated from the HELIO ballistic propagation model for various inputs of CH widths. Left Column (a, c, e) show outputs from the HELIO model with red curves highlighting the longitudinal extent of the HSSW stream at the CH surface, $\Delta\theta_{CH}$, and at 1AU, $\Delta\theta_{SW}$. The blue line highlights plasma that was emitted from the solar surface simultaneously when its faster boundary reaches 1AU. Right column (b, d, f) shows a comparison of the derived model of f_{FT} (blue curve) to values calculated from the HELIO model (grey points) at three steps: (b) $\Delta\theta_{CH} = 179°$, (d) $\Delta\theta_{CH} = 51°$, (f) $\Delta\theta_{CH} = 2°$.

using CH width as an operational predictor for HSSW speed, namely its simplicity, ease of use and lower relative margin of error.

From the strong correlation of HSSW stream duration to CH width in Figure 5.7b it is clear these properties are fundamentally linked. Hence it is possible to predict the duration of an incoming stream of HSSW using the best fit linear relation, $\Delta t_{SW} = 0.09(\pm 0.01)\ \Delta\theta_{CH} + 0.38(\pm 0.37)$. Combined with empirical measurements, such as in Vršnak *et al.* (2007), and the expanded study by Verbanac *et al.* (2011), a prediction of the start and end time of a HSSW streams interaction with Earth is possible. $\Delta\theta_{CH}$ is a more accurate predictor of the duration of the HSSW stream than A_{CH}, likely due to the angular latitudinal component of CHs not afecting their durations.

From these measurements of CH width and stream duration an average longitudinal solar wind expansion factor of 1.2 ± 0.1 is calculated. This value implies the HSSW always expands longitudinally from $1R_\odot$ to 1AU. This consistent expansion is likely a composite of the HSSW flux-tube expanding and an increased longitudinal width caused by differing arrival times of the leading and trailing boundaries at 1AU. By correcting for this variation in arrival times, it is possible to estimate the projected longitudinal expansion of the HSSW flux-tube at R_F from Equation 5.20, which ranges from $f_{SW} \gtrsim f_{FT}^{long} \gtrsim 0.5$. Then, by approximating the structure of the flux-tube as a spiral, it is possible to estimate the coronal hole flux-tube expansion factor from Equations 5.24 and 5.25, which ranges from $f_{SW} \gtrsim f_{FT} \gtrsim 0.8$. These values of flux-tube expansion are very low compared to empirical area flux-tube expansion values found by Wang *et al.* (1997) of <3.5 to >18, or modeled values by Pinto & Rouillard (2017) from 1 to ~100. This discrepancy is likely due to the focus here on the longitudinal flux-tube expansions and the potential of flux-tubes expanding non-uniformly in the longitudinal and latitudinal directions, as well as this study focusing on expansions from the corona to 1AU where previous studies have focused on the expansion from the magnetic footpoints in the photosphere to the corona. Furthermore, previous studies have focused on the expansion of flux-tubes originating in polar CH regions or the expansion of individual magnetic funnels within a CH boundary, as in the Pinto & Rouillard work. This work instead averages the expansion factors of all magnetic funnels within the CHs anywhere on the solar disk that correlates with geomagnetic storm activity.

These average values of f_{SW} determined here and the empirical relationship found between $\Delta\theta_{CH}$ and Δt_{SW} are useful for operational space weather forecasting efforts. For the first time it is possible to make simple predictions of the durations and maximum speeds of HSSW streams and the expansion of the HSSW flux-tubes merely from an estimation of longitudinal width of CH regions. These results are potentially useful for solar wind/radiation belt forecasting tailored for satellite operators.

6

Long-term Coronal Hole Statistics and Machine Learning Models of Solar Wind

The varying properties of CHs have been observed and correlated with the solar wind for over 40 years (Nolte *et al.*, 1976). However, analysis of CH properties are typically focused on a fractional period of a given solar cycle, i.e., < 11 years. The long-term variability of CH properties across a solar cycle, or multiple solar cycles, have not yet been studied sufficiently. Long-term observations of CHs and their properties can give important new insights into the processes that create them, and their governing effects on the solar wind. In this chapter, the robust CHIMERA algorithm is utilized to analyse the properties of CHs across two solar cycles (1998-2019) using observations from both SOHO and SDO. Furthermore, these long term properties are used as inputs to a variety of ML methods to build a more accurate predictive model than humans are capable of creating. This chapter is based on work which is currently under preparation for publication to multiple peer-reviewed journals.

6.1 Long-term Observations of Coronal Holes

CHs have long been observed and manually segmented from the surrounding coronal regions by humans. Human segmentation, while effective and robust, particularly in the early years of computing, has no logical consistency and is not typically replicable. This effect combined with the relatively few creations of long-term running CH segmentation algorithms indicates that there are no consistent and reliable long-term studies performed on CHs and their variations across multiple solar cycles. The creation of the CHIMERA algorithm, and the subsequent recalibrations, ensures a reliable and logically consistent segmentation of CH regions from the entirety of the SOHO and SDO spacecraft lifetimes (1998-2019). For the first time, a large set of logically consistent CH segmentations and properties has been created. This large database can now be used to analyse the statistical distribution of CH properties across a solar cycle. Furthermore, the database can be used in tandem with established correlations between CH properties and associated solar wind properties to predict the distribution of solar wind properties in a given solar cycle. Hence, the number of significant geo-effective space weather storms.

Figure 6.1 presents how the total CH percentile area varies across the two solar cycles, from 1998 to 2019. The figure illustrates the hourly variation of CH percentile area (black). For ease of viewing, these values are averaged into smoothed monthly bins and are overplotted in light blue. It is difficult to extract meaning from this data, however, by comparing to the well established relationship between the solar cycle and sunspot number (light red) it is possible to discern some structure in CH behaviours in tandem with the solar cycle. For reference the established dates of the solar max and min are highlighted in the plot using yellow and pink vertical lines respectively. Notably, CH area rises sharply after the established times of solar max, with peaks occurring at an approximate phase shift of a quarter wavelength relative to the sunspot cycle. Furthermore, the amplitudes of the CH cycle appear to be inversely proportional to the previous amplitude of sunspot number. These relationships and possible phase shifts, however, are difficult to claim with certainty due to only two solar cycles of observations to analyse. Surprisingly, a significant dip in CH percentile area occurs during the solar minimum, when CHs are seen as the governing cause of space weather events. An investigation into the reprojection of the CH areas into spherical based measurement was performed to account for the possibility of CHs appearing predominantly as large polar CHs, which typically occurs at the dipolar solar min, however this did not account for this trough in CH area.

Figure 6.1 (b-d) illustrate CHIMERA segmentations taken from solar max and min in 2001, 2008 and 2014 respectively. Segmentations are visibly accurate for the solar max images in 2001 and 2014, however the CHIMERA segmentations present inaccurate segmentations for 2008. In Figure 6.1 (c) the image is of notably lower quality with a higher presence of single pixel anomalies across the three wavelengths used to create the segmentation. The functioning of CHIMERA attempts to normalise its thresholds with respect to the average of each observing wavelength which may lead to a incorrect segmentation threshold. The three wavelengths used to create this image originate from the 171Å, 195Å, and 284Å passbands on-board SOHO. In 2008 SOHO had long outlived its lifetime and it is possible that its degradation has created these fuzzy observations.

To examine this hypothesis and estimate the reliability of CH segmentations for further work in this chapter, an investigation was performed on a single segmentation per year for the period 1998 to 2019. Figure 6.2 displays an array of yearly CH segmentations across the entirety of the investigate time range observed every June 1st. Segmentations are seen to perform well by CHIMERA for 1998 to 2005 and for 2010 to 2019. The worst identifications occur from 2006 to 2009, when the background tri-colour images have significant noise and the SOHO instrument is far past its expected lifetime. Segmentations rapidly improve in 2010 with the launch of the SDO instrument, whereby all following segmentations are performed on SDO images. To fix this issue, the CHIMERA algorithm must be recalibrated for poor quality SOHO era images and the data-set for 2006 to 2009. Due to the relatively short time scale this period covers being unlikely to affect the large scale statistics of CH properties and the time constraints on this structured PhD program, this recalibration and rerun will not be performed for the research present in this chapter. This research assumes segmentations for this period are reasonably accurate and the recalibration of CHIMERA will be performed in future work (see Chapter 7).

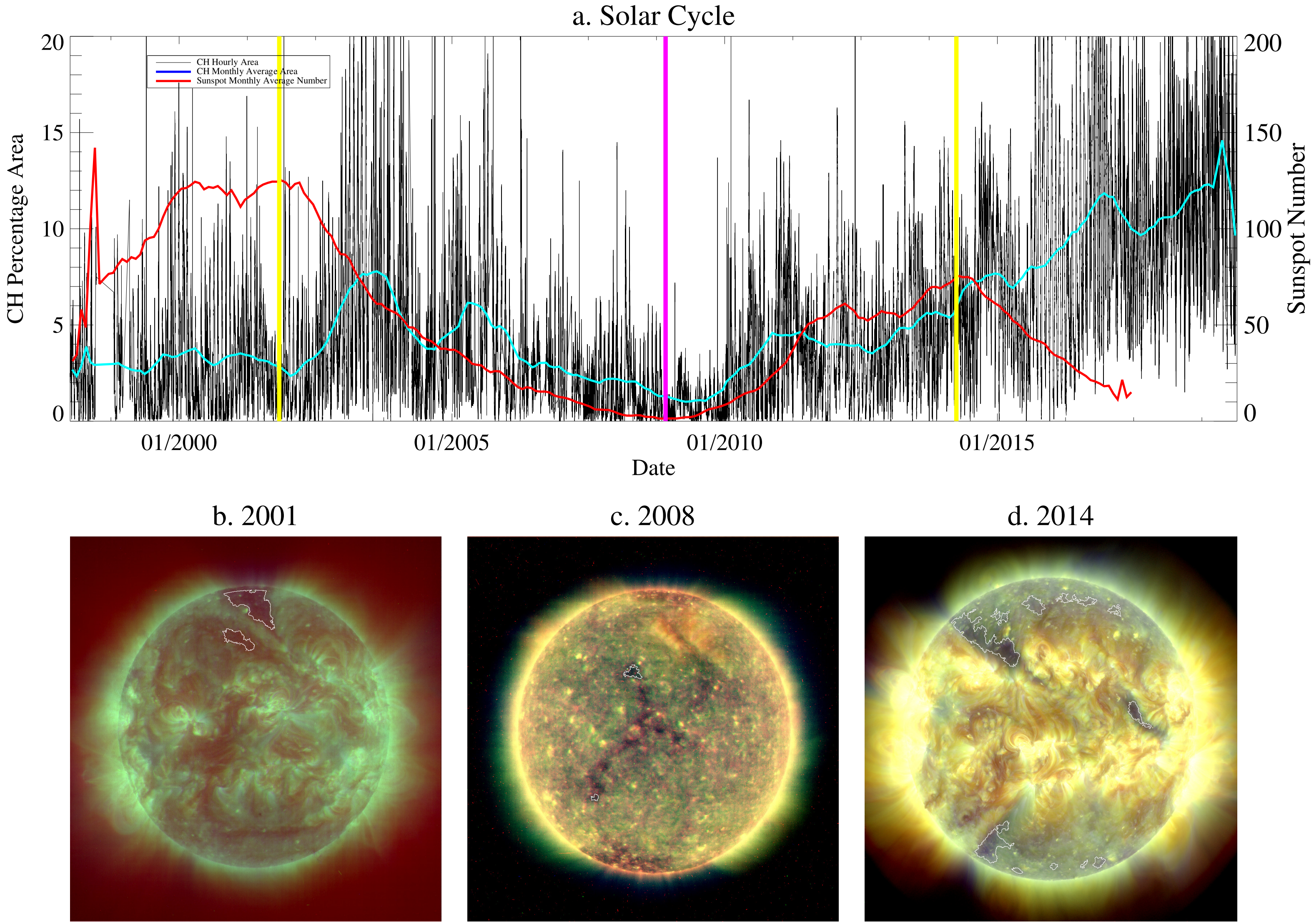

Figure 6.1: (Top) Hourly total CH Area (black) across two solar cycles from 1998-2019. The smoothed mean monthly area (light blue) and smoothed monthly sunspot number (light red) demonstrating the activity of the solar cycle are plotted for comparison. (Bottom) Three CH segmentation performed by CHIMERA for dates indicated in the top plot corresponding to solar maximum (yellow) and solar minimum (pink).

6.2 Statistical Properties of Coronal Holes

As mentioned in Chapter 4, CHIMERA extracts 17 unique physical and magnetic properties of CHs for correlation with the solar wind to gain a greater understanding of their connections. In Chapter 5 the correlation of CH geometric with solar wind properties is performed as an example of the possible undiscovered connections between the corona and solar wind. Here, an investigation is performed on the long-term variability and range of CH properties which can lead, through already established relationships, to predictive models for HSSW flows.

6.2.1 Geometric Properties

As discussed in Chapter 5, the areas of CHs have long been associated with the resulting HSSW velocity and the severity of space weather storms. Hence, an investigation into the range and distribution of CH areas across the solar cycle similarly renders the distribution of HSSW velocity and geomagnetic storm severity. Figure 6.3(a) presents the hourly distributions of CH area in percentiles of the solar disk and Figure 6.3(b) presents the same distribution in a semi-log space. To create a predictive model, it is important to fit this data-set with a probability distribution function (PDF). From the shape of the dataset, an exponential subset of the gamma probability distribution is judged by eye to be the best fit. This distribution is described by a PDF of the form:

$$PDF = \lambda e^{-\lambda x} \tag{6.1}$$

and a cumulative distribution function (CDF) of the form:

$$CDF = 1 - e^{-\lambda x} \tag{6.2}$$

where λ is a parameter which decides the shape of the distribution. Fitting the CH percentile area with this probability distribution renders a value for λ of 0.26, with a normalization factor such that:

$$N = 4.58 \times 10^{4} e^{(-0.26)A} \tag{6.3}$$

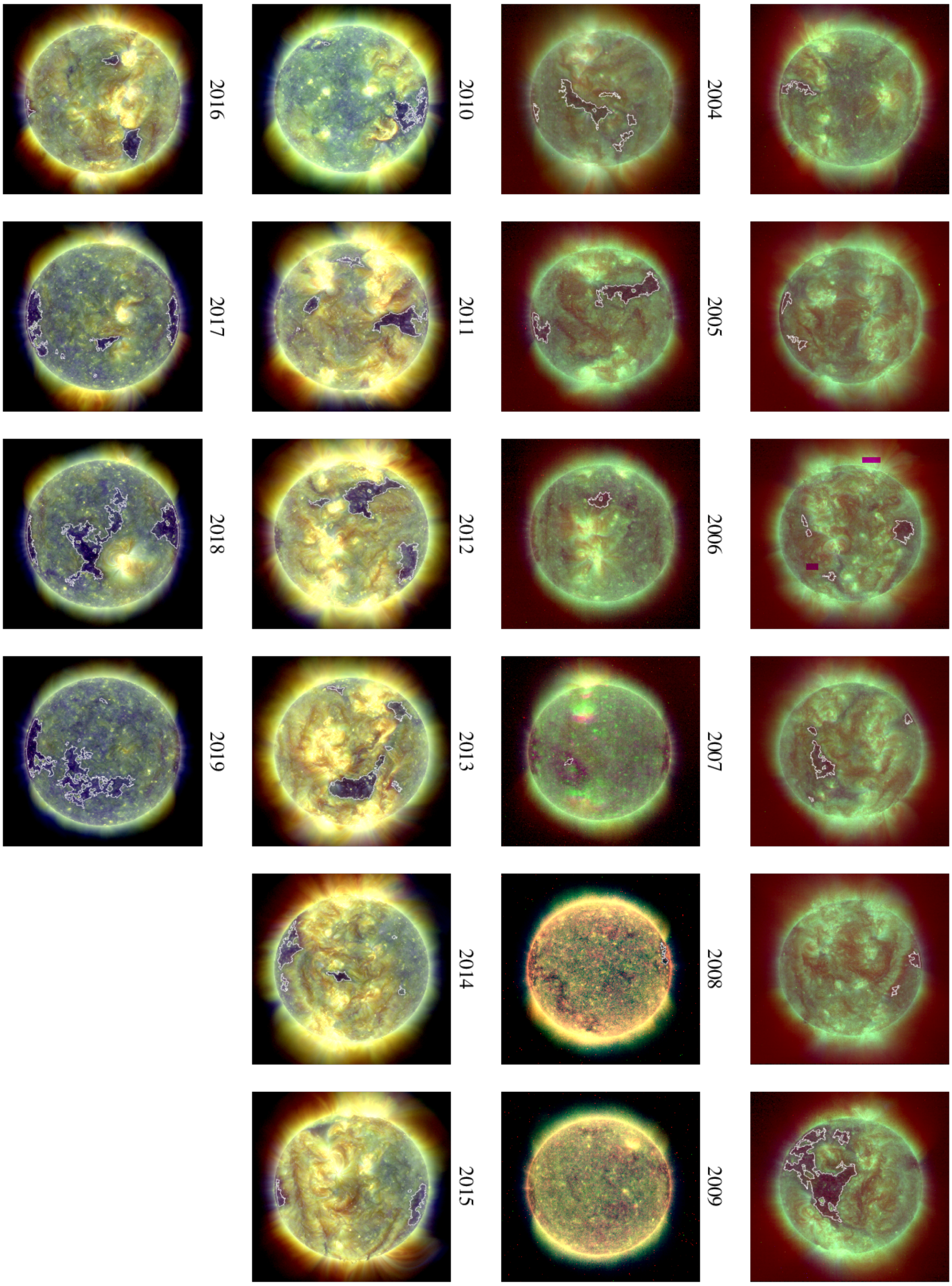

Figure 6.2: CHIMERA yearly segmentations between 1998 and 2019 observed on June, 1st.

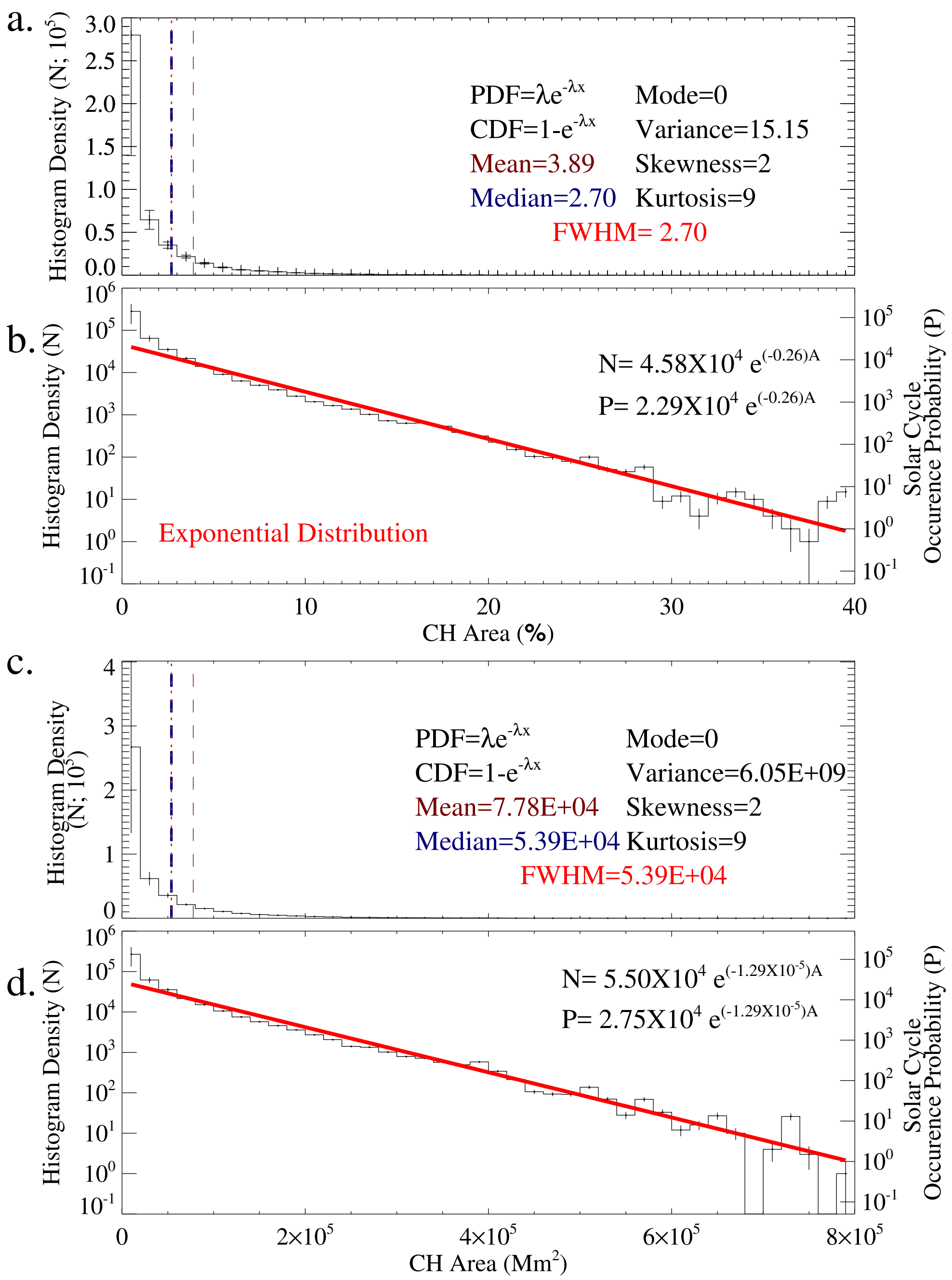

Figure 6.3: (a) Histogram of CH percentile areas across two solar cycles, from 1998 to 2019, with parameters calculates from an exponential distribution fit. (b) Log histogram of CH percentile areas for the same time frame as (a) with an exponential distribution fit. The displayed equations describe the exponential fit in terms of histogram Density (N) and of occurrence probability within a single solar cycle (P). Values of P above one estimate the number of CHs with a specific area that will occur within the solar cycle and values below one predict the probability of a specific CH area occurring during a given solar cycle. (c) Similar plot to (a) for reprojected CH area in Mm^2. (d) Similar plot to (b) for reprojected CH area in Mm^2.

where N is the histogram density of CH percentile areas, A, across two solar cycles. This function gives a simplified description of the distribution curve of CH percentile areas. By fitting this type of distribution, it is possible to estimate the mean, variance, skewness and kurtosis of the distribution which are indicated within Figure 6.3(a). For an exponential distribution, the mean is calculated as λ^{-1}, the variance is calculated as λ^{-2}, and both the skewness and kurtosis have established constant values of 2 and 9 respectively. This value of kurtosis is of interest due to it being greater than three as it implies this distribution is leptokurtic (i.e. the distribution has a fatter tail than a typical univariate normal distribution). This leptokurtic nature accounts for the relatively broad range of observed CHs Areas within a solar cycle. The distribution denotes a significant deviation of observations from the mean of 3.89%. To build a simple predictive model, this distribution can be normalised with respect to the solar cycle to obtain an estimate of solar cycle occurrence probability, P:

$$P = 2.29 \times 10^4 e^{(-0.26)A} \tag{6.4}$$

The function P describes the probability of a given CH area occurring within a given solar cycle from hourly observations. Hence a CH projected area of 20% is expected to be observed 126 times during a solar cycle. This function further allows the prediction of extreme events and their occurrence rate, such as a CH projected area of 50% with an occurrence probability of 0.05, indicating a CH of this size is expected to be observed once every 20 solar cycles, or approximately every 220 years. Notably, Equation 6.4 has non-zero probabilities for all positive potential CH areas, however the Sun has a limited restriction on surface area. For example, a CH percentile area of greater than 200%, covering the entirety of the front and back of the solar disk, is expected with a non-zero probability. Due to the physical spatial restrictions this is evidently impossible, thus some unknown maximum CH percentile area exists above which CHs cannot grow to.

Figure 6.3(c) and (d) illustrate similar distribution plots to (a) and (b) for CH reprojected area in megameters, respectively. These reprojection areas are the result of calculating the true surface area occupied by the CHs when the curvature of the Sun is accounted for. The distributions of CH reprojected areas are described by:

$$N = 5.5 \times 10^4 e^{(-1.29\times10^{-5})A} \tag{6.5}$$

$$P = 2.75 \times 10^4 e^{(-1.29\times10^{-5})A} \tag{6.6}$$

Distributions for CH area are very similar for both the disk projection and the reprojected area with significant differences only observed for large CH areas. The most significant difference in fits are within the power of the exponent. The reprojected area exponent is fractionally smaller, however, this is due to the different scale of units between percentile and megameter measurements. It is worth noting that the conclusions reached above are only from 22 years of observations, and are then normalised to occurrence probability per 11 years. Due to this short relative time-span and the variance observed from solar cycle to cycle, this predictive model should only be used for rough predictions of observations. A more robust predictive model would require a minimum of 10 solar cycles worth of observation, or 110 years, to accurately account for a linear covariant discrepancy between solar cycles. This time-span of observations does not exist due to CHs and the dynamics of the corona being a relatively new field of research. To build a truly accurate model for solar cycle predictions, newly made observations must be combined with this current model and continually updated for multiple solar cycles.

Figure 6.4 illustrates the distribution of CH widths across the time-span defined at the start of this chapter. Similar to Figure 6.3, Figure 6.4 is split into a normal space histogram (top) and a semilog space histogram (bottom). Figure 6.4(top) shows a high propensity for CHs to appear in sub 10° widths, with a peak observed at 5°, however the distribution is significantly tailed, with 95% of CHs occurring with widths less than 118°. This distribution can be described using a double log normal distribution of the form:

$$N = \frac{3.58 \times 10^4}{ln(\Delta\theta_{CH})} e^{\frac{-(ln(ln(\Delta\theta_{CH}))-0.65)^2}{0.35}} \tag{6.7}$$

The effects of log normal distributions are discussed in Diwakar (2017), and furthermore the effects of a double log normal distribution are discussed in Taagepera

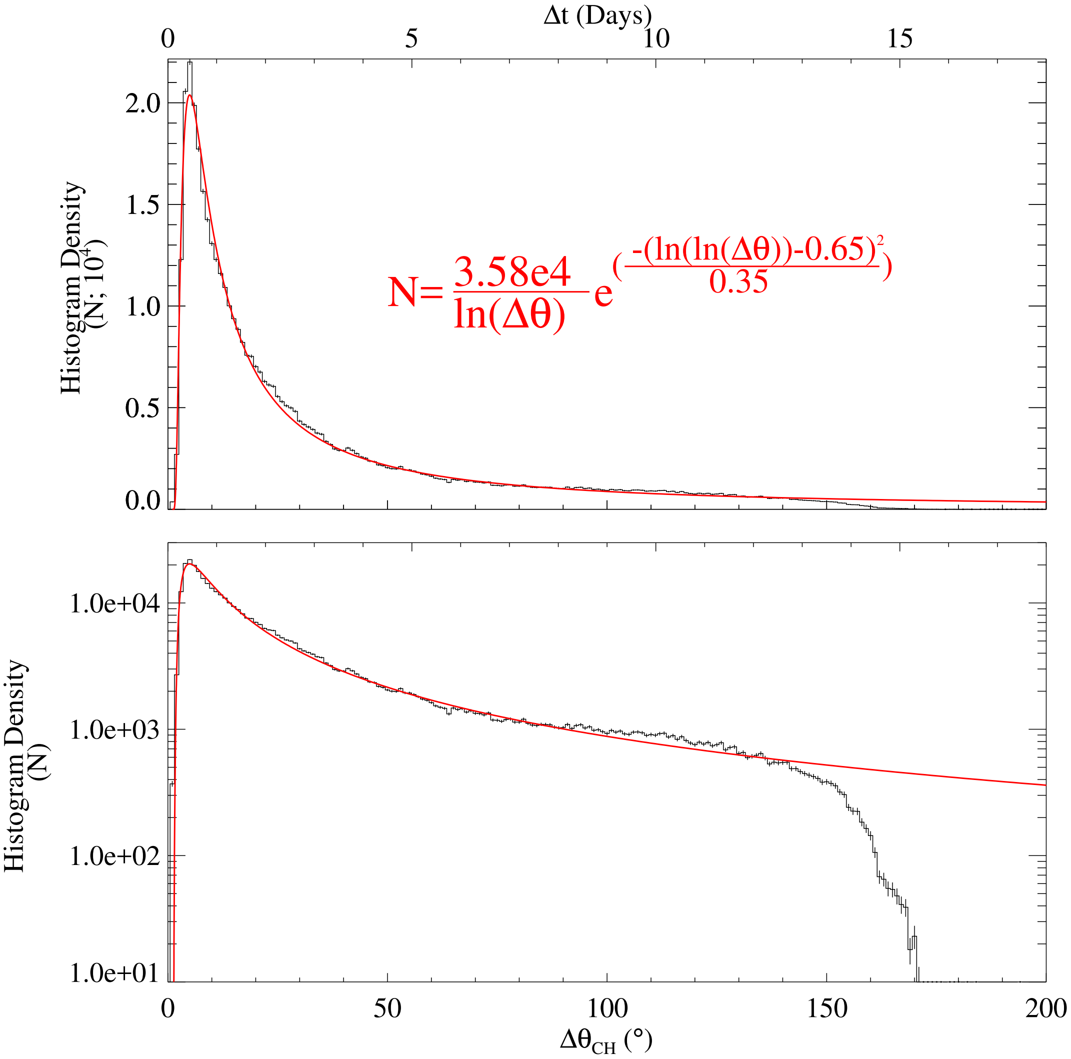

Figure 6.4: (Top) Histogram of CH widths ($\Delta\theta_{CH}$) observed across two solar cycles (black) with a double log normal distribution fit (red). (Bottom) Similar histogram to top displayed in a semilog space. Due to the relationship found in Chapter 5, measurements of CH width are also displayed in terms of expected associated HSSW stream duration (Δt).

(2008). In essence, a log normal distribution is bounded by a lower conceptual limit of zero, which when log transformed into a normal distribution becomes negative infinity. This negative infinity lower limit is a required feature for a normal distribution. A double log normal distribution contains a lower conceptual limit of one, which becomes zero under a log transformation. This distribution must undergo a second log transformation to obtain normality in its distribution. The double log normal distribution limit of 1 is physically consistent with the measured widths of CHs. For a CH to exist, it is required to have a lower limit of width. In this instance, the lower limit is created from the resolution and relative certainty of the CHIMERA segmentation algorithm and the relative wavelength resolutions it uses for segmentation. The conformity of the physical boundaries of CH structure with the statistical background of the double log normal distribution ensures this distribution is an accurate representation of the statistical and physical distribution of CH widths. The physical implications of this distribution are currently unknown. The use of double log normal distributions are a relatively new concept and a full analysis of physical implications of regular log normal distribution has been studied in depth across the sciences (Limpert *et al.*, 2001) but has still not reached a stage of completeness. Simply, CHs have a preferential existence within a 10° width. Furthermore, rarer, more extreme CHs have a significantly wider distribution than small CHs, lending to a more significant variation in resulting HSSW streams. This variation may account for the associated difficulty in constructing general solar wind predictive models.

Notably, an upper limit cut off exists in this CH width distribution which is clearly observed in the semi-log representation in Figure 6.4(bottom). This upper cut off approaches a limit of 180° for two reasons. Firstly, the CHIMERA algorithm calculates CH widths observed only on the side of the solar disk facing the Earth, with a limited field-of-view of 180°. This accounts for the sudden drop off of CH widths occurring between 150 - 180°, and subsequent bump above the double log normal distribution at ∼100°. Secondly, the solar magnetic field is limited to a dipolar magnetic field in its simplest form. The magnetic PIL in this form is not limited to the solar equator and can vary in latitude. For a simple magnetic field, this allows for an upper limit on similar magnetic polarity regions of 180°.

6.2.2 Magnetic Analysis

Investigations into the connections between HSSW properties and the magnetic structure of CHs are in their infancy. The presence of open magnetic fields governs the appearance of CH regions, however, no established connections exist between CH magnetic properties and associated HSSW properties. CHs with a high absolute magnetic polarity are assumed to generate higher speed solar wind streams than similarly sized but magnetically weaker CH regions. Here, a distribution of magnetic properties of CH regions is observed and described for future potential investigations into the magnetic correlation between CHs and the HSSW observed at Earth.

Figure 6.5 displays the variation of CH mean magnetic polarities across two solar cycles. Figure 6.5(a) illustrates the total magnetic polarity of on disk CH regions from 1998 to 2019. The sunspot cycle is overplotted on this time-line for reference to position along the solar cycle. From the investigation discussed in section 6.1, CH magnetic properties are unreliable between the range 2006 to 2009. However, outside of this range a possible pattern of variance exists. After the peak of the first displayed solar cycle (2005), the variation of the total mean magnetic field within coronal holes becomes more severe than after the second displayed solar maximum. Whether this variation in magnetic field is dependant on the relative severity of the previous solar maximum is unclear. However, the distribution of magnetic fields currently suggests such a dependence. The extremely significant difference in variation of magnetic polarities between solar cycles is likely due to the presence of more smaller CH regions occurring after the first presented solar cycle. For smaller CHs, the mean magnetic polarity is often observed to be higher due to the higher abundance of open magnetic field lines relative to closed field lines within the CH boundary. Notably, across the investigated time range the magnetic profile of CHs is concentrated around a magnetic polarity of $\sim$0 G, thus conserving magnetic polarity on the Sun.

Figure 6.5(b-d) illustrates the distribution of CH magnetic polarities across the entire time range, across 1998 to 2008, and across 2009 to 2019 respectively. Each of these distributions are double peaked with a significant dip in the presence of 0 G CHs, likely due to the inherent unipolar nature of CHs. It is however

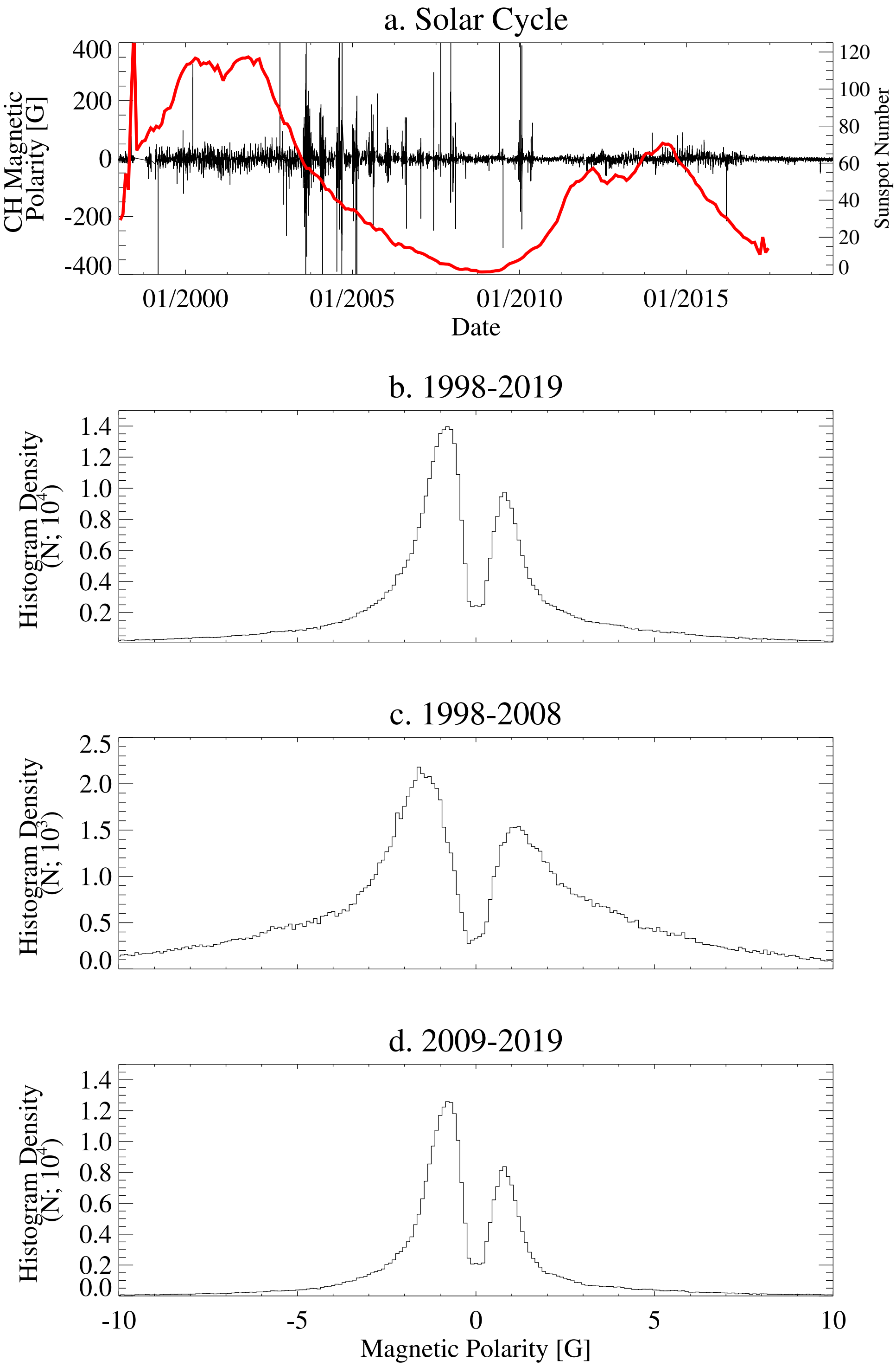

Figure 6.5: (a) Total hourly magnetic polarity of CH regions from 1998 to 2019 (black) compared to the sunspot number for the same period (red). (b) Distribution of mean magnetic polarity of CH regions across the full investigated time range. (c) Distribution of mean magnetic polarity of CH regions from 1998 to 2008. (d) Distribution of mean magnetic polarity of CH regions from 2009 to 2019.

possible this dip exists due to the magnetic selection criteria of the CHIMERA algorithm. The vast majority of CH polarities are concentrated within a range of $| < B > | \leq 10\ G$, thus agreeing with the expected magnetic profile of CHs outlined in Chapter 1. The distribution in (b) is semi-symmetrical about 0 G with two peaks existing at $\sim \pm 1$ G. A higher peaked distribution of negative polarity CHs is identifiable in the distribution, and similar behaviours are identified within Figure 6.5(c) and (d). Two primary differences are identifiable in (c) and (d), namely the different locations of peaks in the distributions and their relative amplitudes. Figure 6.5(c) exhibits lower amplitudes and two peaks at $\sim \pm 1.2$ G, which can be accounted for due to the lower relative abundance of MDI observations available per day than HMI provides for SDO. This lower abundance of observations creates a lower abundance of CH segmentations available within a period, hence affecting the distribution amplitude. Figure 6.5(d) exhibits two peaks located at $\sim \pm 0.8$ G. Despite its lower amplitude, the distribution in (c) demonstrates significant variance in magnetic polarities compared to (d) and has similarly higher peak values. This observation matches the differing variance with time observed in Figure 6.5(a).

Figure 6.6 demonstrates the distributions of some niche properties of CHs that are uniquely observed by the CHIMERA algorithm. Specifically, Figure 6.6 is divided into (a) distribution of mean negative and positive magnetic polarities for CHs, (b) similar distribution to (a) in a semi-log space, (c) distribution of the maximum and minimum magnetic polarities found within CH boundaries, and (d) similar distribution to (c) in a semi-log space. Figure 6.6(a) and (b) illustrate a complex structure for preferential magnetic balance within CHs. CHs have an overwhelming preference to balance their average positive and negative magnetic balance within an absolute range of < 10 G, with peaks at $\sim \pm 4$ G. A secondary peak is observed in these distributions in the $\pm 16 - 20$ G range. The physical mechanisms behind these apparent preferences are unclear, however it is more likely to observe CHs with mean absolute magnetic polarities within the 16-20 G range than in the 10-14 G range. Figure 6.6(c) and (d) exhibit a similarly peculiar distribution. The shape of this distribution, mirrored about its axis, is similar to the double log normal distribution observed in CH width distributions with a notable plateau at 50-100G. This plateau implies the mechanisms that govern

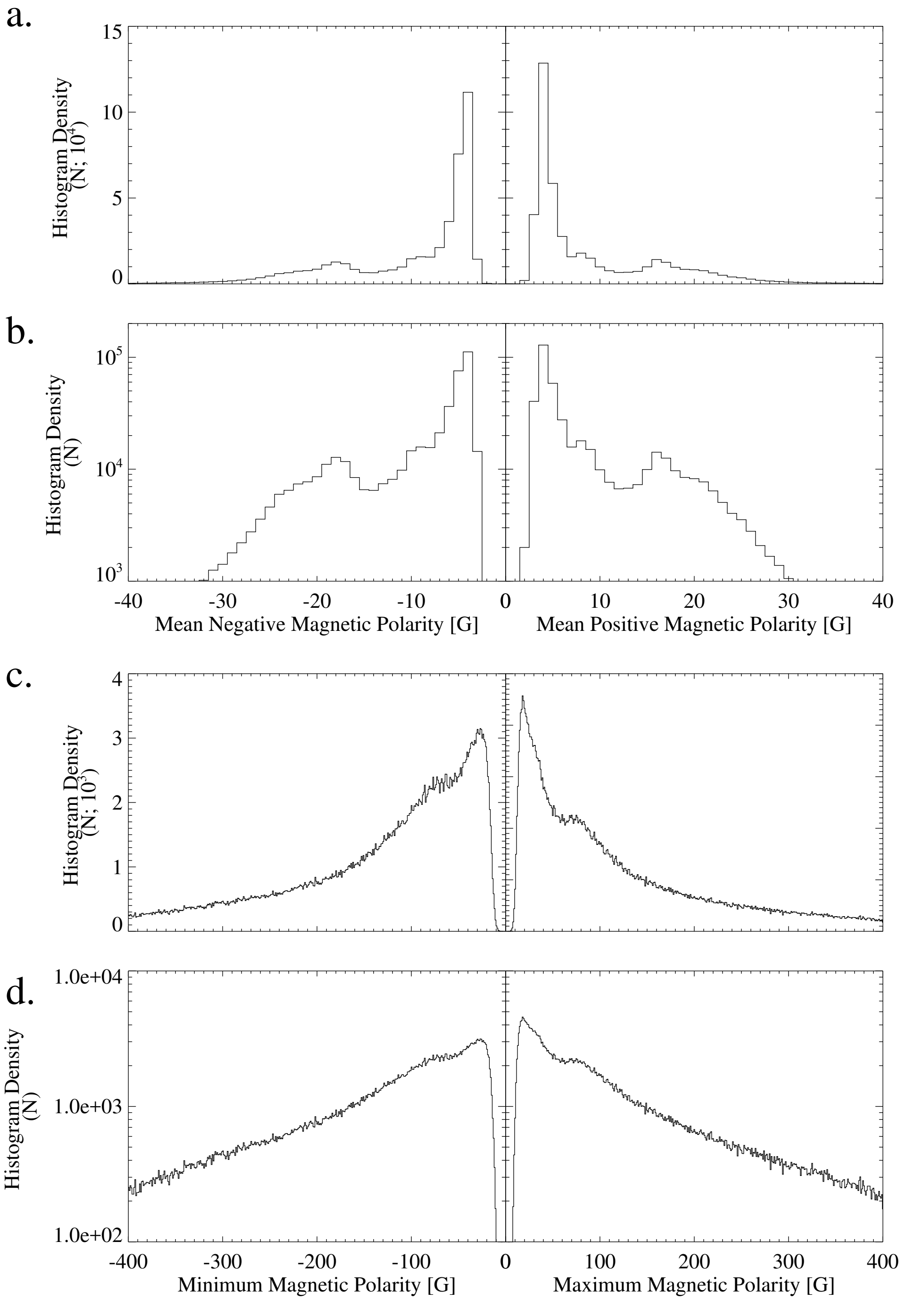

Figure 6.6: Distribution of magnetic structure within CHs observed from 1998 - 2019. (a) Distribution of mean negative and mean positive magnetic polarities within CH boundaries. (b) Similar distributions to (a) displayed in a semilog format. (c) Distribution of both minimum and maximum magnetic polarities within CH boundaries. (d) Similar distributions to (c) displayed in a semi-log format.

the maximum and minimum magnetic polarities within a CH are scale invariant within the 50-100 G range. However, the maximum polarity of a given CH is calculated as the maximum pixel value within the boundary and hence is subject to significant errors. Assuming these distributions are accurate, it is possible that these anomalies can be explained as two combined distributions for two potential types of CHs, such as polar and equatorial CHs.

6.2.3 Long-Term Spherical Harmonics in Coronal Hole Structure

Equatorial CHs are of particular interest to space weather forecasting due to their path of procession projecting a HSSW stream directly towards Earth. Multiple studies have been performed on this particular type of CH and their long term effects (Heidrich-Meisner *et al.*, 2017; Krista *et al.*, 2018). However an investigation into the prevalence of equatorial versus polar CHs with the solar cycle has yet to be performed. Figure 6.7 illustrates the average of area occupied by CH regions per year across the same time range as in Section 6.2.1. It is difficult to discern the prevalent structure of CHs from these images, however at solar maximum (2001 and 2014) they begin to exhibit a more stable preference for equatorial CHs which lasts into the solar minima (2008, and likely sometime in 2019 or 2020). Due to the poor representation of CH observations in the 2006 to 2009 range it is difficult to accurately estimate the structure of CH magnetic fields during solar minimum. From the observations of the current cycle using measurements from SDO (2010 to 2019) it is clear that CHs exhibit no locational preference on the solar disk in the inclining phase of the solar cycle (2010 to 2013). At solar maximum and thereafter (2014 and on) a significant preference in favour of equatorial CHs exist. On the approach to the current year, 2019, the CH areas begin to exhibit an even preference between equatorial and polar locations. Notably, in 2019, and possibly in 2018 a structure of a spherical harmonics becomes visible, namely a $l=2$ and $m=0$ Laplace spherical harmonic.

Figure 6.8 illustrates the average magnetic polarity of CH regions per year across the full 1998 to 2019 time range. Most notably within these images are the full magnetic polarity reversal that occurs between the two solar cycles, 22 year

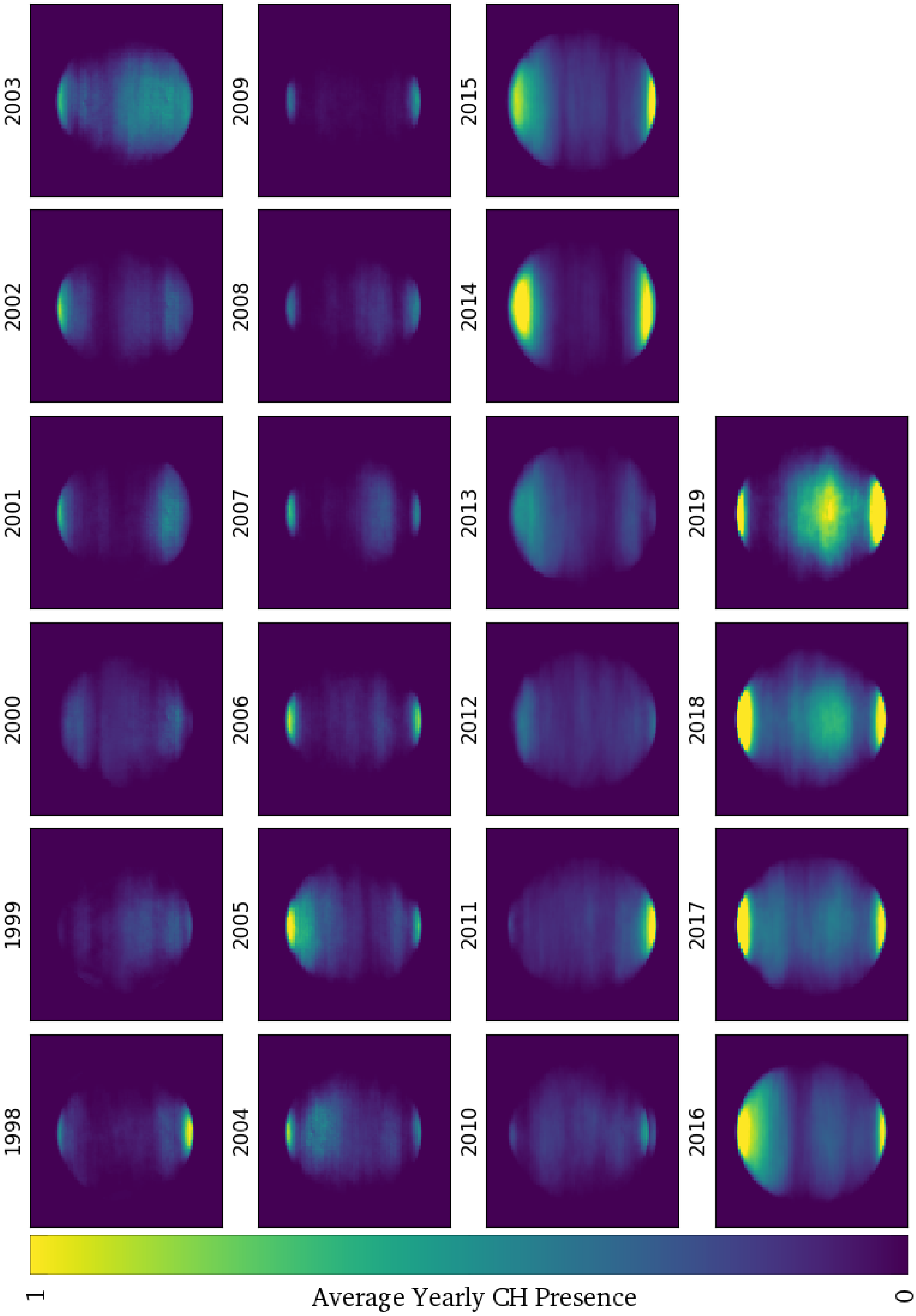

Figure 6.7: Long term structure of areas occupied by CHs.

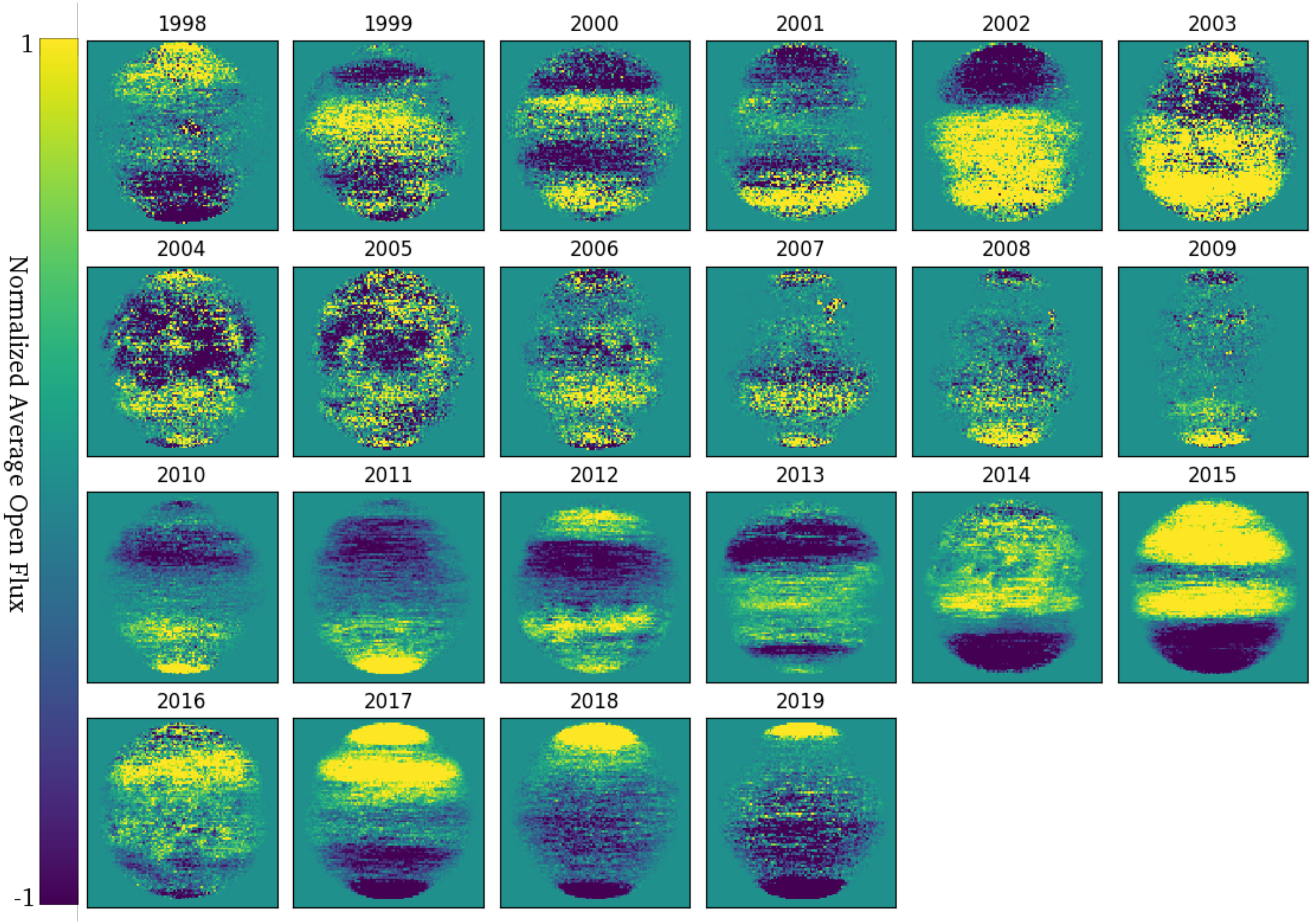

Figure 6.8: Long term structure of CH magnetic polarity.

period. Furthermore, observable within the magnetic structure are a repeated banding structure demonstrating a similar appearance to Laplace Spherical Harmonics. For example, 2000 and 2012 illustrate a similar, but polarity inverted, l=3, m=0 spherical harmonic. This structure is observed to extend into higher harmonic modes such as in 2017 with a m=0 and l=4, or l=5, spherical harmonic. Some years do not exhibit this structure, such as in 2004 and 2005. This discrepancy is possibly due to a $l \gg 1$ mode spherical harmonic not being easily represented in the data, or a $m \neq 0$ mode which, due to the rotational nature of the Sun, will not be properly averaged and represented in the images. Despite this potential misrepresentation, these plots demonstrate a well defined structure existing in the open magnetic field topology, and hence may render, from further analysis, a predictive model for the yearly structure of open magnetic field regions of the corona.

6.3 Machine Learning Predictions of Solar Wind Streams

The long term source of reliable, logically consistent segmentations of CHs created during this research has never been available before. The large sample size, which spans multiple solar cycles, enables a more complete estimation on the connection between CHs and their corresponding solar wind, thus enabling the construction of a robust model of solar wind prediction. The motivation for the creation of a ML approach to solar wind predictions is the vast improvement in accuracy that ML methods have over human constructed prediction models. Previous models have been constructed based on observations of CH boundaries that are either inaccurate, or do not remain logically consistent, hence adding a layer of noise into potential models. In this section, the long term CH segmentation data-set forms a large historical catalogue to construct a new ML solar wind prediction model based on CH occupation and location on the solar disk. These models are then compared to a 27-day recurrence/persistence model, which is selected as a benchmark result since it is regularly used by forecasters at the UK Met Office, it performs well despite its simplicity, and it produces relatively consistent predictions regardless

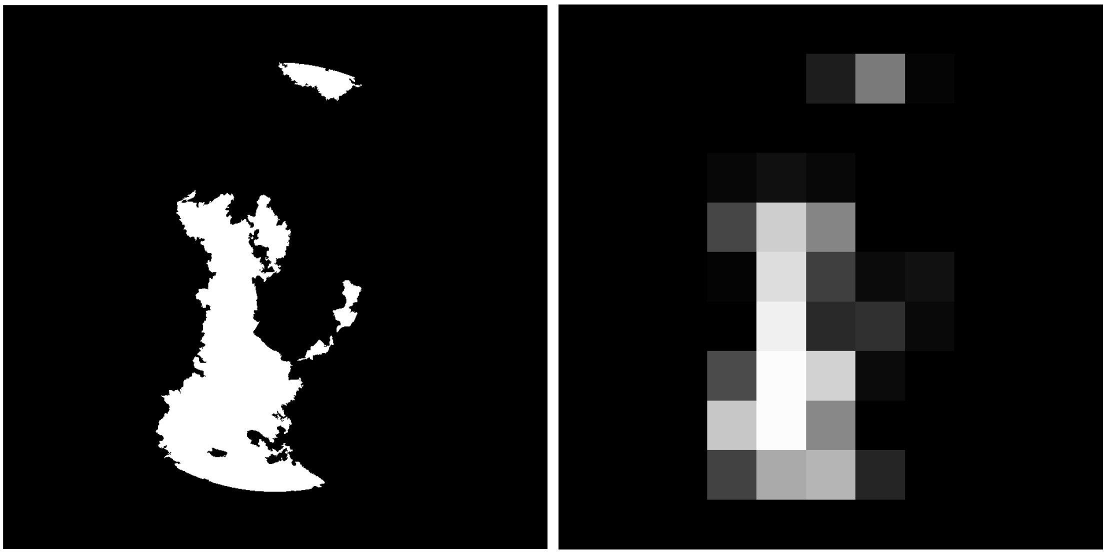

Figure 6.9: (Left) Original 4096×4096 resolution masks created from a CHIMERA segmentation for January 1st, 2017. (Right) Similar CHIMERA mask averaged to an 11×11 resolution for a reasonably sized input to an artificial neural network. Each macro-pixel is the average of all binary values of the pixels they encompass.

of period of the solar cycle. The operation of the 27-day persistence model is described as an estimation of solar wind speeds to be identical to those observed exactly one Carrington rotation (∼27 days) previous. This model is established to be accurate due to the relatively slow evolutionary timescale of CHs on the solar disk, as mentioned in Chapter 1.

For the ML methods described in Chapter 3, the high resolution masks, 4096×4096 pixels, created by CHIMERA are far too large to be used as input parameters to the majority of machine learning algorithms. This is due to the associated computational time required to sufficiently examine possible configurations of the constructed model for verification. To accommodate restrictions on computational time, the resolution of input CH masks are actively reduced to a simplified 11×11 mask, as illustrated in Figure 6.9. This decrease converts the binary pixels in the base CH mask to a collection of floating macropixels, where the value of a given macropixel is the average of all the binary pixels within its borders. This reduction of resolution drastically reduces a constructed models ability to identify subtle nuances in a given CH caused by its shape. However, the overarching structure of the solar wind is dependant on the large scale structure of the solar magnetic

Prediction models	Coherence	RMS	Prediction Efficiency
Persistance	0.52	93.7	-0.04
Linear Regression	0.48	89.3	0.21
Random Forest Regression	0.49	87.7	0.24
Artificial Neural Networks	0.55	79.0	0.25
Running ANN	0.59	77.4	0.28

Table 6.1: Evaluation of hourly solar wind forecasting performance comparing persistence model predictions to a number of ML predictive models.

fields.

Due to time constraints placed on this research, an examination of CHs and solar wind velocities was performed only for the years 2010 to 2018. This time range was separated into individual time ranges to be used in the construction of the predictive models. The data-set from 2010 to 2016 was randomly divided evenly into a training and test data-set. The 2017 and 2018 data-sets were kept as a form of validation set that the model would not get to observe during its construction. This separation is an established method in ML which prevents the constructed model from being validated against exact instances it has already observed (Shah, 2017). Doing so skews the accuracy of the model implying it is better in predictive cases than it truly is. Predictive measurements for the models used are available in Table 6.1 compared to predictive measurements for a persistence model. All models except the running ANN are described in detail in Chapter 3. A running ANN begins as a simple ANN, however, after each month of the validation set is predicted, the NN is then retrained to include the current month of solar wind measurements in order to improve the prediction for the following month. This method was used due to an observable decrease in prediction accuracy for dates significantly later than the end of the test and training set dates. This effect was likely due to the varying nature of the solar cycle creating an environment that the ML algorithm had never encountered before.

Three validation metrics were used in this work, namely: coherence, root mean squared (RMS), and prediction efficiency (PE). Each of these measurements of prediction describe a models accuracy with respect to a particular aspect of the observed measurements of solar wind velocity. Coherence is a measurement of consistency between the modelled and measured values of solar wind. A value of coherence describes the extent to which an observed measurement may be predicted from a model by an optimum linear least squares function. Values of coherence will always be $0 \leq \mathrm{C} \leq 1$, with values of one representing a good fit, and are calculated as:

$$C = \frac{\sum_{i=1}^{N}(m_i - <m>)(p_i - <p>)}{\sqrt{\sum_{i=1}^{N}(m_i - <m>)^2 \sum_{i=1}^{N}(p_i - <p>)^2}} \tag{6.8}$$

where m, p, i and N describe the measured values, predicted values, an index value, and the total number of index values respectively. RMS is a measurement of average difference observed between predicted and observed values. This prediction measurement value ranges from $0 \leq \mathrm{RMS} \leq \infty$, with lower values representing a more accurate fit, and is calculated as:

$$RMS = \sqrt{\frac{\sum_{i=1}^{N}(m_i - p_i)^2}{N}} \tag{6.9}$$

where variables have the same definition as Equation 6.8. Finally, PE is a measurement of how well a particular model represents a measured data-set compared to a simple average taken of the measured data-set. This measurement has a range of $-\infty \leq \mathrm{RMS} \leq 1$, where a fit of one is an accurate fit, and a fit of zero implies that the model is no better at predicting than a simple mean of the measured data. The PE is calculated as:

$$PE = 1 - \frac{\sum_{i=1}^{N}(m_i - p_i)^2}{\sum_{i=1}^{N}(m_i - <m>)^2} \tag{6.10}$$

where variables have the same definitions as Equation 6.8.

Table 6.1 shows a clear improvement in solar wind predictions from CH areas using ML methods. In this table, persistence models refer to a prediction of solar wind properties using the same measurements from a single Carrington rotation previous. This model has a high level of accuracy due to the relatively slow evolution of persistent governing creators of solar wind features, as described in Chapter 1. ML methods outperform persistence models in all utilised statistical measurements except coherence, however the ANN outperforms all other models in all three metrics. The relative improvements made from a ML method can be observed in Figure 6.10. This figure shows a comparison between a persistence model prediction (red) and its associated goodness of fit measurements to the running ANN model (blue) for the month of February, 2017. The running ANN visually and mathematically coheres more to the measured values of solar wind at L1 than the predictive model. The use of ANN methods of prediction come with an additional bonus of relative errors within the prediction which are highlighted using the blue band in Figure 6.10. These errors are calculated as the first sigma errors using Bayesian statistics on the range of predictive models created by the ANN.

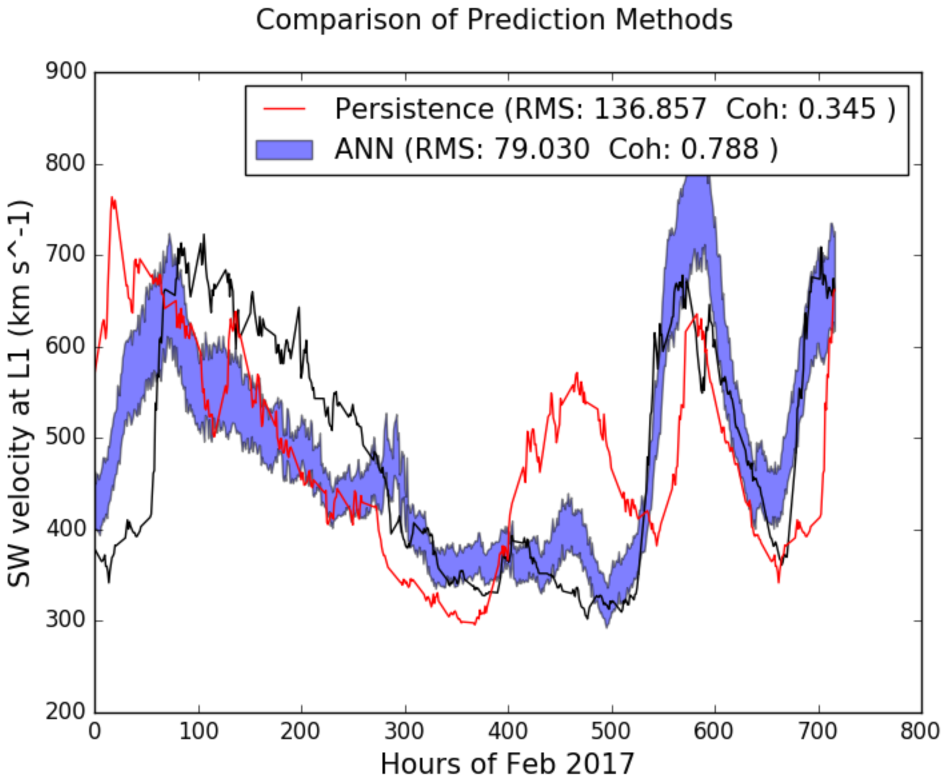

Figure 6.10: Comparison of Solar Wind Predictions at L1 from Persistence (red) and running ANN Methods (blue) for the month of February, 2017. The light blue areas of the predictive model are the first sigma Bayesian errors of the models predictions. Displayed in the top right corner are measurements of goodness of fit between the modelled and observed solar wind.

From this analysis, it is concluded that ML methods stand to make a significant improvement in the field of space weather forecasting. Furthermore, one such model has been created which outperforms one of the current benchmarks. However, this model has significant improvements that can be made to increase its accuracy. First, the training, test, and validation data-sets can and will be expanded to include the full range of CHIMERA segmentations from 1998 to 2019. Secondly, the use of a CNN would allow for the full 4096×4096 CHIMERA masks as input, and would build a model in a reasonable time. The use of this method will improve the accuracy of predictions as it will be able to use finer detail on CH areas to make predictions. Furthermore, the kernels used in CNN can identify other properties of the CHIMERA masks, such as texture, which may further improve the accuracy of the resulting predictive models.

7

Conclusions and Future Work

The research presented in this thesis represents significant advancements made in the field of both solar physics and space weather forecasting, some of which have been published in Garton *et al.* (2018a) and Garton *et al.* (2018b). To continually, quickly, and accurately identify and segment CHs from the surrounding corona, a new automated algorithm has been established and is regularly run at *solarmonitor.org/chimera*. New connections and correlations have been discovered between on disk CHs and the properties of the solar wind they produce. Furthermore, a mathematical relationship describing the expansion of the solar wind through interplanetary space has been derived. Finally, a long-term study on the variations of CHs and hence properties of their resulting solar winds have been examined and discussed. In this chapter, the products and results of this research are summarized and some potential future avenues of research to continue making improvements within the field are highlighted.

CHIMERA

Solar CHs are now being segmented real-time and their properties are being documented by the automated CHIMERA algorithm. This algorithm operates under a multi-thermal, tri-wavelength vector space segmentation method and is the first of its kind used in the field of space weather forecasting. Furthermore, the methodology of CHIMERA ensures it can be further applied to past and future EUV solar observatories to segment images. The algorithm has already been calibrated to operate on observations from both the SDO (171, 193, and 211 Å wavelengths) and the SOHO (171, 195, and 284 Å wavelengths) missions, and can be recalibrated to operate with the recently launched GOES-16 spacecraft mission which has an on-board EUV imager, the Solar Ultraviolet Imager (SUVI, Seaton & Darnel, 2018.). Data products from CHIMERA are stored and displayed at *solarmonitor.org*, ranging from segmented images and binary masks to measurements of magnetic polarity. The algorithm is run approximately four times per day on solarmonitor which has created a significant catalogue of all CHs within the SDO era. This will be continued in the future, and provides a temporal cadence significantly below the evolutionary timescale of CHs. This automated categorisation and documentation allows, for the first time, a true in-depth analysis of CHs and their relationships to space weather phenomenon. The products of CHIMERA are are assumed to be reliable due to the algorithms grounding in physical properties of CHs for its segmentations and the rigorous self validation CH candidates undergo. These products are currently used by scientists for solar analysis as well as by forecasters as part of their operational analysis.

Solar Wind Expansion

An analysis into some of the lesser studied properties of CH and their correlation with solar wind flows has been performed for the first time. This examination resulted in a correlation being found between CH width and the duration of HSSW streams observed at L1. Furthermore, a relationship was found between CH width and the maximum solar wind speed observed at L1, simple enough that rough predictions can be made by eye. This relationship outperformed predictions using the established area based predictive methods, that are pervasive in the field, for the 2016-2017 period. This analysis further rendered a derivation of both the longitudinal expansion of solar wind streams from the Sun to Earth, and the longitudinal expansions of CH magnetic flux tubes through interplanetary space. This derivation of longitudinal expansion of CH flux tubes is rather complex and hence was verified using the HELIO ballistic propagation model. Understanding of CHs, both as a physical phenomenon and a driver of space weather storms, is improved by these derived relationships. These new correlations further assist in the construction of accurate models of the solar wind for space weather forecasting and are useful as a tool for operational forecasters as a simple benchmark estimation of solar wind properties.

Long Term Coronal Hole Statistics

A long-term (22 years/2 solar cycles) analysis of CHs and their properties has been performed which provided the distributions and variances of CH properties. CH geometric properties were found to have relatively simply defined distributions. These distributions are of particular interest not only because they give insight into the preferential appearance of this particular feature, but they also estimate the occurrence probability of larger, more significant CHs. Furthermore, they can be transformed using equations discussed and derived in Chapter 5 to calculate the distribution of solar wind properties that are observed at L1.

Investigations into the distribution of magnetic properties of CHs observed a changing behaviour that appeared to be dependant on the intensity of the previous sunspot cycle. From the research on these long term segmentations an indication of possible spherical harmonics present within the magnetic polarity of CHs was found. This apparent appearance of spherical harmonics may be associated with similar patterns observed in Helioseismology, which could imply an innate connection between the transportation of acoustic and gravitational waves through the Sun with the overarching magnetic topology of the Sun. Furthermore, these spherical harmonics can assist in the predictions of formation of CHs on the solar disk, as well as their possible magnetic polarities which is not currently possible in operational forecasting.

Finally, this extensive catalogue of CH segmentations enables the construction of more accurate space weather models, particularly through the use of machine learning methods. This PhD research has created one such machine learning model in a pilot study using only segmentations from 2010 to 2018 for training, testing, and validation. These constructed models were found to outperform persistence models in the majority of model fitting measurements, with a running ANN performing best across all calculated measurements.

7.1 Future Work

The work presented in this thesis represents significant strides within the field of solar physics research, with the results also being useful in space weather forecasting. Many aspects of the research performed within can be further expanded, and new potential avenues of research in CH and solar wind prediction have become available due to this work.

Improvements in Feature Segmentation

Currently, CHIMERA operates and segments CHs based on commonly accepted properties, such as magnetic unipolarity and being expansive in surface area. However, research into CHs and their defining characteristics is still in its infancy. Therefore, new defining characteristics can be found and utilized as new limits within the algorithm at any given time. CHIMERA must remain updated with the newest physical understanding of CHs to remain at its peak competitive level. This includes converting the segmentation method from three 2D thresholds into a singular 3d or higher threshold. Furthermore, with the use of machine learning methods and the large catalogue of CHIMERA segmentations, a new machine learning based method can be created to automatically segment images of the solar corona, quicker and more accurately than the current model. This machine learning method can be further used to prove and quantify the advantages of multi-thermal/wavelength segmentations over currently popular single, or even dual wavelength segmentation methods. Finally, the method of physics based segmentations of CHs can be further applied to other solar features, such as active regions or prominences, to gain more accurate representation of properties for these features. These more accurate measurements can then be used to refine currently existing models of space weather and its drivers.

Connections between Solar Magnetic Fields and Helioseismology

The observations of spherical harmonics within CH magnetic fields is an entirely new discovery which has not previously been observed due to the lack of long term, high quality, consistent CH segmentations. However, there is still little understanding of their impacts and their drivers. The cause of these harmonics could be attributed to the global magnetic structure of the Sun during a given period. It is well accepted that the global magnetic field is governed by the internal dynamo of the Sun. Hence, these spherical harmonics become representations of the internal structure of the Sun and its convective motions during a given period. Investigations into this connection can give new potential insights into the yet unobserved internal structure of the Sun. Furthermore, the similarity between the global structure of these harmonics and spherical harmonics observed in gravity waves in Helioseismology, as modelled in Figure 7.1, can give further insight into the governing processes beneath the solar surface (McIntosh *et al.*, 2019).

If the spherical harmonics of CH magnetic fields and helioseismology gravity waves are correlated, it can imply a multitude of physical cases. Firstly, it is possible that both processes are governed by a tertiary process, such as the convective motion of ions in the convective zone both creating the magnetic solar dynamo and propagating helioseismic waves. Secondly, the global magnetic fields and hence the solar dynamo govern, through magnetic processes, subsurface convective motion, which in turn governs the propagation of helioseismic waves. Thirdly, the waves caused by helioseimic activity can cause perturbations within the solar dynamo, disrupting the motion of ions. This disruption can lead to the establishment of a new equilibrium state of the dynamo, which is represented in the global magnetic field. This gradual destabilisation could be responsible for the continual evolution of the global magnetic field of the Sun and the associated solar cycle. Finally, the global magnetic structure and the structure of helioseismic activity could be inducing one another, whereby magnetic reconnection creates helioseismic activity

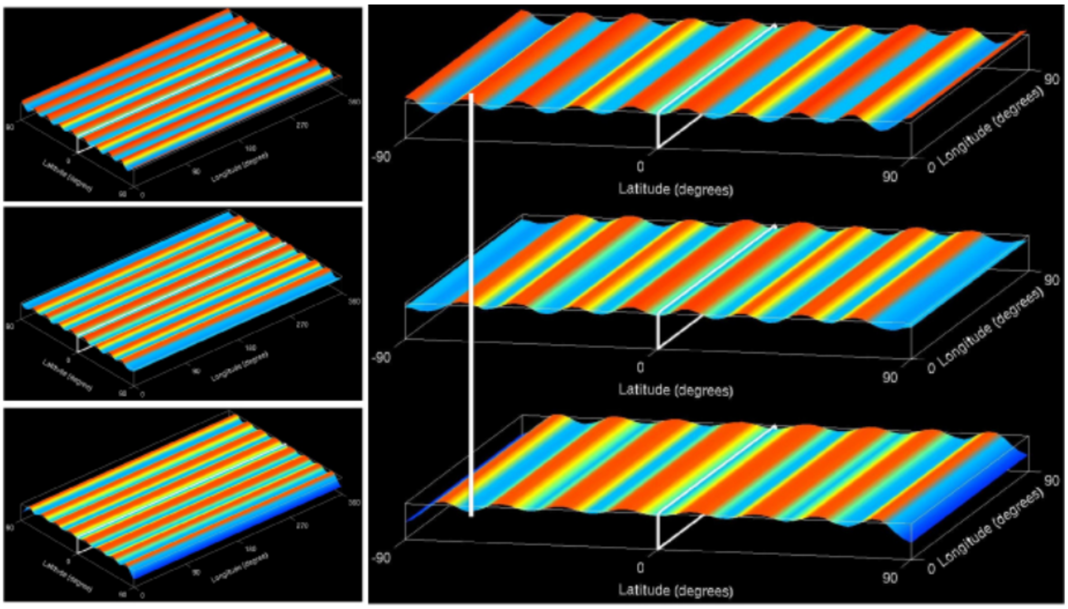

Figure 7.1: Gravity waves produced in a shallow-water (Matsuno, 1966; Pedlosky, 1982) tachocline model are shown in two perspective views taken from McIntosh *et al.* (2019). This illustrative case demonstrates the presence of large scale spherical harmonics in helioseismic gravity waves, with a similar modal structure to that found in Figure 6.8.

which in turn perturbs the solar dynamo, enabling further magnetic reconnections within the corona. This case creates an interesting symbiotic dependency between the solar dynamo and the convective motion of the solar subsurface, however it is important to note that each of these cases are currently wildly speculative. Hence, more research should be invested into studying this particular area to improve our knowledge of the internal solar structure, which can be further extrapolated to other celestial bodies.

Coronal Hole Forecasting

From the presence of these spherical harmonics it is possible to create a predictive model of CH appearance and its extent during a given period of the solar cycle. During a l=1, m=0 Laplacian spherical harmonics period, it is likely for the presence of two coronal holes located at the poles with extents below the solar magnetic equator. This simple case can be extrapolated for higher modes of spher-

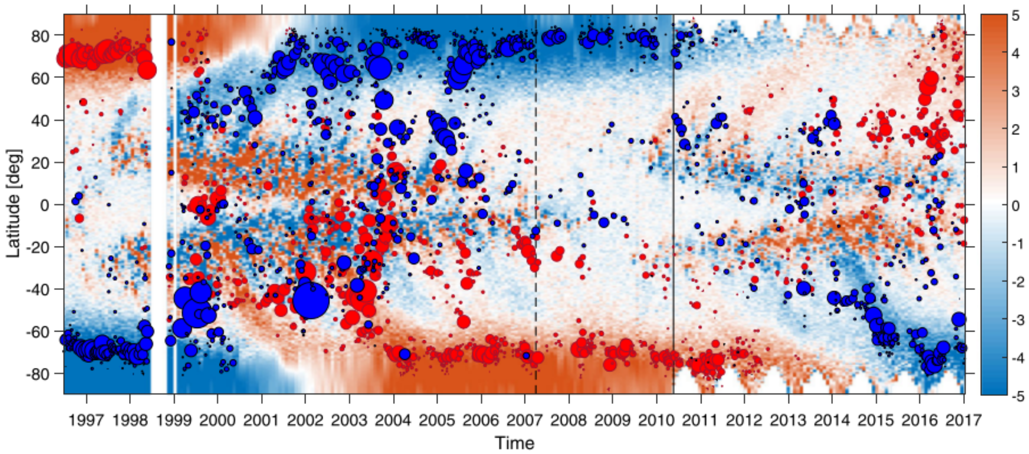

Figure 7.2: Comparison of CH properties (circles) to the average photospheric magnetic field intensity from Hamada *et al.* (2018). Circle size represents CH size on the solar surface and the colours red and blue describe the intensity of the magnetic field polarity, both positively and negatively respectively.

ical harmonics. A longer period of examination will be required to verify these observations across multiple solar cycles and from these observations the probable appearance of a CH can be quantified. If a pattern to the spherical harmonics is found a full solar cycle predictive model for CH appearance will be created, enabling the prediction of significant CHs and consequently significant space weather events, potentially multiple years before their occurrence. Figure 7.2 illustrates a comparison of CH properties relative to the average photospheric magnetic field structure across a 21 year period from Hamada *et al.* (2018). This research focuses on the centroid location and magnetic polarity of CHs but does not account for their large-scale structure and variation in time. To gain a more complete predictive model of CH appearance, a simple butterfly diagram which only considers the magnetic field structure within CH boundaries will enable identification of a global periodicity to CH appearance. If a predictable pattern is observable, as Figure 7.2 suggests, it then becomes possible to predict the appearance and properties of CH regions years before their actual appearance. Investigation into this avenue is of substantial importance due to the potential significant improvements to space weather forecasting it represents.

Further Correlating Coronal Holes and the Solar Wind

This PhD work has collected a large database of CH properties spanning a significant portion of time. These CH properties cover a wide range of both magnetic and physical properties that has never before been investigated. This thesis has merely scratched the surface on the potential connections between CH and their corresponding HSSW streams. A full scale investigation into each of these extracted properties and their correlations with the solar wind properties will improve our understanding of the underlying physical mechanisms in the solar wind and their dependencies. This improved understanding will ultimately lead to more accurate space weather forecasting which is increasingly important considering the ever increasing dependence of humanity on technology and the susceptibility of technology to space weather. Finally, given this significant catalogue of CH properties and already existing large catalogues of solar wind observations, the construction of a more accurate machine learning predictive model of the solar wind is possible. This machine learning model represents an improvement to the current state of the art that may be capable of identifying correlative properties that would be otherwise unidentifiable by humans and traditional methods. Furthermore, these models can be applied as real-time solar wind forecasts at solarmonitor.org. Hence, further research into the application of machine learning methods on space weather forecasting is essential to give new improvements to the field.

Automatic Space Weather Operations

Much of the work within this thesis has focused on the automation, or simplification of current methods of space weather forecasting. Although most operational centers still use a human as a final validator in predictions, improved automated methods ultimately provide an improved starting point for the forecasters. To ensure the legacy of this PhD research, all created models and datasets have been provided and reviewed online on SolarMonitor (data) and GitHub (code). The open source access to these models has encouraged collaborations with other scientists (with code peer-reviewed in the GitHub repository) in the field as well as providing access to useful tools for space weather forecasters, e.g. CHIMERA masks are now provided alongside detections after consutation with the Met Office space weather forecasters.

Since most modern models are designed to be self sufficient in data collection and processing, a fully automated coupled modelling system which sources observations of the Sun and the local space weather around Earth and then makes automated predictions of upcoming space weather represents a new stride in the field forecasting. Observations of the solar environment could be automatically input to a predictive model of the solar wind, which in turn can be input into further automated models to predict the severity of space weather effects, from ionospheric disturbances to geo-magnetically induced currents. This system can then provide predictions of solar wind streams and upcoming space weather storms to scientists and operational users hourly via the solarmonitor.org website, in a similar but fully automated method to the NOAA SWPC forecasts, as illustrated in Figure 7.3. It is planned to provide simple solar wind predictions based on the equations derived in Chapter 5 as well as other space weather prediction models, such as in McCloskey *et al.* (2018), alongside the current CHIMERA detections on the SolarMonitor platform in the near future.

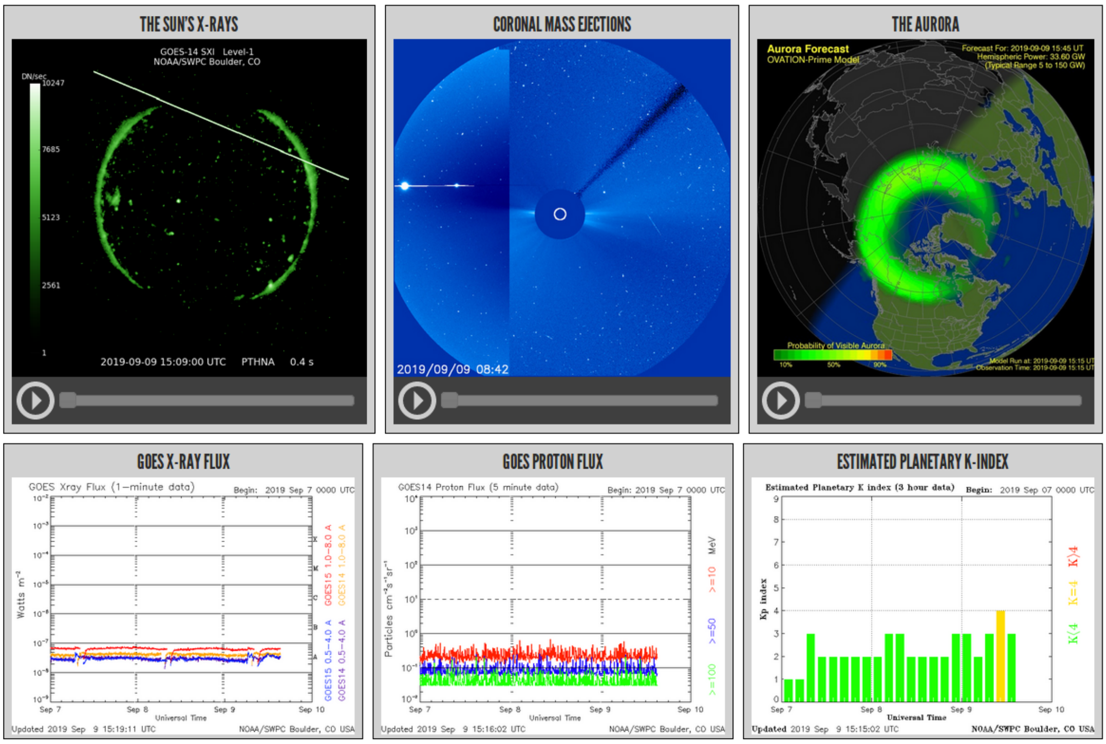

Figure 7.3: Example of data products supplied by the NOAA SWPC website illustrating real time observations paired with corresponding space weather forecasts.

References

Adelberger, E.G., García, A., Robertson, R.G.H., Snover, K.A., Balantekin, A.B., Heeger, K., Ramsey-Musolf, M.J., Bemmerer, D., Junghans, A., Bertulani, C.A., Chen, J.W., Costantini, H., Prati, P., Couder, M., Uberseder, E., Wiescher, M., Cyburt, R., Davids, B., Freedman, S.J., Gai, M., Gazit, D., Gialanella, L., Imbriani, G., Greife, U., Hass, M., Haxton, W.C., Itahashi, T., Kubodera, K., Langanke, K., Leitner, D., Leitner, M., Vetter, P., Winslow, L., Marcucci, L.E., Motobayashi, T., Mukhamedzhanov, A., Tribble, R.E., Nollett, K.M., Nunes, F.M., Park, T.S., Parker, P.D., Schiavilla, R., Simpson, E.C., Spitaleri, C., Strieder, F., Trautvetter, H.P., Suemmerer, K. & Typel, S. (2011). Solar fusion cross sections. II. The pp chain and CNO cycles. *Reviews of Modern Physics*, **83**, 195–246. (Cited on page 3.)

Aggarwal, C. (2018). *Neural Networks and Deep Learning: A Textbook*. Springer International Publishing. (Cited on page 71.)

Allen, R., Landi, E., Landini, M. & Bromage, G.E. (2000). An empirical test of different ionization balance calculations in an isothermal solar plasma. *Astronomy & Astrophysics*, **358**, 332–342. (Cited on page 7.)

Altschuler, M.D., Trotter, D.E. & Orrall, F.Q. (1972). Coronal Holes. *Solar Physics*, **26**, 354–365. (Cited on pages 51 and 62.)

Antiochos, S.K., Dahlburg, R.B. & Klimchuk, J.A. (1994). The magnetic field of solar prominences. *Astrophysical Journal Letters*, **420**, L41–L44. (Cited on page 13.)

Antiochos, S.K., Mikić, Z., Titov, V.S., Lionello, R. & Linker, J.A. (2011). A Model for the Sources of the Slow Solar Wind. *Astrophysical Journal*, **731**, 112. (Cited on pages 21 and 22.)

Antolin, P., Vissers, G. & Rouppe van der Voort, L. (2012). On-Disk Coronal Rain. *Solar Physics*, **280**, 457–474. (Cited on page 7.)

Antonucci, E., Dodero, M.A., Giordano, S., Krishnakumar, V. & Noci, G. (2004). Spectroscopic measurement of the plasma electron density and outflow velocity in a polar coronal hole. *Astronomy & Astrophysics*, **416**, 749–758. (Cited on page 75.)

Arge, C.N. & Pizzo, V.J. (2000). Improvement in the prediction of solar wind conditions using near-real time solar magnetic field updates. *Journal of Geophysical Research*, **105**, 10465–10480. (Cited on pages 60 and 64.)

Arge, C.N., Luhmann, J.G., Odstrcil, D., Schrijver, C.J. & Li, Y. (2004). Stream structure and coronal sources of the solar wind during the May 12th, 1997 CME. *Journal of Atmospheric and Solar-Terrestrial Physics*, **66**, 1295–1309. (Cited on page 65.)

Asai, A., Shibata, K., Hara, H. & Nitta, N.V. (2008). Characteristics of Anemone Active Regions Appearing in Coronal Holes Observed with the Yohkoh Soft X-Ray Telescope. *Astrophysical Journal*, **673**, 1188–1193. (Cited on page 18.)

Aschwanden, M.J. (2005). *Physics of the Solar Corona. An Introduction with Problems and Solutions (2nd edition)*. (Cited on pages 7 and 9.)

Aschwanden, M.J. (2019). *The Quiet-Sun Corona*. Springer International Publishing, Cham. (Cited on page 9.)

Avrett, E.H. (1990). Models of the solar photosphere. In J.O. Stenflo, ed., *Solar Photosphere: Structure, Convection, and Magnetic Fields*, 3–22, Springer Netherlands, Dordrecht. (Cited on page 5.)

Babcock, H.W. (1961). The Topology of the Sun's Magnetic Field and the 22-YEAR Cycle. *Astrophysical Journal*, **133**, 572. (Cited on pages 6 and 9.)

Bame, S.J., McComas, D.J., Barraclough, B.L., Phillips, J.L., Sofaly, K.J., Chavez, J.C., Goldstein, B.E. & Sakurai, R.K. (1992). The ULYSSES solar wind plasma experiment. *Astronomy & Astrophysics Supplemental*, **92**, 237–265. (Cited on page 63.)

Barra, V., Delouille, V. & Hochedez, J.F. (2008). Segmentation of extreme ultraviolet solar images via multichannel fuzzy clustering. *Advances in Space Research*, **42**, 917–925. (Cited on pages 52 and 55.)

Barra, V., Delouille, V., Kretzschmar, M. & Hochedez, J.F. (2009). Fast and robust segmentation of solar EUV images: algorithm and results for solar cycle 23. *Astronomy & Astrophysics*, **505**, 361–371. (Cited on page 55.)

Basu, S., Chaplin, W.J., Elsworth, Y., New, R. & Serenelli, A.M. (2009). Fresh Insights on the Structure of the Solar Core. *Astrophysical Journal*, **699**, 1403–1417. (Cited on page 3.)

Bevington, P.R. & Robinson, D.K. (2003). *Data reduction and error analysis for the physical sciences; 3rd ed.*. McGraw-Hill, New York, NY. (Cited on page 66.)

Biau, G. (2012). Analysis of a random forests model. *J. Mach. Learn. Res.*, **13**, 1063–1095. (Cited on page 69.)

Blake, S.P. (2018). *Modelling and Monitoring Geomagnetically Induced Currents in Ireland*. Ph.D. thesis. (Cited on page 30.)

Boerner, P., Edwards, C., Lemen, J., Rausch, A., Schrijver, C., Shine, R., Shing, L., Stern, R., Tarbell, T., Title, A., Wolfson, C.J., Soufli, R., Spiller, E., Gullikson, E., McKenzie, D., Windt, D., Golub, L., Podgorski, W., Testa, P. & Weber, M. (2012). Initial Calibration of the Atmospheric Imaging Assembly (AIA) on the Solar Dynamics Observatory (SDO). *Solar Physics*, **275**, 41–66. (Cited on page 40.)

Bohlin, J.D. (1977). Extreme-ultraviolet observations of coronal holes. I: Locations, sizes and evolution of coronal holes, June 1973 - January 1974. *Solar Physics*, **51**, 377–398. (Cited on page 18.)

Boucheron, L.E., Valluri, M. & McAteer, R.T.J. (2016). Segmentation of Coronal Holes Using Active Contours Without Edges. *Solar Physics*, **291**, 2353–2372. (Cited on page 57.)

Breiman, L. (2001). Random forests. *Machine Learning*, **45**, 5–32. (Cited on page 69.)

Brekke, P., Hassler, D.M. & Wilhelm, K. (1997a). Doppler Shifts in the Quiet-Sun Transition Region and Corona Observed with SUMER on SOHO. *Solar Physics*, **175**, 349–374. (Cited on page 10.)

Brekke, P., Kjeldseth-Moe, O., Brynildsen, N., Maltby, P., Haugan, S.V.H., Harrison, R.A., Thompson, W.T. & Pike, C.D. (1997b). Flows and Dynamics in the Corona Observed with the Coronal Diagnostic Spectrometer (cds). *Solar Physics*, **170**, 163–177. (Cited on page 10.)

Brooks, D.H., Ugarte-Urra, I. & Warren, H.P. (2015). Full-Sun observations for identifying the source of the slow solar wind. *Nature Communications*, **6**, 5947. (Cited on page 22.)

Brueckner, G.E., Howard, R.A., Koomen, M.J., Korendyke, C.M., Michels, D.J., Moses, J.D., Socker, D.G., Dere, K.P., Lamy, P.L., Llebaria, A., Bout, M.V., Schwenn, R., Simnett, G.M., Bedford, D.K. & Eyles, C.J. (1995). The Large Angle Spectroscopic Coronagraph (LASCO). *Solar Physics*, **162**, 357–402. (Cited on page 24.)

Cameron, R.H., Dikpati, M. & Brandenburg, A. (2017). The global solar dynamo. *Space Science Reviews*, **210**, 367–395. (Cited on page 11.)

Carrington, R.C. (1859). Description of a Singular Appearance seen in the Sun on September 1, 1859. *Monthly Notices of the Royal Astronomical Society*, **20**, 13–15. (Cited on page 2.)

Case, N. (2014). *Solar Wind-Magnetosphere Interactions: A Statistical Analysis of Spacecraft Measurements*. Ph.D. thesis. (Cited on page 27.)

Chamberlain, J.W. (1961). *Physics of the aurora and airglow*. (Cited on page 29.)

Chapman, S. & Zirin, H. (1957). Notes on the Solar Corona and the Terrestrial Ionosphere. *Smithsonian Contributions to Astrophysics*, **2**, 1. (Cited on page 18.)

Charbonneau, P. (2010). Dynamo Models of the Solar Cycle. *Living Reviews in Solar Physics*, **7**, 3. (Cited on page 9.)

Christensen-Dalsgaard, J., Gough, D.O. & Thompson, M.J. (1991). The depth of the solar convection zone. *Astrophysical Journal*, **378**, 413–437. (Cited on page 4.)

Cid, C., Palacios, Judith, Saiz, Elena, Guerrero, Antonio & Cerrato, Yolanda (2014). On extreme geomagnetic storms. *J. Space Weather Space Clim.*, **4**, A28. (Cited on page 31.)

Cliver, Edward W. & Dietrich, William F. (2013). The 1859 space weather event revisited: limits of extreme activity. *J. Space Weather Space Clim.*, **3**, A31. (Cited on page 13.)

Coleman, P.J., Jr. (1968). Turbulence, Viscosity, and Dissipation in the Solar-Wind Plasma. *Astrophysical Journal*, **153**, 371. (Cited on page 21.)

Cox, A. (1973). *Plate Tectonics and Geomagnetic Reversals: Readings, Selected, Edited, and with Introduction*. Series of books in geology, W.H. Freeman. (Cited on page 26.)

Cramer, J. (2002). The Origins of Logistic Regression. Tinbergen Institute Discussion Papers 02-119/4, Tinbergen Institute. (Cited on page 66.)

Cranmer, S.R. (2002a). Coronal holes and the high-speed solar wind. *Space Science Reviews*, **101**, 229–294. (Cited on pages 22, 75, 92, 105 and 111.)

Cranmer, S.R. (2002b). *Solar wind acceleration in coronal holes*, vol. 508 of *ESA Special Publication*. Wilson, A. (Cited on page 22.)

Cranmer, S.R. (2009). Coronal Holes. *Living Reviews in Solar Physics*, **6**. (Cited on pages 14, 15, 18, 75, 105 and 125.)

Cranmer, S.R. & van Ballegooijen, A.A. (2005). On the Generation, Propagation, and Reflection of Alfvén Waves from the Solar Photosphere to the Distant Heliosphere. *Astrophysical Journal Supplemental Series*, **156**, 265–293. (Cited on pages 16 and 17.)

Cushman, G.W. & Rense, W.A. (1976). Evidence of outward flow of plasma in a coronal hole. *Astrophysical Journal Letters*, **207**, L61. (Cited on page 10.)

David, C., Gabriel, A.H., Bely-Dubau, F., Fludra, A., Lemaire, P. & Wilhelm, K. (1998). Measurement of the electron temperature gradient in a solar coronal hole. *Astronomy & Astrophysics*, **336**, L90–L94. (Cited on page 16.)

de Jager, C. (1965). The solar photosphere. In J. Ortner & H. Maseland, eds., *Introduction to Solar Terrestrial Relations*, 13–25, Springer Netherlands, Dordrecht. (Cited on page 5.)

Delaboudinière, J.P., Artzner, G.E., Brunaud, J., Gabriel, A.H., Hochedez, J.F., Millier, F., Song, X.Y., Au, B., Dere, K.P., Howard, R.A., Kreplin, R., Michels, D.J., Moses, J.D., Defise, J.M., Jamar, C., Rochus, P., Chauvineau, J.P., Marioge, J.P., Catura, R.C., Lemen, J.R., Shing, L., Stern, R.A., Gurman, J.B., Neupert, W.M., Maucherat, A., Clette, F., Cugnon, P. & van Dessel, E.L. (1995). EIT: Extreme-Ultraviolet Imaging Telescope for the SOHO Mission. *Solar Physics*, **162**, 291–312. (Cited on pages 44, 45 and 47.)

Delouille, V., Mampaey, B., Verbeeck, C. & de Visscher, R. (2012). The SPOCA-suite: a software for extraction and tracking of Active Regions and Coronal Holes on EUV images. *arXiv e-prints*. (Cited on pages 31, 55 and 56.)

Diwakar, R. (2017). An evaluation of normal versus lognormal distribution in data description and empirical analysis. *Practical Assessment, Research and Evaluation*, **22**, 1–15. (Cited on page 137.)

Domingo, V., Fleck, B. & Poland, A.I. (1995). The SOHO Mission: an Overview. *Solar Physics*, **162**, 1–37. (Cited on pages 43 and 44.)

Dormy, E. (2006). The origin of the earth's magnetic field: Fundamental or environmental research? *Europhysics News*, **37**, 22–25. (Cited on page 26.)

Doschek, G.A., Warren, H.P., Laming, J.M., Mariska, J.T., Wilhelm, K., Lemaire, P., Schühle, U. & Moran, T.G. (1997). Electron Densities in the Solar Polar Coronal Holes from Density-Sensitive Line Ratios of Si VIII and S X. *Astrophysical Journal Letters*, **482**, L109–L112. (Cited on pages 16 and 75.)

Eastwood, J., Biffis, E., Hapgood, M., Green, L., M. Bisi, M., D. Bentley, R., Wicks, R., McKinnell, L.A., Gibbs, M. & Burnett, C. (2017). The economic impact of space weather: Where do we stand?: The economic impact of space weather. *Risk Analysis*, **37**. (Cited on pages 29 and 31.)

Eastwood, J.P., Hietala, H., Toth, G., Phan, T.D. & Fujimoto, M. (2015). What controls the structure and dynamics of earth's magnetosphere? *Space Science Reviews*, **188**, 251–286. (Cited on page 27.)

Faraday, M. (1832). Experimental Researches in Electricity. *Philosophical Transactions of the Royal Society of London Series I*, **122**, 125–162. (Cited on page 28.)

Feldman, U., Doschek, G.A., Mariska, J.T., Bhatia, A.K. & Mason, H.E. (1978). Electron densities in the solar corona from density-sensitive line ratios in the N I isoelectronic sequence. *Astrophysical Journal*, **226**, 674–678. (Cited on page 7.)

Feldman, W.C., Asbridge, J.R., Bame, S.J. & Gosling, J.T. (1976). High-speed solar wind flow parameters at 1 AU. *Journal of Geophysical Research*, **81**, 5054–5060. (Cited on page 63.)

Finlay, C.C., Maus, S., Beggan, C.D., Bondar, T.N., Chambodut, A., Chernova, T.A., Chulliat, A., Golovkov, V.P., Hamilton, B., Hamoudi, M., Holme, R., Hulot, G., Kuang, W., Langlais, B., Lesur, V., Lowes, F.J., Lühr, H., MacMillan, S., Mandea, M., McLean, S., Manoj, C., Menvielle, M., Michaelis, I., Olsen, N., Rauberg, J., Rother, M., Sabaka, T.J., Tangborn, A., Tøffner-Clausen, L., Thébault, E., Thomson, A.W.P., Wardinski, I., Wei, Z. & Zvereva, T.I. (2010). International Geomagnetic Reference Field: the eleventh generation. *Geophysical Journal International*, **183**, 1216–1230. (Cited on page 26.)

Fisk, L.A. (2003). Acceleration of the solar wind as a result of the reconnection of open magnetic flux with coronal loops. *Journal of Geophysical Research (Space Physics)*, **108**, 1157. (Cited on page 21.)

Fletcher, L., Dennis, B.R., Hudson, H.S., Krucker, S., Phillips, K., Veronig, A., Battaglia, M., Bone, L., Caspi, A., Chen, Q., Gallagher, P., Grigis, P.T., Ji, H., Liu, W., Milligan, R.O. & Temmer, M. (2011). An Observational Overview of Solar Flares. *Space Science Reviews*, **159**, 19–106. (Cited on page 11.)

Fossat, E., Boumier, P., Corbard, T., Provost, J., Salabert, D., Schmider, F.X., Gabriel, A.H., Grec, G., Renaud, C., Robillot, J.M., Roca-Cortés, T., Turck-Chièze, S., Ulrich, R.K. & Lazrek, M. (2017). Asymptotic g modes: Evidence for a rapid rotation of the solar core. *Astronomy & Astrophysics*, **604**, A40. (Cited on page 4.)

García, R.A., Turck-Chièze, S., Jiménez-Reyes, S.J., Ballot, J., Pallé, P.L., Eff-Darwich, A., Mathur, S. & Provost, J. (2007). Tracking solar gravity modes: The dynamics of the solar core. *Science*, **316**, 1591–1593. (Cited on page 4.)

Garton, T.M., Gallagher, P.T. & Murray, S.A. (2018a). Automated coronal hole identification via multi-thermal intensity segmentation. *Journal of Space Weather and Space Climate*, **8**, A02. (Cited on pages 32, 75, 80 and 153.)

Garton, T.M., Murray, S.A. & Gallagher, P.T. (2018b). Expansion of High-speed Solar Wind Streams from Coronal Holes through the Inner Heliosphere. *Astrophysical Journal Letters*, **869**, L12. (Cited on pages 32, 105 and 153.)

Gold, T. & Hoyle, F. (1960). On the origin of solar flares. *Monthly Notices of the Royal Astronomical Society*, **120**, 89. (Cited on page 11.)

Gonzalez, R.C. & Woods, R.E. (2006). *Digital Image Processing (3rd Edition)*. Prentice-Hall, Inc., Upper Saddle River, NJ, USA. (Cited on pages 76, 78 and 79.)

Grolier (1998). *The New Book of Popular Science.*. Grolier Society Inc., New York. (Cited on page 3.)

Hamada, A., Asikainen, T., Virtanen, I. & Mursula, K. (2018). Automated Identification of Coronal Holes from Synoptic EUV Maps. *Solar Physics*, **293**, 71. (Cited on page 159.)

Hassler, D.M., Rottman, G.J. & Orrall, F.Q. (1991). Systematic radial flows in the chromosphere, transition region, and corona of the quiet sun. *Astrophysical Journal*, **372**, 710–718. (Cited on page 10.)

Hassler, D.M., Dammasch, I.E., Lemaire, P., Brekke, P., Curdt, W., Mason, H.E., Vial, J.C. & Wilhelm, K. (1999). Solar Wind Outflow and the Chromospheric Magnetic Network. *Science*, **283**, 810. (Cited on page 22.)

Hayakawa, H., Ebihara, Y., Hand, D.P., Hayakawa, S., Kumar, S., Mukherjee, S. & Veenadhari, B. (2018). Low-latitude Aurorae during the Extreme Space Weather Events in 1859. *Astrophysical Journal*, **869**, 57. (Cited on page 29.)

Hayes, L.A. (2019). *Quasi-Periodic Pulsations in Solar Flares and the Earth's Ionosphere*. Ph.D. thesis. (Cited on page 12.)

Hayes, L.A., Gallagher, P.T., McCauley, J., Dennis, B.R., Ireland, J. & Inglis, A. (2017). Pulsations in the earth's lower ionosphere synchronized with solar flare emission. *Journal of Geophysical Research: Space Physics*, **122**, 9841–9847. (Cited on page 29.)

Heber, B., Sanderson, T. & Zhang, M. (1999). Corotating interaction regions. *Advances in Space Research*, **23**, 567 – 579, the Transport of Galactic and Anomalous Cosmic Rays in the Heliosphere: Observations, Simulations and Theory. (Cited on page 23.)

Heidrich-Meisner, V., Peleikis, T., Kruse, M., Berger, L. & Wimmer-Schweingruber, R.F. (2017). Evolution of an equatorial coronal hole structure and the released coronal hole wind stream: Carrington rotations 2039 to 2050. *Astronomy & Astrophysics*, **603**, A84. (Cited on page 144.)

Hickmann, K.S., Godinez, H.C., Henney, C.J. & Arge, C.N. (2015). Data Assimilation in the ADAPT Photospheric Flux Transport Model. *Solar Physics*, **290**, 1105–1118. (Cited on page 65.)

Higgins, P.A., Gallagher, P.T., McAteer, R.T.J. & Bloomfield, D.S. (2011). Solar magnetic feature detection and tracking for space weather monitoring. *Advances in Space Research*, **47**, 2105–2117. (Cited on page 96.)

Hofmeister, S.J., Veronig, A., Temmer, M., Vennerstrom, S., Heber, B. & Vrnak, B. (2018). The dependence of the peak velocity of high-speed solar wind streams as measured in the ecliptic by ace and the stereo satellites on the area and co-latitude of their solar source coronal holes. *Journal of Geophysical Research: Space Physics*, **123**, 1738–1753. (Cited on page 114.)

Kahler, S.W. (1992). Solar flares and coronal mass ejections. *Annual Review of Astronomy & Astrophysics*, **30**, 113–141. (Cited on page 24.)

Kassambara, A. (2018). *Machine Learning Essentials: Practical Guide in R*. Statistical Tools for High-throughput Data Analysis. (Cited on pages 66 and 67.)

Kavanagh, A. & Denton, M. (2007). High-speed solar-wind streams and geospace interactions. *Astronomy & Geophysics*, **48**, 6.24–6.26. (Cited on page 28.)

Khan, S., Rahmani, H., Shah, S.A.A., Bennamoun, M., Medioni, G. & Dickinson, S. (2018). *A Guide to Convolutional Neural Networks for Computer Vision*. Morgan & Claypool. (Cited on page 71.)

Klimchuk, J.A. & Sturrock, P.A. (1992). Three-dimensional force-free magnetic fields and flare energy buildup. *Astrophysical Journal*, **385**, 344–353. (Cited on page 14.)

Koehrsen, W. (2017). Random forest simple explanation. `https://medium.com/@williamkoehrsen/random-forest-simple-explanation-377895a60d2d`. (Cited on page 70.)

Krieger, A.S., Timothy, A.F. & Roelof, E.C. (1973). A Coronal Hole and Its Identification as the Source of a High Velocity Solar Wind Stream. *Solar Physics*, **29**, 505–525. (Cited on pages 92 and 105.)

Krista, L.D. & Gallagher, P.T. (2009). Automated Coronal Hole Detection Using Local Intensity Thresholding Techniques. *Solar Physics*, **256**, 87–100. (Cited on pages 31, 53, 54, 55 and 92.)

Krista, L.D., Gallagher, P.T. & Bloomfield, D.S. (2011). Short-term Evolution of Coronal Hole Boundaries. *Astrophysical Journal Letters*, **731**, L26. (Cited on page 18.)

Krista, L.D., McIntosh, S.W. & Leamon, R.J. (2018). The Longitudinal Evolution of Equatorial Coronal Holes. *Astronomical Journal*, **155**, 153. (Cited on page 144.)

Krizhevsky, A., Sutskever, I. & Hinton, G.E. (2012). Imagenet classification with deep convolutional neural networks. In F. Pereira, C.J.C. Burges, L. Bottou & K.Q. Weinberger, eds., *Advances in Neural Information Processing Systems 25*, 1097–1105, Curran Associates, Inc. (Cited on page 71.)

Landi, E. & Feldman, U. (2008). The Thermal Structure of an Active Region Observed Outside the Solar Disk. *Astrophysical Journal*, **672**, 674–683. (Cited on page 11.)

Lecun, Y., Bengio, Y. & Hinton, G. (2015). Deep learning. *Nature*, **521**, 436–444. (Cited on page 70.)

Leighton, R.B. (1964). Transport of Magnetic Fields on the Sun. *Astrophysical Journal*, **140**, 1547. (Cited on page 18.)

Leighton, R.B. (1969). A Magneto-Kinematic Model of the Solar Cycle. *Astrophysical Journal*, **156**, 1. (Cited on page 18.)

Lemen, J.R., Title, A.M., Akin, D.J., Boerner, P.F., Chou, C., Drake, J.F., Duncan, D.W., Edwards, C.G., Friedlaender, F.M., Heyman, G.F., Hurlburt, N.E., Katz, N.L., Kushner, G.D., Levay, M., Lindgren, R.W., Mathur, D.P., McFeaters, E.L., Mitchell, S., Rehse, R.A., Schrijver, C.J., Springer, L.A., Stern, R.A., Tarbell, T.D., Wuelser, J.P., Wolfson, C.J., Yanari, C., Bookbinder, J.A., Cheimets, P.N., Caldwell, D., Deluca, E.E., Gates, R., Golub, L., Park, S., Podgorski, W.A., Bush, R.I., Scherrer, P.H., Gummin, M.A., Smith, P., Auker, G., Jerram, P., Pool, P., Soufli, R., Windt, D.L., Beardsley, S., Clapp, M., Lang, J. & Waltham, N. (2012). The Atmospheric Imaging Assembly (AIA) on the Solar Dynamics Observatory (SDO). *Solar Physics*, **275**, 17–40. (Cited on pages 9, 39, 41 and 42.)

Levine, R.H., Altschuler, M.D. & Harvey, J.W. (1977). Solar sources of the interplanetary magnetic field and solar wind. *Journal of Geophysical Research*, **82**, 1061–1065. (Cited on page 61.)

Limpert, E., Stahel, W.A. & Abbt, M. (2001). Log-normal distributions across the sciences: Keys and clues. *BioScience*, **51**, 341–352. (Cited on page 139.)

MACKAY, D.H. & YEATES, A.R. (2012). The sun's global photospheric and coronal magnetic fields: Observations and models. *Living Reviews in Solar Physics*, **9**, 6. (Cited on page 5.)

MARISKA, J.T. (1992). *The Solar Transition Region*. (Cited on page 7.)

MATSUNO, T. (1966). Quasi-geostrophic motions in the equatorial area. *Journal of the Meteorological Society of Japan. Ser. II*, **44**, 25–43. (Cited on page 158.)

MAXWELL, J.C. (1865). Viii. a dynamical theory of the electromagnetic field. *Philosophical Transactions of the Royal Society of London*, **155**, 459–512. (Cited on page 28.)

MCCLOSKEY, A.E., GALLAGHER, P.T. & BLOOMFIELD, D.S. (2018). Flare forecasting using the evolution of McIntosh sunspot classifications. *Journal of Space Weather and Space Climate*, **8**, A34. (Cited on page 161.)

MCCOMAS, D.J., VELLI, M., LEWIS, W.S., ACTON, L.W., BALAT-PICHELIN, M., BOTHMER, V., DIRLING JR., R.B., FELDMAN, W.C., GLOECKLER, G., HABBAL, S.R., HASSLER, D.M., MANN, I., MATTHAEUS, W.H., MCNUTT JR., R.L., MEWALDT, R.A., MURPHY, N., OFMAN, L., SITTLER JR., E.C., SMITH, C.W. & ZURBUCHEN, T.H. (2007). Understanding coronal heating and solar wind acceleration: Case for in situ near-sun measurements. *Reviews of Geophysics*, **45**. (Cited on page 22.)

MCINTOSH, P.S. (1990). The classification of sunspot groups. *Solar Physics*, **125**, 251–267. (Cited on page 5.)

MCINTOSH, S.W., LEAMON, R.J., EGELAND, R., DIKPATI, M., FAN, Y. & REMPEL, M. (2019). What the Sudden Death of Solar Cycles Can Tell Us About the Nature of the Solar Interior. *Solar Physics*, **294**, 88. (Cited on pages 157 and 158.)

MENZEL, W.P. & PURDOM, J.F.W. (1994). Introducing GOES-I: The First of a New Generation of Geostationary Operational Environmental Satellites. *Bulletin of the American Meteorological Society*, **75**, 757–782. (Cited on page 13.)

MICHELSON, A.A. (1927). *Studies in optics.*. Chicago, Ill: The University of Chicago Press. (Cited on page 80.)

MITCHELL, T.M. (1997). *Machine Learning*. McGraw-Hill, Inc., New York, NY, USA, 1st edn. (Cited on page 66.)

MITRA, A.P., ed. (1974). *Ionospheric effects of solar flares*, vol. 46 of *Astrophysics and Space Science Library*. (Cited on page 29.)

Molaro, P. (2008). Primordial Light Element Abundances. In J.H. Knapen, T.J. Mahoney & A. Vazdekis, eds., *Pathways Through an Eclectic Universe*, vol. 390 of *Astronomical Society of the Pacific Conference Series*, 472. (Cited on page 3.)

Munro, R.H. & Withbroe, G.L. (1972). Properties of a Coronal "hole" Derived from Extreme-Ultraviolet Observations. *Astrophysical Journal*, **176**, 511. (Cited on page 51.)

N. Obridko, V. & Vaisberg, O. (2017). On the history of the solar wind discovery. *Solar System Research*, **51**, 165–169. (Cited on page 19.)

Nakagawa, Y., Nozawa, S. & Shinbori, A. (2019). Relationship between the low-latitude coronal hole area, solar wind velocity, and geomagnetic activity during solar cycles 23 and 24. *Earth, Planets and Space*, **71**, 24. (Cited on page 114.)

Neugebauer, M. (1976). The quiet solar wind. *Journal of Geophysical Research*, **81**, 4664–4670. (Cited on page 21.)

Neugebauer, M. & Snyder, C.W. (1966). Mariner 2 Observations of the Solar Wind, 1, Average Properties. *Journal of Geophysical Research*, **71**, 4469. (Cited on page 21.)

Nieniewski, M. (2002). Segmentation of extreme ultraviolet (SOHO) Sun images by means of watershed and region merging. In A. Wilson, ed., *From Solar Min to Max: Half a Solar Cycle with SOHO*, vol. 508 of *ESA Special Publication*, 323–326. (Cited on page 57.)

Nolte, J.T., Krieger, A.S., Timothy, A.F., Gold, R.E., Roelof, E.C., Vaiana, G., Lazarus, A.J., Sullivan, J.D. & McIntosh, P.S. (1976). Coronal holes as sources of solar wind. *Solar Physics*, **46**, 303–322. (Cited on pages 31, 60, 61, 92, 114, 116 and 129.)

Nolte, J.T., Krieger, A.S. & Solodyna, C.V. (1978). Short term evolution of coronal hole boundaries. *Solar Physics*, **57**, 129–139. (Cited on page 18.)

Odstrcil, D. (2003). Modeling 3-D solar wind structure. *Advances in Space Research*, **32**, 497–506. (Cited on page 65.)

Odstrčil, D. & Pizzo, V.J. (1999a). Three-dimensional propagation of CMEs in a structured solar wind flow: 1. CME launched within the streamer belt. *Journal of Geophysical Research*, **104**, 483–492. (Cited on page 65.)

Odstrčil, D. & Pizzo, V.J. (1999b). Three-dimensional propagation of coronal mass ejections in a structured solar wind flow 2. CME launched adjacent to the streamer belt. *Journal of Geophysical Research*, **104**, 493–504. (Cited on page 65.)

Oghrapishvili, N.B., Bagashvili, S.R., Maghradze, D.A., Gachechiladze, T.Z., Japaridze, D.R., Shergelashvili, B.M., Mdzinarishvili, T.G. & Chargeishvili, B.B. (2018). Study of the solar coronal hole rotation. *Advances in Space Research*, **61**, 3039–3050. (Cited on page 110.)

Orrall, F.Q., Rottman, G.J. & Klimchuk, J.A. (1983). Outflow from the sun's polar corona. *Astrophysical Journal Letters*, **266**, L65–L68. (Cited on page 10.)

Oughton, E., Hapgood, M., Richardson, G., Beggan, C., Thomson, A., Gibbs, M., Burnett, C., Gaunt, C., Trichas, M., Dada, R. & Horne, R. (2018). A risk assessment framework for the socioeconomic impacts of electricity transmission infrastructure failure due to space weather: An application to the united kingdom. *Risk Analysis*. (Cited on page 31.)

Parenti, S. (2014). Solar prominences: Observations. *Living Reviews in Solar Physics*, **11**, 1. (Cited on page 13.)

Parisi, G.I., Kemker, R., Part, J.L., Kanan, C. & Wermter, S. (2019). Continual lifelong learning with neural networks: A review. *Neural Networks*, **113**, 54 – 71. (Cited on page 70.)

Parker, E. (1959). Extension of the Solar Corona into Interplanetary Space. *Journal of Geophysical Research*, **64**, 1675–1681. (Cited on page 19.)

Parker, E.N. (1958). Suprathermal Particle Generation in the Solar Corona. *Astrophysical Journal*, **128**, 677. (Cited on page 19.)

Parker, E.N. (1965). Dynamical Theory of the Solar Wind. *Space Science Reviews*, **4**, 666–708. (Cited on pages 19, 20 and 21.)

Parker, E.N. (1972). Topological Dissipation and the Small-Scale Fields in Turbulent Gases. *Astrophysical Journal*, **174**, 499. (Cited on page 7.)

Pedlosky, J. (1982). *Geophysical fluid dynamics*. (Cited on page 158.)

Pedregosa, F., Varoquaux, G., Gramfort, A., Michel, V., Thirion, B., Grisel, O., Blondel, M., Prettenhofer, P., Weiss, R., Dubourg, V., Vanderplas, J., Passos, A., Cournapeau, D., Brucher, M., Perrot, M. & Duchesnay, E. (2011). Scikit-learn: Machine learning in Python. *Journal of Machine Learning Research*, **12**, 2825–2830. (Cited on pages 69 and 72.)

Pérez-Suárez, D., Maloney, S.A., Higgins, P.A., Bloomfield, D.S., Gallagher, P.T., Pierantoni, G., Bonnin, X., Cecconi, B., Alberti, V., Bocchialini, K., Dierckxsens, M., Opitz, A., Le Blanc, A., Aboudarham, J., Bentley, R.B., Brooke, J., Coghlan, B., Csillaghy, A., Jacquey, C., Lavraud, B. & Messerotti, M. (2012).

Studying Sun-Planet Connections Using the Heliophysics Integrated Observatory (HELIO). *Solar Physics*, **280**, 603–621. (Cited on page 106.)

Pesnell, W.D., Thompson, B.J. & Chamberlin, P.C. (2012). The Solar Dynamics Observatory (SDO). *Solar Physics*, **275**, 3–15. (Cited on pages 9 and 36.)

Phillips, K. (1995). *Guide to the Sun*. Cambridge University Press. (Cited on pages 3, 7 and 11.)

Piddington, J.H. (1972). A Model of the Quiet Solar Atmosphere. *Solar Physics*, **27**, 402–419. (Cited on page 15.)

Pinto, R.F. & Rouillard, A.P. (2017). A Multiple Flux-tube Solar Wind Model. *Astrophysical Journal*, **838**, 89. (Cited on pages 62, 107 and 127.)

Pirjola, R. (2000). Geomagnetically induced currents during magnetic storms. *IEEE Transactions on Plasma Science*, **28**, 1867–1873. (Cited on page 30.)

Pizzo, V.J. (1985). Interplanetary shocks on the large scale - A retrospective on the last decade's theoretical efforts. *Washington DC American Geophysical Union Geophysical Monograph Series*, **35**, 51–68. (Cited on page 108.)

Press, W.H., Teukolsky, S.A., Vetterling, W.T. & Flannery, B.P. (2007). *Numerical Recipes 3rd Edition: The Art of Scientific Computing*. Cambridge University Press, New York, NY, USA, 3rd edn. (Cited on page 66.)

Quinlan, J.R. (1986). Induction of decision trees. *Mach. Learn.*, **1**, 81–106. (Cited on page 67.)

Reiss, M.A., Hofmeister, S.J., De Visscher, R., Temmer, M., Veronig, A.M., Delouille, V., Mampaey, B. & Ahammer, H. (2015). Improvements on coronal hole detection in SDO/AIA images using supervised classification. *Journal of Space Weather and Space Climate*, **5**, A23. (Cited on page 57.)

Riley, P., Linker, J.A. & Mikić, Z. (2001). An empirically-driven global MHD model of the solar corona and inner heliosphere. *Journal of Geophysical Research*, **106**, 15889–15902. (Cited on pages 62, 63, 64 and 109.)

Riley, P., Mikic, Z., Linker, J. & Zurbuchen, T.H. (2003). Understanding the Solar Sources of In Situ Observations. In M. Velli, R. Bruno, F. Malara & B. Bucci, eds., *Solar Wind Ten*, vol. 679 of *American Institute of Physics Conference Series*, 79–82. (Cited on pages 63 and 125.)

Riley, P., Linker, J.A. & Arge, C.N. (2015). On the role played by magnetic expansion factor in the prediction of solar wind speed. *Space Weather*, **13**, 154–169. (Cited on page 65.)

Rotter, T., Veronig, A.M., Temmer, M. & Vršnak, B. (2012). Relation Between Coronal Hole Areas on the Sun and the Solar Wind Parameters at 1 AU. *Solar Physics*, **281**, 793–813. (Cited on page 60.)

Ryan, D.F., Milligan, R.O., Gallagher, P.T., Dennis, B.R., Tolbert, A.K., Schwartz, R.A. & Young, C.A. (2012). The Thermal Properties of Solar Flares over Three Solar Cycles Using GOES X-Ray Observations. *Astrophysical Journal Supplemental Series*, **202**, 11. (Cited on page 12.)

Ryan, S. & Norton, A. (2010). *Stellar Evolution and Nucleosynthesis*. Cambridge University Press. (Cited on page 4.)

Sabine, E. (1852). VIII. On periodical laws discoverable in the mean effects of the larger magnetic disturbance.No. II. *Philosophical Transactions of the Royal Society of London.*, **142**, 103–124. (Cited on page 2.)

Saha, S. (2018). A comprehensive guide to convolutional neural networks the eli5 way. `https://towardsdatascience.com/a-comprehensive-guide-to-convolutional-neural-networks-the-eli5-way-3bd2b1164a53`. (Cited on page 73.)

Salpeter, E.E. (1952). Nuclear Reactions in the Stars. I. Proton-Proton Chain. *Physical Review*, **88**, 547–553. (Cited on page 3.)

Sazli, M. (2006). A brief review of feed-forward neural networks. *Communications, Faculty Of Science, University of Ankara*, **50**, 11–17. (Cited on page 71.)

Schatzman, E. (1949). The heating of the solar corona and chromosphere. *Annales d'Astrophysique*, **12**, 203. (Cited on page 7.)

Scherrer, P.H., Bogart, R.S., Bush, R.I., Hoeksema, J.T., Kosovichev, A.G., Schou, J., Rosenberg, W., Springer, L., Tarbell, T.D., Title, A., Wolfson, C.J., Zayer, I. & MDI Engineering Team (1995). The Solar Oscillations Investigation - Michelson Doppler Imager. *Solar Physics*, **162**, 129–188. (Cited on pages 44, 48 and 49.)

Scherrer, P.H., Schou, J., Bush, R.I., Kosovichev, A.G., Bogart, R.S., Hoeksema, J.T., Liu, Y., Duvall, T.L., Zhao, J., Title, A.M., Schrijver, C.J., Tarbell, T.D. & Tomczyk, S. (2012). The Helioseismic and Magnetic Imager (HMI) Investigation for the Solar Dynamics Observatory (SDO). *Solar Physics*, **275**, 207–227. (Cited on pages 36 and 42.)

Schmidhuber, J. (2015). Deep learning in neural networks: An overview. *Neural Networks*, **61**, 85 – 117. (Cited on page 70.)

SCHOU, J., ANTIA, H.M., BASU, S., BOGART, R.S., BUSH, R.I., CHITRE, S.M., CHRISTENSEN-DALSGAARD, J., DI MAURO, M.P., DZIEMBOWSKI, W.A., EFF-DARWICH, A., GOUGH, D.O., HABER, D.A., HOEKSEMA, J.T., HOWE, R., KORZENNIK, S.G., KOSOVICHEV, A.G., LARSEN, R.M., PIJPERS, F.P., SCHERRER, P.H., SEKII, T., TARBELL, T.D., TITLE, A.M., THOMPSON, M.J. & TOOMRE, J. (1998). Helioseismic Studies of Differential Rotation in the Solar Envelope by the Solar Oscillations Investigation Using the Michelson Doppler Imager. *Astrophysical Journal*, **505**, 390–417. (Cited on page 6.)

SCHWARTZ, S.J., CHALONER, C.P., CHRISTIANSEN, P.J., COATES, A.J., HALL, D.S., JOHNSTONE, A.D., GOUGH, M.P., NORRIS, A.J., RIJNBEEK, R.P., SOUTHWOOD, D.J. & WOOLLISCROFT, L.J.C. (1985). An active current sheet in the solar wind. *Nature*, **318**, 269–271. (Cited on page 16.)

SEATON, D.B. & DARNEL, J.M. (2018). Observations of an Eruptive Solar Flare in the Extended EUV Solar Corona. *Astrophysical Journal Letters*, **852**, L9. (Cited on page 154.)

SERVISS, G.P. (1909). *Curiosities of the Sky: A Popular Presentation of the Great Riddles and Mysteries of Astronomy*. Harper & Brothers, New York. (Cited on pages 15 and 51.)

SHAH, T. (2017). About train, validation and test sets in machine learning. `https://towardsdatascience.com/train-validation-and-test-sets-72cb40cba9e7`. (Cited on page 149.)

SHEELEY, N.R., JR. (2017). Origin of the Wang-Sheeley-Arge solar wind model. *History of Geo- and Space Sciences*, **8**, 21–28. (Cited on page 65.)

SHEELEY, N.R., JR., HOWARD, R.A., MICHELS, D.J., KOOMEN, M.J., SCHWENN, R., MUEHLHAEUSER, K.H. & ROSENBAUER, H. (1985). Coronal mass ejections and interplanetary shocks. *Journal of Geophysical Research*, **90**, 163–175. (Cited on page 25.)

SHIBATA, K., NITTA, N., STRONG, K.T., MATSUMOTO, R., YOKOYAMA, T., HIRAYAMA, T., HUDSON, H. & OGAWARA, Y. (1994). A gigantic coronal jet ejected from a compact active region in a coronal hole. *Astrophysical Journal Letters*, **431**, L51–L53. (Cited on page 18.)

SHUE, J.H., SONG, P., RUSSELL, C.T., STEINBERG, J.T., CHAO, J.K., ZASTENKER, G., VAISBERG, O.L., KOKUBUN, S., SINGER, H.J., DETMAN, T.R. & KAWANO, H. (1998). Magnetopause location under extreme solar wind conditions. *Journal of Geophysical Research*, **103**, 17691–17700. (Cited on page 28.)

SMITH, E.J. (2001). The heliospheric current sheet. *Journal of Geophysical Research*, **106**, 15819–15832. (Cited on page 22.)

SPIEGEL, E.A. & ZAHN, J.P. (1992). The solar tachocline. *Astronomy & Astrophysics*, **265**, 106–114. (Cited on page 4.)

Spruit, H.C. (1974). A model of the solar convection zone. *Solar Physics*, **34**, 277–290. (Cited on page 4.)

Stein, R.F. & Nordlund, A. (1989). Topology of convection beneath the solar surface. *Astrophysical Journal Letters*, **342**, L95–L98. (Cited on page 4.)

Stephenson, F.R., Willis, D.M. & Hallinan, T.J. (2004). The earliest datable observation of the aurora borealis. *Astronomy & Geophysics*, **45**, 6.15–6.17. (Cited on page 2.)

Stone, E.C., Frandsen, A.M., Mewaldt, R.A., Christian, E.R., Margolies, D., Ormes, J.F. & Snow, F. (1998). The Advanced Composition Explorer. *Space Science Reviews*, **86**, 1–22. (Cited on pages 49 and 50.)

Taagepera, R. (2008). *Making Social Sciences More Scientific: The Need for Predictive Models*. Oxford scholarship online: Political Science module, OUP Oxford. (Cited on page 137.)

Tan, P.N., Steinbach, M. & Kumar, V. (2005). *Introduction to Data Mining, (First Edition)*. Addison-Wesley Longman Publishing Co., Inc., Boston, MA, USA. (Cited on pages 67 and 68.)

Thompson, W.T. (2006). Coordinate systems for solar image data. *Astronomy & Astrophysics*, **449**, 791–803. (Cited on page 6.)

Timothy, A.F., Krieger, A.S. & Vaiana, G.S. (1975). The Structure and Evolution of Coronal Holes. *Solar Physics*, **42**, 135–156. (Cited on page 18.)

Tsurutani, B.T., Gonzalez, W.D., Lakhina, G.S. & Alex, S. (2003). The extreme magnetic storm of 1-2 September 1859. *Journal of Geophysical Research (Space Physics)*, **108**, 1268. (Cited on page 2.)

Tu, C.Y., Zhou, C., Marsch, E., Xia, L.D., Zhao, L., Wang, J.X. & Wilhelm, K. (2005). Solar Wind Origin in Coronal Funnels. *Science*, **308**, 519–523. (Cited on pages 22, 62 and 105.)

van Ballegooijen, A.A. & Martens, P.C.H. (1989). Formation and eruption of solar prominences. *Astrophysical Journal*, **343**, 971–984. (Cited on page 13.)

Verbanac, G., Vršnak, B., Veronig, A. & Temmer, M. (2011). Equatorial coronal holes, solar wind high-speed streams, and their geoeffectiveness. *Astronomy & Astrophysics*, **526**, A20. (Cited on page 127.)

Vernazza, J.E., Avrett, E.H. & Loeser, R. (1981). Structure of the solar chromosphere. III - Models of the EUV brightness components of the quiet-sun. *Astrophysical Journal Supplemental Series*, **45**, 635–725. (Cited on page 6.)

Vršnak, B., Temmer, M. & Veronig, A.M. (2007). Coronal Holes and Solar Wind High-Speed Streams: I. Forecasting the Solar Wind Parameters. *Solar Physics*, **240**, 315–330. (Cited on pages 60 and 127.)

Waldmeier, M. (1956). Synoptische Karten der Sonnenkorona. Mit 16 Textabbildungen. , **38**, 219. (Cited on page 14.)

Wang, Y.M. & Sheeley, N.R., Jr. (1990). Solar wind speed and coronal flux-tube expansion. *Astrophysical Journal*, **355**, 726–732. (Cited on pages xix, 17, 61, 62, 63 and 118.)

Wang, Y.M. & Sheeley, N.R., Jr. (1991). Why fast solar wind originates from slowly expanding coronal flux tubes. *Astrophysical Journal Letters*, **372**, L45–L48. (Cited on page 61.)

Wang, Y.M. & Sheeley, N.R., Jr. (1992). On potential field models of the solar corona. *Astrophysical Journal*, **392**, 310–319. (Cited on page 62.)

Wang, Y.M. & Sheeley, N.R., Jr. (1995). Solar Implications of ULYSSES Interplanetary Field Measurements. *Astrophysical Journal Letters*, **447**, L143. (Cited on page 61.)

Wang, Y.M., Sheeley, N.R., Jr., Phillips, J.L. & Goldstein, B.E. (1997). Solar Wind Stream Interactions and the Wind Speed-Expansion Factor Relationship. *Astrophysical Journal Letters*, **488**, L51–L54. (Cited on pages 61 and 127.)

Warren, H.P. & Brooks, D.H. (2009). The Temperature and Density Structure of the Solar Corona. I. Observations of the Quiet Sun with the EUV Imaging Spectrometer on Hinode. *Astrophysical Journal*, **700**, 762–773. (Cited on page 7.)

Webb, D.F., Gibson, S.E., Hewins, I.M., McFadden, R.H., Emery, B.A., Malanushenko, A. & Kuchar, T.A. (2018). Global solar magnetic field evolution over 4 solar cycles: Use of the mcintosh archive. *Frontiers in Astronomy and Space Sciences*, **5**, 23. (Cited on page 18.)

Wenzel, K.P., Marsden, R.G., Page, D.E. & Smith, E.J. (1992). The ULYSSES Mission. *Astronomy & Astrophysics Supplemental*, **92**, 207. (Cited on page 63.)

Woods, T.N., Eparvier, F.G., Hock, R., Jones, A.R., Woodraska, D., Judge, D., Didkovsky, L., Lean, J., Mariska, J., Warren, H., McMullin, D., Chamberlin, P., Berthiaume, G., Bailey, S., Fuller-Rowell, T., Sojka, J., Tobiska, W.K. & Viereck, R. (2012). Extreme Ultraviolet Variability Experiment (EVE) on the Solar Dynamics Observatory (SDO): Overview of Science Objectives, Instrument Design, Data Products, and Model Developments. *Solar Physics*, **275**, 115–143. (Cited on page 36.)

Yang, S.H., Zhang, J., Jin, C.L., Li, L.P. & Duan, H.Y. (2009). Response of the solar atmosphere to magnetic field evolution in a coronal hole region. *Astronomy & Astrophysics*, **501**, 745–753. (Cited on page 8.)

Zirin, H. (1998). *The Astrophysics of the Sun*. (Cited on page 22.)

Zou, K., Tuncali, K. & G Silverman, S. (2003). Correlation and simple linear regression. *Radiology*, **227**, 617–22. (Cited on page 66.)

8

Appendix

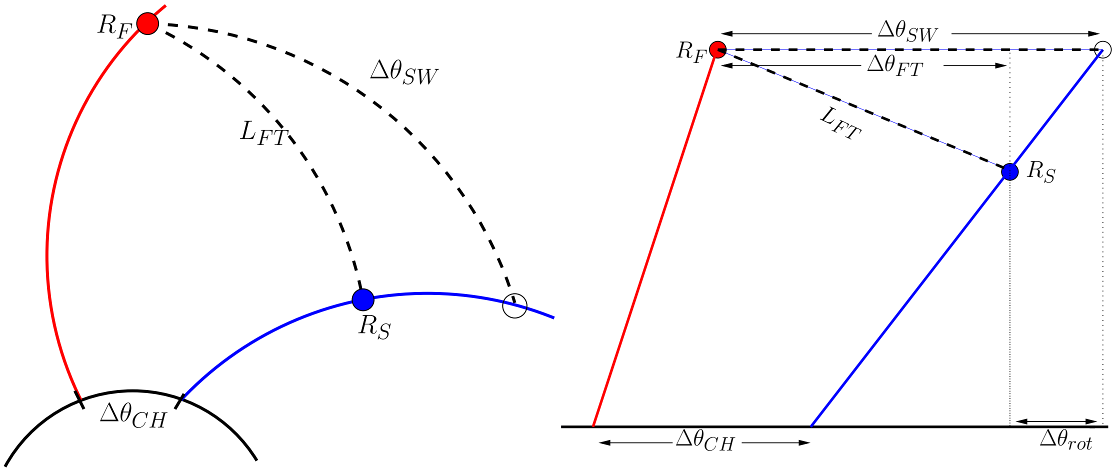

Figure 8.1: (a.) Projection of a HSSW stream with a leading boundary (red) originating from the western CH boundary and a trailing boundary (blue) originating from the eastern CH boundary. R_F and R_S show the distance traveled by plasma packets emitted at the same time but traveling at different velocities. $\Delta\theta_{SW}$ represent the path of Earth through the HSSW stream and L_{FT} approximates the continuous line of plasma packages, emitted from the Sun at the same time, when the leading boundary reaches some R_F (b.) An identical projection of the HSSW in polar space. $\Delta\theta_{rot}$ here represents the angular difference between the trailing boundary of the HSSW at R_F and R_S and $\Delta\theta_{FT}$ is the longitudinal angular width of the HSSW flux-tube projected out to R_F.

8.1 Full Derivation of the Longitudinal CH Flux Tube Expansion Equation

From the WSA model:

$$f = \frac{A_r}{A_\odot}\left(\frac{r_\odot}{r}\right)^2 \tag{8.1}$$

Applying the WSA model linearly returns a ratio of two angular widths:

$$f_{SW} = \frac{\Delta\theta_{SW}}{\Delta\theta_{CH}} = \frac{l_{SW}}{r_{SW}}\left(\frac{r_{CH}}{l_{CH}}\right) \tag{8.2}$$

where l_{SW} and l_{CH} are the respective arclengths of the HSSW and CH surface. By correcting for delayed arrival time of leading and trailing HSSW boundary, a corrected flux tube expansion factor is found as:

$$f_{FT} = \frac{L_{FT}}{r}\left(\frac{r_{CH}}{l_{CH}}\right) = \frac{1}{\Delta\theta_{CH}}\int_0^{L_{FT}} \frac{\delta L_{FT}}{r} \tag{8.3}$$

Assuming the plasma emitted at equal times from the CH surface will form a spiral shape as it travels through the heliosphere, the length of a spiral can be calculated as:

$$L_{FT} = \int_0^{L_{FT}} dL_{FT} = \int_0^{\Delta\theta_{FT}} \sqrt{r^2 + \frac{\delta r}{\delta\theta}^2}\,\delta\theta \tag{8.4}$$

Hence, the corrected flux tube expansion factor, f_{FT}, is the sum of many small expansions along a spiral arm, or:

$$\therefore f_{FT} = \frac{1}{\Delta\theta_{CH}}\int_0^{\Delta\theta_{FT}} \frac{\sqrt{r^2 + \frac{\delta r}{\delta\theta}^2}}{r}\delta\theta \tag{8.5}$$

$$f_{FT} = \frac{1}{\Delta\theta_{CH}}\int_0^{\Delta\theta_{FT}} \sqrt{\frac{r^2 + \frac{\delta r}{\delta\theta}^2}{r^2}}\delta\theta \tag{8.6}$$

$$f_{FT} = \frac{1}{\Delta\theta_{CH}}\int_0^{\Delta\theta_{FT}} \sqrt{1 + \frac{1}{r^2}\frac{\delta r}{\delta\theta}^2}\,\delta\theta \tag{8.7}$$

For a spiral arm, the radius changes as:

$$r = c + m\theta \tag{8.8}$$

where c is the initial radius of the spiral and m is the slope of the spiral in polar coordinates. Here the radius changes as:

$$r = R_S + \frac{(R_F - R_S)}{\Delta\theta_{FT}}\theta \tag{8.9}$$

where $\Delta\theta_{FT}$ is the angular width of the spiral, R_S is the radius of the trailing boundary at some time t and R_F is the radius of the leading boundary at that same time. Hence, R_S can be calculated as a function of R_F as:

$$R_S = R_F\left(\frac{v_S}{v_F}\right) \tag{8.10}$$

Hence, the radius of a spiral can now be calculated as:

$$r = R_F\left(\frac{v_S}{v_F}\right) + \frac{\left(R_F - R_F\left(\frac{v_S}{v_F}\right)\right)}{\Delta\theta_{FT}}\theta \tag{8.11}$$

$$r = R_F\left[\left(\frac{v_S}{v_F}\right) + \frac{\left(1 - \left(\frac{v_S}{v_F}\right)\right)}{\Delta\theta_{FT}}\theta\right] \tag{8.12}$$

$$r = R_F\left[\frac{v_S\Delta\theta_{FT} + (v_F - v_S)\,\theta}{v_F\Delta\theta_{FT}}\right] \tag{8.13}$$

By substituting $\Delta v = v_F - v_S$

$$r = R_F\left[\frac{v_S\Delta\theta_{FT} + \theta\Delta v}{v_F\Delta\theta_{FT}}\right] \tag{8.14}$$

$$\frac{\delta r}{\delta\theta} = R_F\left[\frac{\Delta v}{v_F\Delta\theta_{FT}}\right] \tag{8.15}$$

Substituting Equation 14 and 15 into 7 becomes:

$$f_{FT} = \frac{1}{\Delta\theta_{CH}}\int_0^{\Delta\theta_{FT}}\sqrt{1 + \frac{1}{R_F^2}\left[\frac{v_F\Delta\theta_{FT}}{v_S\Delta\theta_{FT} + \theta\Delta v}\right]^2\left(R_F\left[\frac{\Delta v}{v_F\Delta\theta_{FT}}\right]\right)^2}\,\delta\theta \tag{8.16}$$

which simplifies to:

$$\therefore f_{FT} = \frac{1}{\Delta\theta_{CH}}\int_0^{\Delta\theta_{FT}}\sqrt{1 + \left[\frac{\Delta v}{v_S\Delta\theta_{FT} + \theta\Delta v}\right]^2}\,\delta\theta \tag{8.17}$$

This Integral can be solved to be Equation 30 using the following methods:

Substitute $w = \theta\Delta v + v_S\Delta\theta_{FT}$ and $\delta\theta = (1/\Delta v)\delta w$

$$f_{FT} = \left(\frac{1}{\Delta v\Delta\theta_{CH}}\right)\int_{w_1}^{w_2}\sqrt{1+\left(\frac{\Delta v}{w}\right)^2}\delta w \tag{8.18}$$

Substitute $y = \sqrt{w^2+\Delta v^2}$ and $\delta w = (\sqrt{w^2+\Delta v^2})/w$

$$f_{FT} = \left(\frac{1}{\Delta v\Delta\theta_{CH}}\right)\int_{y_1}^{y_2}\frac{y^2}{(y-\Delta v)(y+\Delta v)}\delta y \tag{8.19}$$

$$f_{FT} = \left(\frac{1}{\Delta v\Delta\theta_{CH}}\right)\left[\Delta v^2\int_{y_1}^{y_2}\frac{1}{(y-\Delta v)(y+\Delta v)}\delta y + \int_{y_1}^{y_2} 1\delta y\right] \tag{8.20}$$

$$f_{FT} = \left(\frac{1}{\Delta v\Delta\theta_{CH}}\right)\left[y|_{y_1}^{y_2} + \Delta v^2\int_{y_1}^{y_2}\frac{1}{(y-\Delta v)(y+\Delta v)}\delta y\right] \tag{8.21}$$

Solving $\int_{y_1}^{y_2}\frac{1}{(y-\Delta v)(y+\Delta v)}\delta y$: substitute $z = y - \Delta v$ and $\delta y = \delta z$

$$\int_{y_1}^{y_2}\frac{1}{(y-\Delta v)(y+\Delta v)}\delta y = \int_{z_1}^{z_2}\frac{1}{z(z+2\Delta v)}\delta z = \int_{z_1}^{z_2}\frac{1}{z^2(1+(2\Delta v/z))}\delta z \tag{8.22}$$

Substitute $a = \frac{2\Delta v}{z} + 1$ and $\delta z = -\frac{z^2}{2\Delta v}\delta a$

$$\int_{y_1}^{y_2}\frac{1}{(y-\Delta v)(y+\Delta v)}\delta y = -\frac{1}{2\Delta v}\int_{a_1}^{a_2}\frac{1}{a}\delta a = -\frac{ln(a)}{2\Delta v}|_{a_1}^{a_2} \tag{8.23}$$

$$\therefore f_{FT} = \left(\frac{1}{\Delta v\Delta\theta_{CH}}\right)\left[y|_{y_1}^{y_2} + \Delta v^2(-\frac{ln(a)}{2\Delta v}|_{a_1}^{a_2})\right] \tag{8.24}$$

Undoing $a = \frac{2\Delta v}{z} + 1$:

$$f_{FT} = \left(\frac{1}{\Delta v\Delta\theta_{CH}}\right)\left[y|_{y_1}^{y_2} - \frac{\Delta v}{2}(ln\left(\frac{2\Delta v}{z}+1\right)|_{z_1}^{z_2})\right] \tag{8.25}$$

Undoing $z = y - \Delta v$:

$$f_{FT} = \left(\frac{1}{\Delta v\Delta\theta_{CH}}\right)\left[y|_{y_1}^{y_2} - \frac{\Delta v}{2}(ln\left(\frac{2\Delta v}{y-\Delta v}+1\right)|_{y_1}^{y_2})\right] \tag{8.26}$$

Undoing $y = \sqrt{w^2 + \Delta v^2}$:

$$f_{FT} = \left(\frac{1}{\Delta v \Delta\theta_{CH}}\right)\left[\sqrt{w^2 + \Delta v^2}|_{w_1}^{w_2} - \frac{\Delta v}{2}(ln\left(\frac{2\Delta v}{\sqrt{w^2 + \Delta v^2} - \Delta v} + 1\right)|_{w_1}^{w_2})\right] \tag{8.27}$$

Undoing $w = \theta\Delta v + v_S\Delta\theta_{FT}$:

$$f_{FT} = \left(\frac{1}{\Delta v \Delta\theta_{CH}}\right)\left[\sqrt{(\theta\Delta v + v_S\Delta\theta_{FT})^2 + \Delta v^2}|_0^{\Delta\theta_{FT}} - \frac{\Delta v}{2}(ln\left(\frac{2\Delta v}{\sqrt{(\theta\Delta v + v_S\Delta\theta_{FT})^2 + \Delta v^2} - \Delta v} + 1\right)|_0^{\Delta\theta_{FT}}) \right. \tag{8.28}$$

$$f_{FT} = \left[\frac{\sqrt{(\theta\Delta v + v_S\Delta\theta_{FT})^2 + \Delta v^2}}{\Delta v \Delta\theta_{CH}} - \frac{1}{2\Delta\theta_{CH}}(ln\left(\frac{2\Delta v}{\sqrt{(\theta\Delta v + v_S\Delta\theta_{FT})^2 + \Delta v^2} - \Delta v} + 1\right)\right]|_0^{\Delta\theta_F} \tag{8.29}$$

$$\begin{aligned} f_{FT} = {} & \frac{\sqrt{(v_F\Delta\theta_{FT})^2 + \Delta v^2} - \sqrt{(v_S\Delta\theta_{FT})^2 + \Delta v^2}}{\Delta\theta_{CH}\Delta v} \\ & + \frac{1}{2\Delta\theta_{CH}} ln\left(\frac{[\sqrt{(v_S\Delta\theta_{FT})^2 + \Delta v^2} + \Delta v][\sqrt{(v_F\Delta\theta_{FT})^2 + \Delta v^2} - \Delta v]}{[\sqrt{(v_S\Delta\theta_{FT})^2 + \Delta v^2} - \Delta v][\sqrt{(v_F\Delta\theta_{FT})^2 + \Delta v^2} + \Delta v]}\right) \end{aligned} \tag{8.30}$$

which can be expressed as:

$$f_{FT} = \frac{\alpha - \beta}{\theta_{CH}\Delta v} + \frac{1}{2\theta_{CH}} ln\left(\frac{[\beta + \Delta v][\alpha - \Delta v]}{[\beta - \Delta v][\alpha + \Delta v]}\right) \tag{8.31}$$

$$\alpha = \sqrt{(v_F\Delta\theta_{FT})^2 + \Delta v^2} \tag{8.32}$$

$$\beta = \sqrt{(v_S\Delta\theta_{FT})^2 + \Delta v^2} \tag{8.33}$$

8.2 Lower Limit of CH Flux Tube Expansion Equation

$$f_{FT} = \frac{\alpha - \beta}{\theta_{CH}\Delta v} + \frac{1}{2\theta_{CH}} ln\left(\frac{[\beta + \Delta v][\alpha - \Delta v]}{[\beta - \Delta v][\alpha + \Delta v]}\right) \tag{8.34}$$

$$\alpha = \sqrt{(v_F \Delta\theta_{FT})^2 + \Delta v^2} \tag{8.35}$$

$$\beta = \sqrt{(v_S \Delta\theta_{FT})^2 + \Delta v^2} \tag{8.36}$$

$$\Delta\theta_{FT} = f_{SW}\Delta\theta_{CH} - \omega_{\odot} R_F \left(\frac{1}{v_S} - \frac{1}{v_F}\right) \tag{8.37}$$

Assuming $v_F \propto$ CH area (const * $\Delta\theta_{CH}^2$)

$$\lim_{\Delta\theta_{CH}\to 0} \Delta\theta_{FT}(\Delta\theta_{CH}) = f_{SW}\Delta\theta_{CH} - \omega_{\odot} R_F \left(\frac{1}{v_S} - \frac{1}{v_S + c\Delta\theta_{CH}^2}\right) = f_{SW}\Delta\theta_{CH} = 0 \tag{8.38}$$

$$\begin{aligned}\lim_{\Delta\theta_{CH}\to 0} \alpha(\Delta\theta_{CH}) &= \sqrt{(v_F f_{SW}\Delta\theta_{CH})^2 + (v_S + c\Delta\theta_{CH}^2 - v_S)^2} = \sqrt{(v_F f_{SW}\Delta\theta_{CH})^2} \\ &= v_F f_{SW}\Delta\theta_{CH} = 0\end{aligned} \tag{8.39}$$

$$\begin{aligned}\lim_{\Delta\theta_{CH}\to 0} \beta(\Delta\theta_{CH}) &= \sqrt{(v_S f_{SW}\Delta\theta_{CH})^2 + (v_S + c\Delta\theta_{CH}^2 - v_S)^2} = \sqrt{(v_S f_{SW}\Delta\theta_{CH})^2} \\ &= v_S f_{SW}\Delta\theta_{CH} = 0\end{aligned} \tag{8.40}$$

$$\lim_{\Delta\theta_{CH}\to 0} f_{FT}(\Delta\theta_{CH}) = \frac{\alpha - \beta}{\Delta\theta_{CH}\Delta v} + \frac{1}{2\Delta\theta_{CH}} ln\left(\frac{[\beta + \Delta v][\alpha - \Delta v]}{[\beta - \Delta v][\alpha + \Delta v]}\right) \tag{8.41}$$

$$\lim_{\Delta\theta_{CH}\to 0} f_{FT}(\Delta\theta_{CH}) = \frac{v_F f_{SW}\Delta\theta_{CH} - v_S f_{SW}\Delta\theta_{CH}}{\Delta\theta_{CH}\Delta v} + \frac{1}{2\Delta\theta_{CH}} ln\left(\frac{[v_S f_{SW}\Delta\theta_{CH} + \Delta v][v_F f_{SW}\Delta\theta_{CH} - \Delta v]}{[v_S f_{SW}\Delta\theta_{CH} - \Delta v][v_F f_{SW}\Delta\theta_{CH} + \Delta v]}\right) \tag{8.42}$$

$$\lim_{\Delta\theta_{CH}\to 0} f_{FT}(\Delta\theta_{CH}) = \frac{\Delta v f_{SW}\Delta\theta_{CH}}{\Delta\theta_{CH}\Delta v} + \frac{1}{2\Delta\theta_{CH}} ln\left(\frac{[v_S f_{SW}\Delta\theta_{CH} + \Delta v][v_F f_{SW}\Delta\theta_{CH} - \Delta v]}{[v_S f_{SW}\Delta\theta_{CH} - \Delta v][v_F f_{SW}\Delta\theta_{CH} + \Delta v]}\right) \tag{8.43}$$

As $\Delta\theta_{CH} \to 0$, $v_F \to v_S$

$$\lim_{\Delta\theta_{CH}\to 0} f_{FT}(\Delta\theta_{CH}) = f_{SW} + \frac{1}{2\Delta\theta_{CH}} ln\left(\frac{[v_S f_{SW}\Delta\theta_{CH} + \Delta v][v_S f_{SW}\Delta\theta_{CH} - \Delta v]}{[v_S f_{SW}\Delta\theta_{CH} - \Delta v][v_S f_{SW}\Delta\theta_{CH} + \Delta v]}\right) \tag{8.44}$$

$$\lim_{\Delta\theta_{CH}\to 0} f_{FT}(\Delta\theta_{CH}) = f_{SW} + \frac{ln\,(1)}{2\Delta\theta_{CH}} \tag{8.45}$$

$$\lim_{\Delta\theta_{CH}\to 0} f_{FT}(\Delta\theta_{CH}) = f_{SW} \tag{8.46}$$

Assuming $v_F \propto$ CH width ($\Delta\theta_{CH}$)

$$\lim_{\Delta\theta_{CH}\to 0} \alpha(\Delta\theta_{CH}) = \sqrt{(v_F f_{SW}\Delta\theta_{CH})^2 + (\Delta v)^2} = \sqrt{(v_S f_{SW}\Delta\theta_{CH})^2 + (\Delta v)^2} = \beta = 0 \tag{8.47}$$

$$\lim_{\Delta\theta_{CH}\to 0} f_{FT}(\Delta\theta_{CH}) = \frac{\alpha - \beta}{\Delta\theta_{CH}\Delta v} + \frac{1}{2\Delta\theta_{CH}} ln\left(\frac{[\beta + \Delta v][\alpha - \Delta v]}{[\beta - \Delta v][\alpha + \Delta v]}\right) \tag{8.48}$$

$$\lim_{\Delta\theta_{CH}\to 0} f_{FT}(\Delta\theta_{CH}) = \frac{\beta-\beta}{\Delta\theta_{CH}\Delta v} + \frac{1}{2\Delta\theta_{CH}} ln\left(\frac{[\beta+\Delta v][\beta-\Delta v]}{[\beta-\Delta v][\beta+\Delta v]}\right) \tag{8.49}$$

$$\lim_{\Delta\theta_{CH}\to 0} f_{FT}(\Delta\theta_{CH}) = \frac{\beta-\beta}{\Delta\theta_{CH}\Delta v} + \frac{1}{2\Delta\theta_{CH}} ln\left(1\right) \tag{8.50}$$

$$\lim_{\Delta\theta_{CH}\to 0} f_{FT}(\Delta\theta_{CH}) = \frac{\beta-\beta}{\Delta\theta_{CH}\Delta v} \tag{8.51}$$

$$\lim_{\Delta\theta_{CH}\to 0} f_{FT}(\Delta\theta_{CH}) = \frac{0-0}{0*0} \to 1 \tag{8.52}$$